Metal Modified Boron Doped Diamond Electrodes and their Use in Electroanalysis

Kathryn Ellen Toghill



St John's College
University of Oxford

Supervisor: Prof. Richard G. Compton

Hilary Term **2011**

A Thesis for the Degree of Doctor in Philosophy in Physical and Theoretical Chemistry

Contents

Contents (ii – vi)

Abstract (vii)

CHAPTER 1: Introduction to Electrochemistry **1 - 40**

1.1. The Beginning of Electrochemistry 1 - 2
1.2. Electrochemical equilibria 2 - 6
1.2.1. Chemical and electrochemical equilibriums
1.2.2. Potential difference
1.2.3. Half-cell potentials
1.2.4. The Nernst Equation
1.3. Electrochemical Cells 6 - 10
1.3.1 Galvanic Cells
1.3.2. Electrolytic cells
1.3.3. Electrodes and the arrangement of electrochemical cells
1.3.4. Solvents and electrolyte solutions
1.4. Faradaic processes 11 - 25
1.4.1. Current and flux
1.4.2. Mass Transport
1.4.3. Diffusion
1.4.4 Electrode kinetics
1.5. Non-faradaic processes 26 - 28
1.5.1. The Electrical Double Layer
1.5.2. Capacitative Current and Double Layer Capacitance
1.6. Controlled Potential Techniques 28 - 39
1.6.1. Potential step methods
1.6.2. Potential Sweep methods
1.6.3. Pulse Voltammetric Techniques for Trace Analysis
1.6.4. Stripping analysis
1.7. References 40

CHAPTER 2: Surface Characterisation by Topographic Methods: SEM, AFM and EC-AFM **41 - 70**

2.1. Optical microscopes 41 – 42
2.2. Scanning Electron Microscopes (SEM) 42 - 52
2.2.1 The history of electron microscopes
2.2.2. The formation of an electron beam
2.2.3 Transmission electron microscopy (TEM)
2.2.4. Scanning electron microscopy (SEM)
2.2.5. Advances and limitations of electron microscopy
2.3. Scanning Probe Microscopy 52 - 66

2.3.1. History of scanning probe techniques
2.3.2. Scanning Tunnelling Microscopy (STM)
2.3.3. Atomic Force Microscopy (AFM)
2.4. Electrochemical Atomic Force Microscopy (EC-AFM) 66 - 68
2.4.1. Limitations of ex-situ surface characterisation
2.4.2. The development of dynamic EC-AFM
2.4.3. Current technology
2.5. References 69 - 70

CHAPTER 3: The development of an EC-AFM cell **71 - 83**

3.1 Asylum Research 71 - 73
3.1.1. About the company
3.1.2. Asylum Research technology – the MFP-3D Atomic Force Microscope
3.2. EC-AFM project aims 73 – 74
3.3. The requirements of an EC-AFM cell 74 – 75
3.4. EC-AFM cell – Prototype #1 75 – 78
3.4.1. Working electrode
3.4.2. Counter electrode
3.4.3. Reference electrode
3.4.4. Electrical connection
3.5. EC-AFM cell – Prototype #3 – The final product 78 – 81
3.5.1. Working electrode
3.5.2. Counter electrode
3.5.3. Reference electrode
3.5.3. Reference electrode
3.5.5. Other special features
3.6. In-situ EC-AFM experiments using the AR-Oxford design 81 – 82
3.7. Figure Acknowledgments 83

CHAPTER 4: An Introduction to Modified Boron Doped Diamond Electrodes and their Application to Electroanalysis **84 - 110**

4. 1. Introduction to boron doped diamond 85 - 86
4.2. The electrochemical properties of BDD electrodes 86 - 90
4.3. The fabrication of boron doped diamond electrodes 90 - 92
4.3.1. Growth conditions
4.3.2. Crystalline forms of CVD diamond
4.4. Metal nanoparticle modified BDD electrodes 92 - 104
4.4.1. Diffusional properties on nanoparticle arrays
4.4.2 Electrolytically deposited metal modified BDD electrodes
4.4.2 Metal ion implanted BDD electrodes
4.5 Conclusions 104 – 105

4.6 References 106 - 109

CHAPTER 5: Bismuth and Antimony Nanoparticle Modified Boron Doped Diamond Electrodes and Their Application to the Simultaneous Determination of Lead and Cadmium **110 - 136**

5.1. Introduction 111 - 114
5.1.1 Bismuth modified electrodes
5.1.2 Antimony modified electrodes
5.1.3 Boron doped diamond electrodes in stripping analysis
5.1.4 The analytes of anodic stripping voltammetric analysis
5.2. Experimental 114 – 116
5.3. Results and Discussion 117 - 132
5.3.1. Electroanlaysis at the Bi-BDD electrode
5.3.2. Electroanlaysis at the Sb-BDD electrode
5.4. Conclusions 132 – 134
5.5. References 134 - 136

CHAPTER 6: Electrochemical non-enzymatic glucose sensors **137 – 219**

6.1. Introduction 137 - 138
6.2. Enzymatic glucose sensors 139 – 145
6.2.1 First generation enzymatic glucose sensors
6.2.2 Second generation enzymatic glucose sensors
6.2.3 Third generation enzymatic glucose sensors
6.2.4 The advantages and disadvantages of enzymatic glucose electrodes
6.3. Non-enzymatic glucose sensors 145 – 187
6.3.1. The mutarotation of glucose
6.3.2 Theories of non-enzymatic electrocatalysis
6.3.3 Nanomaterials in glucose sensors
6.3.4 Platinum electrodes
6.3.5 Gold electrodes
6.3.6 Nickel electrodes
6.3.7 Copper electrodes
6.3.8 Alloys and bimetallic systems
6.3.9 Carbon based electrodes
6.4. Electroactive interferences and electrode fouling 187 – 195
6.4.1 Naturally occurring interferences
6.4.2 Pharmacological interferences
6.4.3 Proteins and chloride anions
6.4.4 Non-glucose sugars
6.4.5 Alcohol
6.4.6 Methods to overcome interference effects
6.5. The requirements of glucose monitoring 195 – 200
6.5.1 In vitro glucose monitoring: Single point 'fingerstick' glucose sensors

6.5.2 In vivo glucose monitoring: Continuous glucose sensors

6.6. Requirements of non-enzymatic blood glucose sensors 201 – 202

6.7 Other applications of non-enzymatic glucose electrodes 202 – 205

6.7.1 Industrial processes

6.7.2 Quality control

6.7.3 Fuel cells

6.8. Conclusions 206 – 207

6.9. References 207 – 219

CHAPTER 7: The Non-Enzymatic Determination of Glucose Using an Electrolytically Fabricated Nickel Microparticle Modified Boron Doped Diamond Electrode or Nickel Foil Electrode **220 – 248**

7.1. Introduction 221 – 223

7.2. Experimental 223 – 225

7.3. Results and discussion 225 – 243

7.3.1. Characterisation of the nickel- microparticle modified BDD electrode and nickel foil electrode

7.3.2 The electrochemical determination of glucose

7.3.3 The application and reproducibility of the Ni-BDD electrode

7.3.4 The effect of interferences on glucose oxidation

7.3.5 Stability and lifetime of the Ni-BDD electrode

7.3.6 Comparison of results to the literature review of non-enzymatic electrochemical glucose sensors in Chapter 6.

7.4. Conclusions 243 – 244

7.5. References 244 – 248

CHAPTER 8: The Determination of Primary Alcohols Using an Electrolytically Fabricated Nickel Modified Boron Doped Diamond Electrode **249 - 278**

8.1. Introduction 250 – 251

8.2. Experimental 251 – 253

8.3. Results and discussion 253 - 274

8.3.1 Characterisation of the nickel- nanoparticle modified BDD electrodes

8.3.2. The electrocatalysis of methanol electrooxidation

8.3.3. The electrocatalysis of ethanol and glycerol electrooxidation

8.3.4 Comparison of electrochemical methanol sensors

8.4. Conclusions 274 – 275

8.5. References 276 – 278

CHAPTER 9: Overall Conclusions **279 – 280**

Appendix 1 Asylum Research EC-AFM commercial cell brochure **281 – 282**

Abstract

The experimental work discussed in this thesis explores the effects of metal modification on the electroanalytical ability of boron doped diamond electrodes. Boron doped diamond (BDD) electrodes have found increased application to electroanalysis in the past two decades, yet relatively little of the literature is focused on metal, nano and microparticle modification of the substrate. In this thesis three metals have been used to modify the BDD electrode; bismuth, antimony and nickel.

Bismuth and antimony nanoparticle modified BDD electrodes were directly compared to unmodified BDD and a bulk bismuth electrodes in the determination of trace levels of cadmium and lead using anodic stripping voltammetry. In both instances, the modified electrode allowed for the simultaneous determination of each analyte that was otherwise unattainable at the unmodified BDD electrode.

The nickel modified BDD (Ni-BDD) electrode was used in the determination of organic analytes, namely glucose, methanol, ethanol and glycerol. The nickel nano and microparticle electrodes gave the characteristic $Ni(OH)_2$/NiOOH redox couple in alkali pH, the oxidised form of which (NiOOH) catalysed the oxidation of the organic analytes. The chapter on glucose sensing with the Ni-BDD electrode is preceded by an extensive literature review on the advances of non-enzymatic glucose sensing, and the application of catalytic metals and nanomaterials in this field.

Throughout the course of this DPhil, there has been a collaborative project between Asylum Research and myself within the Compton group to develop a commercial electrochemical atomic force microscope (EC-AFM) cell. The aim was to produce an adaptable EC-AFM cell capable of dynamic electrochemical experiments whilst simultaneously or instantaneously acquiring an AFM image of the modified surface, in-situ. This project was successful, and the EC-AFM cell has contributed to a number of chapters in this thesis, and has now been commercialised.

Chapter 1

An Introduction to Electrochemistry

Electrochemistry is a field dedicated to the processes that occur at the interface of phases that contain different concentrations and different types of charged species. It is a broad topic and therefore a highly interdisciplinary area of science, relating to numerous fields including chemistry, physics, biology, materials science and surface science. From photosynthesis, to lithium batteries, nerve propagation to the corrosion of water pipes, electrochemical processes are occurring. Understanding electrochemistry is therefore essential to gaining further insight into the world in which we live and to further advance technology. This chapter will introduce electrochemistry with respect to the kinetics and thermodynamics of electrode processes, and the information obtained from electrochemical experiments relevant to this thesis.

1.1. The beginning of electrochemistry

Electrochemical processes were first explored by Luigi Galvani at the end of the 18th century, following an accidental discovery involving frog legs. Galvani, a lecturer of anatomy at the University of Bologna, noticed that frog legs hanging out to dry on brass hooks would twitch if the hook came into contact with an iron fence. Galvani proceeded to experiment with what he called “animal electricity”, demonstrating that muscle contractions could be induced in a dead frog by placing two different metals at either side of the limb.

A contemporary of Galvani, and an experienced scientist in the field of electricity, Alessandro Volta contested Galvani’s findings. He claimed, correctly, that the cause of the muscle contraction was not ‘animal electricity’ but due to the external interaction of the two

metals, brass and iron. At Pavia University in Lombardy, Volta was a professor of experimental physics, and in papers published in 1792 and 93 he argued against Galvani's conclusions. In the following years Volta strove to prove his theories, and in a letter to the Royal Society of London in 1800 he outlined the invention that did exactly this. Volta described a stack of alternating silver and zinc discs which were separated by brine soaked cloth. On connecting the two ends with an external wire, a steady flow of electrical current was obtained, and as such the voltaic pile as it was known, became the precursor to modern day batteries, and the first step towards harnessing electrochemistry.

1.2 Electrochemical equilibrium

1.2.1. Chemical and electrochemical equilibria

At equilibrium and at constant pressure and temperature the standard Gibbs energy change of a system may be expressed as

$$\Delta G^0 = -RT \ln K_{eq} \qquad [1.1]$$

In equation 1.1, R and T are the gas constant and absolute temperature respectively, and K_{eq} is the equilibrium constant for a given chemical reaction such as shown in equation 1.2a. Depending on whether the reaction is gaseous or in solution, the equilibrium can be expressed in partial pressures or in concentrations, the latter, and most relevant to electrochemistry being shown in equation 1.2b.

$$\alpha A + \beta B \rightleftharpoons \gamma C + \delta D \qquad [1.2a]$$

$$K_{eq} = \frac{[C]^{\gamma}\,[D]^{\delta}}{[A]^{\alpha}\,[B]^{\beta}} \qquad [1.2b]$$

An electrochemical equilibrium is considered when an electrode is placed in a solution of ions, such that a transfer of charge to or from the electrode occurs to achieve an energetically stable system. The transfer of charge distinguishes an electrochemical reaction from a chemical reaction, as the chemical energies *and* the electrical energies must be considered.

1.2.2. Potential difference

An electrical current is observed due to various potential differences between the two metals and the solutions in which they are immersed. A potential difference arises when two dissimilar conducting materials come into contact. In electrochemistry, the transfer of charge is most frequently explored between a metallic electrode (*m*) and an ionic solution phase species (*aq*). Consider an aqueous solution of potassium ferrocyanide (Fe^{2+}) and ferricyanide (Fe^{3+}) into which a metal electrode is immersed. In this instance charge will exchange between the metal and the solution with a view to establish equilibrium between the two, based on the process in Equation 1.3.

$$\mathrm{Fe(CN)}_6^{3-}{}_{(aq)} + e^-_{(m)} \rightleftharpoons \mathrm{Fe(CN)}_6^{4-}{}_{(aq)} \qquad [1.3]$$

Electrons pass from the metal to the solution ions at the interface, or vice versa depending on the relative concentrations of ferri and ferrocyanide and the energy of the Fermi level relative to the unoccupied molecular orbitals of the solution species. Once the electrode and the solution are in energetic equilibrium then the transfer of electrons stops, and no further current is observed, yet due to the transfer of electrons a charge separation will generally occur with net electrical charge on both phases. The energy diagram in Figure 1.1 illustrates this process, and indicates the final charge on the metal and solution.

Consequently all the species in the system have an electrochemical potential, $\bar{\mu}_j$, which is the sum of two terms, one for the chemical energy (μ_j) and a second for the electrical energy.

$$\bar{\mu}_j = \mu_j + Z_j F\phi \qquad [1.4]$$

The electrical energy term is comprised of the charge on molecule j (Z_j), the Faraday constant (F) and the potential of the particular phase (ϕ). At equilibrium the electrochemical potentials of the species involved will be balanced in a manner akin to the

chemical expression, as demonstrated in Equation 1.5 using the iron centre of the system in Eq. 1.3.

$$\bar{\mu}_{Fe(III)} + \bar{\mu}_{e^-} = \bar{\mu}_{Fe(II)} \quad [1.5]$$

The potential difference across the electrode-electrolyte interface is shown in Eq. 1.6, where ϕ denotes the potential of the particular phase, metal (m) or solution (s).

$$\Delta_{m/s} = \phi_m - \phi_s \quad [1.6]$$

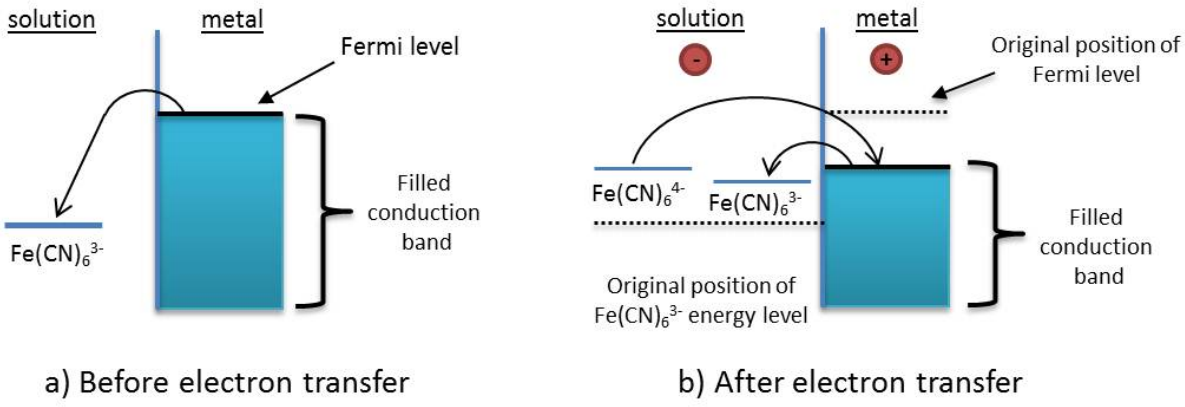


Figure 1.1: *An energy diagram of the electrode –solution interface, illustrating the energy difference between the metal and the solution phase before and after equilibrium is established. (Adapted from reference [2])*

1.2.3. Half-cell potentials

The quantity $\Delta\phi_{m/s}$ has a fixed and exact value, yet is not directly measurable, and can only be determined relative to a reference electrode of known, constant potential drop at its solution interface. As such, measurements of potential difference, E, may be made between the two electrodes based on Eq. 1.7 for the Fe^{3+}/Fe^{2+} system

$$E = \Delta\phi_{m/s}(Fe^{3+}/Fe^{2+}) - \Delta\phi_{m/s}(\text{reference}) \quad [1.7]$$

As the reference potential is considered a constant, the value E may be termed the electrode potential for the electrode process of interest. These values may be established for any electrochemical system using a simple electrochemical cell.

A simple electrochemical cell consists of two half-cells; one in which the species of interest is contained (e.g. ferro/ferricyanide) with a chemically inert electrode, and the other in which the reference electrode is contained. Both are in solution, but separated by a porous membrane or salt bridge, and the two electrodes are connected externally, passing through a voltmeter. This is depicted in Figure 1.2, in which the reference electrode is the standard hydrogen electrode (SHE).

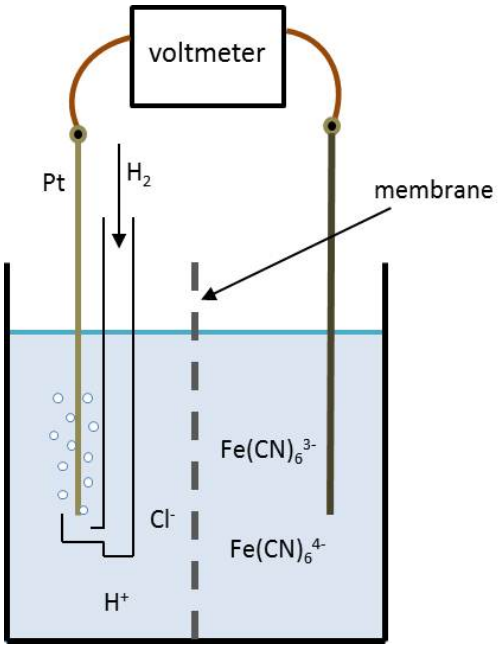


Figure 1.2: *A simple electrochemical cell consisting of two half cells.*

The SHE is the standard reference electrode by which all standard electrode potentials, E^o, are established, and is therefore considered to possess a potential of absolute zero. It consists of a platinum wire in HCl where the activity is 1, under a constant flow of gaseous hydrogen.

1.2.4. The Nernst Equation

The Nernst equation was derived in the late 19th century by Hermann Walther Nernst, a professor of Physical Chemistry at the Universities of first Gottingen and later Berlin. Nernst related the potential generated by an electrochemical cell to the chemical species that partake in the electrochemical reaction. It is derived from the combination of the thermodynamic expression for a chemical reaction (Equations 1.1-1.2) and the thermodynamic expression for electrical work done, where the number of electrons is *one*

$$\Delta G_{T,P} = -FE \qquad [1.8]$$

Electrical work done is defined as the work done when an electrical charge (F) moves through an electrical potential difference, $\Delta\phi_{m/s}$ (E). Combination of these equations gives Eq. 1.9.

$$-FE = \Delta G^{\circ} + RTln\frac{[C]^{\gamma}[D]^{\delta}}{[A]^{\alpha}[B]^{\beta}} \qquad [1.9]$$

The expression $-\Delta G^{\circ}/F$ may be defined as the standard electrode potential, E^{o}. Consequently we derive the Nernst equation, which at equilibrium as shown in Equation 1.10, the standard potential is equal to the equilibrated cell potential derived experimentally.

$$E_e = E^{\circ} - \frac{RT}{\mathrm{F}} ln\frac{[C]^{\gamma}[D]^{\delta}}{[A]^{\alpha}[B]^{\beta}} \qquad [1.10]$$

1.3. Electrochemical Cells

The key discovery made by Galvani and Volta were that a spontaneous electrical current is obtained when two different metals are connected by a suitably ionic medium and an external wire. This is a fundamental description of an electrochemical cell, in which electrochemical processes occur across a collection of electrode/solution interfaces.

Electrochemistry is primarily concerned with the transfer of charge across an electronic conductor (electrode) and ionic conductor (electrolyte), the interface of which

being the main focus. In general an electrochemical cell is a system in which electrical energy is either generated by a chemical reaction, or used to induce a chemical reaction, and it may therefore be classified in two ways; galvanic or electrolytic.

1.3.1 Galvanic Cells

By definition a galvanic cell is an electrochemical cell in which a current is passed through an external conductor driven solely by a chemical reaction. The reaction occurs once the electrodes are connected owing to a potential difference between the metals in the electrolyte. The reaction is spontaneous and no work is done to the electrochemical cell. In Figure 1.3(A) a galvanic cell is illustrated in which the two metal electrodes are copper and zinc.

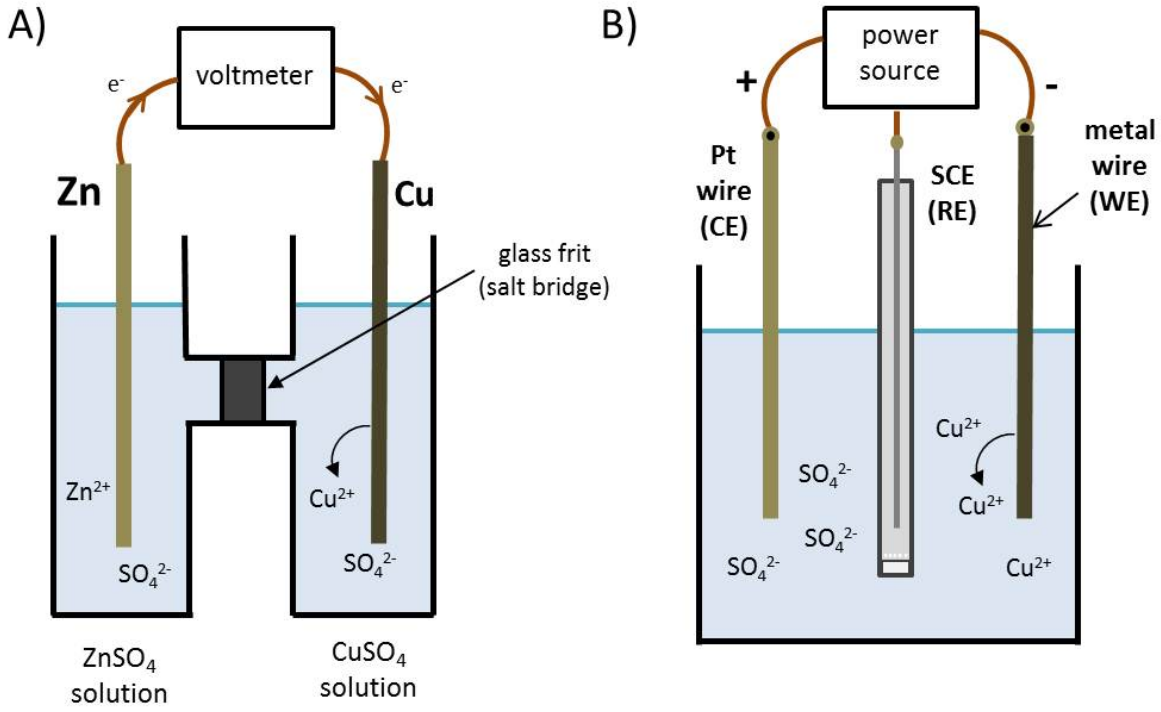


Figure 1.3: *A) The Daniell cell, a galvanic electrochemical cell consisting of a copper and a zinc electrode immersed in copper sulphate and zinc sulphate respectively, in which copper is reduced. (Adapted from [4]). B) A three electrode electrolytic cell of $CuSO_4$ in which a potential is applied, thus reducing copper at the generic metal electrode. The SCE measures the potential difference.*

They are each immersed in a sulphate solution of their own metal which are separated by salt bridge in the solution, and connected to a metal wire with a voltmeter externally. The galvanic cell is essentially what a battery is and the figure is actually depicting the electrochemical cell devised by John F. Daniell in 1836, an electrochemical cell invented to produce electrical energy before the invention of electric generators [4].

1.3.2. Electrolytic cells

An electrolytic cell is a cell in which current flows due to the application of an external energy (voltage) that drives an electrochemical reaction at the electrode/electrolyte interface. The oxidation or reduction of a species in this way is termed *electrolysis*. An electrolytic cell is shown in Figure 1.3(B) in which the reduction of copper ions is forced by a negative potential applied at the metal wire electrode.

1.3.3. Electrodes and the arrangement of electrochemical cells

Experimental electrochemistry can be performed using cells of two or three electrodes, depending on the nature of the cell (i.e. galvanic or electrolytic), or the quantity of current passing through the circuit. These are the working electrode (WE), reference electrode (RE) and optional counter electrode (CE). The electrodes are obviously key components of an electrochemical cell, and there are a wide variety of materials that serve as suitable electrodes depending on their application.

The *working electrode* is the electrode at which the processes of interest occur. The material of the working electrode is limitless so long as it is conducting or even semiconducting. Metals were originally used, and still are extensively. The conductivity of graphite has also made carbon a common electrode material, with such carbon electrodes as glassy carbon, carbon paste, edge and basal plane pyrolytic graphite, and screen printed carbon regularly used. More recently the use of carbon has extended to fullerene type species and carbon nanotubes, as well as semiconducting boron doped diamond.

The *reference electrode* is the electrode of known, constant electrode-solution potential difference that is used as a reference to measure the potential difference at the WE. It was described previously in the discussion regarding half-cell potentials and establishing potential difference and standard potentials. The standard reference electrode is the standard hydrogen or normal hydrogen electrode (SHE or NHE respectively) which is deemed to have the absolute zero potential. Due to complicated design of hydrogen bubbling over a platinum electrode in HCl, the SHE is not commonly used in electrochemical experiments. More common are the saturated calomel electrode (SCE), Ag/AgCl or the $Hg/HgSO_4$ electrodes.

The *counter electrode (or auxiliary)* is used in a three electrode arrangement and serves as a means to pass the counter current in the circuit when a current is induced at the working electrode. This can be any 'inert' conducting material of sufficient size that will not cause an interfering counter redox reaction in the electrochemical cell. Common CE materials are platinum or silver wire, or a graphite rod.

All electrochemical experiments require at least *two electrodes,* the working electrode at which the process of interest takes place, and the reference electrode to provide a basis for a potential difference. The galvanic cell in Figure 1.3 has a two electrode arrangement, in which there is a potential difference between the copper and zinc electrodes. When determining the standard electrode potential for an electrode, as is obtained from half-cell potentials, the second electrode is a RE of known and constant potential.

A *three electrode* arrangement is necessary when applying a voltage to the working electrode in an electrolytic cell. The electrode of interest if again the WE, and the voltage at the WE is measured against the RE. Electrolytic processes incur large currents, which if allowed to pass through the RE could compromise the stability of the measurement. This is due to the possible chemical change that the current may induce within the RE, and also the addition of a third term, iR (the electrical resistance of the bulk solution), in the fixed potential difference, E, between the working and reference electrode.

$$E = (\phi_M - \phi_S)_{working} + iR - (\phi_M - \phi_S)_{reference} \quad [1.11]$$

The counter current to the flow through the working electrode is therefore passed through a third electrode, the CE. In some cases an electrolytic cell may use two electrodes, the reference and working, only. When using a microelectrode the currents involved in electrolysis are so small that they are negligible with respect to changes at the RE, and as such the reference may serve as a CE as well.

1.3.4. Solvents and electrolyte solutions

The solvent is the medium in which the electrodes are placed to complete an electrochemical cell. A wide range of solvents may be used, and the choice of medium is decided by a range of properties; the solubility and redox activity of the analyte, and the electrical conductivity, electrochemical activity and chemical activity of the solvent.

Aqueous solutions are most common in electrochemistry, though non-aqueous solvents such as acetonitrile, dimethylformamide (DMF), dimethylsulfoxide (DMSO), methanol and many others are regularly used. Due to the sensitivity of the experiments often conducted in electrochemistry, and the very low concentrations of species often encountered, it is necessary for the solvents to be of high analytical grade or be prepared by drying or purification procedures. Water is required to be doubly or preferably triply distilled before use, particularly when undertaking trace species analysis (e.g. stripping analysis).

The electrochemical medium must be sufficiently ionic to allow the passage of the charged species of interest to the electrode interface. To avoid the effects of solution resistance, migratory mass transport limits, large double layer capacitance and inconsistent ionic strength, a supporting electrolyte is often added to the solvent. The electrolyte must be inert with respect to electrode processes, and may be an inorganic salt, mineral acid or a buffer. Concentrations of 0.1 M or greater are generally sufficient.

1.4. Faradaic processes

Faradaic processes are named after Michael Faraday, a brilliant chemist and physicist of the 19th century. Owing to a large body of work that greatly advanced our understanding of electricity, a number of electrochemical terms and experimental tools are named after him. These include the Faraday constant (the charge on a mole of electrons), the Faraday cage, and faradaic processes. The latter term is based on Faraday's laws of electrolysis, and correspondingly describes electrochemical processes in which a current is observed due to induced electron transfer across the electrode/solution interface.

1.4.1. Current and flux

The processes discussed in section 1.3 consider electrochemical cells in which no current is passed beyond establishing equilibrium. Current flow may be achieved by applying a potential to the cell that differs from E_e. The consequence of applying a current is to drive an oxidation or reduction of the electroactive species in solution, a process termed electrolysis. The flow of electrons *from* the electrode *to* the solution corresponds to the general reaction

$$O_{(aq)} + e^-_{(m)} \rightarrow R_{(aq)} \qquad [1.12]$$

and is a reductive process termed a *cathodic reaction.* The corresponding back reaction, in which electrons flow *to* the electrode, is an oxidative process and termed an *anodic reaction*.

For the reaction shown in 1.12 the magnitude of the cathodic current (i) is proportional to the area of the electrode (A), the number of moles of electrons (n), the charge per mole (F) and the flux of O reaching the electrode surface (j).

$$i = n\mathrm{FAj} \qquad [1.13]$$

The flux, j, is the quantity of O reaching the electrode area per second (moles cm^{-2} s^{-1}) and may therefore be considered kinetically as the rate of the electrode reaction. This can be described using the rate law

$$j = k^0 [O]_0 \qquad [1.14]$$

in which k^0 is the heterogeneous rate constant for the process and $[O]_0$ is the concentration of O at the electrode surface. It is evident that the flux, and therefore the current observed, is dependent on the rate at which the oxidised species reaches the electrode surface from the bulk solution, and the rate at which electron transfer, k^0, occurs.

1.4.2. Mass Transport

When the rate of a reaction is entirely dependent on the rate of mass transport of the reactants to the electrode, the corresponding current observed is said to be *mass transport limited.* The mass transport of the electroactive species to the electrode surface can occur in three ways;

1. *Diffusion* – the movement of molecules under the influence of a concentration gradient, to homogenise a system and maximise entropy
2. *Migration* – the electrostatically induced movement of charged species to or from the electrode interface due to the electric field at the electrode.
3. *Convection* – the transport of molecules caused by physical movement by mechanical (e.g. magnetic stirrer) or natural means (e.g. thermal or density gradients)

The mass transport limitations imposed by migratory effects can be avoided by using a supporting electrolyte. This has the effect of swamping the solution with charged species, such that the electroactive species are not impeded by solution resistance, and electric fields do not build up in the solution during electrolysis, thus maintaining electroneutrality. Thus,

with a high concentration of chemically and electrochemically 'inert' electrolyte ions, generally at concentrations of 0.1 M and above, migratory transport effects may be neglected.

Convection is readily controlled in experimental electrochemistry by performing experiments in non-steady state conditions. That is to say the experiments are performed in quiescent solutions, without mechanical stirring, and at a timescale to prevent natural convection of species. Natural convection, such as thermal gradients or density differences within the solution, typically becomes a significant mass transport process over timescales of approximately 20 s. To control convection over time limits beyond 20 s it is therefore common to introduced forced convection, (e.g. by stirring) thus overwhelming natural convection and improving the reproducibility of the experiment. Forced convection is also used when diffusional limits impede experimental investigation, such as in a standard addition current-time plot when the bulk concentration is of interest and not the interfacial, diffusion limited, concentration.

1.4.3. Diffusion

Diffusion is the most important and influential mode of mass transport, and in controlled potential methods it is generally diffusion or electrode kinetics that contribute most significantly to the rate law and therefore limit electrode processes. The following section discusses diffusion in more detail.

1.4.3.1. Fick's laws of diffusion

Diffusion occurs in accordance with a concentration gradient, so as to fully homogenize the composition of a system. A concentration gradient imposes a rate of diffusion that is dependent on the particular location under investigation (e.g. the electrode/solution interface).

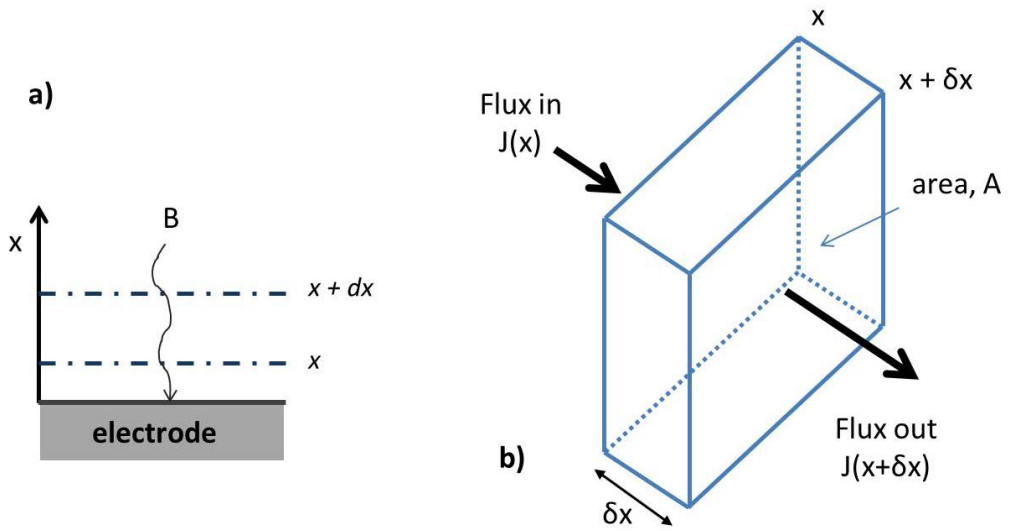


Figure 1.4: *a) Linear diffusion at a large planar electrode surface, b) an illustration of the flux of a species within the region x to x + dx, where A is area.*

Considering the simple case of linear diffusion, shown in Figure 1.4a, in which B is the diffusing species, the flux (j) of species B through a unit area per second (moles cm^{-2} s^{-1}) may be mathematically represented by Fick's first law of diffusion,

$$j = -D_B \frac{\partial [B]}{\partial x} \qquad [1.15]$$

where D_B and [B] are the diffusion coefficient and concentration of species B respectively. Experimentally it is more useful to know the change in concentration at a point (i.e. the electrode/solution interface) over a period of time, *dt.* The flux of material within a region of *x* to *x* + *dx* is shown in Figure 1.4b, and illustrates the difference in the flux of B at point *x* and at point *x* + *dx* during a time interval. This may be represented mathematically by the general conservation equation for species B

$$\frac{\partial}{\partial t}[B]_{(x,t)} + \frac{\partial}{\partial x} j_{(x,t)} = 0 \qquad [1.16]$$

Which on substitution of Eq. 1.15 into Eq. 1.16, we obtain Fick's second law of diffusion, Eq. 1.17, which predicts the concentration change of species B at the electrode surface over time.

$$\frac{\partial[B]}{\partial t} = D_B\left(\frac{\partial^2[B]}{\partial x^2}\right) \quad [1.17]$$

This equation may be extended into three dimensional coordinates (*x, y* and *z*) and cylindrical coordinates (*z, ϕ, r)* in a manner akin to that described in Equations 1.16 and 1.17, thus allowing non-linear diffusion at microdisc electrodes or non-planar surfaces (e.g. nanoparticles) to be derived.

1.4.3.2. The diffusion coefficient

The diffusion coefficient, D, of a molecule is a highly important value in electroanalysis. It provides a measure of how far a molecule will diffuse in a specified time interval. Derivation of the diffusion coefficient gives the differential in Eq. 1.18

$$D = \frac{(\delta x)^2}{2\delta t} \quad [1.18]$$

from which we can see that the time/distance relationship of D is

$$\sqrt{< x^2 >} = \sqrt{2Dt} \quad [1.19]$$

thus allowing distances diffused in a time, *t,* to be estimated.

The diffusion coefficient is very sensitive to temperature, often following an Arrhenius type relationship

$$D = D_\infty\, e^{-E_a/RT} \quad [1.20]$$

Where $-E_a$ (in kJ mol^{-1}) is the activation energy for D, and D_∞ is the hypothetical value of D at an infinite temperature. The implication of this requires that voltammetric experiments be thermostatically regulated and the temperature always noted.

The value of a diffusion coefficient can vary considerably depending on the viscosity and temperature of the medium, and the size of the diffusing molecule. The units

of D are $cm^2\ s^{-1}$, therefore the larger the value the faster the diffusion rate. Generally the diffusion coefficient decreases with increasing particle size, and typical values range between 10^{-6} to $10^{-5}\ cm^2\ s^{-1}$.

1.4.3.3. The Cottrell Equation

The Cottrell equation is an equation used to solve Fick's second law of diffusion. The equation considers the situation at the electrode surface for an electrode in a solution of species B. To solve Fick's second law, it is necessary to apply a series of boundary conditions such that at zero time, the concentration of B at the surface, $x = 0$, is the same as in the bulk, $[B]_{bulk}$, but at time immediately after zero, a large potential is applied such that a redox process occurs that depletes the concentration of B at the surface to zero. These conditions may be shown thus:

$$t = 0,\ all\ x,\ \ [B] = [B]_{bulk}$$

$$t > 0,\ x = 0,\ [B] = 0$$

$$t > 0,\ x \rightarrow \infty,\ [B] = [B]_{bulk}$$

It also involves introducing a new variable, Γ, which equates to

$$\Gamma = \frac{x}{2\sqrt{Dt}} \qquad [1.21]$$

This value may be substituted into Fick's laws, and by integrating and applying the boundary conditions listed above, as well as relating back to Eq. 1.13 where I = nFAj, the Cottrell equation is derived.

$$i = \frac{nFA\sqrt{D}[B]_{bulk}}{\sqrt{\pi t}} \qquad [1.22]$$

The Cottrell equation shows that when the potential is stepped the current decays to zero in inverse proportion to the square root of time (i.e. $i \propto 1/\sqrt{t}$). The behaviour is illustrated as

a current density transient in the chronoamperometric waveform shown in Figure 1.9 of section 1.6.

Based on the relationship of current to charge over time (i.e. $i = \frac{\partial Q}{\partial t}$), one can also use the Cottrell equation to derive the charge passed over time in the experiment, thus quantifying the extent of electrolysis in terms of moles of reactant, N, consumed in accordance with

$$N = \frac{Q}{nF} = 2A\frac{\sqrt{Dt}}{\sqrt{\pi}}[B]_{bulk} \qquad [1.23]$$

As time passes the amount of B at the electrode surface is depleted as more and more is consumed, thus increasing the distance at which [B] = $[B]_{bulk}$ relative to the electrode surface. This distance is the distance across which the electroactive species, B, must traverse to reach the electrode surface, and is called the *diffusion layer, δ.* Consequently, as time progresses the thickness of the diffusion layer increases, thus decreasing the rate of diffusion according to Eq. 1.19, and correspondingly decreasing the current.

1.4.3.4. The Nernst diffusion layer and limiting current

The Cottrell equation predicts that $i \propto 1/\sqrt{t}$, implying that over a relatively long time the current will fall to zero. This is not observed experimentally however, as the current in fact falls to an approximately steady value. This observation is consistent with the Nernst diffusion layer model depicted in Figure 1.5.

The Nernst diffusional layer model proposes that beyond the critical distance of the diffusion layer, δ, the bulk solution is well mixed by natural convection, such that the concentration of the electroactive species in the bulk is maintained at the constant bulk value (i.e. $[B]_{bulk}$).

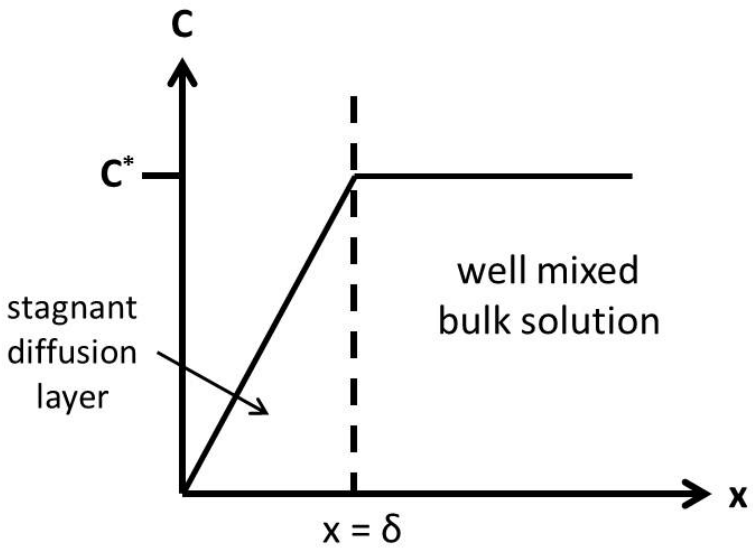


Figure 1.5: *An illustration of the Nernst diffusion layer model of a steady state solution (adapted from [2])*

Natural convection is lost towards the electrode due to its rigidity and frictional forces, thus concentration changes only occur within the diffusion layer (between $x = 0$ and $x = \delta$). The steady state diffusional flux determined by Fick's 1st law may therefore be expressed as

$$j = D\frac{\partial[B]}{\partial x} = \frac{D[B]_{bulk}}{\delta} \qquad [1.24]$$

with the corresponding, steady state current therefore expressed as

$$i_{ss} = \frac{nFAD[B]_{bulk}}{\delta} = nFAm_T[B]_{bulk} \qquad [1.25]$$

where D/δ, in units of cm s^{-1} becomes m_T, the mass transport coefficient. This has the same units as the electrochemical rate constant, k^0, discussed in the following section, and therefore allows direct comparison of the two quantities, providing an indication of the relative speeds of mass transport and electron transfer.

The *limiting current* is observed when the potential is sufficiently large to completely deplete (i.e. zero concentration) the electroactive species at the electrode surface.

The Cottrell equation predicts that the limiting current will decrease over time which is indeed the case at macro electrodes. The Nernst diffusion layer dictates that the limiting current is given by Eq. 1.25 however, when the concentration decays from $[B]_{bulk}$ to zero at the electrode surface over the distance of the diffusion layer, δ.

1.4.4 Electrode kinetics

We refer once more to the rate law shown in equation 1.14, in which $j = k^0$ [O]. In the previous section the effect of [O] on j was explored in terms of mass transport. Herein we discussed the influence of the heterogeneous rate constant for electron transfer, k^0, on the rate of electrochemical reactions.

1.4.4.1. The rate of electron transfer

In this section let us consider the general redox reaction

$$O_{(aq)} + e^-_{(m)} \underset{k_{ox}}{\overset{k_{red}}{\rightleftharpoons}} R_{(aq)} \qquad [1.26]$$

In which the two species O and R are interconverted by a one electron transfer, and the rate constants k_{red} and k_{ox} are first order rate constants for the reduction of species O to R (forward reaction) and the oxidation of species R to O (back reaction) respectively. Based on previous equations regarding current and flux the forward and back reactions may be presented in terms of current as equations 1.27a and b.

$$i_c = -FAk_{red}[O]_0 \qquad [1.27a]$$

$$i_a = FAk_{ox}[R]_0 \qquad [1.27b]$$

The terms $k_{red}[O]_0$ and $k_{ox}[R]_0$ are the respective fluxes for the reduction and oxidation processes, with the subscripts *c* and *a* representing cathodic and anodic. The net current that flows for the reaction in Eq. 1.26 is a combination of the two expressions

$$i = i_c + i_a = FA(k_{ox}[R]_0 - k_{red}[O]_0) \quad [1.28]$$

At equilibrium this net current, and therefore the net rate of reaction, is zero. That is to say that the concentration of reactants and products are in complete equilibrium, and no current is passed.

1.4.4.2. Transition State Theory

The constants k_{red} and k_{ox} are both potential dependent, such that the cathodic reaction would predominate at a relatively negative potential and the anodic reaction would dominate at relatively positive potentials. The energy required to drive the reaction forwards or backwards may be represented by a reaction profile (Figure 1.6), very similar to that observed in transition state theory (TST).

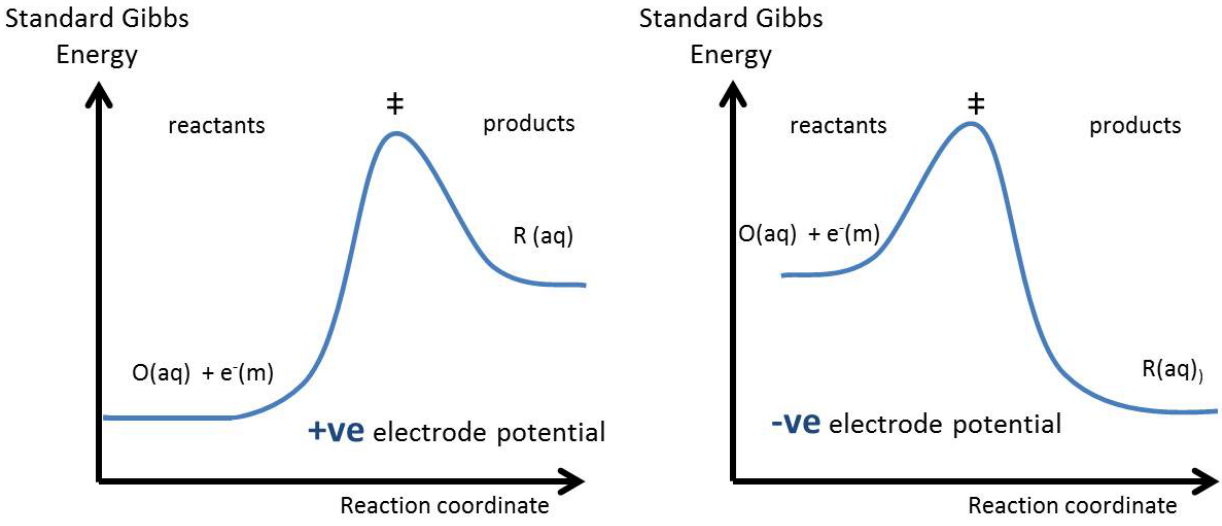


***Figure 1.6**: Reaction profiles for the electrode process $O_{(aq)} + e^-_{(m)} \rightleftharpoons R_{(aq)}$. The profile on the left shows the relative energy of the reactants to the products when a positive potential is applied, and the right shows the relative energy when the electrode has a negative potential.(Adapted from [2])*

TST dictates that there is an activation energy barrier, E_a, between the reactants and products, the energy of which is the energy of the transition state or activated complex, $G^{\ddagger}$. This is in accordance with the Arrhenius equation, and may be represented in terms of Gibbs energy of activation as

$$k = Ae^{-\Delta G^{\ddagger}/RT} \quad [1.29]$$

The energy profile shown in Figure 1.6 shows the energy of the reactants and products when the electrode is held positively ($k_{ox} >> k_{red}$) or negatively ($k_{ox} << k_{red}$) relative to the potential of the solution. Increasing the relative energy of the reactants or products has the result of driving the thermodynamic process in the energetically favourable direction.

1.4.4.3. Butler-Volmer kinetics

For any redox couple it is convenient to refer to the energy required to drive the reactions forwards or backwards in terms relative to the formal potential, E^0, of the couple. If the electrode potential is set at the formal potential, the anodic and cathodic free energy change may be expressed as $\Delta G_{0a}^{\ddagger}$ and $\Delta G_{0c}^{\ddagger}$ respectively, and may be considered the formal activation energy. If the potential is changed by ΔE, then the energy of the electrons on the electrode are raised or lowered correspondingly, by a value

$$-F\Delta E = -F(E - E^0) = -F\eta \quad [1.30]$$

F the Faraday constant for the charge per mole of electrons, and η is the overpotential ($E - E^0$). Assuming a positive overpotential is applied, the profile energy drops on the reactant (reduction) side and the transition state energy decreases relative to the reduced species. This decrease in $\Delta G_a^{\ddagger}$ results in the more favourable anodic reaction, thus a current corresponding to the potential change is observed. The difference between $\Delta G_{0a}^{\ddagger}$ and $\Delta G_a^{\ddagger}$ is a fraction of the energy change and is called the transfer coefficient, α.

The transfer coefficient reflects the sensitivity of the transition state to the potential drop at the metal – solution interface, and has a value that lies between 0 and 1. For the reduction reaction the products are considered 1 and the reactants 0. Therefore, if α tends to zero it most resembles the oxidised species, whereas if it tends to 1 it resembles the reduced species. Most often the value is about 0.5 however, indicating a truly intermediate transition state. As such the fraction is expressed as –α for the reduction reaction and 1-α for the oxidation.

We may now determine how the rate constants k_{red} and k_{ox} depend on the overpotential by re-expressing Eq. 1.29 for the forward and back reactions

$$k_{red} = A\, exp\left(\frac{\Delta G_{red}^{\ddagger}}{RT}\right) exp\left(\frac{-\alpha \mathrm{F}\eta}{RT}\right) = k_{red}^{0}\, exp\left(\frac{-\alpha \mathrm{F}\eta}{RT}\right) \qquad [1.31a]$$

$$k_{ox} = A\, exp\left(\frac{\Delta G_{ox}^{\ddagger}}{RT}\right) exp\left(\frac{(1-\alpha)\mathrm{F}\eta}{RT}\right) = k_{ox}^{0}\, exp\left(\frac{(1-\alpha)\mathrm{F}\eta}{RT}\right) \qquad [1.31b]$$

Where the terms that are independent of η are expressed as the new constants, k_{ox}^{0} and k_{red}^{0}. These equations may be expressed as net flux, j, in accordance with Eqs. 1.14 and 1.28 to form the Butler-Volmer equation.

$$j = k_{red}^{0}\, exp\left(\frac{-\alpha \mathrm{F}\eta}{RT}\right)[O]_0 - k_{ox}^{0}\, exp\left(\frac{(1-\alpha)\mathrm{F}\eta}{RT}\right)[R]_0 \qquad [1.32]$$

When in equilibrium the rate constants k_{red}^{0} and k_{ox}^{0} are equal, as no net current flows, and may be considered as just k^0 , the *standard electrochemical rate constant*, with units of cm s^{-1}.

The Butler-Volmer equation is highly important to electrode kinetics, as it relates the change in observed current to the overpotential, η, and transfer coefficient, α. A solution that is well stirred and equilibrated has a simpler version of Eq. 1.32, as the concentration

ratios are unity. In this instance the flux solely depends on the rate constants for the reaction, and has the form of Eq. 1.33

$$j = k^0 \left(exp\left(\frac{-\alpha \mathrm{F}\eta}{RT}\right) - exp\left(\frac{(1-\alpha)\mathrm{F}\eta}{RT}\right)\right) \qquad [1.33]$$

1.4.4.4. Tafel Analysis

The practical application of the Butler-Volmer equation involves consideration of two limiting cases; a fully reversible case (where k^0 is large), and an irreversible case (when k^0 is small). In the reversible system the value of k^0, and consequently i_0 (the exchange current), is so large that very little voltage is required to drive the reaction backwards or forwards depending on the overpotential sign, and therefore a steady current flows. Also, the large value of i_0 means that the net current is contributed to by both i_a and i_c at all but very high overpotentials.

In the irreversible case the influence of i_0 is negligible, and a significant overpotential is required to induce current flow. Correspondingly, at cathodic potentials, there is negligible oxidation current, and vice versa. In the irreversible limiting case the Butler-Volmer equations can therefore be simplified to

$$lni = lni_0 + \frac{(1-\alpha)F}{RT}\eta \qquad [1.34a]$$

$$\ln(-i) = lni_0 + \frac{-\alpha F}{RT}\eta \qquad [1.34b]$$

for the oxidation and reduction currents respectively. From equations 1.35 we have the experimental opportunity to derive the value of α, which is a process termed Tafel analysis. From experimental data the current and potential are known, thus plotting ln(i) against E will give a plot similar to that shown in Figure 1.7.

In Figure 1.7 both the anodic and cathodic currents have been plotted, which allows for i_0, to be determined. This is achieved by extrapolating the linear parts of the Tafel plot and intersecting at zero current.

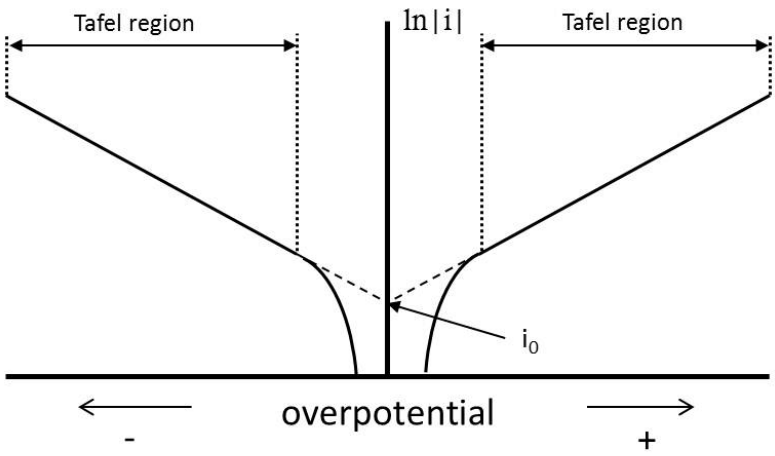


Figure 1.7: *A Tafel plot corresponding to the ln(i) vs. E for both the anodic and cathodic processes.(Based on a figure from [5])*

1.4.4.5. Electron transfer reactions and Marcus Theory

The process of charge transfer between a metal and solution may be considered as electron tunneling from the molecular orbitals of the relative species. The orbital from which the electron tunnels must be of higher energy relative to the receiving orbital. In a metal the electrons lie in a continuum of energy levels, the maximum of which is termed the Fermi level. In solution, the molecular energy levels (orbitals) of the electroactive species must be considered, specifically the energy of the highest occupied molecular orbital (HOMO) and the lowest unoccupied molecular orbital (LUMO). In the discussion of potential difference in section 1.2. it was established that a metal immersed in solution will transfer electrons either to or from the metal depending on the Fermi level of the metal relative to the energy of the electroactive species. The process of electron transfer is therefore thermodynamically driven by a difference in energy levels at the electrode/solution interface.

The electrochemical reduction of species O to R occurs by electron tunneling from the electrode to the LUMO of species O. Beyond equilibrium this can be forced by applying a negative potential to the electrode, thus raising the Fermi level of the electrode above that of the LUMO in O. Tunneling occurs over *very* fast timescales of approx. 10^{-15} to 10^{-16} s. This is considerably faster (some 2-3 orders of magnitude) than nuclear motions within the solvent shell of species O.

Electron transfer reactions are constrained by the Franck-Condon Principle due to the speed at which electron transfer occurs. The principle dictates that when electron transfer occurs the reactant and product must possess the same molecular shape (i.e. bond angles, bond lengths) and solvent shell. Secondly, no energy change can accompany the electron transfer, thus the immediate product must have the same energy as the reactant at the instant of transfer. The consequence of these limitations is that for electron transfer to proceed, species O and R must be in an energetically comparable excited state. This is the activated complex, or transition state discussed previously, in which the excited state of O is essentially equal to the excited state of R (i.e. $\Delta G_{ox}^{\ddagger} = \Delta G_{red}^{\ddagger}$).

It follows that the greater the energy required to achieve the transition state, then the smaller the value of k^0 and the slower the rate of electron transfer. This is the case for reactants and products that are geometrically (in terms of bond angles and bond lengths etc.) very different, such that a relatively large energy input is required to sufficiently excite the species to a transition state. The rate constant of a species therefore gives an indication as to the size and shape, degree of solvation and nature of charge transfer of the reactants and products. Fast reactions generally occur in simple electron transfer (outer sphere) processes, when O and R have comparable geometry (e.g. $Fe(CN)_6^{3-}$to $Fe(CN)_6^{4-}$), and reversible kinetics are consequently observed.

1.5. Non-faradaic processes

Other processes can occur at the electrode interface that do not cause the oxidation or reduction of a species, but do incur an external current when the potential, electrode area or solution composition is changed. Processes such as adsorption or desorption may occur or the electrode surface may chance, thus producing a non-faradaic current. The following section briefly discuss such processes.

1.5.1. The Electrical Double Layer

When an electrode is inserted into a solution a charge will be established in the solution equal and opposite to that at the electrode. If the electrode potential is changed, the corresponding charges change. At the electrode surface the layer of charge represents an excess or deficiency of charge (electrons and holes) and is very thin (< 0.1 Å). The counter charge in the solution is made up of an excess of charged species in the solution (anions or cations, species of oriented dipole) at the electrode/solution interface. These solution phase species crudely form two layers of charge at the interface, thus forming the basis for the electrical double layer.

The electrical double layer depicted in Figure 1.8 is separated into four distinct parts. These are the electrode surface, the inner Helmholz plane (IHP), the outer Helmholz plane and the diffuse layer. The charge at the electrode dictates the nature of the double layer (i.e. anionic or cationic), and is varied by changing the potential externally. The IHP is the solution layer closest to the electrode surface, and consists of solvent molecules and specifically adsorbed ions. The OHP is a layer of non-specifically adsorbed solvated ions, which are attracted to the electrode by coulombic forces, with its boundary set at the center of solvated ions at their nearest approach to the electrode surface. These two Helmholz layers form the compact layer, which is a charged layer strongly bound to the surface, even when the electrode is removed from the solution.

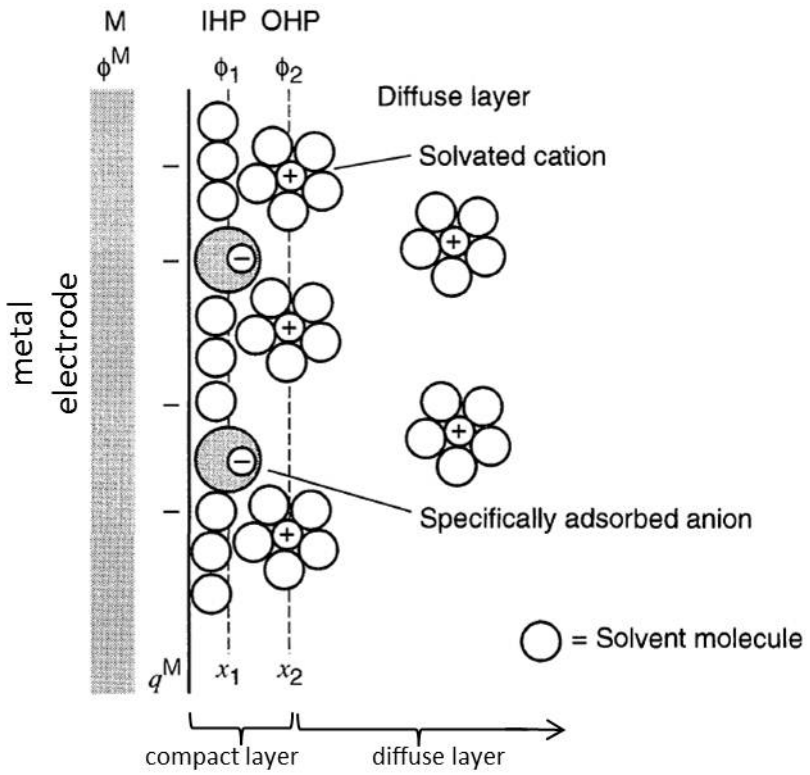


Figure 1.8: *A schematic of the electrical double layer for a negatively charged electrode [1]*

The region beyond the OHP is often termed the diffuse layer (also called the Gouy layer). It is considered to be a region of relatively high ion concentration that gradually extends three-dimensionally into the bulk ion concentration. It therefore represents the transition from an ordered distribution of ions controlled by the interfacial electrical field to an equilibrated distribution of ions controlled by natural convection.

The total charge of the Helmholz and diffuse layers equal (in opposite sign to) the net charge on the electrode surface according to Eq. 1.35, in which q is charge.

$$q_m = -(q_{IHP} + q_{OHP} + q_{\text{diff}}) \qquad [1.35]$$

A plot of the potential vs. distance from the electrode shows two distinct regions; a linear region corresponding to the Helmholz plane, and an exponential region corresponding to the diffuse layer.

1.5.2. Capacitative Current and Double Layer Capacitance

A capacitor is composed of two metal sheets in an electrical circuit separated by a dielectric material. The two metal sheets have an equal and opposite charge (q) that is directly proportional to the potential across the capacitor

$$q = C.E \qquad [1.36]$$

thus leaving the value C, capacitance (measured in farads, F), which is the ratio of stored charge to potential. A metal electrode in solution resembles a capacitor, in which the second metal is replaced with the solution double layer. As such a potential-charge relationship may be derived for the electrical double layer in terms of capacitance, as shown in Eq. 1.37.

$$q = C_{dl}A(E - E_{pzc}) \qquad [1.37]$$

A is the electrode area (cm^2) and E_{pzc} is the potential of zero charge, which is the potential at which the electrode charge reverses, and no net current exists in the double layer. The double layer capacitance, C_{dl}, in aqueous solution is typically 10-40 $\mu F\ cm^{-2}$.

The double layer capacitance is responsible for the background current in controlled potential techniques, and can be problematic in electroanalysis if the charging current is too great. When an experiment requires the detection of sub microamp currents, the faradaic current can be swamped by the charging current. A large body of work surrounds the processes and effects of the double layer, but these go beyond the scope of this introduction. Chapter 13 of the text by Bard and Faulkner [1] gives further discussion on the topic.

1.6. Controlled Potential Techniques

Experimental electrochemistry uses a number of techniques to determine the mechanisms of electrochemical reactions and also to use electrochemistry as an analytical tool. Controlled potential techniques measure the electrode current as a function of voltage in an electrolytic

cell. These techniques are briefly discussed herein, and for clarity we will refer once more to the general one electron transfer reaction

$$O_{(aq)} + e^- \rightleftharpoons R_{(aq)}$$

1.6.1. Potential Step Methods

In a potential step experiment the electrode potential is stepped from a potential of no faradaic current E_1 to a potential near or beyond the formal potential for the reduction of O to R, E_2. The effect of this potential step is measured as current versus time, and as such the method is termed chronoamperometry.

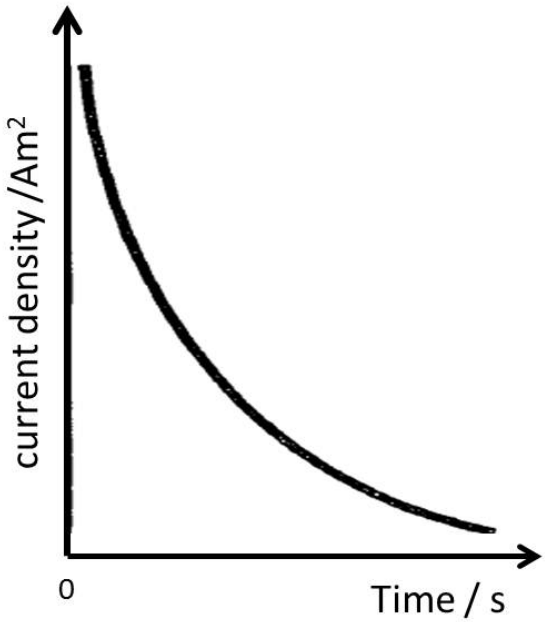


Figure 1.9: *The current density (amps/m^2) transient following a potential step at a planar electrode.(Adapted from [2])*

In Figure 1.9 a typical current-time response to a potential step is shown. It is evident form the curve that the initial response at $t > 0$ is a large current that decreases exponentially with time. The large current is detected due to the rapid electrolysis of species O at the electrode, not yet limited by diffusion. As time progresses, O is depleted at the electrode surface as it reduces to R. The diffusion layer correspondingly thickens, as discussed previously in Section 1.3 and the Cottrell equation, and mass transport of O to the

electrode by diffusion becomes a limiting factor, thus decreasing the measured current proportionally to the increasing diffusion layer. The chronoamperometric plot can be used to determine diffusion coefficients by applying the Cottrell equation, Eq. 1.22.

1.6.2. Potential Sweep Methods

In potential sweep methods the current is measured as the electrode potential changes with time. The method is the most widely employed in the field of voltammetry, owing to a wealth of kinetic, thermodynamic and mechanistic data that can be determined.

1.6.2.1. Linear sweep and cyclic voltammetry

Linear sweep voltammetry (LSV) and cyclic voltammetry (CV) are very similar voltammetric techniques, in which the voltage applied to the working electrode is swept (scanned) at a specific rate, usually over a potential range that encompasses the start and end of the faradaic process of interest. The rate at which the potential is swept is termed the scan rate, ν (V/s).

If we consider the reduction of O to R as before, an LSV measures the current corresponding to a potential sweep from a start potential, E_1, to and end potential E_2. It is usual for E_1 to be suitably positive of E^0 for the reaction, such that no faradaic current is initially observed, and for E_2 to be sufficiently negative of E^0 that the current has peaked and decreased due to mass transport limited diffusion, or when a steady state limiting current at a microelectrode has been achieved. A CV has the same potential ramp from E_1 to E_2, but at E_2 the potential is switched and returned to E_1. As such it is possible to see the back reaction (i.e. the oxidation), provided the process is reversible enough within the limits of E_2-E_1 (ΔE).

The observed voltammogram for the reaction $O + e \rightleftharpoons R$ will depend on a number of factors, as follows;

- The standard electrochemical rate constant, k^0, and the formal potential of the O/R couple
- The diffusion coefficients of O and R
- The voltage scan rate, ν (V/s)
- The start and end (or switch) potentials, E_1 and E_2

Because modern potentiostats record the currents digitally, it is also prudent to set an appropriate step potential for the experiment. The current is actually recorded at incremental changes of potential (potential steps), and the size of the potential steps can be varied depending on scan rate and potential window, to achieve the greatest number of increments per volt.

LSV and CV experiments are performed under non-steady state conditions, therefore diffusional mass transport is a major factor in the waveform. This means Fick's laws of diffusion can be used to predict the transport of species O to the electrode.

$$\frac{\partial[O]}{\partial t} = D_O \frac{\partial^2[O]}{\partial x^2}$$

For a reversible processes, the form of the voltammogram is such that an appreciable current is observed long before E^0 (~E_e) is reached, occurring as soon as the reaction is thermodynamically viable. The voltammetry reflects fast electrode kinetics, typical of a reversible process, and is shown in Figure 1.10.

The current increases approximately exponentially until the formal potential is passed, at which point the current tapers off and reaches a limit before decreasing exponentially. This is because the potential is sufficiently negative to fully deplete O at the electrode surface, and the current becomes mass transport limited. The consequence is a peak shaped curve that encompasses the formal potential.

In the irreversible case, also shown in Figure 1.10, the potential required to drive the electron transfer is considerably more negative than for the reversible system, with

appreciable currents not occurring until potentials very near the formal potential. As the potential is made more negative, the current increases somewhat exponentially, reaching a limit once again before decreasing in accordance with diffusion limited mass transport. The peak produced here is considerably broader than that of a reversible system.

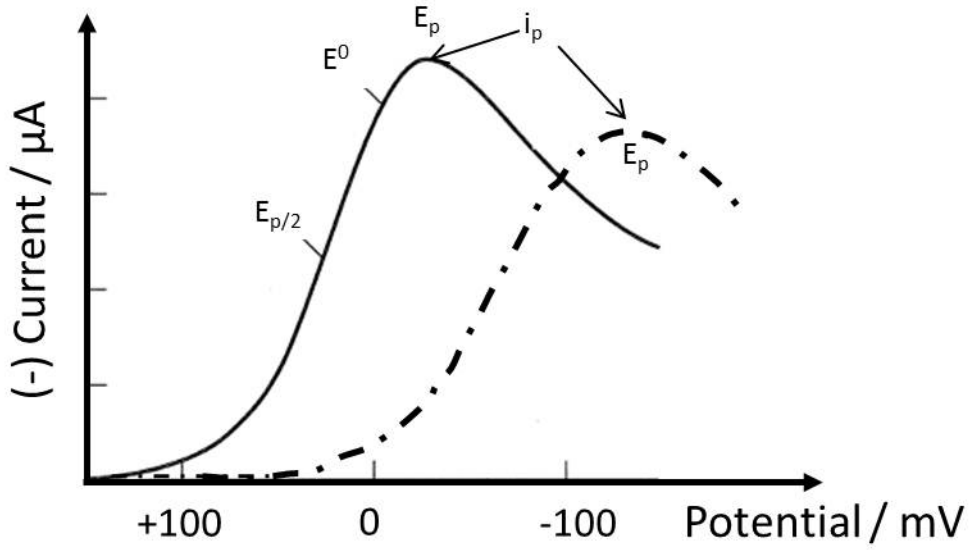


Figure 1.10: *Linear sweep voltammetric waveforms for the reduction of species O to R in a reversible electron transfer (solid line) and an irreversible electron transfer (dashed line). (Adapted from [5])*

For a CV, as shown in Figure 1.11 (blue line), a reversible system has an identical shape to the LSV for the forward scan, depending entirely on the reversibility of the redox couple. On the reverse scan, the oxidation of species R, produced in the forward scan, is observed. The concentration of R in the diffusion layer is high at the point of reversal, and as such a current increase corresponding to $R \rightarrow O + e^-$, is observed immediately

As the potential approaches the formal potential, the oxidation becomes increasingly kinetically favourable, and the current begins to increase exponentially. As with the reversible LSV, the current reaches a limit just after the formal potential, as R is depleted at the electrode surface, and mass transport limits decrease the current exponentially with potential.

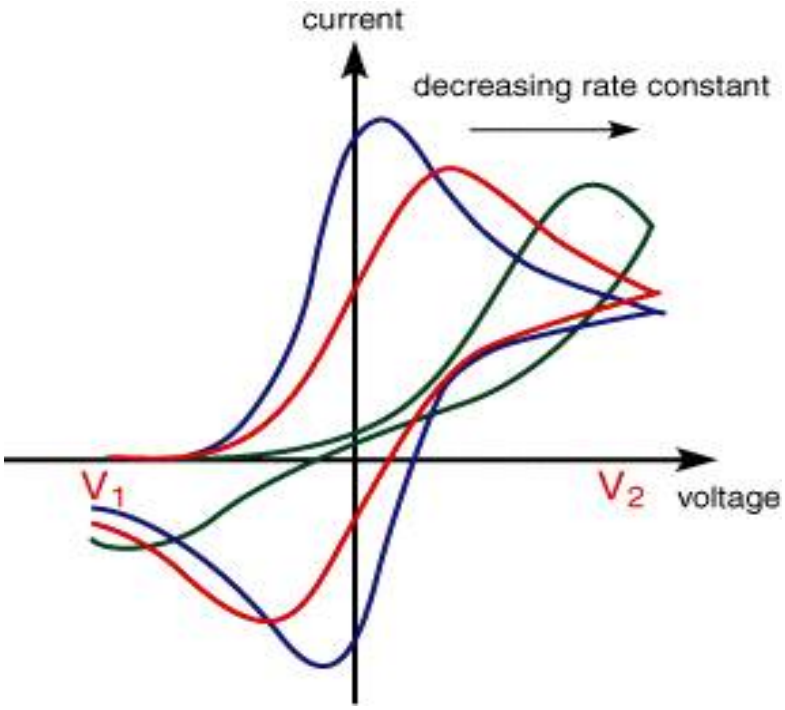


Figure 1.11: *A cyclic voltammogram for a reversible electron transfer (blue),a quasi-irreversible electron transfer and (red) an irreversible electron transfer (green) [7]*

The heights of the forward and back peaks, i_p, are of the same magnitude, and the peak potential, E_p, is separated by approximately 59 mV at 25°C, as predicted by the Nernst equation (where *n* is 1, otherwise the separation is 59/*n* mV).

The CV for an irreversible process has the same shape as the LSV for the forward reaction, requiring a very negative potential relative to the formal potential to obtain the reduction peak. The corresponding back scan is seen to return to non-faradaic current, but does not convert R back to O until an appreciably large oxidative overpotential is observed. As such R has diffused away from the electrode by this point, or the potential window does not encompass both electrode processes due to the wide difference in potential.

For species in which the electrochemical rate constant is intermediately fast, the CV is also observed as intermediate. In this situation the system is called quasi-irreversible, and the peak potential and peak current relationships with scan rate are neither reversible or irreversible, but somewhere in between.

1.6.2.2. Peak potential dependence and the Randles-Ševčik equation

The peak potentials and peak currents obtained from linear sweep or cyclic voltammetry have a specific scan rate dependence that is indicative of the nature of the electrode kinetics and can also provide various electrochemical parameters. The relationship for peak current can be related to the two forms of the Randles- Ševčik equation, one for the reversible system

$$i_p = (2.69\text{x}10^5)n^{3/2}AD_0^{1/2}C_O^*\nu^{1/2} \quad [1.39]$$

and the irreversible system (where n=1 is assumed)

$$i_p = (2.99\text{x}10^5)\alpha^{1/2}AD_0^{1/2}C_O^*\nu^{1/2} \quad [1.40]$$

where *n* is the number of electrons transferred, A the area of the electrode (cm^2), D_O the diffusion coefficient of species O (cm^2/s), C_O^* the bulk concentration of O (mol cm^{-3}), α the transfer coefficient for the reaction, and ν the scan rate (V/s). Plotting the peak current versus the scan rate yields a linear plot in which values for D, n, α or A may be determined from the slope provided all other values are known.

The change in peak potential with scan rate is indicative of whether a reaction is reversible or irreversible. In the reversible system E_p remains constant and independent of scan rate. In the irreversible system however, E_p shifts away from E^0 as scan rate increases. The shift is approximately 1.16 $\frac{RT}{\alpha F}$ for each factor of 10 in the scan rate.

1.6.3. Pulse Voltammetric Techniques for Trace Analysis

Pulsed voltammetry is a technique that was introduced to aid analytical electrochemistry by achieving lower detection limits. As discussed previously, the non-faradaic charging current can obscure small faradaic currents of interest, such that trace amounts of analyte cannot be electroanalytically determined.

Pulse voltammetry works to increase the ratio between the faradaic and non-faradaic currents using sampled current potential-step methods. A number of pulsed techniques exist, but all involve a sequence of potential steps lasting ca. 50 ms (the pulse). The current transients following each step are recorded, and because the charging current decays more rapidly than the faradaic current, the current is measured 'late' into the pulse life with negligible non-faradaic signal.

1.6.3.1. Differential Pulse Voltammetry

This technique is more commonly used electroanlaytically, and is extremely useful in trace analysis of organic and inorganic species. Differential pulse voltammetry (DPV) uses pulses of fixed amplitude (i.e. fixed ΔE), superimposed on a linear potential ramp. When using a hanging mercury drop electrode (HMDE) the pulse is applied immediately before the end of the drop. Figure 1.12 illustrates the waveform for the technique.

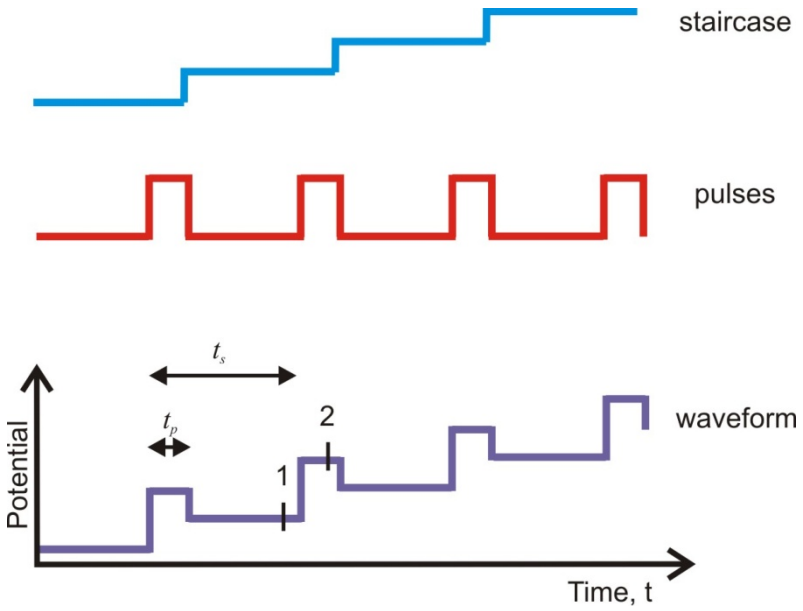


Figure 1.12: *The waveform for differential pulse voltammetry, where 1 and 2 indicate the points at which the currents are measured, t_s the step time and t_p the pulse time. (Adapted from [2])*

The current is sampled twice in DPV; just before the pulse application and again towards the end of the pulse. The current difference is determined by subtracting the first measurement from the second, which is then plotted against potential. The resulting voltammogram is peak shaped, the height of which is directly proportional to the concentration of the analyte.

The peak shaped response of DPV also results in improved resolution between two species with similar redox potentials, thus making it an ideal technique when analysis mixtures of electroactive species. The width of the peak at half height can provide insight into the number of electrons corresponding to the peak based on Eq. 1.41 equaling to 30.1 mV/n at 25°C.

$$W_{1/2} = \frac{3.52RT}{nF} \qquad [1.41]$$

1.6.3.2. Square-Wave Voltammetry (SWV)

SWV is similar in waveform to DPV but uses larger amplitude symmetrical square wave pulses. The waveform consists of square wave pulses superimposed on a potential staircase as shown in Figure 1.13. As with DPV, the pulse is sampled twice during each wave cycle, at the end of each pulse to distinguish between faradaic and non-faradaic current.

The square wave has a large amplitude, ΔE_p, above and below the baseline potential, that is much larger than the staircase height, ΔE_s. The difference between the two current measurements ($i_{forward}$ and i_{back}) is plotted against the base staircase potential, thus 3 plots of current against potential are obtained from the technique; the forward current, the reverse current and the differential current ($i_f - i_b$).

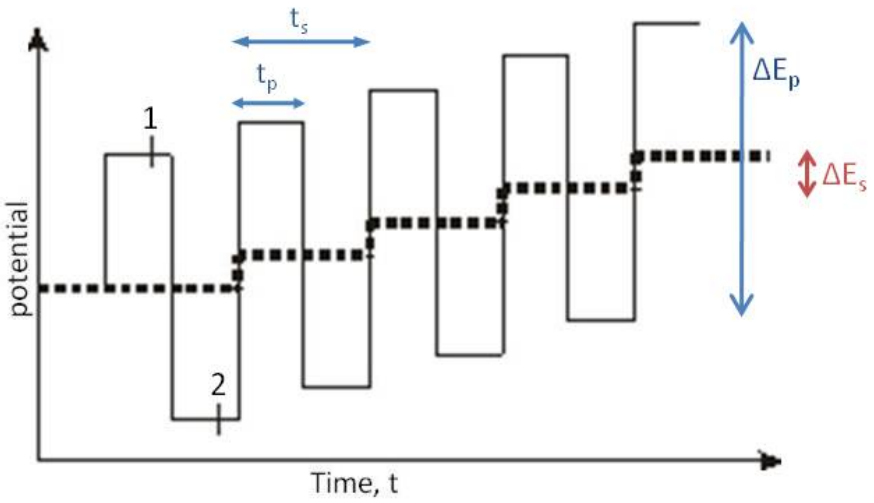


Figure 1.13: Waveform for the SWV technique. Note the potentials of the forward and back pulses are much greater than the staircase potential. (Adapted from [2])

The differential voltammogram is peak shaped (Fig. 1.14), with a symmetrical peak observed at the half-wave potential (i.e. E when $i_p/2$), and a peak current that corresponds to the analyte concentration. The differential peak is larger than the forward and back peaks individually, thus raising the sensitivity of the technique.

Although very similar to DPV, the major difference between the techniques is the length of time spent in each interval. For DPV the time spent before the pulse is significantly longer than the length of the pulse, such that a pseudo equilibrium occurs at the electrode surface before each pulse owing to a larger diffusion layer. In SWV the pulses are of equal length in time, and the difference in the charging currents is deemed negligible enough to allow for a rapid succession of pulses. As such SWV is generally a much faster technique, but can only be applied to solid electrodes.

An effective scan rate may be determined for SWV based on pulse frequency and step height, $f\Delta E$. Frequency is measured in Hz (cycles/s) and E in volts, thus $f\Delta E$ has units of V/s. Scans may therefore be obtained in seconds rather than minutes as is often presumed the case for DPV. However DPV was developed with mercury electrodes in mind, in which the surface was renewed with each pulse. Modern application of DPV with solid

electrodes can use much shorter pre-pulse times and therefore be akin to SWV with respect to experimental time and detection limits attained [1]

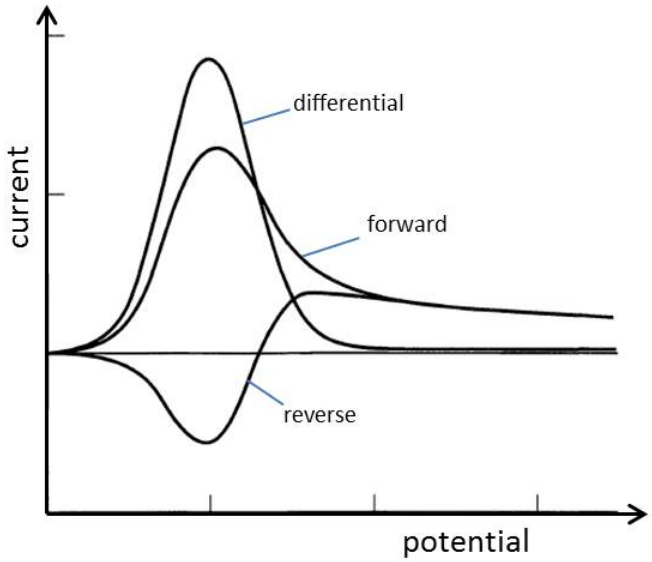


Figure 1.14: *The three voltammograms resulting from analysis. The forward, backward and differential measurements are indicated (Adapted from [2])*

1.6.4. Stripping analysis

Stripping analysis is a method of determining trace amounts of organic and inorganic species using voltammetric techniques. It is highly sensitive, achieving sub nanomolar detection limits in the most favourable cases. There are three categories of the method; anodic (ASV), cathodic (CSV) and adsorptive (AdSV) stripping voltammetry.

The key factor of stripping voltammetry is the pre-concentration step. This involves applying a potential or inducing a chemical process that concentrates the species of interest at the electrode as exemplified here

ASV: $M^{n+}(aq) + ne^- \rightarrow M(electrode)$

CSV: $2M^{n+}(aq) + mH_2O \rightarrow M_2O_m(electrode) + 2mH^+ + "(m\text{-}n)e^-$

AdSV: $M(aq) + L(aq) \rightarrow ML(ads)$

Following pre-concentration, the stripping step occurs in which the potential is swept from the pre-concentrating potential to a potential beyond the oxidation (ASV) or reduction (CSV) of the concentrated material. The faradaic response directly corresponds to the amount of the species pre-concentrated on the electrode.

ASV is commonly used in the determination of trace heavy metals, such as lead and cadmium. A series of additions of the heavy metal(s) allows for a calibration plot of concentration against peak height or peak charge to be formed, such that an unknown concentration of the metal can then be analysed if the plot is linear. Pulsed voltammetric techniques are commonly applied to stripping voltammetry, due to the small currents, and resolving abilities of DPV and SWV, thus allowing a number of metals to be analyzed from one solution.

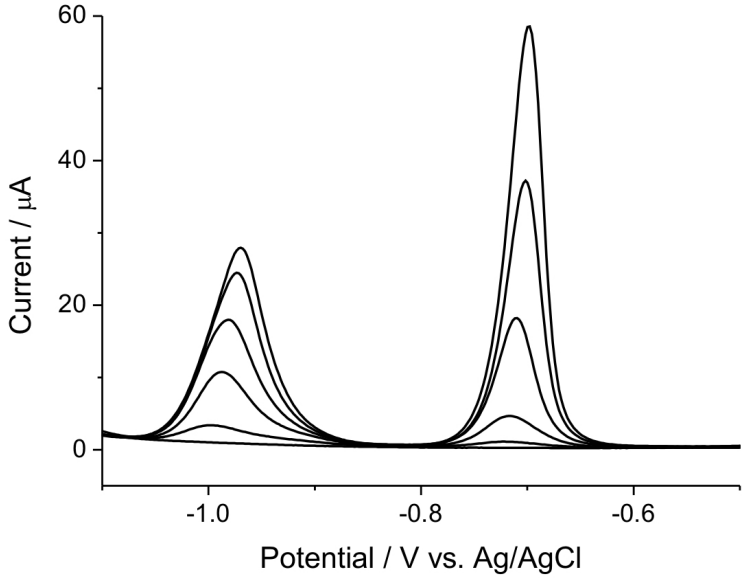


Figure 1.15: *An overlay of SWV anodic stripping voltammograms for additions of trace cadmium and lead to a bismuth modified BDD electrode, in 0.1 M $HClO_4$. (See Chapter 5)*

1.7. References

[1] A. J. Bard and L. R. Faulkner, *Electrochemical Methods: Fundamentals and Applications,* 2nd edn., John Wiley & Sons, Inc., New York, **2001**

[2] R. G. Compton and C. B. Banks, *Understanding Voltammtery,2nd* edn., Imperial College Press**,** London**, 2010**

[3] J. Wang, *Analytical Electrochemistry,* 2nd edn., Wiley-VCH, New York, **1994**

[4] P.H. Rieger, *Electrochemistry,* 2nd edn., Chapman & Hall, New York,, **1994**

[5] A.C. Fisher, Electrode Dynamics, Oxford University Press, Oxford, **1996**

[6] J.R. Gribbin, *Science, a history*, *1543-2001*, Allen Lan; London ; New York, **2002**

[7] Figure from Department of Chemical Engineering and Biotechnology, University of Cambridge website, **2011**, http://www.ceb.cam.ac.uk/pages/linear-sweep-and-cyclic-voltametry-the-principles.html

Chapter 2

Surface Characterisation by Topographic Methods: SEM, AFM and EC-AFM

In this chapter the technological methods involved in the characterisation of electrode surfaces and surface modifications are discussed. The topography of an electrode surface is of great importance from a scale of micrometers and below, which is beyond the magnification limits of any optical microscope. Consequently, methods such as electron microscopy and scanning probe microscopy have been developed extensively to allow for micro and nanoscale surface characterisation. Herein the microscope technology most frequently encountered (and used in this thesis research) in the surface characterisation of unmodified and modified electrodes is discussed.

2.1. Optical microscopes

At the turn of the 17th century the first compound microscope was invented, attributed to a number of inventors; a couple of Dutch eyeglass makers, Hans and Zacharias Janssen in 1590, another Dutch spectacle maker Hans Lippershey in 1608, and also Galileio Galilei in 1609 [1-3]. The inventors were in fact trying to reinvent the telescope, and it was Galileo who developed a microscope he termed an 'occhiolino', consisting of a convex and a concave lens, later named a compound microscope by Giovanni Faber, who also coined the term 'microscope'.

The compound microscope uses a system of lenses to magnify an image of a small sample. They are still in use today, with the most sophisticated optical microscopes using

up to 30 lenses in a complicated arrangement, allowing magnification to the micrometre scale.



Figure 2.1: *A multipurpose optical compound microscope [4]*

The technology associated with optical microscopes and achieving higher quality and varied images is still being developed, and they have been paramount to the advancement of biological science. However, since as early as the mid-19th century the fundamental limitations of optical microscopes have been recognised, owing to a resolution limit, *r*, determined by the equation

$$\boldsymbol{r = \frac{0.61\,\lambda}{n \sin \alpha}} \qquad [\mathbf{2.1}]$$

in which λ is wavelength of light, *n* is the refractive index of the medium in which the object lies, and α is the aperture semi angle [1, 2]. *n* sinα is generally called the numerical aperture (NA). The implication of this limit is that the lowest value of *r* possible is about 1.5 μm, and this is with zero optical aberrations in the whole microscope set-up, green light (400 nm wavelength), maximum aperture and an oil immersion objective lens [1, 2]. In practice therefore, most optical microscopes cannot magnify to sizes below that of a human hair, approximately 50 μm.

2.2. Scanning Electron Microscopes (SEM) [1, 2]

Electron microscopes use a beam of high-energy electrons to create an image of a sample. Where the wavelength of light (400-700 nm) restricts optical microscopes to a resolution of a few microns at best, the wavelength of an electron beam is considerably smaller, between about 0.001 and 0.01 nm [1]. As such a theoretical resolution of 0.02 nm is possible as determined by

$$r = \frac{0.61\,\lambda}{\alpha} \qquad [2.2]$$

Lens aberrations prevent this theoretical value being obtained, however advances in accounting for such limits have allowed for transmission electron microscopes (TEM) to resolve individual carbon atoms in diamond, with separation of 0.089 nm [5]. The use of electrons therefore allows for much greater magnification relative to an optical microscope.

The interaction of high energy electrons with a material can be analysed in a number of ways, and are encompassed by two types of EM; the transmission electron microscope (TEM) and the scanning electron microscope (SEM). Both use a similar electron source and arrangement of beam forming lenses, yet differ in their signal detection methods, sample analysis and sample size. A brief overview of electron microscopy is provided in the following sub-sections with focus on SEM.

2.2.1 The history of electron microscopes

Until the mid-20th century optical light microscopes remained the only type of microscope available to scientists. However, some 50 years prior to this in 1899, Weichert successfully concentrated electrons (cathode rays) into a small spot using an electromagnetic field produced by a long solenoid (a magnetic coil of wire with a metallic core). In 1926 Busch theoretically demonstrated that a beam of electrons may be formed using a short solenoid in a manner akin to the formation of a focused beam of light using lenses. In 1931 Ernst Ruska and Maximillion Knoll put the theory into practice and produced a magnified

electron image, with the first prototype of an electron microscope (EM) being built in 1933 by Ruska. This achievement won Ruska a share in the Nobel Prize for physics in 1986, along with Gerd Binnig and Heinrich Rohrer for the invention of the scanning tunnelling microscope, discussed later in this chapter. The onset of the Second World War delayed the commercialisation and further development of EMs until the 1960's, at which point nano-scale images were readily observed.

2.2.2. The formation of an electron beam

2.2.2.1. The electron gun

The high-energy electrons are produced using an electron gun, the design of which is shown schematically in Figure 2.2. The electrons are emitted from a cathode material which can be a heated filament that releases electrons thermionically, or a field emission gun (FEG) which emits electrons from a single crystal tip held at an extremely negative voltage (kilovolts).

The most widespread approach uses thermionic emission, and a variety of materials may be used as the heated filament. A common material used is tungsten owing to its properties of the highest melting point and lowest vapour pressure of all metals. In general the filament (e.g. tungsten wire) is held at a high negative potential to form a cathode relative to an anode and the rest of the microscope. The filament is then heated to temperatures in excess of 2700 K, at which it thermionically emits an abundance of electrons. These electrons are accelerated across the potential difference towards the anode and subsequently pass through a circular hole into the microscope column. The use of a Wehnelt cap between the anode and cathode, held at a slightly more negative voltage to the filament, allows the original diameter of the electron emission to be controlled and to generate an energy beam of varying wavelength.

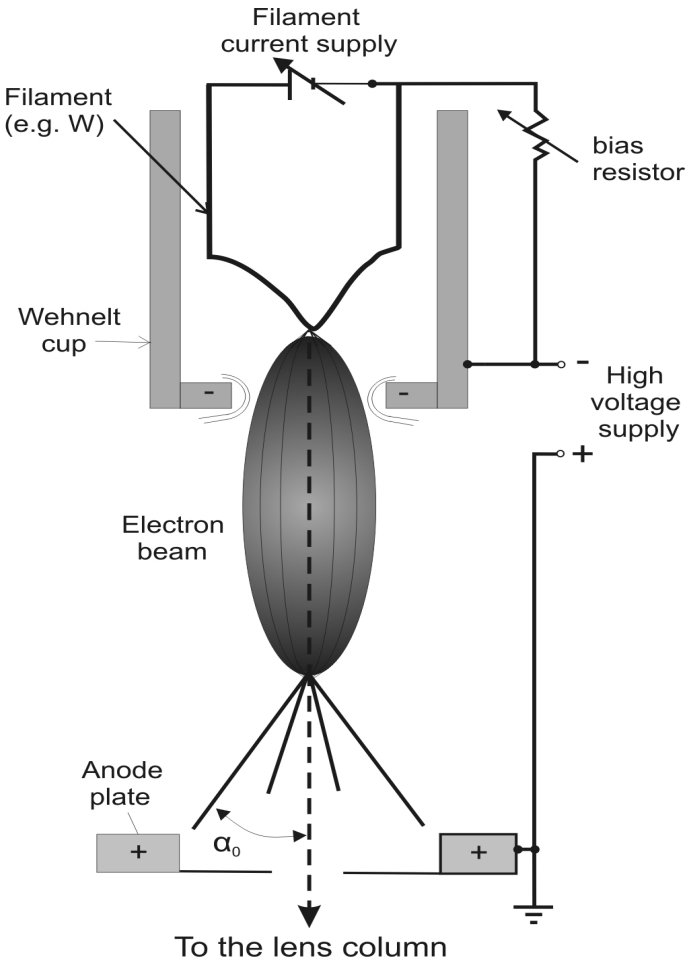


Figure 2.2: *A schematic of an electron gun using a heated filament electron source (Adapted from [2])*

A field emission gun (FEG) can provide electrons of very well defined energies, therefore have the advantage of lower signal-to-noise and the ability to provide a monochromatic supply of electrons. These properties are highly advantageous with regard to analytical and high resolution electron microscopy. Electrons are drawn from an emitter, usually tungsten, which is fashioned into a sharp and precise point of about 0.1 μm, using an extremely high electrical field (>10^9 V/m) such that electron tunnelling occurs. This draws considerably more electrons from the tungsten than is possible using thermionic methods and the corresponding current is directly related to the strength of the applied field.

2.2.2.2. Focusing the beam – magnetic lenses

The electrons are directed using electromagnetic and/or electrostatic lenses. In the basic design by Ruska, which is still the basis of modern day electron microscopes, the electromagnetic lens is a tightly wound coil of wire wrapped around a soft iron core (a solenoid), through which a current is passed to induce an precise electromagnetic field inside the electron column. A typical electromagnetic lens is designed to provide a magnetic field *almost* in parallel with the beam direction, with a slight magnetic field in the radial direction. Consequently the electrons travel in a helical fashion, imposing a velocity component which causes the electrons to spiral and converge into a point, exactly as light is focused by a glass lens. The electrons converge into a high-energy focused beam within the column, which is easily controlled by altering the current passed through the coil.

2.2.3 Transmission electron microscopy (TEM)

The transmission electron microscope (TEM) was the first EM to be built back in 1933. The microscope transmits the high energy beam of electrons *through* an ultrathin sample, with the transmitted signal providing information regarding the structure of the specimen. The transmitted electrons are magnified by another series of magnetic lenses, before striking a fluorescent screen, photographic plate or charge-coupled device (CCD) camera.

The images produced at a TEM are two-dimensional and can have a resolution on an atomic scale. Provided suitable aberration correctors are in the system and software, resolution limitations by spherical and chromatic aberration may be overcome. As such the carbon atoms in diamond and silicon atoms in a silicon structure have been imaged despite separation distances of 0.089 and 0.078 nm respectively [5]. Consequently TEM has become an invaluable tool in the advancement of nanotechnology.

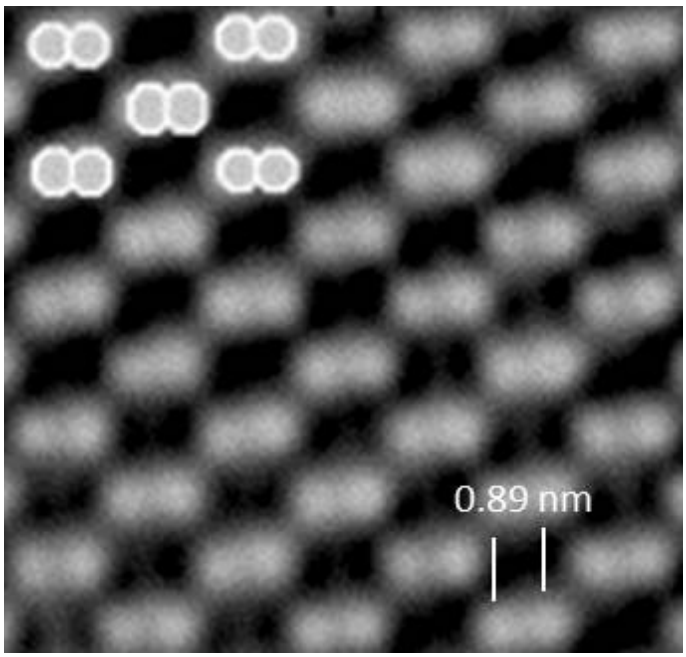


***Figure 2.3**: TEM image of carbon atoms in diamond [110]. Atomic positions are marked. Single carbon columns are resolved at a spacing of 89 pm (from* [5]*)*

2.2.4. Scanning electron microscopy (SEM)

Scanning electron microscopy (SEM) is capable of imaging and analysing bulk specimens, unlike TEM described above. It can provide information about the surface topography, composition of the material and electrical conductivity of the surface due to the wide variety of electrons and quanta emitted during analysis.

As with TEM, high energy electrons are emitted from a thermionic, field-emission or Schottky cathode and accelerated toward the anode across a potential difference ranging 0.1 to 50 keV. Electromagnetic magnifying lenses control the electron beam diameter, except the final probe-forming lens is positioned relatively far from the sample. This is to reduce the magnetic field within the specimen chamber and at the specimen, thus allowing the various electrons and quanta to be detected without deflective interference. Furthermore the probe-forming lens has a specific set of deflectors which direct the electron beam in the x and y axes such that it scans the sample surface in a raster fashion over a rectangular area.

The electron probe aperture (α in equation 2.2) is small and of the order of ten milliradians when used for routine work and high resolution. The smallness of this aperture is the reason why SEM has a much greater depth of focus relative to optical microscopes, and allows for the well resolved, 3D images consistently produced by SEM.

As the electrons strike the surface they interact with the sample in a volume known as the interaction volume. This volume depends on the energy of the electrons, and the atomic number and density of the sample, but ranges from less than 100 nm to 5 μm *into* the sample surface. Within the interaction volume the electrons lose energy by scattering or absorbing into the sample. The scattering may be elastic for primary electrons (i.e. from the beam) or inelastic for secondary electrons (i.e. from the sample). These scattered electrons, as well as electromagnetic radiation that may also radiate in the interaction, are detected at specialised detectors.

The deflection coil system in front of the final probe-forming lens is synchronised with a separate electron beam which is directed at a cathode-ray tube (CRT) display. The intensity of the second beam is modulated by the signals recorded for the emitted electrons and/or transmitted currents, such that a detailed image of the specimen is produced. This is then digitally captured by the computer to which the SEM is connected.

2.2.4.1 The imaging modes of SEM

Electron-specimen interactions generate a large body of information in the form of emitted particles and energy, and transmitted signals. SEM provides a platform to exploit all these signals due to a range of different imaging and operating modes. Each mode analyses one type of signal, and the following briefly described some of the most important interaction signals produced.

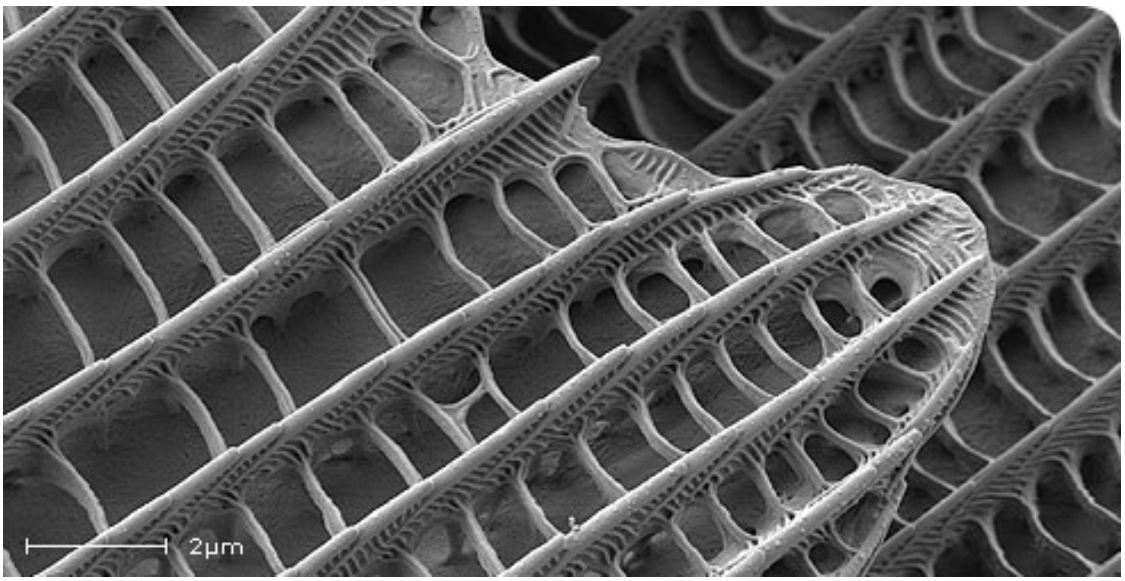


Figure 2.4: *A secondary electron SEM image of a butterfly wing (from* [6]*)*

Secondary electrons

Secondary electron imaging (SEI) is the standard detection mode of most SEMs, and produces high-resolution images to the nanometer scale. Secondary electrons (SE) are generated by inelastic collisions with the specimen such that a specimen electron is excited to energies beyond the work function, and are consequently emitted from the sample. The yield of SEs is dependent of the tilt angle of the surface element, thus enhanced emission is observed at edges and small particles, and incomplete collection causes a shadow contrast in the acquired image, therefore allowing the surface topography to be well defined. Furthermore, a large depth of field, provided by the narrow electron beam, yields three-dimensional images of high resolution to 1-10 nm. Such an image is shown in Figure 2.4 above.

Back-scattered electrons

These are electrons from the primary electron beam that are elastically scattered back off the sample surface. The electrons are more energetic than the SE, ranging from 50 eV to the energy of the primary electron. They provide information regarding the distribution of different elements in a sample due to a direct relation between the backscattering coefficient

and the mean atomic number of the area of interaction. Topographical information is also obtained using BSE as they also respond to specimen inclination, providing further contrast and shadow effects to the acquired image.

X-rays

The SEM may be used to detect characteristic X-rays from the sample by means of energy dispersive x-ray spectroscopy (EDX). The x-rays are emitted when the electron beam removes an inner shell electron from the sample, causing a higher electron to migrate to the position of the lost electron. The migration emits excess energy due to the migration in the form of a characteristic x-ray. The emitted energy is so specific to the element that the peaks in the corresponding spectrum are essentially a 'fingerprint' of the element.

2.2.5. Advances and limitations of electron microscopy

2.2.5.1. The advantages of SEM

SEM is a far superior microscopic technique to TEM, and is a much more useful tool for an electrochemist investigating electrode topography and composition. The TEM is greatly limited in application owing to the requirement of a *very* thin specimen, thus restricting its use to a highly select sample range. Furthermore, the nature of a transmitted signal is that no depth of field is possible, thus rendering all images two-dimensional, which is a problem with regard to topographical studies. Although the resolution of an SEM is less than that of a TEM generally, high end instruments regularly achieve resolution between 1 nm and 20 nm.

The wide range of modes increases the versatility of SEM, allowing the microscope to be used towards understanding the surface topography of a specimen, and gaining critical analytical information such as surface element concentrations and distributions. The high level of control over the electron beam in modern SEM allows the magnification and resolution to be easily controlled at a computer interface, thus rendering the technique

highly user friendly. Image acquisition is rapid, and sample sizes with cm^2 areas may be explored and analysed in their entirety with ease. Furthermore, a sample height of up to 10 cm is possible in most modern SEM, with the specimen mount highly adaptable to considerable variations in sample dimensions.

2.2.5.2. The limitations of SEM

The major limitation of EM is the sensitivity of the electrons used in the electron beam towards ions other than the specimen. Electrons will interact and lose energy with any ion in their path, and as such the partial pressure of an SEM chamber must be below 10^{-2} Pa; basically a vacuum. The samples must be loaded into a decompression chamber prior to entering the SEM chamber, and are then entered into the vacuum atmosphere. Although this has no impact on dry, modified solid specimens, it imposes a major limitation on the possibility of simultaneously or immediately imaging an experimentally modified sample, such as an electrode. The images in this thesis of modified electrodes dried in air are highly informative of the nature of the modification, but the separation between surface modification and topographical and elemental analysis is such that the true nature of the modified electrode following modification is still questionable. This is particularly so in the case of air sensitive modifications which in turn provide irrelevant elemental analysis relative to the experimental arrangement.

Another limitation of SEM is the occurrence of electrostatic charging effects. Charging is observed when non-conducting materials are imaged due to an accumulation of charge from the electron beam. The consequence is that non-conducting or partially non-conducting samples must be prepared by coating with an ultrafine conductive material, usually gold or platinum. Although electrodes are conducting, they are often embedded in a non-conducting body made of PTFE, PEEK or other plastics commonly used in electrode fabrication. The implication is that complete samples must be coated, otherwise the contrast

between the conducting and non-conducting parts can results in image artefact or scanning faults.

A final limitation to SEM is the potential damage of the specimen caused by the intensity of the electron probe. Thermal energy greatly increases at areas under investigation by the electron probe, and if repeat analysis of a very small area is necessary then the sample may be charred or warped. The effect of such thermal aggravation is often seen when the magnification is decreased in anticipation of moving to another site, and the previously scanned area is evident due to a difference in the surface image.

2.3. Scanning Probe Microscopy [7-9]

Scanning probe microscopy (SPM) is a form of microscopy that uses an atomically small probe tip to scan a surface. The interaction between the tip and surface correspondingly produces three dimensional, real-space images of the sample with high spatial resolution. Two types of SPM dominate the technique; scanning tunnelling microscopy (STM) and atomic force microscopy (AFM). They are discussed herein, with emphasis on discussing AFM and the advancement on electrochemical AFM.

2.3.1. History of scanning probe techniques

Scanning probe microscopic techniques were developed in the 1980's, beginning with the invention of the STM by Binnig, Rohrer and Gerber in 1982 [10]. AFM was invented later in the decade by Binnig, Quate and Gerber [11], and was a development of the STM technology to expand the range of samples that could be analysed at the near atomic scale. Both the STM and AFM are advancements of a stylus profilometer, an invention of the 1920s that uses a probe (stylus) to feel the topography of a surface and derive the surface roughness.

The STM was borne out of the concept of electron tunnelling, first proposed in 1928 by Fowler and Nordheim in an explanation of field emission phenomenon [12], following the rise of quantum mechanics in the early 1920s. Over the following 50 years, theory regarding tunnelling became experimentally viable, until in 1982 Binnig et al observed electron tunnelling through a controlled vacuum gap and imaged single atom steps. The invention won Binnig and Roher a share in the Nobel Prize for Physics in 1986.

The AFM was developed in 1986 using technology derived for the STM and Binnig's desire to improve the stylus profilometer. The technique uses the interaction between a small tip and surface caused by intermolecular and electrostatic forces. The idea accelerated in the 1960's when Derjaguin et al published work [13] describing interparticle forces and colloidal interactions, later prompting the invention of the surface forces apparatus by Israelachvil [14]. In 1979 Young et al [15] developed the non-contact profilometer, shortly followed by the STM in 1982, only for the technology to be superimposed and the AFM created.

2.3.2. Scanning tunnelling microscopy

The STM uses electron tunneling to form an atomically detailed image of a sample surface. It is designed in much the same way as a profilometer, in which a fine tip (the stylus) scans the surface of the sample. The main differences between the STM and profilometer is that the STM tip does not make contact with the sample, but maintains a height of 5 to 50 Å above the surface, and also the motion of the scanner is extremely well controlled, moving smoothly on the Angstrom scale.

2.3.2.1. Electron tunneling

The phenomenon of electron tunneling is based on quantum mechanics, and is a branch of the more generalized quantum tunneling theory. In a metal electrons exist in a continuum of energy levels, a finite energy range the maxima of which is the Fermi level represented by

the materials work function. In a semiconductor, electrons reside in a valence band but can be promoted to a conduction band given a certain amount of energy. A schematic of electron tunneling is shown in Figure 2.5.

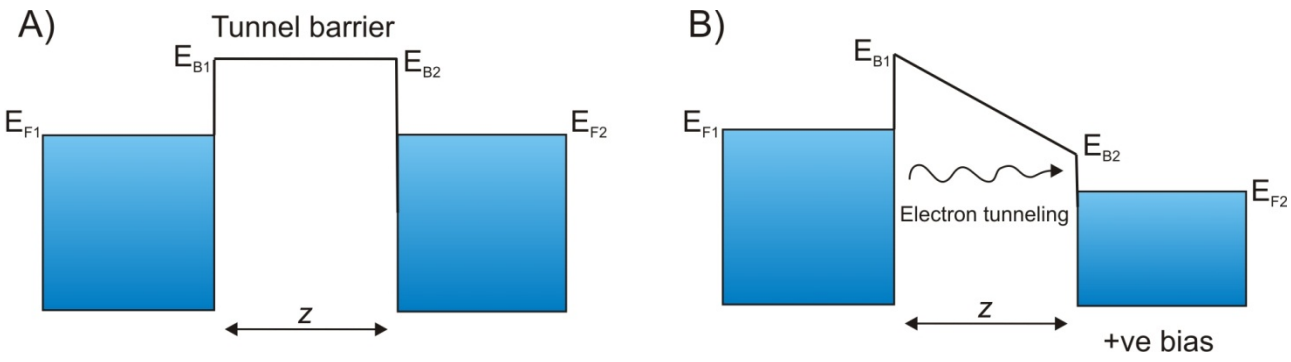


Figure 2.5: *The simplified schematic of the process of electron tunneling in STM. A metal of energy E_1 is brought within distance z to a conducting sample. In A there is not a potential difference between the metals sufficient to overcome the energy barrier. In B a positive bias is placed on the second metal thus lowering the energy of the Fermi level, and allowing electrons to tunnel from the first metal to the second relative to the energy difference $V = E_{F1} – E_{F2}$. (Adapted from [6])*

When placed near an insulator or in a vacuum, the electrons are confined to the Fermi of the metal by an energy barrier. If another metal is placed within a specific distance of the first metal, and a potential difference exists between the two either naturally or externally, then the energy barrier between the two species is altered favorably. At this point electrons may ‘tunnel’ from the conduction band of one metal to the energetically lower lying empty orbitals of the second metal, as shown in Figure 2.5.

In STM the metal tip is brought very close to the conduction surface of interest, which has a potential bias. A tunneling current arises that corresponds to the distance of the tip relative to the surface, thus allowing an extremely sensitive estimate of the tip-to-surface distance to be made solely on the measured current.

2.3.2.2. Piezo electrodes

The use of peizo materials in STM and AFM is the linchpin of the two inventions. On the microscale and below, mechanical means of moving in the x, y and z directions is not ideal, as it would involve parts that move like gears and bearings that are slow to respond and jerky and unpredictable at nanoscale. Piezo materials move smoothly at the nanoscale, owing to special properties relating to the piezo electric effect.

A piezo material is general a crystal in which there is a number of electron dipole moments within the lattice. The density of dipoles per unit cell is termed the polarization, and dipoles near eachother are aligned in regions known as Weiss domains. On the application of an electric field, the randomly orientated Weiss domains can be aligned by a process known as poling. On application of a voltage to a piezo, a physical change occurs in the structure, by means of a contraction or expansion. The contraction or expansion can be up to $1/10^{th}$ of the piezo length, and it provides a motor effect that is easily controlled, smooth, and on a very small scale. Correspondingly, the piezoelectric material can produce a voltage when mechanically compressed or expanded.

In STM the piezo material is used accurately to control the height of the tip relative to the surface by applying a specific voltage, thus maintaining a constant tunnelling current. The corresponding piezo voltage vs. time plots that are measured during the scan can then be recorded and used to provide a very fine image of the conductors surface. The accuracy of the method is so high that modern day STMs can produce images to a resolution of 0.001 nm.

2.3.3. Atomic Force Microscopy [8, 9]

Atomic force microscopy (AFM) is a SPM method that does not use electrons, but rather fundamental forces to form a microscopic image. The probe tip interacts with the sample surface in an attractive and repulsive manner depending on the separation distance between the two components, such that a variety of tip-surface interactions may be measured by an

AFM. In 'contact mode' the tip predominantly experiences repulsive van der Waals forces, but as the separation increases, electrostatic and magnetic forces may dominate.

The technique is very versatile, and most importantly does not depend on there being a potential difference between the tip and the surface, thus allowing non-conducting materials to be imaged to the sub nanoscale. Furthermore, as electrons are not involved, the technique does not need to be performed under vacuum conditions, and may in fact be used in-situ if needs be.

2.3.3.1. The basic elements of AFM instrumentation

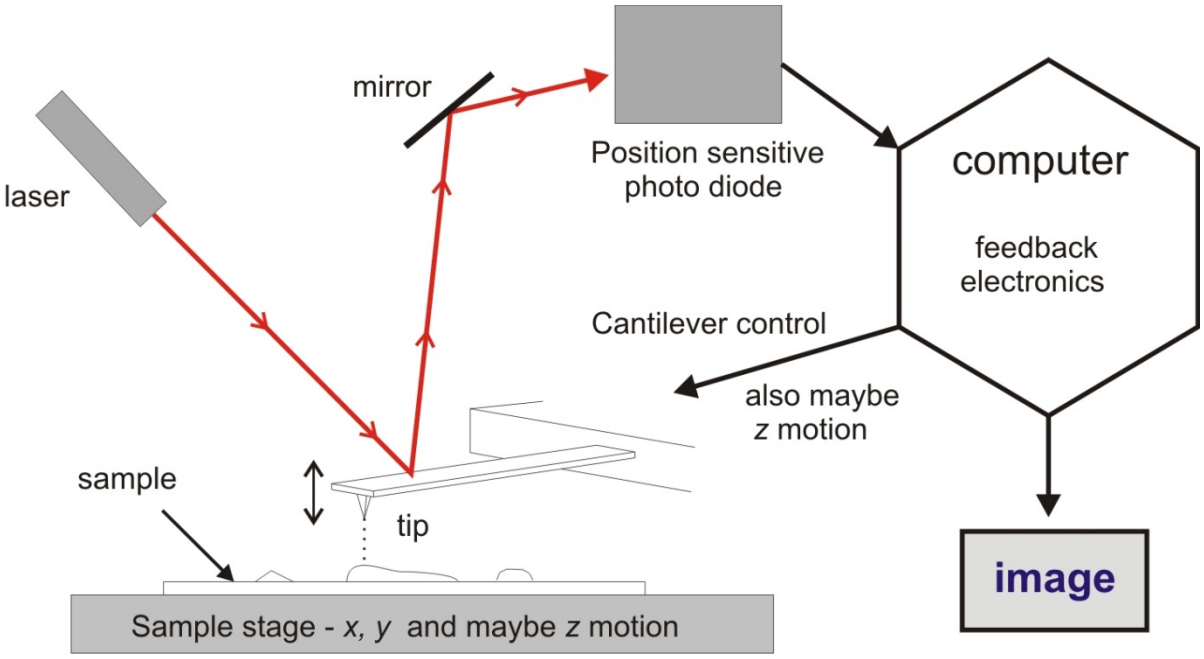


Figure 2.6: *A schematic diagram illustrating the operating principle of an AFM. The cantilever and tip are placed very near the sample surface. The sample-tip distance is then decreased further using piezo electric positioners in the z axis, either in the sample stage or scanner head. Piezo devices move the sample stage in the x and y axis to scan the surface, whilst the z axis is adjusted corresponding to the surface topography. A laser is reflected off the top of the cantilever, and monitors deflection due to force. A computer adjusts the z axis and cantilever oscillation based on information from the photo diode signal.*

In Figure 2.6 is a schematic of the operating principle of an AFM. The AFM can be considered as three main elements; the probe, the positioners and the controller. Each component is discussed in greater detail below.

The probe

In AFM the underlying principle of the technique is that the interactions of the probe tip, which is mounted onto a flexible cantilever, cause a deflection in the cantilever that corresponds to the size of the force experienced. The cantilever was developed in 1988 at IBM, and is based on the stylus of a profilometer. A laser spot is focused onto the reflective back of the cantilever probe, such that the reflected beam falls within the range of a position sensitive sensor. As the tip and surface interact the cantilever is correspondingly deflected thus altering the position of the reflected laser signal. This signal is converted to a digital signal and recorded by a computer.

The positioners

As mentioned previously the key technology that makes SPM methods possible on the nanoscale is the use of piezo materials. The AFM positioner is based on piezoelectric materials just as in the STM. AFMs originally used a piezo tube invented by Binnig for the STM, and some AFM manufactures still use this today.

The hollow tubes, shown in Figure 2.7, are about 8 - 10 cm long and about a cm in diameter. They are segmented, generally into four pieces, so they can provide movement in the *x, y* and *z* axes. Such positioners based on this design can provide 12-13 μm in the *x* and *y* axes, and 1 – 4 μm in the *z* direction.

For the *x* and *y* positioners the tube segments have metal electrodes along the inside and depending on the sign of the applied voltage the piezo material expands or contracts accordingly. In the simple schematic shown in Figure 2.7b a positive voltage is applied to the left hand side and a negative to the right hand side, such that the left hand side contracts

and the right side expands. This has the effect of 'bending' the tube to the left, and with opposite voltages the tube would bend to the right. This gives us a scanning motion in the *x* axis. Similarly, because the positioner is a tube, a complementary voltage may be applied in the *y* axis, such that the tube tilts forwards and backwards relative to the plane of the Figure in 2.7b.

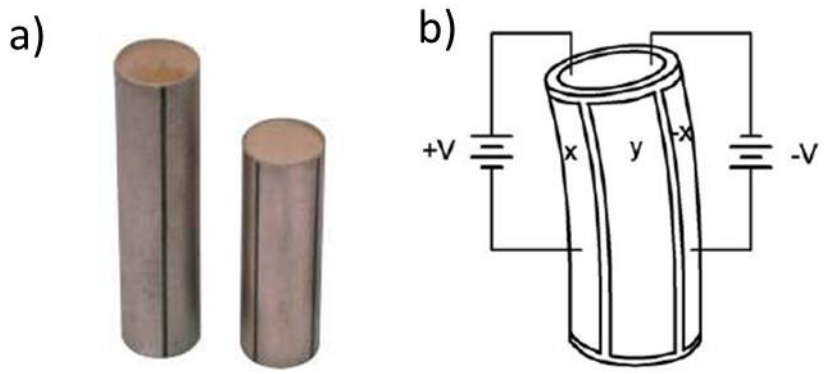


Figure 2.7: *a) a typical ceramic scanning piezo tube b) a schematic image of the piezo tube motion relative to an applied potential, [16, 17]*

Movement in the *z* axis is achieved by a segment of the tube that has two electrodes, inside and out. By applying a positive potential to the outside of the electrode, the tube segment expands radially, thus causing the tube to correspondingly shrink or vice versa. Because the tube is longer than it is thick, the movement in the *z* axis is greater than radially.

A major issue arise from using the piezo tube type positioner. The movement in each axis is not completely separate of the other directions (i.e. purposeful movement in the *x* axis also causes a degree of movement in the *y* and *z* axes). This problem is called *coupling* and it results in a distortion, often significant, of the acquired image.

The MFP-3D AFM developed by Asylum Research (AR) in 2000 has a different mechanism for the positioners in which the *x* and *y* positioners lie in a nested yet separated

arrangement underneath the sample, and the *z* positioner is contained within the scanner head, along with the cantilever holder [9]. This arrangement is shown in Figure 2.8.

The nested design of the *x* and *y* positioners use flexures instead of sliding the sample, as the gentle flexing motion is less jerky than a sliding motion. More importantly, the piezo material used is individual piezo stacks instead of tubes. The stacks only move in a single direction, and they are controlled independently of one another. When a potential is applied to the stack it can move up to 45 µm in one direction with an enormous force against the flexure. The design is such that when the piezo stack expands it pushes against a metal bar, which in turn flexes against a fulcrum and pushes the inner stage on a spring. The force of the stack is translated to the inner stage and smoothly moves the sample back and forth in the x or y direction relative to the applied potential and stack length.

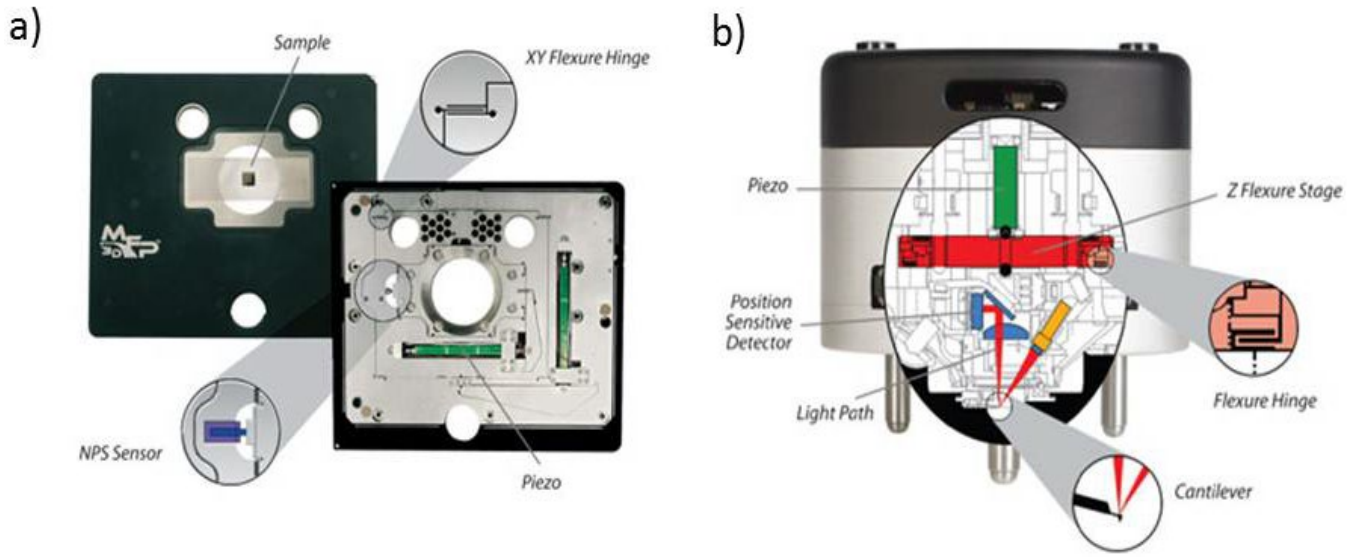


Figure 2.8: *A separated positioners design used in the MFP-3D AFM by Asylum Research. a) the sample stage showing the nested design for the x and y axes and the corresponding piezo stacks, b) the scanner head which contains the z axis piezo stack and the cantilever. (Figures from the AR website and brochure for the MFP-3D SA system.)*

By separating the movement of the positioners the effect of coupling is avoided, and the images obtained at the AFM are free of such distortive effects and possible artefacts. Furthermore, by placing the *x* and *y* positioners underneath the sample on the stage, and placing the *z* positioner in the scanner head, the sample can be observed from underneath using an optical microscope, and a greater range of experimental arrangements can be easily accommodated.

The controller

The controller in an AFM is the computer that receives a digital signal converted from the laser beam deflection. Based on the information obtained from the position sensitive photodiode detector, the computer adjusts the separation distance from the sample and the oscillation of the cantilever. This process is known as a feedback circuit, and means that the output of the system is fed-back into the input. AFM can also be controlled in an open loop system, in which no feedback from the output is employed.

2.3.3.2. Force detection and AFM imaging

Contact mode (dc mode)

There are several modes of imaging based on atomic forces. The measurement of the cantilever deflection is the most obvious imaging mode, and is akin to the determinations made by a profilometer. When the AFM is in contact mode (also termed dc mode) the cantilever is set to have a constant deflection. This provides a constant force image based on the variation in the z axis and the voltage necessary across the piezo to accommodate the surface topography. This method is analogous to the constant current image produced by STM. The tip must be sufficiently close to the surface to obtain a van der Waals dominated image. The method is not comparably sensitive to the STM however, and has a relatively small signal-to-noise ratio.

Non-contact mode (ac mode)

A more sensitive AFM measurement of surface topography is obtained using the vibrational characteristics of the cantilever. The dimensions of the structure and the properties of the materials from which the cantilever is made determine the mechanical resonant frequency. The cantilever may be considered as a one-dimensional, lightly loaded beam, such that it has a resonant frequency (kHz) and a spring constant (N/m) associated with it. The resonance frequency is found by oscillating the cantilever at a range of frequencies and determining the frequency at which the oscillation is most amplified.

The resonance frequency of the cantilever will shift and the amplitude will be dampened when placed in a force gradient. By merely measuring the change in amplitude it is therefore possible to determine the magnitude and sign of the force gradient at the surface. The cantilever amplitude at a particular frequency may be kept constant by varying the *z* axis, thus producing a constant force gradient image. This is called non-contact mode AFM (also ac mode) because the cantilever oscillates above the sample surface as it is scanned. It has a larger signal-to-noise ratio than contact mode, and is more appropriate for imaging softer and/or easily moved samples such as polymers, DNA or nanotubes.

Tapping mode

In some circumstances it arises that the probe tip can stick to the sample surface, such as in in-situ conditions or when a sample forms a liquid meniscus layer in ambient conditions. To avoid the anomalous signals associated with sticking to the surface, or the possibility of attaching a nanoparticle to the end of the tip, the cantilever is driven to oscillate at or near its resonance frequency with amplitude greater than 10 nm, usually hundreds of nanometers. The amplitude of the large oscillation if observed to slow down as it approaches the sample surface due to the many forces present. The image is produced by measuring the intermittent contact of the tip with the surface, essentially providing a non-constant force image.

2.3.3.3. AFM cantilevers and probes

The original probe used by Binnig et al was a diamond shard stuck at the end of a metal cantilever. More sophisticated and varied cantilevers are available today, made by a range of manufactures, and in a wide range of materials, and are of varying length, stiffness and tip size.

The cantilever is a beam, supported at one end, and can be of the traditional rectangular form, but also in a triangular form, the latter having a considerably lower force constant for use with softer samples and in-situ environments. The cantilever comes in a variety of lengths and can be of variable stiffness. This allows the resonance frequency of the cantilever to be varied for different samples and environments. An SEM image of different length triangular and a beam type cantilevers are shown in Figure 2.9, in which the micrometer size of the lever is emphasised.

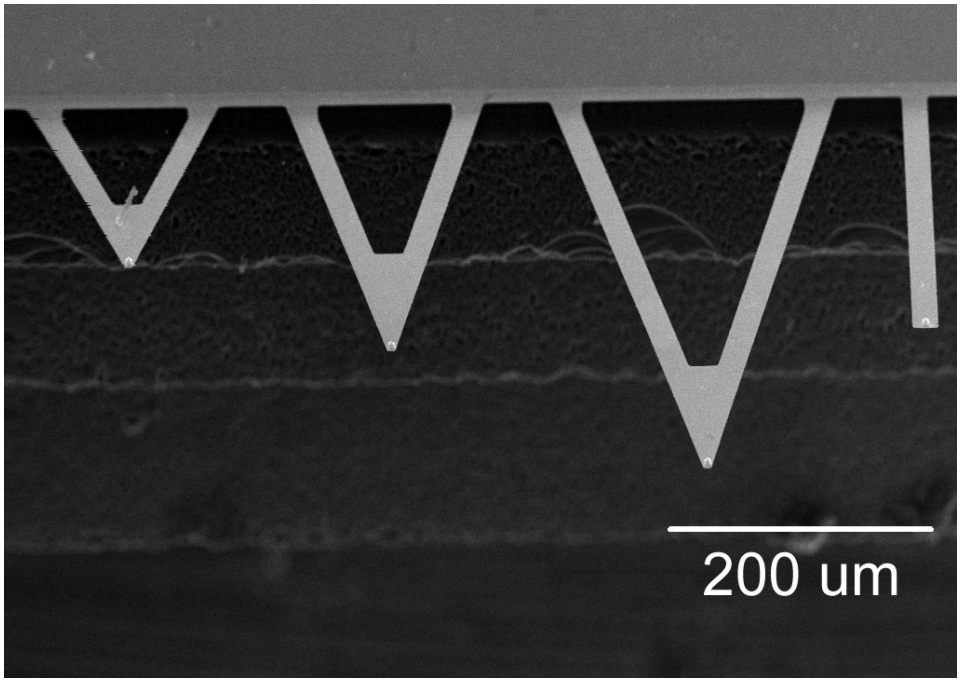


Figure 2.9: *An SEM image of a range of AFM cantilevers attached to a holding chip. On the far right the traditional rectangular type cantilever with a single point of support is show [18]*

AFM tips are nanofabricated from silicon, silicon nitride, quartz or carbon nanotubes. In Figure 2.9 the tips are just visible at the end of each cantilever. Figure 2.10 is a higher magnification of the cantilever end, showing the pyramidal shape and conical shape of the respective tips.

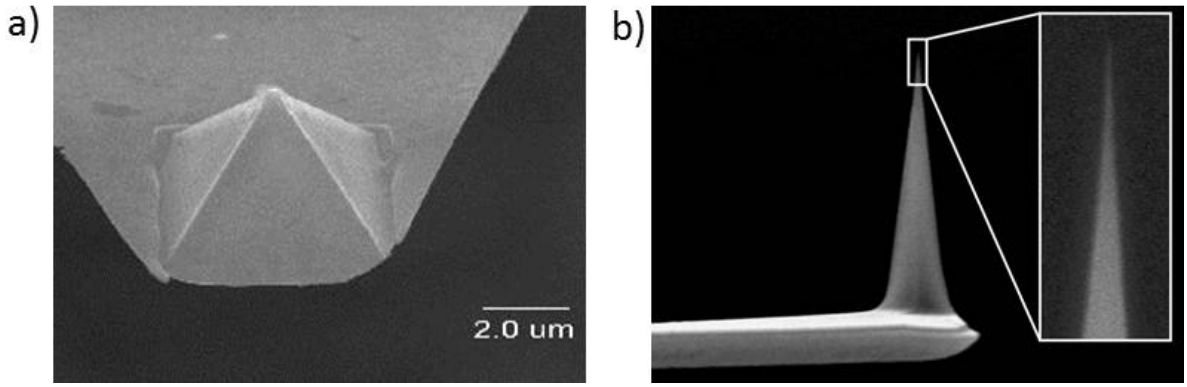


***Figure 2.10**: a) a pyramidal b) a conical tip AFM tip and made of Si [18, 19]*

2.3.3.4. Sample preparation and AFM environment

The surfaces that can be studied by AFM are essentially boundless with respect to their constituents as there are no limits imposed by conductivity or vacuum conditions. Unlike STM and the EM methods described previously, AFM can be performed in ultrahigh vacuum, ambient air, high humidity, elevated temperatures, inert gases or even in a liquid environment. The benefit of analysing force changes is that these forces are present regardless of the nature of the sample or the environment in which it is in.

One of the only major limits of AFM sample preparation is the *z* axis limit, generally only a few tens of microns in the AFMs produced today. Furthermore, a surface with extensive peaks and troughs with a relatively large and sudden difference in height can lead to distorted images and artefacts in which the aspect ratio is completely wrong. It is therefore a requirement of the AFM that the sample be complementary to the limited range of the *z* axis. Most frequently the application of AFM is to study samples of these

dimensions, which are unobservable by any other microscopic means, such as DNA, viruses, organic molecules and in-situ grown nanomaterials.

With regard to AFM preparation, the sample requires little or no attention, unless the objective is to image a highly polished surface and observe atomically or near atomically resolved surface defects. In which case, the surface must be polished and cleaned of any possible polishing residue such as diamond microparticles or alumina. It is necessary to prepare certain environments when intending inert air or temperature controlled experiments, but most commercial AFMs available today have the means of adapting the AFM set up to the experimental needs.

2.3.3.5. Advantages and disadvantages of AFM

2.3.3.5.1. Advantages of AFM

Relative to the SEM and TEM, AFM has several advantages. The images produced at an SEM often have the appearance of a 3D image, owing to the depth of field in the secondary electron SEM scan. However, the projection is not technically 3D and gives no real sense of height and relative range in the *z* axis of the surface topography. In AFM the entire image is a three dimensional surface profile, derived from the forces between the tip and sample.

AFM can be performed on materials regardless of whether they are conductive or not. As such it may be used on a wider range of samples than STM, and also means that it is not necessary to coat the entire sample in a conducting material. This is an advantage over SEM as it avoids the potentially destructive process of sample preparation.

As electrons are not directly involved in the acquisition of an AFM image, the instrument environment can be anything from a vacuum to ambient air to a liquid. This is not the case for EM which is confined to vacuum or near vacuum conditions. Furthermore the AFM environment may also be increased in temperature or pumped with inert gases as well as many more experimental and environmental arrangements continually being

developed. It is an ideal stage for analysing biological samples, even living organisms, owing to the environmental controls and non-destructive sample analysis.

The resolution of AFM has been shown to be comparable to that of STM and TEM, allowing a true atomic resolution image to be formed in ultra-high vacuum, and also in liquid.

2.3.3.5.1. Disadvantages and limitations of AFM

Despite the clear advantages of AFM over EM methods it is still limited relative the SEM due to the much smaller maximum scan area of about 150 x 150 μm in the AFM relative to the millimetres squared area of the SEM. The AFM is very limited in the *z* axis as well on the order of 5-20 μm depending on the quality of the AFM and the scope of the scanner in the *z* axis.

A more frustrating disadvantage of AFM is the scanning speed. Although advances have recently been made in developing fast scanning AFMs, the past 25 years have been limited to a scanning speed that can take up to 15 minutes depending on the nature of the material being scanned. SEM images, at varying magnification can be scanned within minutes, and even at near real time provided the resolution quality can be low. The slow scan rate of AFM is not only time consuming, but can lead to thermal drift in the image, particularly when the sample is in-situ, causing image distortions.

Image artefacts are a potential problem in AFM, and are encountered with great frequency when using soft sample or difficult environments. A common problem is when material from the sample or sample environment stick to the tip, causing a double image. Image artefacts or distortion may also be caused by coupling of the scanner axes when a single, open loop piezo tube is used, as discussed previously. This can be avoided with a system of separated scanners in each dimension. Imaging issues can also arise when steep 'walls' and deep overhangs are encountered in the sample topography. Tapping mode AFM

can be used to address such variable topography, but a loss in resolution is often a consequence.

2.4. Electrochemical Atomic Force Microscopy

Electrochemical AFM (EC-AFM) is a development of AFM that takes advantage of the in-situ capabilities of AFM. The opportunity to perform electrochemical experiments that are immediately imaged on the nanoscale is highly beneficial scientifically. Herein, and in the following chapter, the development of EC-AFM will be discussed.

2.4.1. Limitations of ex-situ surface characterisation

Although the topographical data gleaned from EM, STM and AFM can be very useful and informative with regard to the surface modification of electrodes, the processes on the whole are retrospective and possibly not fully representative of the actual modified surface at the point of modification and possible application. Electrochemical processes almost entirely occur in liquid environments, with the process of electron transfer across a solution/electrode interface at the centre of the field. As such, a way of observing the processes occurring *at* this interface would be more beneficial than post reaction analysis outside of the experimental environment.

With regard to EM and STM methods, a further limitation is that the surface must be entirely conducting, such that the electrons can tunnel or do not impose charging effects that distort the acquired image. Electrochemically modified surfaces are for the most part conductive, but surface modification by adsorption of insulating materials is also an aspect of electrochemical experiments and in-situ processes, as is the formation of non-conducting surface oxides on electrodeposited materials on exposure to air. AFM avoids the limitations of variable conductivity in samples, and can also avoid the surface changes that can occur on exposure to air by preforming microscopic analysis in-situ.

2.4.2. The development of dynamic EC-AFM

EC-AFM has been explored since the 1990s, owing to the opportunity of in-situ analysis. A number of electrochemical or conductive measurement techniques have been coupled with AFM in a bid to produce topographical and electrochemical images of a surface, including scanning ion conductance microscopy (SICM) and scanning electrochemical microscopy (SECM).

Conductance measurements are almost routine at modern day commercial AFMs, with combined SICM-AFM capable of acquiring conductivity and topographical data, simultaneously. SECM was developed in the late 1980s and involves measuring a current through an ultramicroelectrode (UME) held or scanned near the substrate surface in a solution which contains an electroactive species. The substrate can vary greatly from a variety of solid materials such as metals, polymers, glass, to soft biological materials, or to liquids such as mercury. The substrate perturbs the electrochemical response of the tip, and this perturbation provides information about the nature and properties of the substrate. In 2000 Macpherson and Unwin [20] claimed the first combined SECM-AFM for imaging under fluids, capable of providing simultaneous topographical and electrochemical measurements, with high spatial resolution.

Dynamic EC-AFM requires a potential to be applied to the working electrode, such that electrochemical processes are induced, such as metal deposition. The probe then develops a physical, topographical image of the surface regardless of the electrochemical activity of conductivity of the modification. The electrochemical modification of electrodes with metal and metal oxide nanoparticles has been investigated microscopically using EC-AFM since the early 1990s following the first in-situ analysis of gold nanoparticles on mica [21]. That same year the in-situ underpotential deposition of copper nanoparticles on Au(111) working electrodes was reported [22].

Since these early experiments a number of groups worldwide have endeavoured to explore EC-AFM as a means to characterise nanoparticle growth and further understand the

nature of electrodeposition. The major disadvantage of EC-AFM is that the working electrode must be near atomically flat, or at least have height variation of a few nanometers at most across the surface when unmodified. This greatly restricts the number of electrodes that can be utilised in the AFM and also complicates the experimental procedure. The experimental set up has also been a limiting factor in developing EC-AFM owing to the need for an electrode connection to the working electrode which is positioned underneath the probe, and under an electrolyte solution.

2.4.3. Current technology

Although EC-AFM has been explored since the commercialisation of the first AFM in 1989, only a few AFM companies offer the capability to perform dynamic electrochemical experiments with a dedicated set-up. Park Scientific Instruments, the manufacturers of the first commercial AFM in 1989 have yet to develop a suitable AFM cell, as have JPK, NanoScan Tech, Jeol and NT-MDT.

Veeco (now part of Bruker) has offered an electrochemical cell for EC-AFM since the early 2000s, though the design had a number of flaws such as leaking and a difficult set-up. Presently they sell very simple electrochemical equipment for the EnviroScope^{TM}, consisting of a 1 inch magnetic disc with a one quarter-inch deep tapered cup. Agilent Technologies advertise an AFM cell capable of electrochemical experiments in their Agilent 5500 AFM in which the potentiostat/galvanostat is a part of the microscope equipment.

In the following chapter the development of a commercial EC-AFM cell as part of collaboration with Asylum Research is discussed. The cell is highly adaptable to a range of electrochemical needs, and is another example of advancement in the ever developing field.

2.5 References

[1] P.J. Goodhew, J. Humphreys, R. Beanland, *Electron microscopy and analysis*, 3rd edition, London : Taylor & Francis, London, **2000**, p. 251.

[2] L. Reimer, *Scanning electron microscopy : physics of image formation and microanalysis*, 2nd edition, Berlin : Springer, Berlin, **1998**.

[3] J.R. Gribbin, *Science, a history*, *1543-2001*, Allen Lan, London ; New York, **2002**.

[4] Ningbo Optical Microscope Co., Ltd, *Biological, multipurpose research microscope*, **2011,** http://www.microscope-manufacturers.com/research-microscope.html

[5] M.A. O'Keefe, C.J.D. Hetherington, Y.C. Wang, E.C. Nelson, J.H. Turner, C. Kisielowski, J.-. Malm, R. Mueller, J. Ringnalda, M. Pan, A. Thust, *Ultramicroscopy* **2001** 89, 215.

[6] Natural History Museum, *Secondary electron images of butterfly scales*, **2011**, http://www.nhm.ac.uk/resources-rx/images/secondary-electron-sem-butterfly-scales_48235_1.jpg.

[7] *Scanning probe microscopy and spectroscopy : theory, techniques, and applications,* Wiley-VCH, New York ; Chichester, **2001** .

[8] P. Eaton, P. West, *Atomic force microscopy*, Oxford University Press, Oxford, **2010**, p. 248.

[9] Asylum Research, *Understanding AFM,* DVD, **(2005)** .

[10] G. Binnig, H. Rohrer, *Helv. Phys. Acta* **(1982)** 55, 726.

[11] G. Binnig, C.F. Quate, C. Gerber, *Phys. Rev. Lett.* **(1986)** 56, 930.

[12] R.H. Fowler, L. Nordheim, *Proc. R. Soc. London, Ser. A* **(1928)** 119, 173.

[13] B.V. Derijaguin, N.V. Churaev, V.M. Muller, *Surface forces*, New York ; London : Consultants Bureau, New York ; London, **1987**, .

[14] J.N. Israelachvili, *Intermolecular and surface forces*, 2nd ed edition, London : Academic Press, London, **1991**, .

[15] R. Young, J. Ward, F. Scire, *Rev. Sci. Instrum.* **(1972)** 43, 999.

[16] PI Ceramic GmbH, *XY scanning tubes with quartered out ceramics,* **(2011)** http://www.piceramic.com/site/piezotubes.html

[17] AZoNano - The A to Z of Nanotechnology **(2011),** http://www.azonano.com/images/Article_Images/ImageForArticle_2114(3).jpg

[18] J. W. Cross, accessed (**2011**), http://www.mobot.org/jwcross/spm/graphics/cantilevers.jpg

[19] Nanoscience Instruments, Inc., *Aspire CT120 Conical Tapping Mode AFM Probes,* **(2011),** http://www.nanoscience.com/store/pc/catalog/03_oem-probe-series_tn_165_detail.jpg

[20] J.V. Macpherson, P.R. Unwin, *Anal. Chem.* **(2000)** 72, 276.

[21] S. Manne, H.J. Butt, S.A.C. Gould, P.K. Hansma, *Appl. Phys. Lett.* **(1990)** 56, 1758.

[22] S. Manne, P.K. Hansma, J. Massie, V.B. Elings, A.A. Gewirth, *Science,* **(1991)** 251, 183.

Chapter 3

The development of an EC-AFM cell

The work reported in this DPhil thesis was funded by a collaborative project (Industrial CASE award) with Asylum Research UK. The collaboration was initiated with a view to developing an atomic force microscope cell suitable for performing in-situ electrochemical experiments alongside nanoscale image capture of the electrode surface. The concept of EC-AFM was discussed in detail in the previous chapter, where as in this Chapter the project as a whole is discussed, with focus on the product aims and development, culminating in the final product design and abilities.

3.1 Asylum Research

3.1.1. About the company

Asylum Research (AR) is a company based in Santa Barbara, CA, involved in the manufacture and development of scanning probe (SPM) and atomic force microscopes (AFM). Asylum Research was founded in 1999 by former members of the Veeco SPM Company, scientists, engineers and software developers who wanted to take a different direction to Veeco. 12 years on and AR is well established and considered a technology leader for SPM/AFM systems, for both materials and bioscience applications.

AR manufactures instruments that may be used for a variety of nanoscience applications in material science, physics, polymers, chemistry, biomaterials, and bioscience. These include single molecule mechanical experiments on DNA, protein unfolding and polymer elasticity, as well as force measurements for biomaterials, chemical sensing,

polymers, colloidal forces, and adhesion. The technology in Asylum's product line offers imaging and measurement capabilities for a wide range of samples, including advanced techniques such as electrical characterization (CAFM, KFM, EFM), high voltage piezoresponse force microscopy (PFM), magnetic force microscopy (MFM) with their unique variable field module, quantitative nanoindenting, and a wide range of environmental accessories and application-ready modules. However, until recently, one capability that was not offered by AR was the capacity to perform in-situ electrochemical experiments, EC-AFM.

3.1.2. Asylum Research technology – the MFP-3D Atomic Force Microscope

Asylum's MFP-3D™ (Figure 3.1) is the main AFM system manufactured by AR, and the 'stand-alone' AFM is the system used in all the EC-AFM presented in this thesis.



Figure 3.1: *The Asylum Research MFP-3D™ Stand Alone atomic force microscope*

Unlike other AFM systems the MFP-3D was introduced with unprecedented precision and flexibility owing to the independent piezo positioning in all three axes, combined with low noise closed-loop feedback sensor technology. This was the first AFM with such design features, and also allowed the option of *both* top and bottom sample viewing, thus allowing integration with most commercially-available inverted optical microscopes.

The MFP-3D Stand Alone AFM is the most applicable AR AFM to the development of an EC-AFM cell. It provides a wide range of AFM and SPM capabilities as standard, and is therefore ideal for general materials science applications, such as electrochemical engineering and surface analysis. The AFM has a closed-loop positioning system, i.e. the system is constantly adjusting relative to feedback, thus providing the user with exceptional resolution, accuracy and reproducibility. Furthermore, due to a low-coherence light source, interference artifacts are almost entirely removed.

3.2. EC-AFM project aims

In the course of this DPhil the aim of the project was to design and develop an adaptable hydrodynamic electrochemical atomic force microscope (EC-AFM) cell. The objectives were to generate a simple cell that will be capable of doing electrochemistry whilst simultaneously scanning and imaging.

Working closely with United Kingdom based AR company representatives and application scientists, Chris Mulcahy, Amir Moshar and Michael Philips, we sought to produce a practical electrochemical cell that could be used in real experimental systems, offer diversity in application, and provide consistent and reproducible results that offered a new dimension to surface characterisation of a real system.

During the development of the cell, testing of the system was conducted via in-situ electrochemical deposition of nanoparticles and their analysis. Some of these results have been presented in the subsequent chapters owing to their practical application to analytical

experiments. A system that can carefully control the growth of nanoparticles, and characterise them immediately, in-situ, is highly desirable in scientific research. Furthermore, an understanding of growth mechanisms and in-situ surface topography of electrodes immediately after deposition has much application in electroanalysis.

3.3. The requirements of an EC-AFM cell

In order for the EC-AFM cell to be directly applicable to everyday electrochemical experiments the development required fulfilling a certain number of requirements. These required features are discussed in detail below, in which the problem and solution are discussed.

In-situ experiments: As electrochemical experiments most often occur across a solution – electrode interface, it is necessary for the EC-AFM cell to operate in a liquid environment. As such the body of the cell must be able to hold a reasonable amount of fluid, whilst providing sufficient coverage of the electrode surface and other electrodes. It is of vital importance that the holder be leak free and for the liquid to be easily removed and replaced.

Interchangeable electrodes: Owing to the variety of electrode substrates to be investigated using EC-AFM, and also the variety of electrolyte solutions and substances for deposition, it is a requirement that the EC-AFM cell be flexible and allow the substitution of electrodes. In the EC-AFM cell developed herein this has been addressed by offering interchangeable electrodes and platforms appropriate to the experiment.

Corrosive and chemical resistant materials: A variety of electrolyte and chemical solutions maybe used in the course of in-situ AFM investigations, and as such the cell must be resilient against corrosion and chemical modification. Other than the electrodes, which are interchangeable, the entire cell is therefore fabricated in poly ether ketone (PEEK). PEEK

is an colourless organic polymer, semicrystalline thermoplastic that exhibits a high chemical resistance retained to high temperatures, far beyond those of electrochemical experiments.

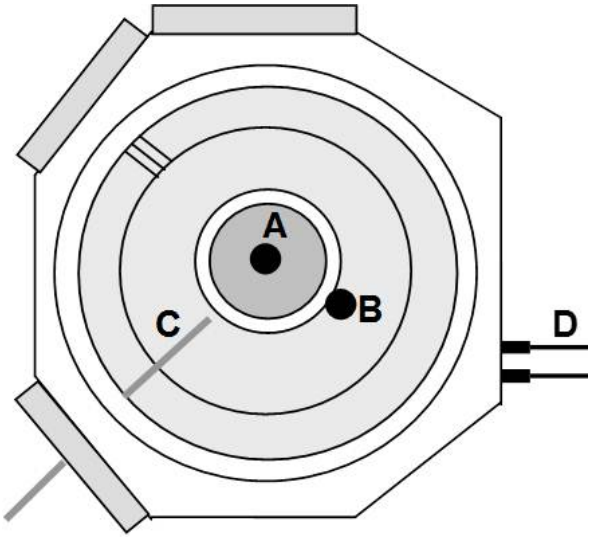


Figure 3.2: *A schematic top-down view of Prototype* ***#1*** *of the EC-AFM cell. A – the working electrode stub, B – graphite rod counter electrode, C –Ag wire quasi-reference electrode and D – the working and counter electrode external connections.*

3.4. EC-AFM cell – Prototype #1

In 2007/8 the first prototype of the EC-AFM cell for use in an AR MFP-3D Stand Alone system was fabricated and developed. The cell was a modified PEEK fluid cell that was already manufactured by AR for use in biological applications of AFM. Figure 3.2 shows a top view schematic of the cell prototype.

This prototype of the EC-AFM cell was successfully applied to an investigation into the growth of bismuth nanoparticles at a boron doped diamond electrode surface, discussed in section 3.5 of this chapter and in greater detail in Chapters 5.

3.4.1. Working electrode

At the centre of the fluid cell a hollow cylindrical piece was inserted of approximately 1cm internal diameter with a central thread running to the base of the EC-AFM cell. At the base

was a copper plate which was a direct electrical contact to the working electrode external connection pin.

In the schematic of Figure 3.2, the working electrode position at A is filled with a custom made BDD electrode. The BDD disc was chosen as an ideal electrode substrate to develop EC-AFM technology, owing to the near atomic flatness of the commercially polished diamond film. The very flat surface, at which a variation in height of a few nanometres (at most) across a 25 μm^2 area may be seen, is ideal for AFM and the nanoscale measurements involved. A resistance to surface adsorption (as discussed in the following Chapter) also places BDD electrodes in a unique position relative to other electrode materials, as in-situ characterisation of the bare BDD surface is not marred by varying amounts of adsorbing materials from the electrolyte. Furthermore, the relatively long time frame for AFM image capture, especially in-situ, is not interfered with by gradual surface fouling and changes in the electrode surface.

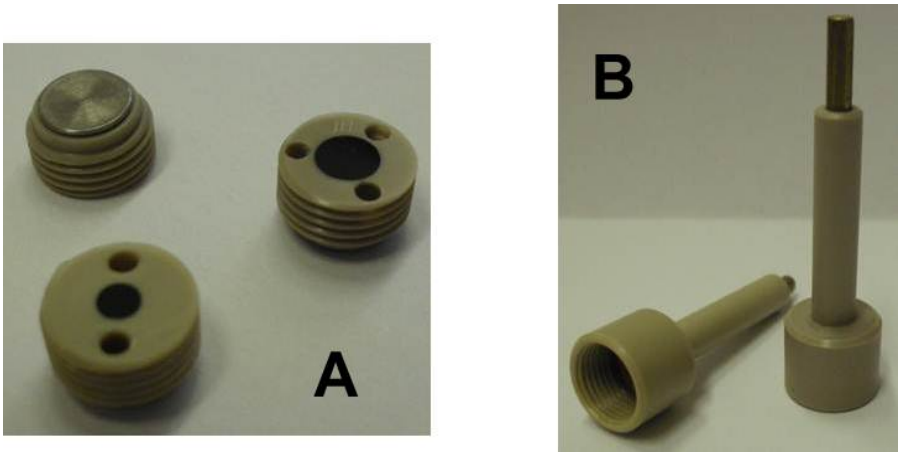


Figure 3.3*: A) BDD electrode stubs of 3 mm and 5 mm BDD diameter, and one inverted to show the stainless steel backing B) experimental holders for the BDD stubs for use in laboratory based electrochemical experiments.*

The BDD electrode was fabricated into a PEEK stub (Figure 3.3a) which could be screwed into the cylinder at position A to form a water tight seal and electrical connection to

the base, and therefore the external power source. This design further allowed for the electrode to not only be interchangeable with other electrodes of the same 'stub' design, but also to be used in practical electrochemical experiment in the laboratory. Experimentally the BDD electrodes were used in the laboratory by screwing into a PEEK holder shown in Figure 3.3b. The holder also has a stainless steel or copper base which is part of a stainless steel piston that allows external connection at the end of a sufficiently long stalk.

3.4.2. Counter electrode

In this EC-AFM cell design the counter electrode was a machined piece of graphite obtained from Erodex Ltd (UK). The counter electrode, shown in position B of the schematic above, was positioned adjacent to the working electrode site, and was electrically connected to a pin at D via the base of the cell.

3.4.3. Reference electrode

In this design of the EC-AFM cell the reference electrode used was a silver wire pushed through a fluid port in the original fluid cell design. The quasi reference could be easily removed and cleaned or replaced, and was calibrated relative to a stable reference electrode such as the saturated calomel electrode (SCE) by use of a digital voltmeter (DVM). This was achieved by filling the AFM cell with KCl solution and holding the SCE electrode in the solution. The SCE and silver wire were both attached to the DVM and the potential difference between the two reference electrodes was measured and recorded.

3.4.4. Electrical connection

Electrical connection was made to the cell using an Autolab Type II USB potentiostat. The working and counter electrodes were electrically connected at the appropriate pins using custom made extension wires and crocodile clips. These pins connected to the counter or

working electrode via two metallic strips that ran through the customised base of the fluid cell. The silver wire reference electrode was directly connected using a crocodile clip.

3.5. EC-AFM cell – Prototype #3 – The final product

Following the success with Prototype #1 of the EC-AFM cell in the observation of in-situ bismuth deposition the EC-AFM cell was developed at the AR laboratories based on the Oxford University design. Although similar in many ways, some subtle and major changes to the design allowed for a greater range of samples to be analysed, and more stringent leak detection technology. The final design of the AR EC-AFM cell is shown in Figure 3.4 and some major changes are immediately evident.

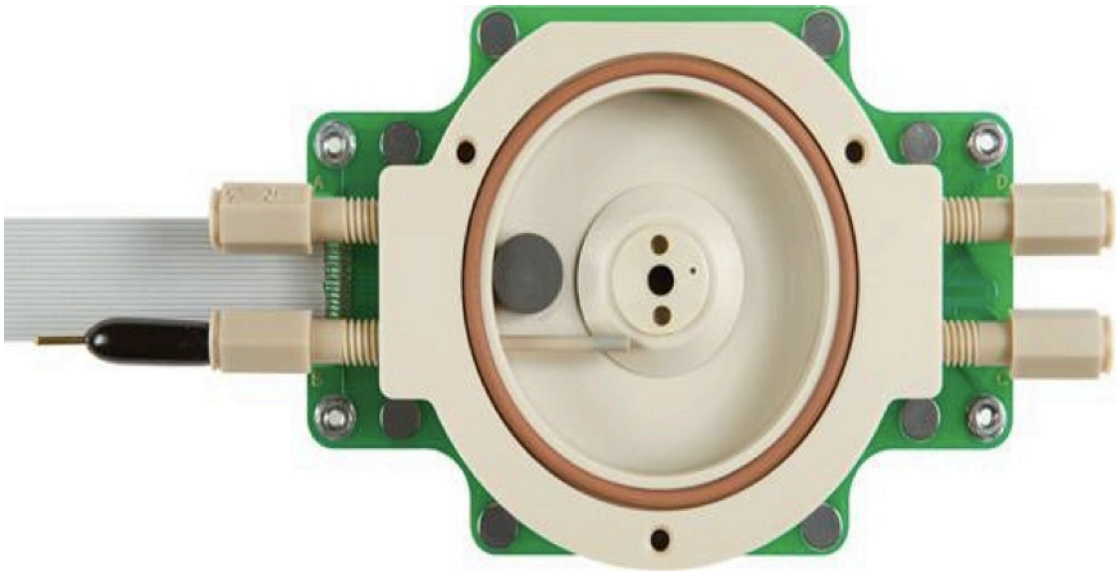


Figure 3.4: *The final design and commercially available AR EC-AFM cell.*

One feature is the entirely new PEEK container as opposed to a modified fluid cell, with a number of ports for fluid exchange, reference electrodes and even inert gases for de-aerated electrochemical systems. The cell has a volume of 3 mL of electrolyte which can be reduced accordingly using various sized PEEK inserts. All parts of the equipment that come into contact with electrolyte are made of PEEK polymer.

3.5.1. Working electrode

The third prototype of the EC cell retained the central working electrode platform, however to increase versatility the central piece is interchangeable with other mounts allowing the user to use electrode stubs such as the BDD electrode stub as one mount, or sample mounts that allow press fitting or epoxy potting other electrode materials. As such the design is extremely adaptable to accept customized sample mounts or electrodes thus expanding the applicability of the EC-AFM cell.

3.5.2. Counter electrode

The counter electrode in this EC cell is also interchangeable, with a graphite electrode included as standard akin to the original design, but an optional platinum ring counter electrode that can be inserted at the same position as the graphite piece. Furthermore, metal wires of up to 1/16" diameter may be inserted into the cell via one of the four ports if platinum or graphite are not suitable counter electrodes for a system.

3.5.3. Reference electrode

The reference electrode supplied with the AR EC-AFM is a custom made and stable Ag/AgCl electrode that is simply inserted into the cell via a fluid port as shown in Figure 3.4. The Ag/AgCl reference consists of a chlorinated silver wire in a PEEK, fritted tube of KCl. Should this be unsuitable for the system under investigation however, alternative metal wire quasi reference electrodes, or other custom made stable references may be fabricated to be inserted via a fluid port. Teflon tubing of a variety of internal diameters specifically sized to seal the fluid ports when using small diameter wires are supplied with the EC-AFM cell equipment.

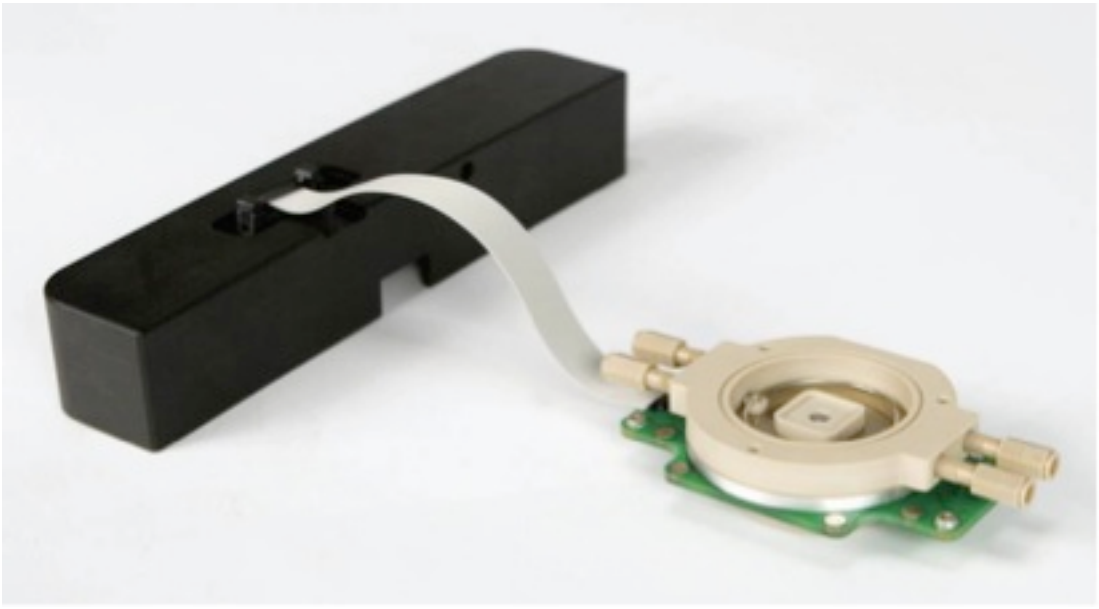


Figure 3.5: *The EC-AFM cell with the junction box for external connection to the potentiostat and environmental controls. A square working electrode mount for epoxy and press fitted samples, and platinum ring counter electrode are pictured inside the cell.*

3.5.4. Electrical connection

Beneath the main body of the AFM cell is a circuit board that is built into the AFM cell and connects all the electrodes to a junction box, shown in Figure 3.5. All electrical signals are passed via the ribbon wire to the junction box, which is in turn easily connected to any potentiostat using standard banana-plug or 2 mm connectors. The junction box is secured to the base of the AFM, and not only provides a simple and tidy experimental arrangement, but also minimalizes the risk of short circuits and provides a constant and stable earth.

3.5.5. Other special features

The cantilever holder supplied with the EC-AFM cell kit has a specialised design such that only the PEEK body and a small quartz window are in contact with the electrolyte to avoid any contamination of the sample.

The junction box not only connects the EC-AFM cell to external potentiostats, but may also be employed to drive the electrolyte heater via the MFP-3D Environmental Controller. This provides the user with the opportunity to investigate the effect of fundamental thermodynamics and kinetics on the electrochemical experiment, as well as optimise deposition process and gain greater insight into processes such as nucleation and growth at the nanoscale. It also provides that opportunity to investigate electrolytes that are solid at room temperature.

3.6. In-situ EC-AFM experiments using the AR-Oxford design

To date the EC-AFM cells developed in the course of this DPhil have been used to explore the in-situ deposition of bismuth and nickel at boron doped diamond electrodes. Nucleation and growth mechanisms are of great interest to electrochemists and material scientists as they can provide insight into the nature of an electrolytically modified surface based on deposition time, solution concentration and pH.

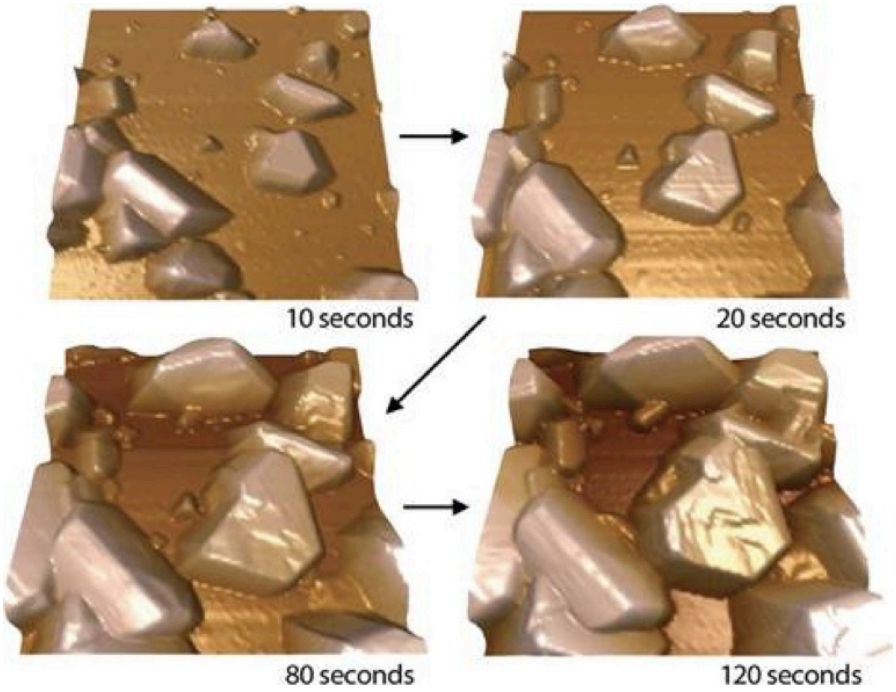


Figure 3.6: *The deposition of bismuth at a BDD electrode at increasing intervals of deposition at -1.1 V vs. a Ag wire quasi reference electrode. In a solution of 0.1 M $HClO_4$ with 1 mM Bi(III).*

A boron doped diamond electrode was modified with bismuth with a view to apply the modified electrode to the electroanlaysis of heavy metals. Using the EC-AFM cell (prototype #1) the deposition of bismuth was observed in a staged process at increasing deposition intervals. The 3D results of the latter are shown in Figure 3.6.

The figure shows the growth of the initial particles with each deposition, and demonstrates an instantaneous nucleation and growth mechanism. It also demonstrated the extent to which nanoparticle growth may be controlled at a BDD electrode using electrochemical methods. The results of these experiments are discussed in much greater detail in Chapter 5.

The most recent version of the EC-AFM cell was used in the development of a nickel nanoparticle modified BDD electrode for application to the analysis of small organic molecules. The EC-AFM cell allowed for in-situ characterisation of the electrode surface before and after nickel deposition, and provided corroborative evidence for a progressive nucleation and growth mechanism that produced hemispherical nanoparticles at specifically active areas of the BDD surface. A 3D AFM image of the unmodified and nickel modified surface is shown in Figure 3.7. The results of the corresponding experiments are discussed extensively in Chapters 7 and 8.

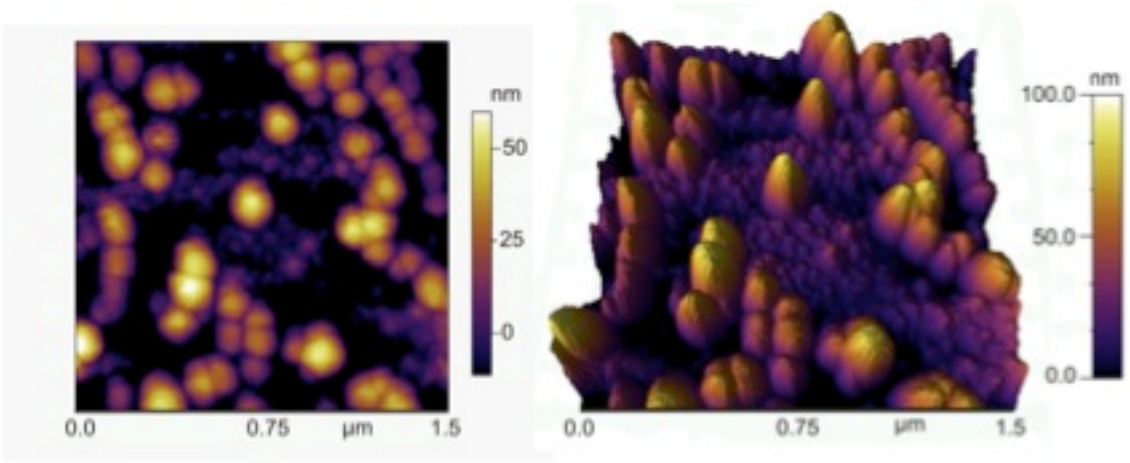


Figure 3.7: *The real and 3D in-situ EC-AFM image of the nickel modified BDD electrode following nickel deposition at -1.2 V (vs. Ag/AgCl) for 180 s from a 1mM $Ni(NO_3)_2$ in a non-degassed 0.1 M sodium acetate buffer solution (pH 5).*

3.7. Figure Acknowledgements

A number of images and details provided in this chapter were sourced from the commercial details of the Asylum Research EC-AFM cell as a result of this collaboration. The Data sheet can be found in *Appendix.*



Chapter 4

An Introduction to Modified Boron Doped Diamond Electrodes and their Application to Electroanalysis

The work presented in this chapter has been published in

Electroanalysis, **2010,** *Vol*. *22*, 1947

And was also presented at the Heyrovsky Nobel Prize memorial conference entitled

Modern Electroanalytical Methods, **2009,** Prague, Czech Republic

Due to the near atomic flatness (few nanometers) of commercial, polished boron doped diamond (BDD) electrodes it is an excellent electrode substrate for investigation using electrochemical atomic force microscopy (EC-AFM). The low capacitance of a BDD electrode also makes it an ideal substrate for sensitive dynamic electroanalytical experiments. In its 15 year history as an electrode in analysis, BDD has been used unmodified and modified, towards the analysis of a wide range of organic and inorganic analytes. In the past decade, metal nanoparticle modification of BDD has been used, providing a simple yet effective approach to enhancing the electroanalytical ability of the electrode material.

In this chapter, BDD electrodes are introduced with a particular focus on a number of metal nanoparticle modified BDD systems that have been utilized in electroanalysis. Metal nanoparticle modified boron-doped diamond (BDD) electrodes have been used in the electroanalysis of a number of inorganic and organic analytes. This simple surface

modification has enhanced the sensitivity and analytical ability of BDD effectively and consistently, as reported in a number of publications overviewed herein.

4. 1. Introduction to boron doped diamond

Semiconducting diamond materials have been investigated since 1952 following the discovery of naturally semiconducting diamonds by Custers et al [1, 2]. Ion implantation of natural, and later synthetic, diamond then became the focus of much research, as discussed in the 1975 review by Vavilov [3] and observed in a number of Russian and Japanese publications in the subsequent decades [4-8]. The significant step in the development and widespread use of boron doped diamond (BDD) was its fabrication via chemical vapour deposition (CVD) techniques to form a conducting polycrystalline thin film, introduced by Fujimori et al [7] in 1986. Investigations into the electrical and optical properties of these films soon followed, utilising cathodluminescence [9, 10], electroluminescence [9], and Raman and IR spectroscopy [11]. It was not until 1993 that Swain and Ramesham [12] first noted the electrochemical potential BDD films held, with the first electroanalytical experiment performed by Tenne et al [13], also in 1993, involving the reduction of nitrate to ammonia.

Since the addition of BDD electrodes to the electrochemist's 'toolbox', the material has greatly advanced and become a significant asset. Now commercially available in a variety of forms and at varying levels of doping, the electrode is used in numerous areas of electrochemistry, ranging from analysis [13-16], to synthesis [17, 18], and catalysis [19, 20], as well as having significant application to waste water treatment (owing to a very wide potential window and resistance to fouling) [21-24], uses in lithium batteries [25, 26] and as superconductors [27-29]. Electroanalysis at BDD electrodes specifically has over 250 publications to date, including unmodified, pre-treated, metal-modified, polymer modified, nanocrystalline and arrayed BDD electrode systems.

Over the past decade, metal nanoparticle modification has developed to improve selectivity and sensitivity of BDD electrodes, increasing their diversity and application as electroanalytical sensors. Herein, boron doped diamond electrodes, and a range of metal nanoparticle modifications are introduced and their analytical applications are discussed.

4.2. The electrochemical properties of BDD electrodes

Diamond has numerous unique properties that require little introduction, most notably an extreme hardness and thermal conductivity, a high level of chemical inertness and a wide electronic bandgap of approximately 5.5 eV at a temperature of 300 K. Diamond naturally occurs slightly doped with nitrogen or boron, producing yellow or blue diamonds respectively as shown in Figure 4.1.



Figure 4.1: *Naturally occurring boron (a) and nitrogen (b) doped diamond. The famous Hope Diamond, a 45 carat electrically conducting blue diamond on exhibition at the Smithsonian is shown in Figure (c)*

Naturally occurring blue diamond, known as IIb diamond, was the first semiconducting diamond to be discovered [1]. These days highly doped polycrystalline films, fabricated by chemical vapour deposition (CVD) methods, observe good electrical conductivity analogous to semi-metallic levels [30, 31].

The introduction of boron atoms into the diamond lattice of tetrahedrally bonded carbon atoms imposes p-type doping, in which the boron atom inserts electron accepting holes owing to its electron deficiency relative to the substituted carbon atom. Doping levels are in the range of 10^{18}-10^{21} atoms cm^{-3}, the higher doping value giving an approximately 1:100, boron to carbon ratio [30, 31]. Conductivity increases with doping due to the increase in boron acceptor states approximately 0.37 eV above the diamond valence band, as illustrated in Figure 4.2.

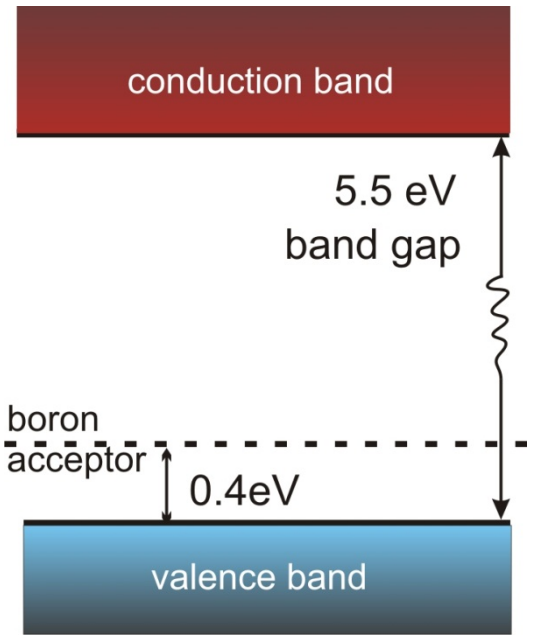


Figure 4.2: *An illustration of the diamond electronic band gap, and the introduction of boron doping mid states and pseudo conduction band up to the dotted line.*

At the highest levels of doping, in the region of 100:1 carbon/boron ratio, films with resistivities less than 0.1 Ω.cm are achievable [31]. This conductivity coupled with the unique attributes of diamond give an electrode with a number of highly desirable electrode properties. For high-quality BDD films, a working potential window of 4 V (-2 to +2 V) is easily achieved before the hydrogen or oxygen overpotentials are reached indicating the almost ideally polarizable diamond-electrolyte interface. The voltammetric response is also

flat and featureless over a range of -0.8 to +1.8 V in solutions of an acidic to neutral pH [32], depending on the degree to which any non diamond impurity has been removed from the surface. This allows for the investigation of numerous materials that are only electroactive at highly anodic or cathodic potentials.

An equally striking electrochemical property of BDD film electrodes is the very low background capacitance relative to other carbonaceous and metallic electrodes. Double-layer capacitance and background voltammetric currents are found to be an order of magnitude lower than observed for glassy carbon electrodes of the same geometric area [33-35]. It is a feature of boron doped diamond that makes them ideal for use in electroanalysis, as the resulting signal-to-background noise is enhanced considerably, and detection limits may be vastly reduced.

The low capacitance is attributed to a number of possible factors. At hydrogen-terminated diamond electrodes there is a relative absence of specifically adsorbed species and carbon-oxygen functionalities that may be ionized. The electrochemical properties of diamond may be altered by electrochemically oxidizing the BDD surface and introducing carbon-oxygen functionalities [36].

The surface of a BDD electrode is often regarded to be similar to a 'microelectrode array', due to the evident areas of high, low or zero electroactivity. Different electroactivity is shown at diamond crystals that have grown in different planes, as well as the variable density of doping, that is not necessarily consistent throughout the structure. Figure 4.3 demonstrates the variable surface of polycrystalline BDD following modification by nickel nanoparticles. This is also discussed later in this thesis in Chapters 5, 7 and 8. In Figure 4.3 the electroactive areas are evident as large, unmodified crystal grains next to densely modified areas.



Figure 4.3: *SEM of a nickel modified BDD electrode. Nickel deposited from a 1 mM $Ni(NO_3)_2$ in 0.1 M acetate buffer solution, at -1.3 V vs. SCE under constant stirring and fully degassed for 150 s. The density of deposition indicates the diamond grains and their relative electrochemical activity.*

Another possible factor contributing to the low capacitance of BDD electrodes is the semiconducting nature of diamond films. Unlike a metal or fully conducting carbon electrode, the density of surface electronic states in BDD is potential dependent [32]. Therefore at a given potential a lower density of surface electronic states at the Fermi level exists at the electrode-electrolyte interface. As such, a lower electrode surface charge density would require a lower counter-balance of charge from the double layer. Also, the presence of nondiamond carbon and carboxylic functional groups across the BDD surface can greatly increase the double-layer capacitance of the electrode. However, such impurities may be removed by acid washing (e.g. potential cycling of the BDD electrode in moderately concentrated (5M) H_2SO_4 or HNO_3) and re-hydrogenation in a hydrogen plasma [32].

High quality BDD electrodes not only show a lack of carbon-oxygen functionalities at the surface, but also a resistance to adsorbing species such as AQDS, presumably due to the absence of surface carbonyl functionalities, thus making them highly resistant to electrode fouling [33, 35]. Resilience against organic contaminants, coupled with a mechanical and chemical robustness to extreme experimental conditions [20, 30, 37-42] therefore makes BDD thin films highly versatile and unique electroanalytical tools.

4.3. The fabrication of boron doped diamond electrodes

As naturally occurring diamond is, at most, only lightly doped with boron, it is not sufficiently conductive to be used as a practical electrode. Despite properties of extreme hardness and physical robustness, diamond is a less stable carbon allotrope than graphite, and requires very specific conditions to be formed. Natural diamond is formed at high pressures and high temperatures approximately 100 miles deep into the Earth mantel. This process takes billions of years however, but early attempts at synthetic diamond fabrication strove to recreate the mantel conditions. These are aptly named high-pressure high-temperature (HPHT) techniques, and produce diamond substrates with millimeter sized crystal grains [31]. This method is used to implant conducting diamond millicrystals into conducting or non-conducting substrates, but not to produce electrode materials [31].

The technique most often used in the fabrication of boron doped diamond films for electrochemical applications is a more amenable and controllable process called chemical vapour deposition (CVD). CVD is a low pressure technique that allows the deposition of a solid material onto a substrate from a gas or mixture of gases. In diamond synthesis, a thermally activated plasma of carbon and hydrogen is used. The plasma conditions are essential to the diamond quality, with a high amount of atomic hydrogen required to suppress graphitic bonds forming, a suitable supply of hydrocarbon radicals, and in the case of doped diamond, a dopant source [30, 31, 33].

4.3.1. Growth conditions

The plasma may be activated by hot filament or microwave methods depending on the substrate size. Smaller substrates generally use microwave radiation, whereas larger substrate use a number of filaments. The plasma must maintain a temperature of 2500 ºC ± 300 ºC, whilst the pressure is held between ca. 0.01 – 0.25 atm [30, 31]. Carbon is sourced from simple hydrocarbons such as methane at concentrations of 0.5-5 % in an atomic hydrogen gas carrier, with variable concentrations of B_2H_6, or other less toxic boron sources, introduced as the boron dopant. Hydrogen is essential to the synthesis, and must be present in a radical form for the process to work. Hydrogen radicals etch away any graphite forming on the substrate up to 100 times faster than they can remove diamond, thus removing the otherwise thermodynamically preferred allotrope. The doped diamond film is usually hydrogen terminated by the hydrogen available in the plasma [31, 33], thus stablising the surface and avoiding the growth of graphitic layers. These conditions may vary depending on the termination or crystal size desired.

4.3.2. Crystalline forms of CVD diamond

CVD methods can be used for the growth of both single crystal and polycrystalline forms of diamond. The actual conditions required for making each type of diamond are very similar as it is the choice of substrate that determines whether single or polycrystalline diamond will grow. For polycrystalline thin films of doped diamond a non-diamond substrate is required, and a variety of materials may be used. Most commonly CVD processes use silicon, silicon carbide or carbide forming metals, such as tungsten and molybdenum. For single crystal diamond, the substrate must also be a single crystal diamond of the desired orientation.

Crystal size in the BDD film may be controlled by further optimization of the growth process, such that boron doped diamond is commercially available as polycrystalline

microcrystal thin films (MCD), and as single crystal diamond (SCD), and has recently been introduced as nanocrystalline (NCD) and is now developing into ultrananocrystalline (UNCD) thin films. A comparison of SEM images of micro and nanocrystalline BDD surfaces is shown in Figure 4.4 obtained from [43].

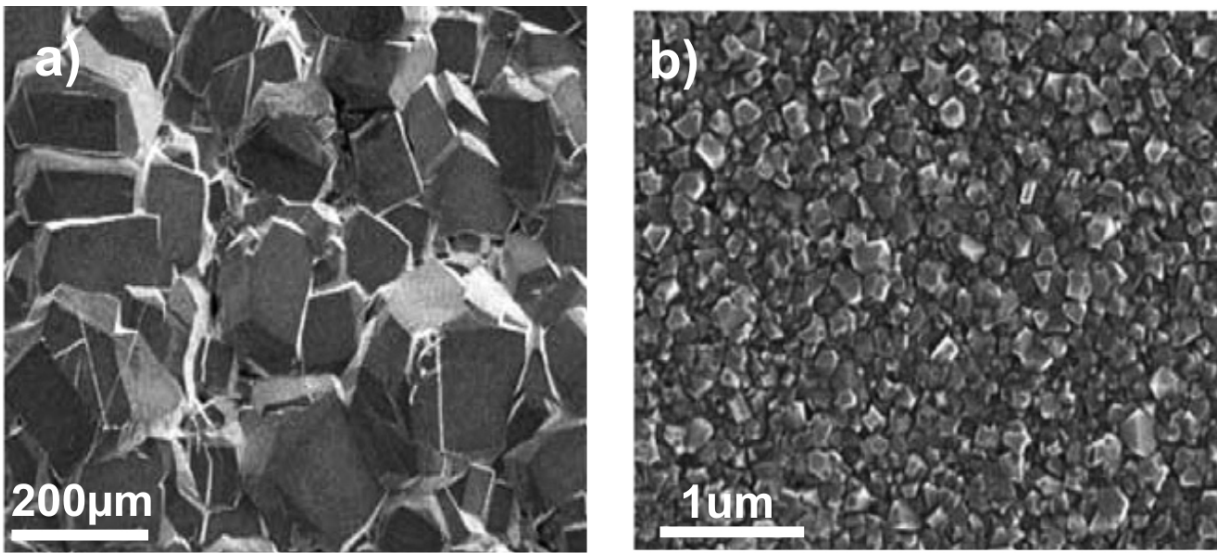


Figure 4.4: *SEM images of BDD surfaces of different crystal size. a) microcrystalline BDD and b) nanocrystalline BDD. Both images edited and reproduced from* [43]

4.4. Metal nanoparticle modified BDD electrodes

The metal nanoparticle modification of electrodes is a recently established approach aimed to improve the electrocatalytic and/or electroanalytical ability of the unmodified electrode. The modification of BDD electrodes in this way is no exception, with ion implantation [16, 44-46], electrodeposition from metal salts [14, 19, 47-54] and physical deposition [55, 56] techniques commonly used. Table 4.1 summarizes all the metal nanoparticle modified BDD electrodes, and their analytical application, so far reported in the literature.

Table 4.1: *Metal nanoparticle modified BDD electrodes and their application to electroanalysis.*

Modification	Analyte	Ref.	Modification	Analyte	Ref.
Inorganic analytes					
Antimony	cadmium & lead	[47]	Iridium (implant)	arsenic	[45]
Bismuth	cadmium & lead	[14]	Iron	none	[20]
Bismuth film	manganese	[57]	Palladium	hydrogen and H+	[58]
Bismuth film	lead	[59]	Palladium	hydrazine	[50]
Cobalt	none	[48]	Platinum	oxygen	[60]
Copper	nitrate	[49, 61, 62]	Platinum	arsenite	[53]
Gold	arsenic	[49, 63]	Platinum (implant)	hydrogen peroxide	[44]
Lead	none	[51][52]	Silver	hydrogen peroxide	[49]
Organic analytes					
Copper	glucose	[64]	Nickel	methanol	[54]
Copper (implant)	glucose	[16]	Nickel (implant)	tetracyclines	[46]
Gold clusters	dopamine and AA	[65]	Nickel (implant)	glucose	[16, 66]
Nickel	glucose	[64, 67]	Platinum	methanol	[65]
Nickel	ethanol & glycerol	[19]	Platinum/Tin	ethanol	[55]

Nanoparticle modified electrodes are known to have a number of attributes that make them highly appealing to electrochemists, especially for use in electroanalysis. At the nanoscale, materials may exhibit certain properties otherwise unobserved in the bulk or macro material. These include a higher surface area and therefore improved catalytic activity, thus allowing for the use of much less material, something of particular importance when using expensive, precious metals such as platinum, gold or silver. Another advantage is the enhanced diffusion and mass transport observed at nanoparticles. This is based on convergent rather than linear diffusion at smaller nanoparticles and relatively slow scan rates, or planar diffusion at higher scan rates but with much less material required [68-70]. Signal-to-noise ratios are also known to greatly increase and selectivity can be improved, due to the enhanced diffusion and increase in active sites relative to a bulk electrode. The benefits and use of nanoparticles in electroanalysis are discussed in more detail in the extensive review by Welch et al [71] in 2006 that was recently updated by Campbell and Compton [72].

4.4.1. Diffusional properties on nanoparticle arrays

As mentioned above, the distribution of nanoparticles can improve the electroanalytical ability of an electrode by altering diffusional conditions. The fabrication of a nanoparticle array, whether random or intentional, leads to the diffusional domains illustrated in Figure 4.5. The figure specifically illustrates what would occur at a nanoparticle modified BDD electrode with metal deposits rather than implanted ions, the latter with a system more akin to that referred to in the paper by Simm et al [48]. Four regimes of behaviour emerge:

1 – short time scales and low surface coverage leading to planar diffusion and non - steady-state, peak-shaped voltammetric behaviour at each individual nanoparticle,

2 - slower scan rate yet the coverage is still low and therefore the isolated nanoparticles show independent, *convergent* diffusion resulting in enhanced mass transport and corresponding steady state behaviour,

3 – increased surface coverage or faster experimental time leading to mixed convergent and planar diffusion as partial overlap of diffusion zones with neighbouring nanoparticles occurs,

4 –scan rates and coverage in which there is complete overlap of diffusion domains and therefore planar diffusion across the whole nanoparticle assembly so that a cyclic voltammetric response is generated, characteristic of the geometric area of the entire electrode, not the nanoparticle surface area.

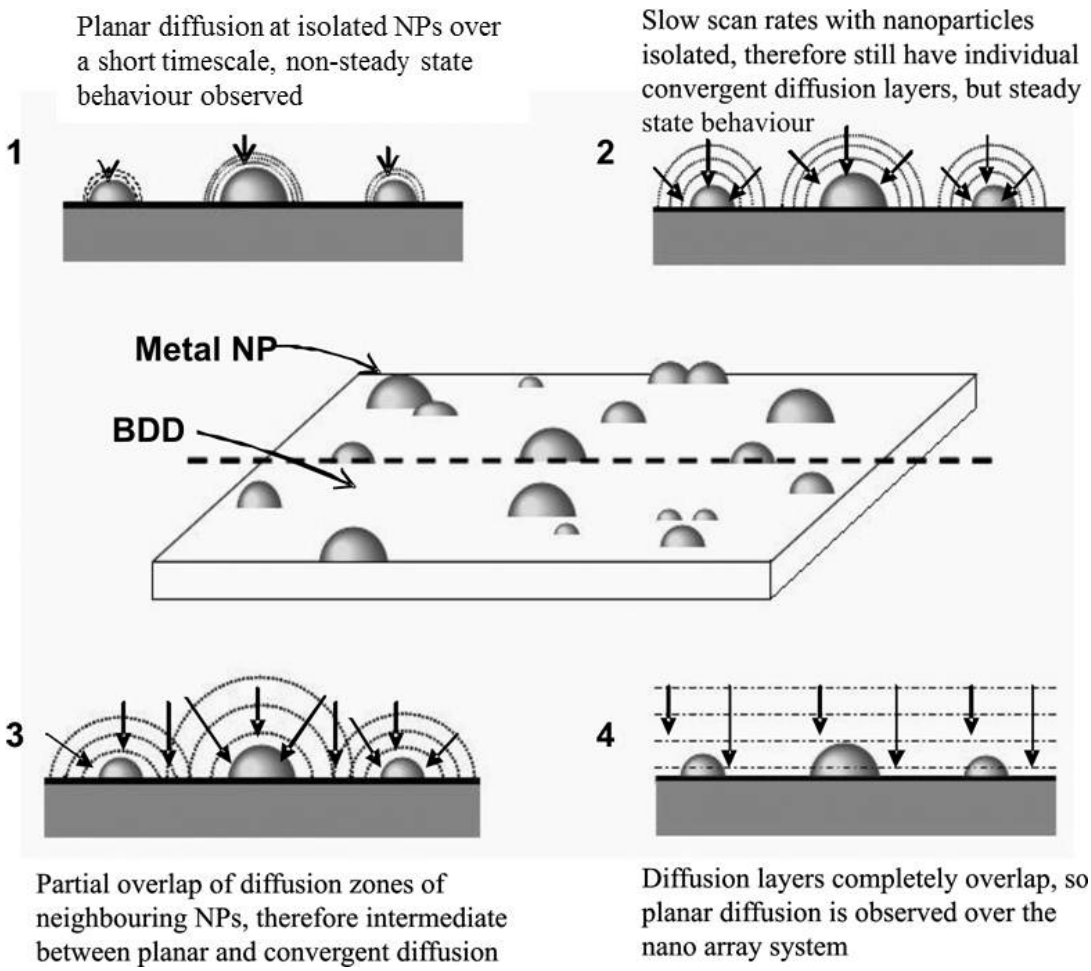


Figure 4.5: *Illustration of the different diffusion processes possible at a nanoparticle modified electrode surface (Adapted from [72])*

Modifying BDD electrodes with nanoparticulate metal species is not only advantageous with respect to increased active surface area and enhanced diffusion, but also in making the BDD sensitive to analytes that would not be ordinarily observed at the electrode. Modification with redox active materials can facilitate electron transfer across the BDD electrode surface. This can have the effect of reducing the activation overpotential of some ordinarily unobservable analytes to values within the electrode's potential window, as demonstrated by iridium modified electrodes in the detection of arsenite [45]. Furthermore, metal modification can give the BDD electrode a selectivity otherwise unattainable at the bare surface, such as in the case of simultaneous lead and cadmium detection in which there

was interference in the pre-concentration step unless bismuth or antimony nanoparticles were present [14, 47] (see Chapter 5).

4.4.2 Electrolytically deposited metal modified BDD electrodes

The electrodeposition of metals and metal oxides onto electrode materials is a highly convenient and attractive technique for modifying electrodes. It is adaptable to a wide range of substrates, requires little or no advanced equipment with expensive or elaborate technology, the methodology is simple, quick and reproducible, and the procedures may occur at room temperature, though degassing is frequently required. Furthermore, the modification can be readily controlled by monitoring deposition parameters such as deposition time, deposition potential, metal ion concentration and deposition stages, as demonstrated in a number of publications [14, 48, 50, 51, 61].

Controlled growth of nanoparticles is becoming increasingly easier with the advent of improved surface characterization techniques such as scanning electron microscopy (SEM) and atomic force microscopy (AFM) discussed in Chapter 2. The latter has been of particular interest in recent years, as in-situ AFM has greatly developed and electrochemical AFM techniques have vastly improved [14, 48, 51]. This is consequently allowing the immediate imaging of electrodes post deposition, without removal from the deposition solution and potentially changing the surface conditions, thus allowing the characterization of nanoparticle modified electrode surfaces in their as-deposited analytical state.

Over the past decade a number of metals have been investigated as modifications to BDD electrodes, as shown in Table 4.1. A significant number of these have been investigated by the Compton group [14, 19, 47-51, 57-59, 61, 62] which first investigated the deposition of metal oxides in 2000 [51, 52, 73-75]. The deposition of lead metal [51] in 2004 utilised novel in-situ EC-AFM techniques to observe the nucleation and growth of the lead nuclei over a series of deposition intervals. A similar investigation into the deposition and growth of cobalt nanoparticles on BDD electrodes was conducted in 2006 by Simm et al

[48]. EC-AFM images of the cobalt modification (reproduced from [48]) are shown in Figure 4.5).

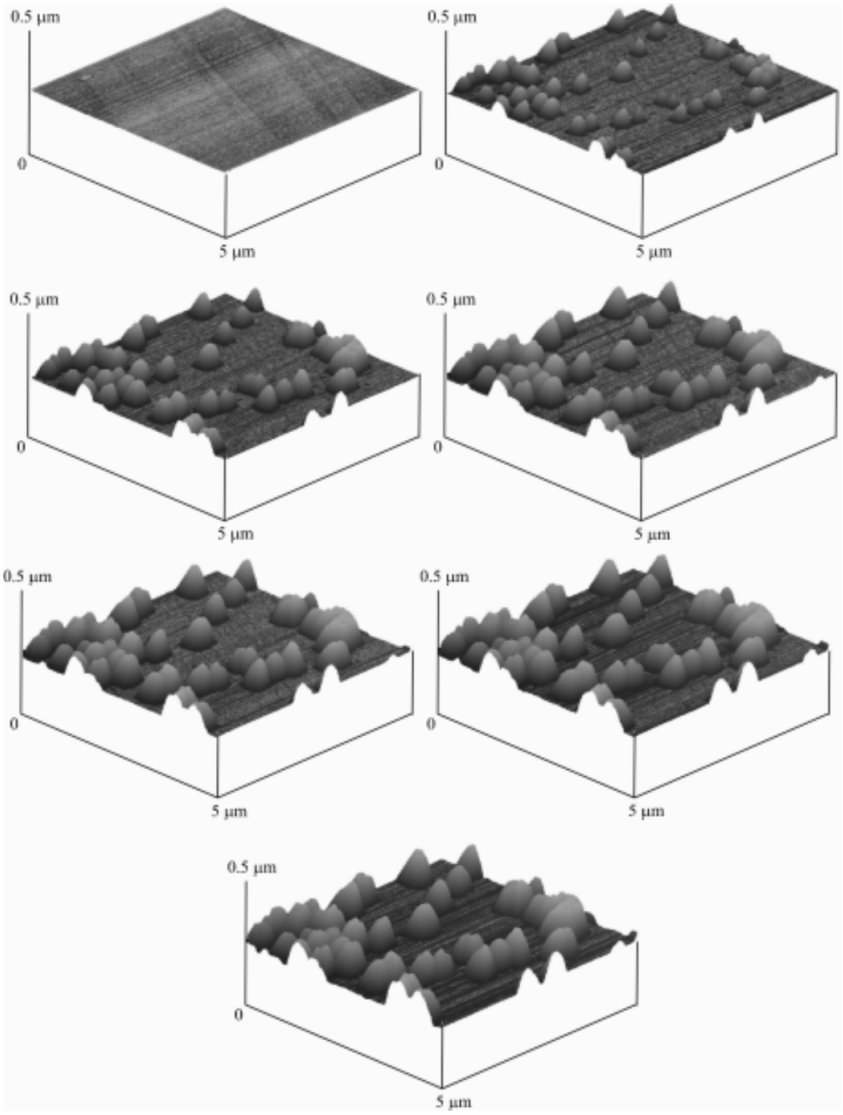


Figure 4.5: *In-situ EC-AFM of cobalt nuclei growth, deposited from 10 mM Co(II) solution at -1.15 V vs. SCE for a-g) 0, 10, 20, 30, 40, 50 and 60s (from* [48]*)*

Platinum nanoparticles were investigated at BDD electrodes as catalytic centers for methanol oxidation [65], noting that the Pt-BDD electrodes modified by a multistep deposition process were catalytically better than the continuously deposited Pt-BDD electrode. That paper also reported the inherent instability associated with electrolytically modified BDD electrodes, in which potential cycling of the Pt-BDD lead to quite significant loss of nanoparticle coverage.

Methanol and other primary alcohols have been electroanalytically determined by other metal nanoparticle modified BDD electrodes, namely a platinum/tin bimetallic nanoparticle modification [55] and a nickel nanoparticle modified electrode [19, 54]. The former were fabricated by a microemulsion technique, whilst the latter Ni-BDD electrode was fabricated by electrodeposition methods. Figure 4.6 is a selection of SEM images for the Ni-BDD following a 150 s, 300 s and 600 s deposition at ca. -1.25 V vs. SCE in a 1mM Ni (II) solution. The spherical nanoparticles are evident in the images, and are directly compared to the bare BDD electrode, also shown in the figure.

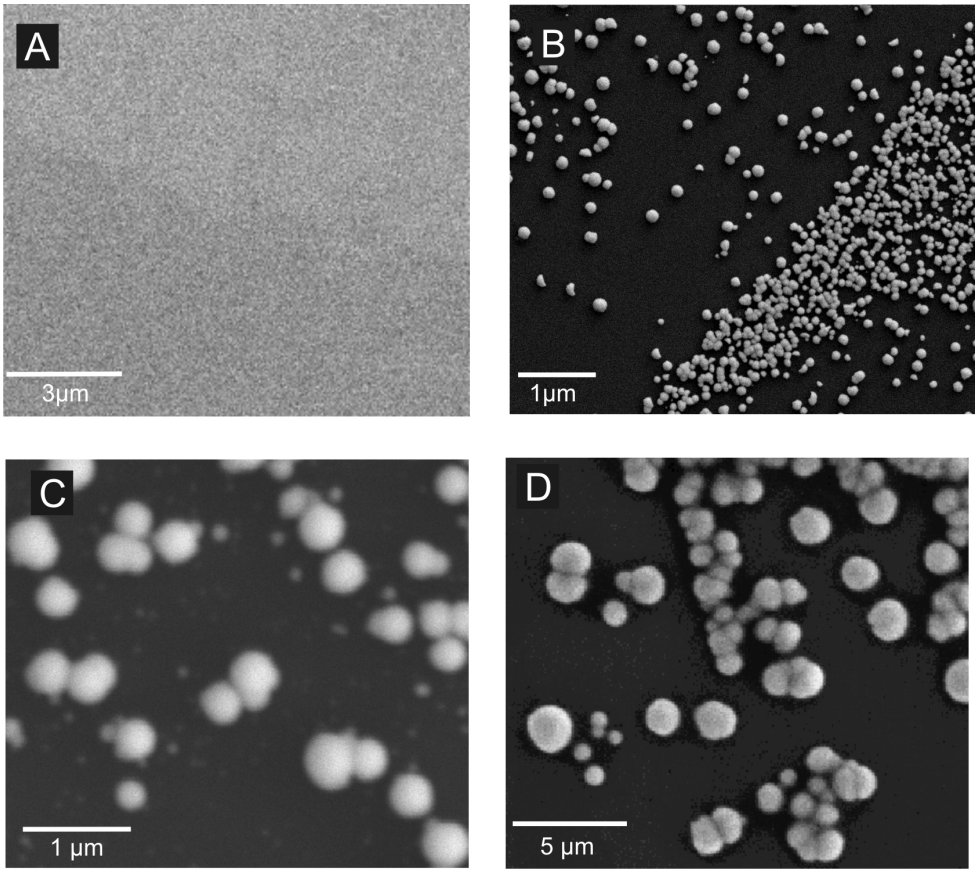


Figure 4.6: *A comparison of four SEM images of a BDD electrode modified with nickel nano and micro particles. Nickel was electrodeposited from a 1 mM* $Ni(NO_3)_2$ *in 0.1 M acetate buffer solution, degassed and under constant stirring, and held at -1.2V for B) 150 s, C) 300 s and D) 600s. Figure 4.6 (A) shows the unmodified BDD electrode. (Figures C and D are discussed further in Chapters 7 and 8, whereas Figures A and B are unpublished).*

This Ni-BDD electrode, simply and reproducibly fabricated, was analytically electrocatalytic toward methanol, ethanol, glycerol and glucose to comparable limits of detection as other nickel based electrodes, all of which are discussed in detail later in Chapters 7 and 8. A clear advantage of the Ni-BDD electrode however was the low background current and resistance to electrode fouling and surface oxidation.

Heavy metals have frequently been explored at metal modified electrodes, most famously on hanging mercury drop electrodes via stripping analysis. The past few decades have observed a decline in the use of mercury however, due to environmental and health concerns of using the toxic element. The use of BDD electrodes as alternative heavy metal sensors have been explored with promising results however [76-78], as have bismuth electrodes with substantially more success [79, 80]. Bismuth was therefore electrodeposited on BDD electrodes in a number of experiments by our group [14, 57, 59], most recently as bismuth nanoparticles for the determination of low concentrations of cadmium and lead [14], and previously as a film in the determination of manganese and lead [57, 59]. Figure 5.2 in the following chapter is an in-situ EC-AFM image of the bismuth modified BDD electrode, demonstrating the controlled deposition and growth of a stepped modification process. Using square wave stripping voltammetry, trace metal analysis of a series of simultaneous lead and cadmium additions at a bare BDD electrode and a Bi-BDD electrode was conducted. What is significant about the results is that the cadmium was only detected at the Bi-BDD electrode, due to interference effects in the pre-concentration step at the bare electrode [78].

This is another example of how modification of a BDD can enhance and improve selectivity at the electrode. In a similar experiment, BDD was modified with antimony, also discussed extensively in Chapter 5, with a view to observe the same alloying properties as bismuth and achieve the same improvement to simultaneous lead and cadmium detection. This was achieved, though not to the same sensitivity as the bismuth BDD.

Nitrate detection was achieved using a copper modified BDD electrode [61], the deposition of which was extensively studied with regard to deposition potential, deposition time and copper concentration to provide a nanoparticle coverage of varying size and density, shown by in-situ AFM images in Figure 4.7 [61]. Optimization of the electrodeposition process led to the very low limit of detection of 1.5 μM for nitrate, a detection limit of particular interest when using nitrate at an assay for determination of nitric oxide levels in the body [61].

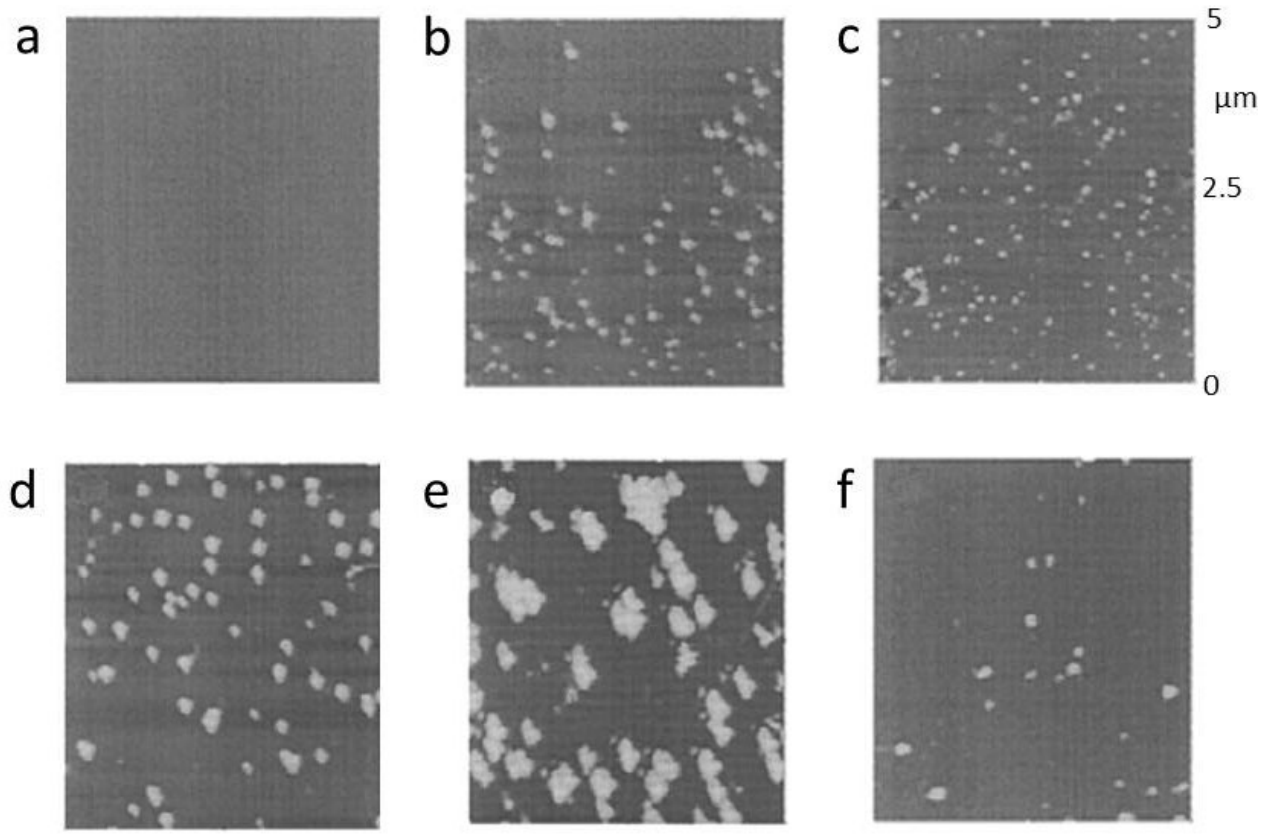


Figure 4.7: *In-situ AFM images of a BDD electrode with various degrees of copper deposition in 0.1 M Na_2SO_4 solution containing 0.1 M Cu^{2+} a) the bare BDD, b) deposition at -0.8 V for 5 s (vs. SCE), c-e) dep. At -0.8 V for 5 s then LSVs in the same solution at scan rates of c) 1000 mV s^{-1}, d) 50 mV s^{-1}, e) 10 mV s^{-1}, f) the surface after (e) is held at +0.5 V for 20s. From reference* [61].

Palladium was deposited on BDD electrodes for use in the determination of hydrazine, a highly toxic and potentially carcinogenic substance [50] and also in an investigation of molecular hydrogen adsorption at the metal surface [58]. The Pd-BDD electrode exhibited very low electrochemical detection limits for the hydrazine, observing a 2.6 μM limit compared to the 1.8 μM limit for the palladium microarray. The palladium random nanoparticle array was discerned to have the same electrochemical properties as a microarray of palladium, but with significantly better cost effectiveness and ease of fabrication.

Finally, gold and platinum modified BDD electrodes have been fabricated and applied to the electroanalysis of arsenic [49, 53, 63]. The Pt-BDD was modified by a multistep electrodeposition process, and was found to be a much superior sensor toward arsenite, observing detection limits of 0.5 ppb. Furthermore, the use of BDD as the substrate electrode, and the fabrication of nanoparticles, led to improved signal-to-noise ratios, as well as a resistance to two of the main platinum interferences, Cl^- and Cu^{2+} [53]. Much lower As(III) detection limits were reported by Song and Swain in their 2007 paper [63] reporting gold modified BDD electrodes however. In this publication the authors are keen to recognize the merits of using a BDD substrate electrode, as the Au-BDD is directly compared to a gold foil and a Au-glassy carbon electrode. Metallic gold clusters were also electrodeposited on BDD for use in the determination of dopamine and ascorbic acid [81], in which the use of a Au-BDD electrode significantly improved the reversibility of the dopamine reaction. Excellent selectivity was observed even in significantly greater ascorbic acid to dopamine concentrations, providing detection limits of 1.0 nM in the optimized procedure.

4.4.2 Metal ion implanted BDD electrodes

Ion implantation is an elaborate process compared to electrodeposition, in which the boron doped diamond film is subject to metal ion bombardment, resulting in a diamond film

containing implanted metal species. Unlike electrodeposition techniques, ion implantation is insensitive to the conductivity of the BDD surface, and forms a more uniform and permanent metal modification of the electrode. This technique has so far used nickel [16, 46, 66], copper [16], iridium [45] and platinum [44] metal species, and been applied to the electroanalytical detection of tetracyclines, glucose, arsenic and hydrogen peroxide respectively.

Fabrication of the ion implanted BDD electrode involves heavy ion bombardment of the BDD surface, similar to the fabrication of semiconductors such as silicon and gallium arsenide. The metal species are implanted at approximately 800 keV M^{n+} (M = metal) from the target metal ion source, and the modified BDD is then annealed once more at high temperatures in the presence of ambient H_2 to recover the metastable diamond structures produced by the ion bombardment [16, 44-46]. The annealing processes appears paramount to the modification, not only because it recovers, at least in part, the diamond structure, but also as it is thought to draw up the implanted ions to the surface of the diamond film, possibly forming metal particulates in the process. This is difficult to fully establish as the altered surface is characterized as being covered in sub-nano sized holes or surface defects, rather than the evident nanoparticles grown by electrodeposition and physical deposition techniques, as can be observed in Figure 4.8.

One of the first electroanalytical applications of metal ion implanted BDD electrodes was by Ohnishi et al [66] who ion-implanted nickel into a BDD surface in a bid to develop a durable and reusable electrocatalytic glucose sensor. This was inspired by an investigation a year previously in 2001 [64] in which the BDD surface was chemically modified with nickel and copper nanoparticles. The latter were formed by depositing nickel nitrate or copper sulphate onto the electrode surface and allowing the metal to precipitate out during an 8 hour drying procedure at 30ºC. Electrode stability of the chemically modified Ni-BDD and Cu-BDD electrodes was relatively high compared to glassy carbon electrodes modified

in the same manner, providing electrochemical stability for at least one week [64]. Ion implantation gave an improved durability again however, with excellent stability reported for over 5 months, even following sonication [16, 66].

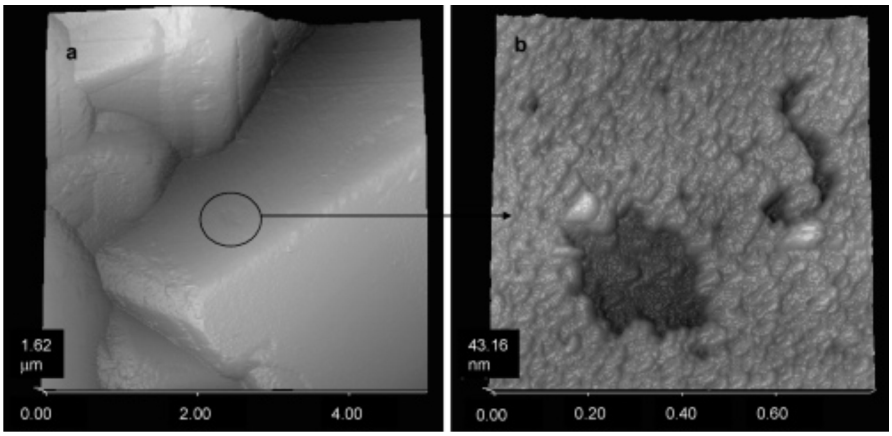


Figure 4.8: *An AFM image of a iridium modified BDD electrode fabricated using the metal ion implantation technique. The figure shows an annealed Ir-BDD surface with a hole approximately 200 nm in diameter. This is the result of rearrangement in the BDD surface following ion implantation and annealing, in which diamond bonds are broken, and then graphitized carbon is removed as carbon gas, resulting in surface defects. From reference* [45].

The oxidation of glucose at Ni-implanted BDD electrodes, as well as Cu-implanted BDD electrodes was also investigated by Ivandini et al [16] in 2004, in which the ion-implantation technique was discussed in greater detail. Here the electroanalytical response to 1mM glucose of the nickel and copper implanted electrodes were compared to bulk electrodes of the metals, in which the improved limits of detection of the implanted electrodes were evident, particularly in the case of the Ni-implanted BDD electrode. Ni-implanted BDD electrodes have since been used in the electroanalytical detection of tetracyclines [46], although the improvement in detection was not significantly greater than

that observed at the bare BDD electrode, with both electrodes providing well defined cyclic voltammograms.

Ivandini et al have subsequently investigated the electrochemical ability of platinum [44] and iridium [45] implanted BDD electrodes. Platinum implanted BDD electrodes were used towards the determination of hydrogen peroxide in 2005 [44], and found to give the BDD sensitivity it otherwise did not have towards the analyte, and improve the limit of detection and lower the background current compared to a platinum bulk electrode. Iridium implanted BDD electrodes were used towards the detection of arsenic (III) using cyclic voltammetry and flow injection analysis (FIA) [45]. The performance of the Ir-BDD was directly compared to bare BDD and iridium wire (bulk) electrodes, and found that the Ir-BDD system was quite superior to that of the bare and bulk electrodes. The detection limits for arsenic (III) at the Ir-BDD were found to be comparable with those of an earlier investigation in which an IrO_2 film was deposited on BDD electrolytically [75, 82]. The latter two papers [44, 45] give a highly detailed account of ion implantation methods and the impact of the modification method on the BDD surface.

4.5 Conclusions

Boron doped diamond electrodes have been demonstrated to be excellent substrate materials for modification by metal nanoparticles and subsequent application to electroanalysis. The characteristic low background current offered by boron doped diamond seems to be a consistent advantage to the systems described, resulting in reduced signal-to-noise and consequently lower detection limits. Improved selectivity and sensory ability is also frequently noted, as the otherwise insensitive bare BDD electrode is electrochemically activated towards certain analytes by the presence of the metal modification.

Electrodeposition methods have been predominantly used for surface modification, demonstrating as simple fabrication method with the allowance for significant control over the growth of the deposited metals. The increasing development and application of EC-

AFM techniques is shown to be further improving the extent of particle growth control, allowing for surface characterization almost simultaneously to deposition. Furthermore, despite claims [16, 44-46] that electrodeposited metals are unstable, BDD metal modified electrodes seem to exhibit high stability in some cases, such as with the nickel [19, 54] and iron [20] nanoparticle modified electrodes.

Metal ion implanted BDD electrodes have been reported by Fujishima et al, and found to provide a permanent, modification of the diamond film. Ion implanted electrodes have shown good electroanalytical responses, and are considered to be more resilient towards extreme analytical conditions such as under sonication and extensive potential cycling. The method of modification is relatively elaborate however, requiring high powered heavy ion bombardment with specially designed equipment, thus significantly increasing the costs associated with surface modification.

Overall, the low capacitance of BDD makes it an ideal substrate for sensitive, dynamic electroanalytical experiments. The electrode is similar to the hanging mercury drop electrode, in respect of its large cathodic potential window, but in contrast the electrode also has a large anodic potential window. Presently only a few metal nanoparticle modifications have been investigated at the substrate, thus there is much potential for further research with respect to alternative modifications and analytes as well as further investigation of the established modified BDD electrodes.

The BDD electrode is readily and renewably modified with a variety of metals, allowing one substrate for many nanoparticle modifications. Specifically, the electrodeposited metal nanoparticle modification of BDD offers a simple yet effective approach to enhancing the electroanalytical ability of the relatively unexplored electrode material.

4.6. References

[1] J.F.H. Custers, *Physica* **(1952)** 18, 489.

[2] J.F.H. Custers, *Nature* **(1955)** 176, 173.

[3] V.S. Vavilov, *Phys. Status Solidi A* **(1975)** 31, 11.

[4] T.N. Nesterenko, S.M. Rotner, Y.M. Rotner, L.Y. Mil'man, *Fiz. Tekh. Vys. Davlenii* **(1982)** 9, 58.

[5] G. Braunstein, R. Kalish, *J. Appl. Phys.* **(1983)** 54, 2106.

[6] K. Okano, H. Naruki, Y. Akiba, T. Kurosu, M. Iida, Y. Hirose, T. Nakamura, *Jpn. J. Appl. Phys. , Part 1* **(1989)** 28, 1066.

[7] N. Fujimori, T. Imai, A. Doi, *Vacuum* **(1986)** 36, 99.

[8] Y. Sato, M. Kamo, N. Setaka, *Mater. Sci. Monogr.* **(1987)** 38B, 1719.

[9] H. Kawarada, Y. Yokota, Y. Mori, K. Nishimura, A. Hiraki, *J. Appl. Phys.* **(1990)** 67, 983.

[10] J.A. Freitas Jr., U. Strom, A.T. Collins, *Diamond Relat. Mater.* **(1993)** 2, 87.

[11] K. Okano, T. Kurosu, M. Iida, T. Eickhoff, H. Wilhelm, D.R.T. Zahn, *Vacuum* **(1990)** 41, 1387.

[12] G.M. Swain, R. Ramesham, *Anal. Chem.* **(1993)** 65, 345.

[13] R. Tenne, K. Patel, K. Hashimoto, A. Fujishima, *J. Electroanal. Chem.* **(1993)** 347, 409.

[14] K.E. Toghill, G.G. Wildgoose, A. Moshar, C. Mulcahy, R.G. Compton, *Electroanalysis* **(2008)** 20, 1731.

[15] H. Dejmkova, M. Scampicchio, J. Zima, J. Barek, S. Mannino, *Electroanalysis* **(2009)** 21, 1014.

[16] T.A. Ivandini, R. Sato, Y. Makide, A. Fujishima, Y. Einaga, *Diamond Relat. Mater.* **(2004)** 13, 2003.

[17] R. Fardel, U. Griesbach, H. Puetter, C. Comninellis, *J. Appl. Electrochem.* **(2006)** 36, 249.

[18] U. Griesbach, D. Zollinger, H. Puetter, C. Comninellis, *J. Appl. Electrochem.* **(2005)** 35, 1265.

[19] N.R. Stradiotto, K.E. Toghill, L. Xiao, A. Moshar, R.G. Compton, *Electroanalysis* **(2009)** 21, 2627.

[20] V. Saez, J. Gonzalez-Garcia, M.A. Kulandainathan, F. Marken, *Electrochem. Commun.* **(2007)** 9, 1127.

[21] M. Panizza, E. Brillas, C. Comninellis, *J. Environ. Eng. Manage.* **(2008)** 18, 139.

[22] V. Schmalz, T. Dittmar, D. Haaken, E. Worch, *Water Res.* **(2009)** 43, 5260.

[23] X. Zhu, J. Ni, P. Lai, *Water Res.* **(2009)** 43, 4347.

[24] O. Scialdone, S. Randazzo, A. Galia, G. Silvestri, *Water Res.* **(2009)** 43, 2260.

[25] A.Y.M.T. Christy, K.S. Nahm, Y.J. Hwang, E.K. Suh, M.A. Kulandainathan, T. Premkumar, A.M. Stephan, *Ionics* **(2008)** 14, 157.

[26] N.G. Ferreira, L.L. Mendonca, V.J.T. Airoldi, J.M. Rosolen, *Diamond Relat. Mater.* **(2003)** 12, 596.

[27] J.J. Mares, M. Nesladek, P. Hubik, D. Kindl, J. Kristofik, *Diamond Relat. Mater.* **(2007)** 16, 1.

[28] Y. Takano, *J. Phys. : Condens. Matter* **(2009)** 21, 253201.

[29] X. Blase, E. Bustarret, C. Chapelier, T. Klein, C. Marcenat, *Nat. Mater.* **(2009)** 8, 375.

[30] R.G. Compton, J.S. Foord, F. Marken, *Electroanalysis* **(2003)** 15, 1349.

[31] J.H.T. Luong, K.B. Male, J.D. Glennon, *Analyst* **(2009)** 134, 1965.

[32] M.C. Granger, M. Witek, J. Xu, J. Wang, M. Hupert, A. Hanks, M.D. Koppang, J.E. Butler, G. Lucazeau, M. Mermoux, J.W. Strojek, G.M. Swain, *Anal. Chem.* **(2000)** 72, 3793.

[33] J. Xu, M.C. Granger, Q. Chen, J.W. Strojek, T.E. Lister, G.M. Swain, *Anal. Chem.* **(1997)** 69, 591A.

[34] J. Wang, G.M. Swain, M. Mermoux, G. Lucazeau, J. Zak, J.W. Strojek, *New Diamond Front. Carbon Technol.* **(1999)** 9, 317.

[35] J. Xu, Q. Chen, G.M. Swain, *Anal. Chem.* **(1998)** 70, 3146.

[36] M.C. Granger, G.M. Swain, *J. Electrochem. Soc.* **(1999)** 146, 4551.

[37] C.H. Goeting, J.S. Foord, F. Marken, R.G. Compton, *Diamond Relat. Mater.* **(1999)** 8, 824.

[38] R.G. Compton, F. Marken, C.H. Goeting, R.A.J. McKeown, J.S. Foord, G. Scarsbrook, R.S. Sussmann, A.J. Whitehead, *Chem. Commun.* **(1998)**1961.

[39] C.H. Goeting, F. Jones, J.S. Foord, J.C. Eklund, F. Marken, R.G. Compton, P.R. Chalker, C. Johnston, *J. Electroanal. Chem.* **(1998)** 442, 207.

[40] C.H. Goeting, F. Marken, A. Gutierrez-Sosa, R.G. Compton, J.S. Foord, *New Diamond Front. Carbon Technol.* **(1999)** 9, 207.

[41] C.H. Goeting, F. Marken, A. Gutierrez-Sosa, R.G. Compton, J.S. Foord, *Diamond Relat. Mater.* **(2000)** 9, 390.

[42] G.M. Swain, *J. Electrochem. Soc.* **(1994)** 141, 3382.

[43] C.E. Nebel, D. Shin, B. Rezek, N. Tokuda, H. Uetsuka, H. Watanabe, *J. R. Soc. Interface* **(2007)** 4, 439.

[44] T.A. Ivandini, R. Sato, Y. Makide, A. Fujishima, Y. Einaga, *Diamond Relat. Mater.* **(2005)** 14, 2133.

[45] T.A. Ivandini, R. Sato, Y. Makide, A. Fujishima, Y. Einaga, *Anal. Chem.* **(2006)** 78, 6291.

[46] S. Treetepvijit, A. Preechaworapun, N. Praphairaksit, S. Chuanuwatanakul, Y. Einaga, O. Chailapakul, *Talanta* **(2006)** 68, 1329.

[47] K.E. Toghill, L. Xiao, G.G. Wildgoose, R.G. Compton, *Electroanalysis* **(2009)** 21, 1113.

[48] A.O. Simm, X. Ji, C.E. Banks, M.E. Hyde, R.G. Compton, *ChemPhysChem* **(2006)** 7, 704.

[49] A.O. Simm, C.E. Banks, S. Ward-Jones, T.J. Davies, N.S. Lawrence, T.G.J. Jones, L. Jiang, R.G. Compton, *Analyst* **(2005)** 130, 1303.

[50] C. Batchelor-McAuley, C.E. Banks, A.O. Simm, T.G.J. Jones, R.G. Compton, *Analyst* **(2006)** 131, 106.

[51] M.E. Hyde, R.M.J. Jacobs, R.G. Compton, *J. Phys. Chem. B* **(2004)** 108, 6381.

[52] M. Hyde, A.J. Saterlay, S.J. Wilkins, J.S. Foord, R.G. Compton, F. Marken, *J. Solid State Electrochem.* **(2002)** 6, 183.

[53] S. Hrapovic, Y. Liu, J.H.T. Luong, *Anal. Chem.* **(2007)** 79, 500.

[54] K.E. Toghill, L. Xiao, N.R. Stradiotto, R.G. Compton, *Electroanalysis* **(2010)** 22, 491.

[55] G. Sine, G. Foti, C. Comninellis, *J. Electroanal. Chem.* **(2006)** 595, 115.

[56] M. Wei, Z. Xie, L. Sun, Z. Gu, *Electroanalysis* **(2009)** 21, 138.

[57] C.E. Banks, J. Kruusma, R.R. Moore, P. Tomcik, J. Peters, J. Davis, S. Komorsky-Lovric, R.G. Compton, *Talanta* **(2005)** 65, 423.

[58] C. Batchelor-McAuley, C.E. Banks, A.O. Simm, T.G.J. Jones, R.G. Compton, *ChemPhysChem* **(2006)** 7, 1081.

[59] J. Kruusma, C.E. Banks, R.G. Compton, *Anal. Bioanal. Chem.* **(2004)** 379, 700.

[60] L. Hutton, M.E. Newton, P.R. Unwin, J.V. Macpherson, *Anal. Chem.* **(2009)** 81, 1023.

[61] C.M. Welch, M.E. Hyde, C.E. Banks, R.G. Compton, *Anal. Sci.* **(2005)** 21, 1421.

[62] C.M. Welch, A.O. Simm, R.G. Compton, *Electroanalysis* **(2006)** 18, 965.

[63] Y. Song, G.M. Swain, *Anal. Chem.* **(2007)** 79, 2412.

[64] R. Uchikado, T.N. Rao, D.A. Tryk, A. Fujishima, *Chem. Lett.* **(2001)**144.

[65] F. Montilla, E. Morallon, I. Duo, C. Comninellis, J.L. Vazquez, *Electrochim. Acta* **(2003)** 48, 3891.

[66] K. Ohnishi, Y. Einaga, H. Notsu, C. Terashima, T.N. Rao, S. Park, A. Fujishima, *Electrochem. Solid-State Lett.* **(2002)** 5, D1.

[67] K.E. Toghill, L. Xiao, M.A. Phillips, R.G. Compton, *Sens. Actuators, B* **(2010)** B147, 642.

[68] T.J. Davies, S. Ward-Jones, C.E. Banks, J. Del Campo, R. Mas, F.X. Munoz, R.G. Compton, *J. Electroanal. Chem.* **(2005)** 585, 51.

[69] T.J. Davies, R.G. Compton, *J. Electroanal. Chem.* **(2005)** 585, 63.

[70] T.J. Davies, C.E. Banks, R.G. Compton, *J. Solid State Electrochem.* **(2005)** 9, 797.

[71] C.M. Welch, R.G. Compton, *Anal. Bioanal. Chem.* **(2006)** 384, 601.

[72] F.W. Campbell, R.G. Compton, *Anal. Bioanal. Chem.* **(2010)** 396, 241.

[73] A.J. Saterlay, S.J. Wilkins, C.H. Goeting, J.S. Foord, R.G. Compton, F. Marken, *J. Solid State Electrochem.* **(2000)** 4, 383.

[74] A.J. Saterlay, S.J. Wilkins, K.B. Holt, J.S. Foord, R.G. Compton, F. Marken, *J. Electrochem. Soc.* **(2001)** 148, E66.

[75] C. Terashima, T.N. Rao, B.V. Sarada, N. Spataru, A. Fujishima, *J. Electroanal. Chem.* **(2003)** 544, 65.

[76] C. Prado, S.J. Wilkins, F. Marken, R.G. Compton, *Electroanalysis* **(2002)** 14, 262.

[77] E.A. McGaw, G.M. Swain, *Anal. Chim. Acta* **(2006)** 575, 180.

[78] A. Manivannan, R. Kawasaki, D.A. Tryk, A. Fujishima, *Electrochim. Acta* **(2004)** 49, 3313.

[79] J. Wang, *Electroanalysis* **(2005)** 17, 1341.

[80] C. Kokkinos, A. Economou, *Curr. Anal. Chem.* **(2008)** 4, 183.

[81] J. Weng, J. Xue, J. Wang, J. Ye, H. Cui, F. Sheu, Q. Zhang, *Adv. Funct. Mater.* **(2005)** 15, 639.

[82] A. Salimi, M.E. Hyde, C.E. Banks, R.G. Compton, *Analyst* **(2004)** 129, 9.

End of Part 1

Kathryn E. Toghill

DPhil thesis

Part 2

Chapters 5 - 9

Chapter 5

Bismuth and antimony nanoparticle modified boron doped diamond electrodes and their application to the simultaneous determination of lead and cadmium

The work presented in this chapter has been published in

Electroanalysis, 20, **(2008)** 1731, and

Electroanalysis, 21, **(2010)**, 1113,

This chapter reports the simultaneous electroanalytical determination of lead and cadmium by anodic stripping voltammetry (SWASV) using a bismuth nanoparticle modified boron doped diamond (Bi-BDD) electrode and an antimony modified BDD electrode (Sb-BDD). Lead and cadmium could not be detected simultaneously at the unmodified BDD electrode, as only the lead stripping peak was observed.

Bismuth deposition was performed in-situ with the analytes, from a solution of 0.1mM $Bi(NO_3)_3$ in 0.1 M $HClO_4$ (pH 1.2), and gave detection limits of 1.9 μgL^{-1} and 2.3 μgL^{-1} for Pb(II) and Cd(II) respectively. On a bulk bismuth macro electrode (BiBE) the limits of detection for the simultaneous determination of lead and cadmium were approximately ten times higher.

In situ electrochemical atomic force microscopy (EC-AFM) was performed to characterise the bismuth nanoparticle growth on the BDD surface over a period of 120 s. The average final size of the bismuth nanoparticles was 45 ± 25 nm in height with a number

density on the electrode surface of ca. $7x10^9$ np/cm^2. The *in situ* AFM characterisation suggests that the bismuth nanoparticles are deposited by an "instantaneous" nucleation and growth mechanism.

Antimony was deposited in-situ with the analytes, from a solution of 1 mgL^{-1} (8.2 μM) $SbCl_3$ in 0.1 M HCl (pH 0.8). In the presence of antimony, both cadmium and lead peaks were readily discernable and quantifiable over the linear range 50 – 500 μgL^{-1}. Ex-situ AFM characterisation of the Sb-BDD electrode showed a distribution of nanoparticles ranging from 3 to 110 nm in height, and 8.5 to 506.5 nm in diameter across the electrode surface, which corresponded well to the low mass of antimony expected on the BDD electrode with respect to the voltammetric data.

5.1. Introduction

Stripping voltammetry is a well-established electroanalytical technique, providing an efficient, versatile and highly sensitive method of detecting a wide range of inorganic and organic substances to concentrations as low as 10^{-10} M [1, 2]. Anodic stripping voltammetry (ASV) is one of the most efficient techniques in this field, owing to an effective cathodic pre-concentration step, in which the analyte is reduced and deposited onto the electrode surface as a thin layer, followed by a stripping step, the results of which are readily quantifiable.

During the development of ASV over the past 50 years, mercury film electrodes (MFE) and the hanging mercury drop electrode have proved invaluable and, until recently, have been the electrodes of choice for the electroanalytical determination of metals [1-10]. However, with increasing concern regarding the extreme toxicity and environmentally hazardous nature of mercury and its salts [11], coupled with the greater demand for disposable and on-site analytical devices, the use of mercury in such systems is no longer feasible. As such, environmentally benign and less toxic alternative electrodes of equivalent or superior performance to that of their mercury counterparts are highly sought after.

5.1.1 Bismuth modified electrodes

In 2000, Wang et al [12] introduced bismuth film electrodes (BiFE) as an environmentally friendly alternative. These BiFE offered a highly comparable ASV performance to that of mercury electrodes, due to the ability of bismuth to form multicomponent "fusible" alloys with various heavy metals, similar to the way in which metal-to-mercury amalgams form on the surface of MFEs [13]. The metal-to-mercury amalgams are responsible for the superior analytical ASV performance of mercury electrodes, as the metals are concentrated onto the surface during the reductive pre-concentration step [1, 2, 11]. Similarly, the formation of alloys on the bismuth film facilitates the nucleation, and therefore deposition, of heavy metals onto the electrode surface [14], resulting in a comparably efficient stripping performance.

5.1.2 Antimony modified electrodes

Bismuth and mercury modified electrodes are advantageous for use in electroanalysis due to their ability to form 'fusible' alloys and amalgams with the analyte metals. The successful application of bismuth has therefore naturally led to investigation of other elements with similar properties such as antimony [15], gallium [16] and tin [17] .

Antimony is positioned above bismuth in Group 15 of the periodic table, and is therefore a metalloid of more non-metallic character than bismuth. The intermetallic compound and alloys it forms are comparable to those of bismuth however, with alloy formation with heavy metals leading to its wide spread use in certain industrial applications such as in lead acid batteries [18-20]. Despite the fact that some trivalent antimony compounds may be toxic [21-23], the electroanalytical properties of antimony and its alloy-forming capabilities have yet to be fully explored and may offer advantages that could outweigh any environmental or health concerns.

5.1.3 Boron doped diamond electrodes in stripping analysis

Metal film-modified electrodes are often supported on carbon based electrode substrates such as glassy carbon [24-28], carbon paste [29] and graphite [30, 31], as well as other inert metals such as gold [32]. However, over the past decade or so, a new carbon based electrode, namely thin-film boron doped diamond (BDD), has found increasing use within the electroanalytical field [24, 33, 34].

Over the past decade, BDD electrodes have been investigated as an alternative to mercury electrodes in their own right [24, 33-36], owing to electrochemical properties similar to those of mercury films [24, 34]. Such properties include large aqueous and non-aqueous potential windows, a low background current, over a magnitude lower than that of glassy carbon electrodes [37, 38], chemical inertness, and a readily renewable surface. Furthermore they have high durability as well as significant corrosion resistance [36].

Bare, unmodified BDD electrodes themselves have been shown to provide detection limits comparable to mercury electrodes [24], and in a few reports of modified BDD electrodes, detection limits and sensitivity have been further improved [33]. The corrosion resistance and robustness of the electrode also allow for its use in more extreme environments, such as in highly corrosive media [39] and in conjunction with the application of high power ultrasound [33].

It is therefore a potentially ideal substrate electrode for modification with bismuth or antimony films. Due to the surface heterogeneity of BDD electrodes, corresponding to different doping levels of boron within the crystallites and at grain boundaries, metals are deposited on the more active sites as nanoparticles rather than thin metal films on the substrate. Nanoparticles have been known to enhance electroanalytical properties in some areas, primarily due to their increased surface area coupled with enhanced mass transport effects [37, 38, 40, 41]. Though there have been many attempts to synthesize bismuth nanoparticles, problems have often arisen in terms of contamination by surfactants [42, 43], the presence of matrices [44] or more commonly the formation of bismuth oxides [45].

Bismuth oxides readily form in aerated water [46], and can significantly impede the electroactivity of bismuth nanoparticles [45] thus a method to simply produce pure bismuth nanoparticles that have a readily renewable surface, is highly desirable.

5.1.4 The analytes of anodic stripping voltammetric analysis

One of the main electroanalytical uses of ASV is in the detection of heavy and toxic metal ions. Two such heavy metals of environmental and clinical concern are lead and cadmium, the toxicity of which are well known, particularly that of lead [47, 48]. Due to continued extensive use of lead and cadmium in industry and society, substantial and concerning amounts of the elements are persistently being added to the environment. Accurate quantification of their concentrations in environmental and clinical situations is therefore highly important and the focus of much research [15, 24, 30, 31, 33, 35, 49, 50].

In this chapter the simultaneous detection of lead and cadmium from standard solutions is explored, comparing the ability of bare BDD, bismuth modified BDD and antimony modified BDD electrodes.

5.2. Experimental

Apparatus

All voltammetric measurements were recorded using an Autolab PGSTAT20 computer controlled potentiostat (EcoChemie, Utrecht, The Netherlands). A standard three-electrode configuration was used throughout, consisting of a boron doped diamond (BDD, diameter 3mm, Windsor Scientific, Slough, UK) working electrode, with a graphite rod counter electrode, and either a saturated calomel electrode (SCE) or a silver wire pseudo-reference electrode (calibrated to SCE). The BDD disk working electrode was incorporated into a custom built PEEK housing, equipped with a stainless steel piston to make electrical contact.

The bismuth bulk electrode (BiBE) was prepared from bismuth foil, 0.025mm thick on a polyester support (Goodfellow Advanced Materials, Surrey, UK). The bismuth foil electrode was fabricated to have the same surface area as the BDD electrode to allow direct comparison to be made.

In-situ atomic force microscopy (AFM) of the bismuth modified BDD electrode was conducted on a MFP-3D stand-alone microscope (Asylum Research, Santa Barbara, CA) using SiN TR400 PSA cantilevers (Olympus) of 100 μm length suitable for contact and AC mode AFM in liquid. The software used for data acquisition and analysis was IGOR Pro 6.0 (Wavemetrics) with 3D imaging provided by Argyle-3D imaging software. Electrochemical deposition of bismuth onto the BDD surface was performed using the adapted AFM liquid cell design discussed in Chapter 3 (Prototype #1), allowing the electrode to remain in situ throughout the AFM characterisation, and the electrode surface to be imaged immediately after deposition.

Ex-situ AFM measurements of the antimony modified BDD electrode were performed using a Digital Instruments MultiMode SPM (Veeco, Santa Barbara, CA) operating in tapping mode using NST-NCHFR silicon AFM cantilevers with a reflective coating (Nascatec GmbH, Germany). The software used in data acquisition and analysis was NanoScope version 5.12 (Digital Instruments, Veeco Metrology Group, CA).

Reagents and solutions

All chemicals were purchased from Sigma-Aldrich (Gillingham, UK) were of analytical grade and were used as received without any further purification. These were cadmium(II) nitrate tetrahydrate, lead(II) nitrate, bismuth(III) nitrate and a standard stock solution of antimony (III) trichloride (1000 mgL^{-1} absorption standard solution). Perchloric acid ($HClO_4$) and hydrochloric acid (HCl) solutions were prepared from trace metal analysis grade concentrated solutions, also purchased from Aldrich.

Stock solutions of cadmium(II) and lead(II) were prepared to a 1 gL^{-1} stock solution using deionized water of resistivity not less than 18.2 MΩ cm^{-1} at 298 K (Millipore UHQ, Vivendi, UK). A 0.1 mM stock solution of Bi(III) nitrate was prepared in 0.1 M perchloric acid ($HClO_4$). The antimony was prepared to a 1 mgL^{-1} (8.2 μM) concentration in 0.1 M HCl.

Experimental procedure

Prior to each set of standard additions the surface of the BDD electrode was cleaned using a diamond slurry of 0.1 μm particle size, followed by sonication for 2-3 minutes in ethanol/water and thorough rinsing using Millipore water.

Stripping voltammetry experiments of the bismuth modified electrode were performed using square wave voltammetry (SWV), with a pulse frequency of 12.5 Hz, a potential step of 2 mV and a pulse amplitude of 25 mV. A deposition potential of -1.2 V was applied for 120 s with stirring followed by a 15 s equilibration time without stirring. The potential was then swept from -1.2 V to +0.3 V i.e. beyond the potential at which bismuth is stripped from the surface. Note that for the BBiE, the potential was not swept beyond -0.4 V to prevent bismuth from being stripped away.

For the antimony experiments stripping voltammetry was performed using linear sweep voltammetry (LSV). A deposition potential of -1.1 V was applied for 120 s with stirring followed by a 10 s equilibration time without stirring. The potential was then swept from -1.1 V to +0.5 V i.e. beyond the potential at which antimony is stripped from the surface. The electrode potential was held at +0.5 V for 20 s following each measurement to further “clean” the working electrode surface and ensure the removal of all the anitmony. The cell was thoroughly degassed in nitrogen for 20 minutes prior to the experiment, and remained under nitrogen throughout.

5.3. Results and Discussion

5.3.1. Electroanlaysis at the Bi-BDD electrode

5.3.1.1 Characterisation of the bismuth nanoparticle random array on BDD

The deposition of bismuth from a 1mM solution following 120 seconds at -1.2 V, was characterised by in-situ EC-AFM of the BDD surface, immediately after deposition. The image in Figure 1 shows that bismuth grows in active areas of the surface forming a random nanoparticle array.

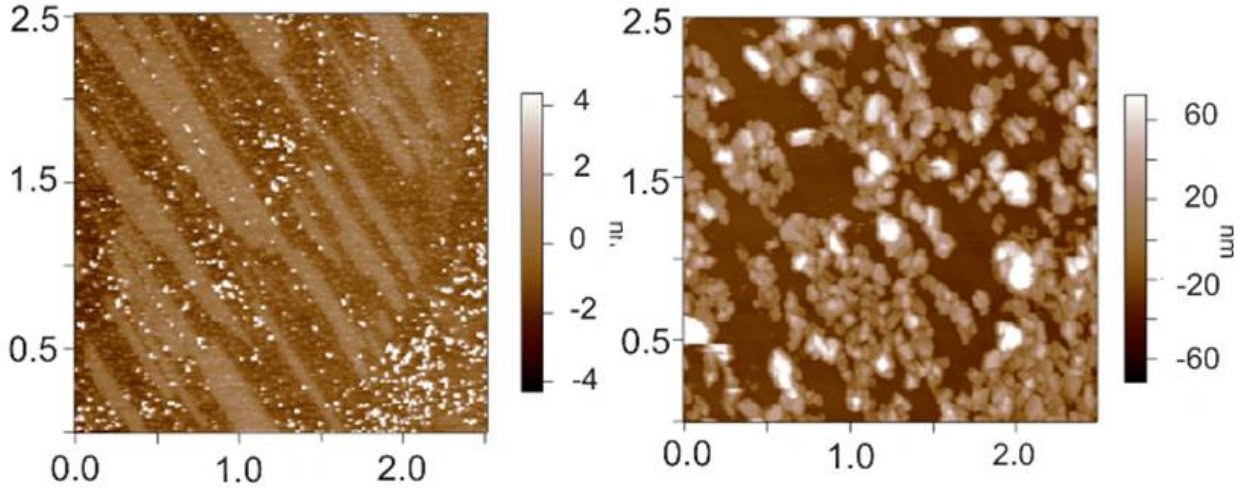


Figure 5.1: *AFM images of the BDD surface a) before deposition and b) after a 120 s deposition at -1.0 V in 1 mM $Bi(NO_3)_3$ in 0.1 M $HClO_4$ M solution. Note the scales on the right of the images.*

The particle size varies somewhat across the electrode surface, but has an average nanoparticle size of 45 nm in height, with distribution mainly confined to a 20 to 70 nm range, as determined via cross section analysis of the images obtained. Surface coverage was approximated to be 600 nanoparticles per 9μm^2 area. In the course of this investigation the bismuth stripping peak was consistently 0.16 ± 0.04 mA with respect to the deposition time, thus implying that a similar amount of bismuth is deposited and stripped each time.

Figure 5.2 illustrates a sequential deposition process, in which a potential of -1.2 V was applied to the AFM electrochemical cell for increasing periods of time.

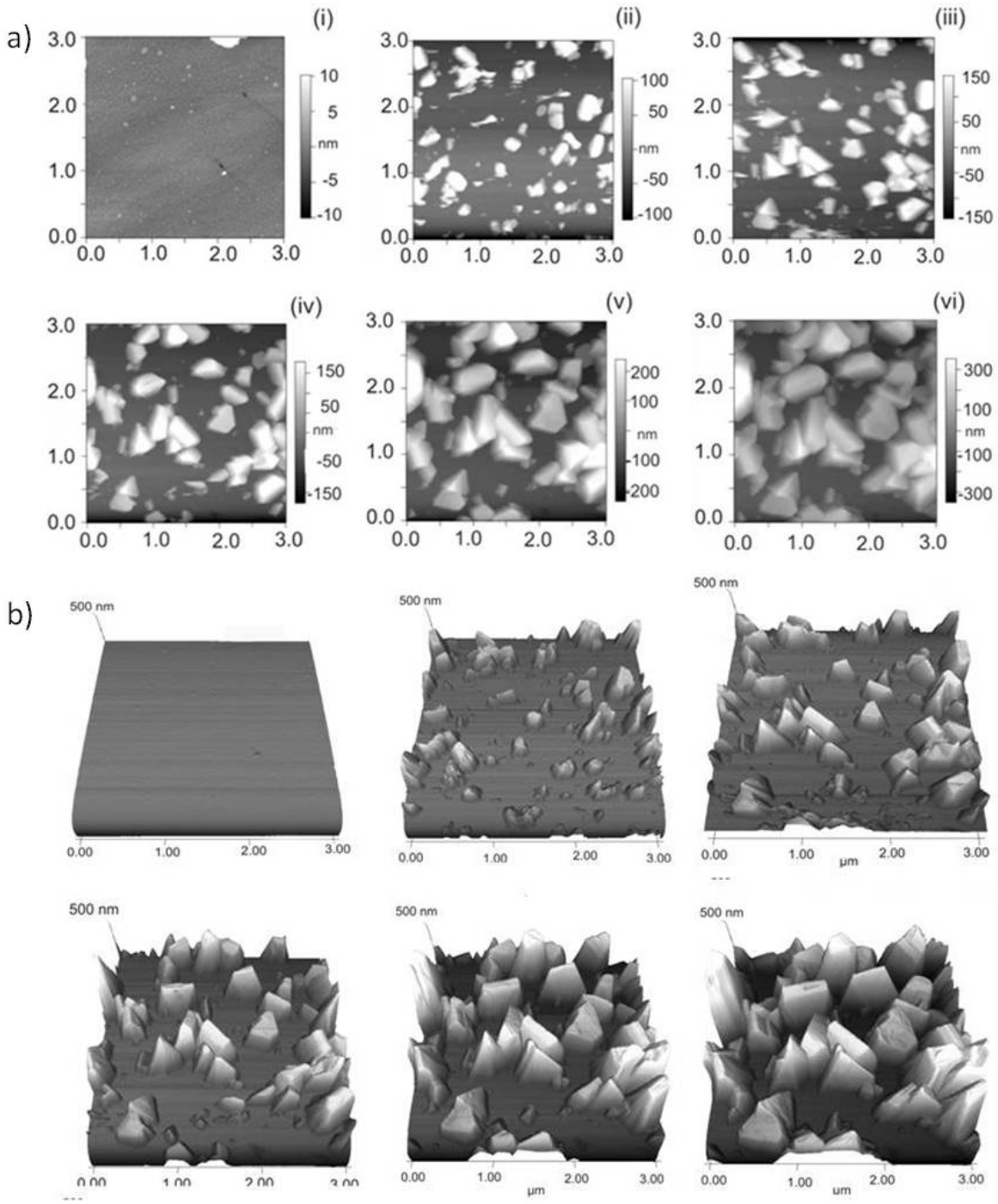


Figure 5.2:

a) AFM images of a 9 μm^2 area of a BDD electrode undergoing a series of bismuth depositions at increasing time intervals. The deposition potential was -1.0 V, and deposition times prior to the image being taken are (i) 0 s (ii) 5 s (iii) 10s (iv) 20 s (v) 60 s and (vi) 120 s. Note the scales to the right of the images

b) The AFM images reported in Fig. 5.2a, but in 3D format to further illustrate the nanoparticle growth.

The same area of the BDD surface was imaged immediately after each deposition period for approximately 15 minutes, with deposition time increasing with each step, ending in a total deposition time of 120 s. Nucleation of the bismuth nanoparticles is immediately observed following the first 5 s deposition, with the successive images showing the growth and merging of these initial particles rather than further nucleation of bismuth onto the bare BDD surface. This is consistent with an "instantaneous" nucleation and growth mechanism [51, 52]. The nanoparticles grown on the BDD in this sequential process are much larger and more defined at 120 s than the particles grown in a single continuous 120 s deposition as discussed above.

Approximately 35 particles are observed in the final 120 s AFM scan, with the average particle size found in the range of 200 to 350 nm in height, and approximately 300 to 500 nm in diameter. This is very interesting, as it illustrates the extent to which nanoparticle growth may be electrochemically controlled on the electrode surface, thus allowing for a greater variety and density of nanoparticle arrays and potentially a significant variance in electroanalytical behaviour.

5.3.1.2 ASV of lead and cadmium at a bare BDD electrode

The electroanalytical response of the BDD electrode, without the presence of Bi, toward the presence of Pb(II) and Cd(II) was first investigated. Standard additions of 4µL of a stock Pb(II) and Cd(II) solution (100 mgL^{-1}) were added to the cell containing 40 mL of 0.1 M $HClO_4$ (pH 1.2) and electrodeposition performed at -1.2 V for 120 s. An overlay of the square wave voltammograms, over a 20 to 200 μgL^{-1} (0.096 –0.96 µM) lead and cadmium concentration range is given in Figure 5.3.

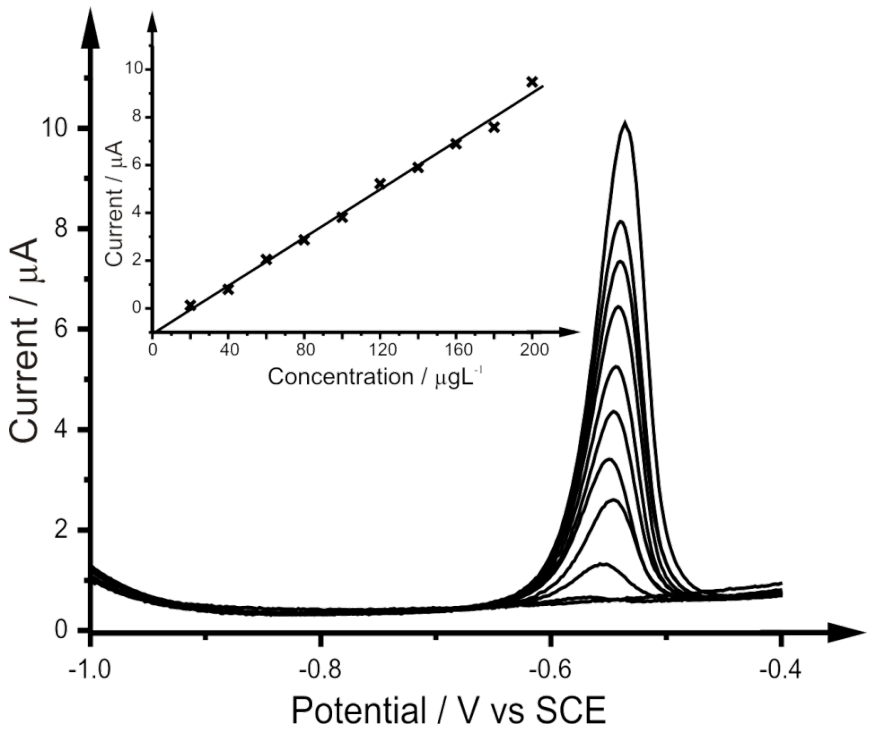


Figure 5.3: *SWASV at a bare BDD electrode in 0.1 M $HClO_4$ from the simultaneous standard additions of Pb^{2+} and Cd^{2+} over a concentration range of 20 to 200 µg L^{-1}. Deposition time 120 s at a potential of -1.2 V vs. SCE. The peak observed is that of lead only. (Inset) Linear calibration plot of peak current against lead concentration.*

It is evident that a single stripping peak is observed, at a potential expected of the lead stripping potential on BDD [24, 53]. No activity is observed in the expected cadmium [24, 34] region of approximately -0.8 V vs. SCE. Based on the observations of Manivannan et al. [34] this is presumably due to an interaction between the Cd^{2+} and Pb^{2+} during co-deposition, in which lead deposits before the cadmium, and a large portion of cadmium forms a monolayer on the lead nanoparticles as opposed to the BDD surface. Foord et al [54] noted that it appears to be the metal with the most negative redox couple that is inhibited following similar experiments with copper, cadmium and zinc on BDD. During the stripping process, the more readily oxidised metal, in this case cadmium is stripped off the bare BDD surface, but the remainder is not stripped until the lead oxidising potential is met

The resulting calibration plot (inset Figure 5.3) is linear over the concentration range of 20 to 200 μgL^{-1}, with a correlation coefficient of 0.993 and a calculated limit of detection (3σ) [55] of 15.8 μgL^{-1}. The lead stripping peak could not be observed above the background current at concentrations lower than 20 μgL^{-1}.

5.3.1.3 Electroanalysis of trace lead and cadmium using the Bi- BDD electrode

Bismuth was deposited *in-situ* onto a cleaned BDD electrode from a solution of 0.1mM $Bi(NO_3)_3$ in 0.1 M $HClO_4$ (pH 1.2). A typical voltammogram of bismuth stripping from the electrode surface during square-wave anodic stripping voltammetry is shown in Figure 5.4, following a 120 s deposition time at -1.0 V. The peak current shape and potential remained consistent regardless of the heavy metal concentration, with a peak current of ca. 12 mA, and a stripping peak potential of -0.1 V (vs. SCE).

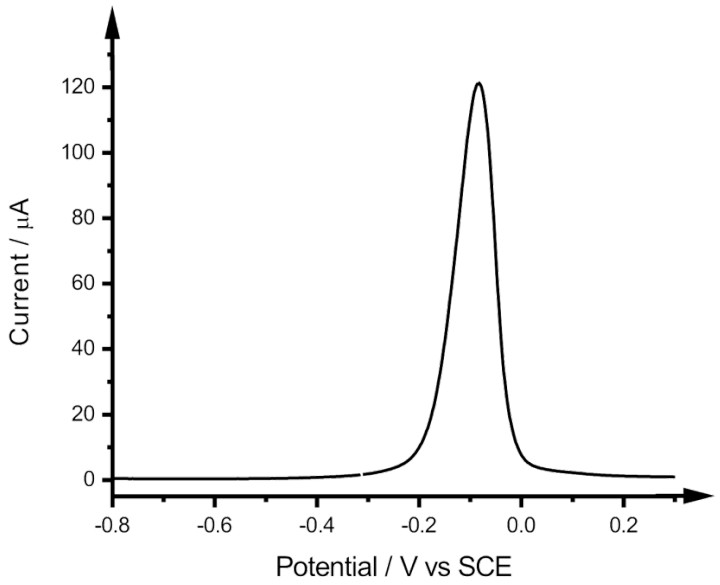


Figure 5.4: *Typical SWASV for 0.1 mM $Bi(NO_3)_3$ in 0.1 M $HClO_4$ solution on BDD electrode. Deposition time 120 s at -1.0 V, degassed and stirred.*

Standard additions of Cd(II) and Pb(II) were simultaneously analysed over a concentration range of 20 to 200 μgL^{-1} using square wave voltammetry, following a pre-concentration step of 120 s at -1.2 V. Separate stripping peaks for the cadmium and lead

were immediately observed, at the expected potentials of approximately -0.85 V and -0.575 V vs. SCE respectively, and are illustrated in Figure. 5.5.

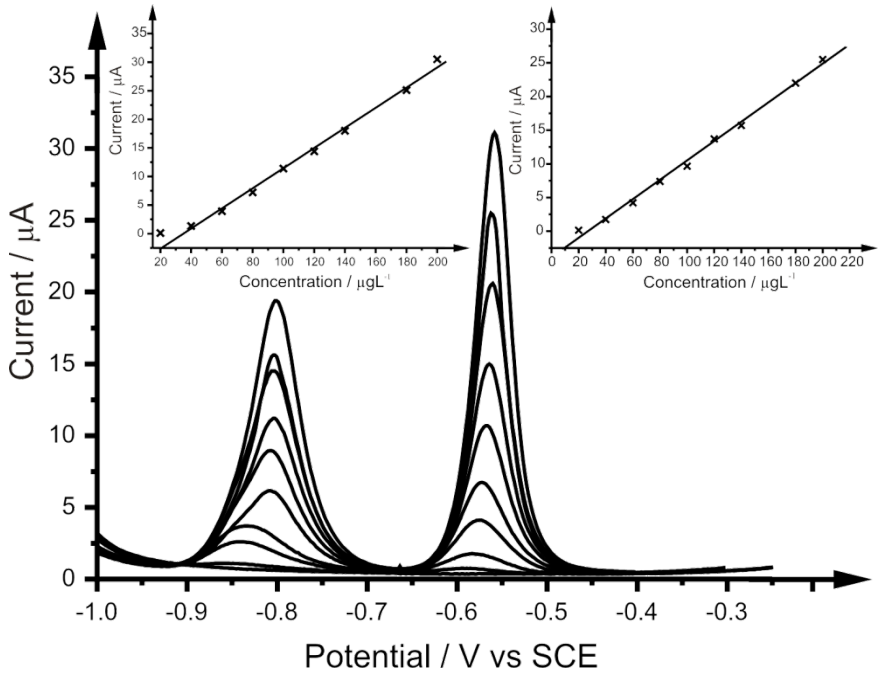


Figure 5.5: *SWASVs for the simultaneous standard additions of Pb^{2+} and Cd^{2+} of 20 to 200 µg L^{-1} to a 0.1 mM $Bi(NO_3)_3$ in 0.1 M $HClO_4$ solution, following deposition at -1.2 V for 120 s. Cadmium peak at ca. -0.85 V and lead at ca. -0.575 V. (Inset) The resulting calibration plots for cadmium and lead.*

The calibration plots obtained for this concentration range was linear for both the cadmium and lead peak height currents. Cadmium gave a correlation coefficient of 0.989 and lead a coefficient of 0.995, although there was a deviation from linearity at the first addition of each metal analyte. The analytes were detected from the lowest concentration at readily measurable peak currents of 25 and 34 µA, indicative of lower detection limits than those observed in this concentration range. The experiment was therefore repeated at a second concentration range of 0.05 to 20 μgL^{-1}. The calibration plots were again linear with correlation coefficients are 0.987 (Cd) and 0.993 (Pb), and gave low limits of detection of 2.3 μgL^{-1} and 1.9 μgL^{-1} for lead and cadmium respectively.

In accordance with the Pourbaix diagram for bismuth [46], from the deposition potential of -1.2 V through to the stripping potential of approximately -0.1 V, the deposited bismuth on the electrode surface should have remained in a pure metallic form as opposed to the oxide, with the acidic medium of pH 1.2 maintaining a transition from $Bi^0 \rightarrow Bi^{3+} + 3e^-$. As the electrode surface was completely stripped of bismuth with each addition, bismuth oxide formation was further avoided, and a renewed nano-bismuth array was formed for each analysis.

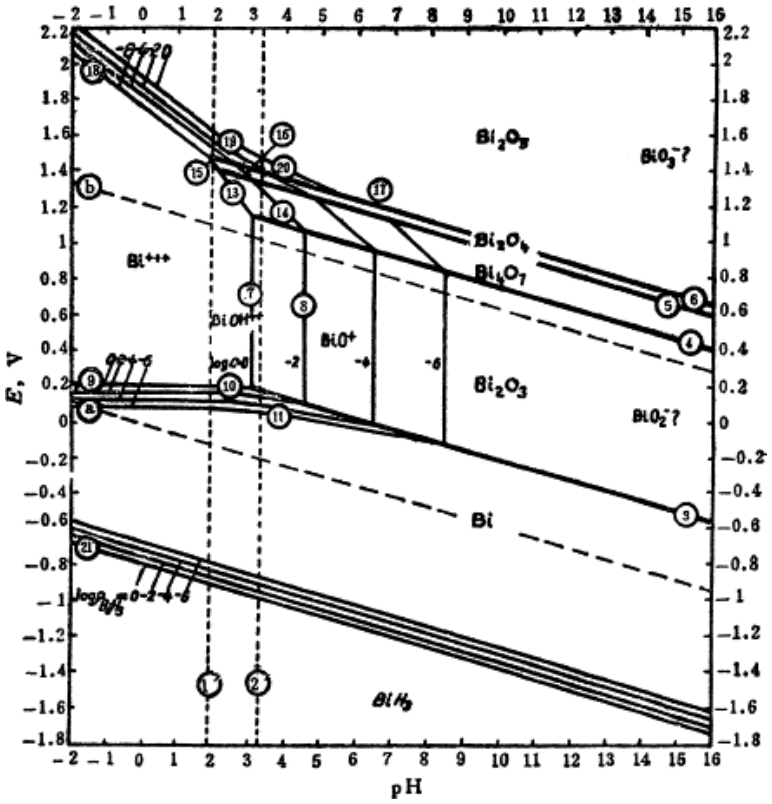


Figure 5.6: *Pourbaix diagram for bismuth in water* [46]

5.3.1.4 Electroanalysis of trace lead and cadmium using a BiBE

A bulk bismuth electrode (BiBE) was prepared to equivalent surface dimensions as the BDD electrode, thus exposing a working surface area of approximately 7 mm^2. Standard additions of Cd^{2+} and Pb^{2+} were made to the 0.1 M $HClO_4$ electrolyte over two concentration ranges, 20 to 200 μgL^{-1} and 1 to 20 μgL^{-1}. The cell was held at a pre-concentration potential of -1.2 V for 120 seconds.

Figure 5.7 illustrates the BiBE voltammetry over the concentration range of 20 to 200 μgL^{-1}. The cadmium peak is once again detectable, and linear calibration plots are obtained for both analytes. Cadmium and lead detection over this range is comparable to that of the bismuth modified BDD electrode, with cadmium observed with a correlation coefficient of 0.989 and limit of detection of 19.9 μgL^{-1}, and lead with a coefficient of 0.992 and detection limit of 17.7 μgL^{-1}. The electroanalysis was then conducted at a 10-fold lower analyte concentration of 1 to 20 μgL^{-1}. Over this range the lead was detectable from 7μgL^{-1}, but the calibration plot gave a poorly linear correlation coefficient of 0.951, whereas the cadmium remained undetected. As such the data gathered at this concentration range was not analytically useful.

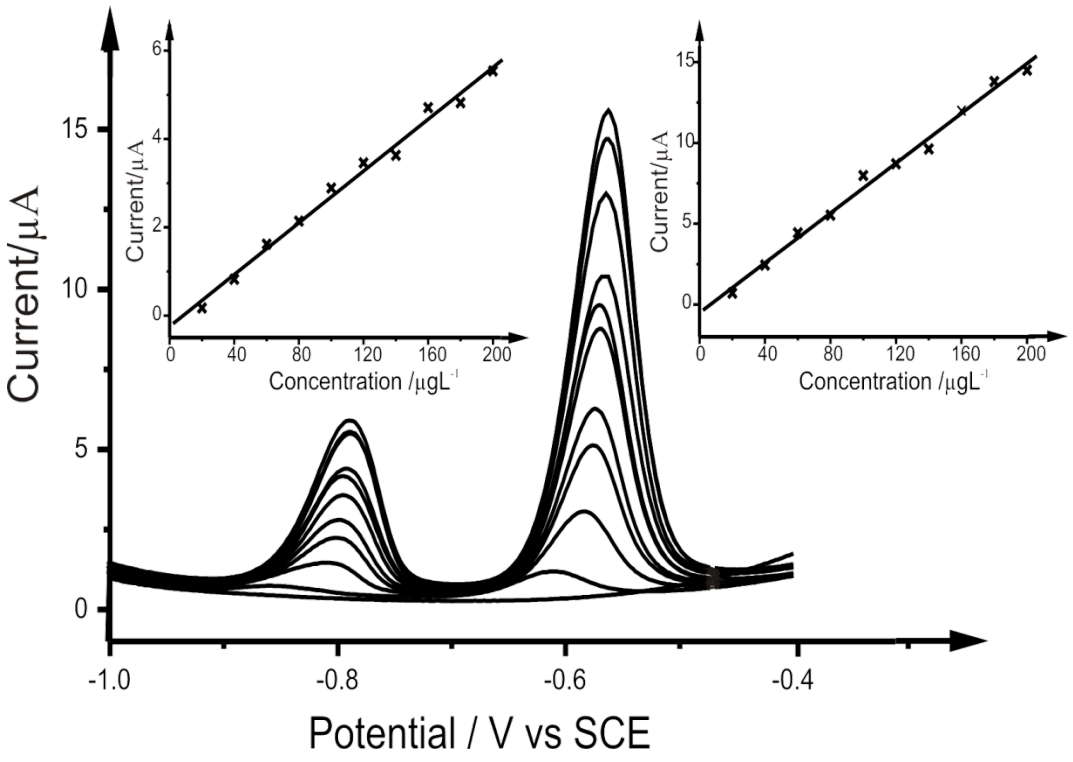


Figure 5.7: *Overlay of SWASVs at a bulk bismuth electrode in 0.1 M $HClO_4$ from the simultaneous standard additions of Pb^{2+} and Cd^{2+} over a concentration range of 20 to 200 $\mu g\ L^{-1}$. Deposition time 120 s at a potential of -1.2 V vs. SCE. (Inset) Calibration plots for the cadmium and lead peaks.*

The presence of the cadmium peak in the higher concentration range is indicative of the bismuth to metal interaction during deposition, an effect evidently lost at the bare BDD electrode. The lower peak currents observed for the analytes may be due to the difference in morphology between the bulk and nano bismuth surfaces. It is possible that the BiBE, due to its formation prior to pre-concentration step, was coated in a Bi_2O_3 film, a feature evident in the experimental procedure as thorough polishing of the surface was required to remove the white oxide residue prior to each experiment involving the bulk electrode. This would explain the lesser analytical performance of the BiBE compared to the Bi-BDD electrode at the lower concentrations of analyte.

5.3.2 Electroanlaysis at the Sb-BDD electrode

5.3.2.1. Characterisation of the antimony modified BDD electrode

Due to the environmental toxicity and health risks associated with antimony, it was desirable to use as low a concentration of the metal as was viable. The electrochemical response of antimony on the BDD electrode was first investigated at increasing concentrations, to establish a suitable 'standard' antimony concentration. 0.5 mgL^{-1} additions of Sb were made to a 0.1 M HCl (ca. pH 1) solution, and deposited at -1.1 V for 120 s under stirring. From concentrations of 0.5 to 2.5 mgL^{-1} a single stripping peak for antimony was observed at ca. 0.05 V vs SCE, corresponding to the three electron oxidation of Sb^0 to Sb (III). Given the highly acidic pH (<1) of the electrolyte, this corresponds to the following reaction in accordance with the Pourbaix data [46] for antimony in aqueous media.

$$Sb + H_2O \rightarrow SbO^+ + 2H^+ + 3e^- \quad (5.1)$$

Figure 5.8 shows the voltammogram for 1.0 mgL^{-1} of antimony stripping from the BDD electrode. This concentration was used as the optimum concentration for antimony deposition. Using the peak area under the antimony stripping peak and Faraday's Law we

calculate that approximately 2.7 ng of antimony was stripped from the BDD electrode surface, which is almost a factor of 10 lower than the theoretical mass required to observe a monolayer on the electrode surface, therefore suggesting a nanoparticle modified surface.

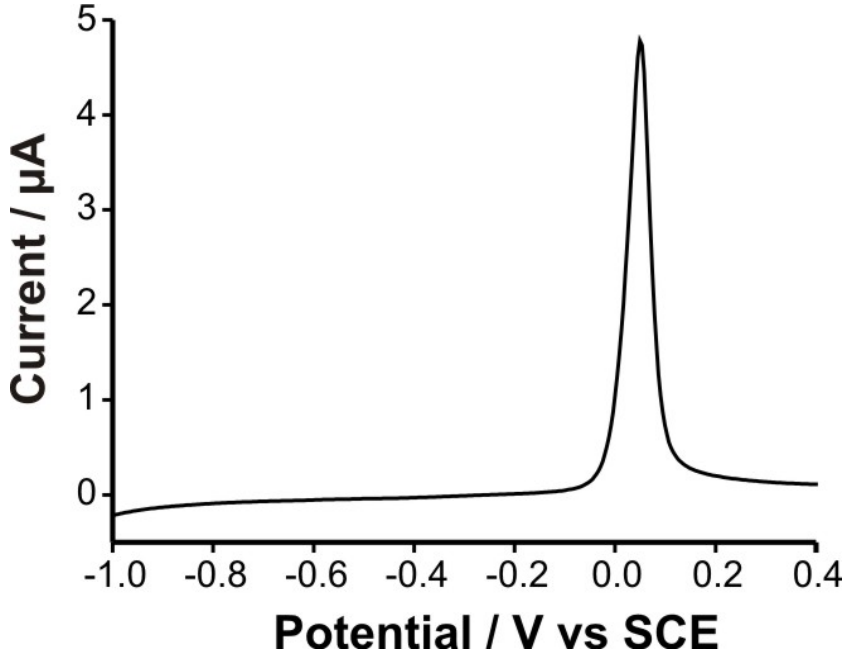


Figure 5.8: *LSV of 1 mgL^{-1} antimony in 0.1 M HCl stripping from a BDD electrode following stirred deposition at -1.1 V for 120 s, scan rate 50 mVs^{-1}*

The nature of the electrode surface following antimony deposition was characterized using ex-situ atomic force microscopy (AFM). The antimony was deposited onto the electrode at -1.1 V from a 1 mgL^{-1} Sb(III) in 0.1 M HCl solution, under stirring. The electrode was removed under potential, and dried at 40°C in an oven to evaporate any water. Figure 5.9 shows an image of the bare BDD surface, and subsequently a series of images after the antimony deposition (Figures 5.9b-d).

From the images in Figure 5.9 b-d it is evident that the antimony is present on the BDD surface as nanoparticles. The nanoparticles range in height from 3 nm to 110 nm with a mean height of 23± 10 nm, and the diameters range from 8.5 nm to 506.5 nm with a mean diameter of 108 ± 70 nm.

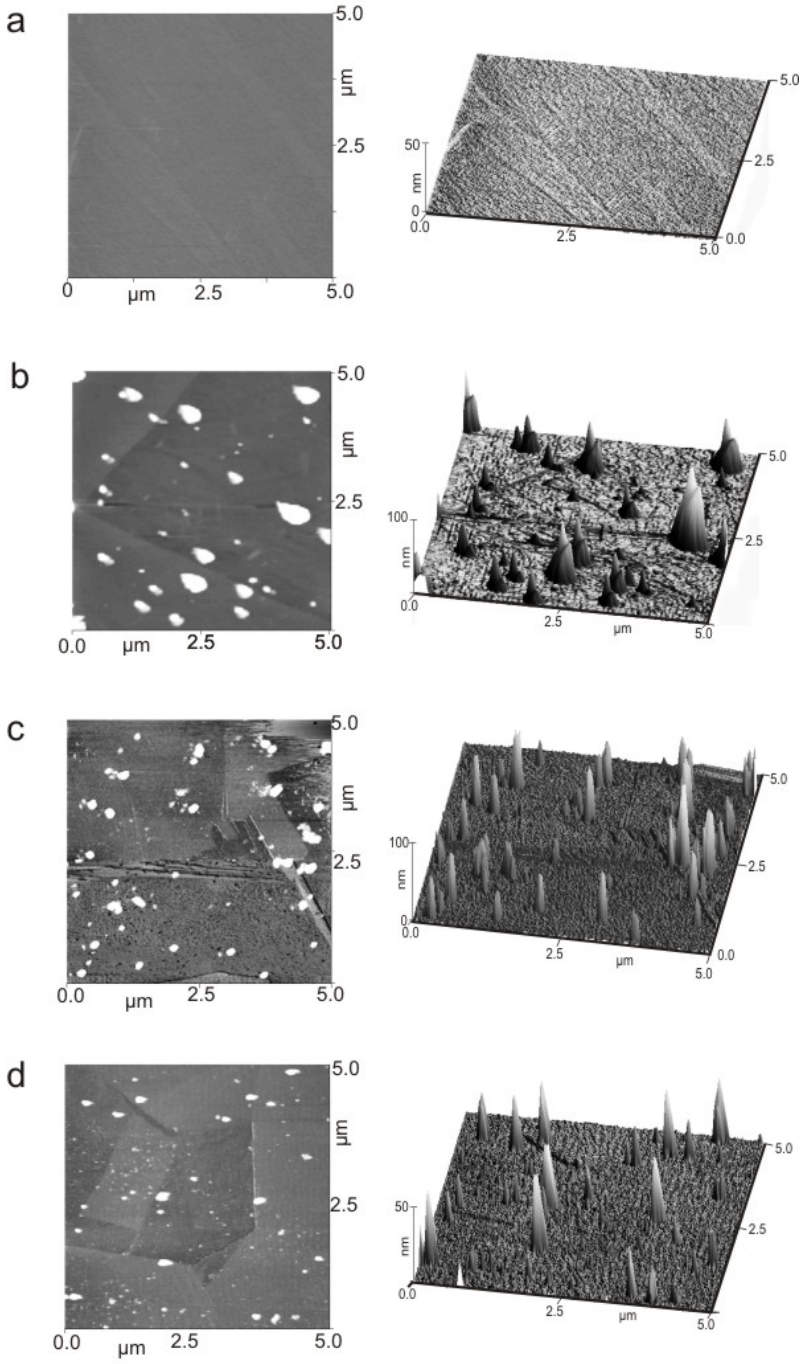


Figure 5.9: *Ex-situ AFM images of the BDD surface before (a) and after (b-d) antimony deposition from a 1mgL^{-1} Sb (III) in 0.1 M HCl solution, deposited at -1.1 V for 120 s under stirring.*

The low coverage of antimony across the surface is as expected given the mass of antimony calculated to be present from the stripping voltammetry data. Particle distribution and density varied considerably across the electrode surface, with some areas of few but

relatively large nanoparticles, and others with numerous but small particles. Based on the area of the particles multiplied by their height, a rough over-estimate of the mass of antimony per 25 μm^2 area is found between $5x10^{-14}$ g and $5x10^{-13}$ g. This value corresponds well to the average surface coverage of $1x10^{-14}$ g of antimony per 25 μm^2 area based on the voltammetric stripping data.

5.3.2.2 ASV of cadmium on the bare BDD and Sb-BDD electrodes

The linear sweep anodic stripping response of the BDD electrode, with and without the presence of Sb(III), toward the presence of Cd(II), was first investigated. The Cd(II) standard additions were made to a 0.1 M HCl (ca. pH 1) solution, at a bare BDD in the absence of any antimony, and also separately with 1 mgL^{-1} Sb(III) dissolved in the electrolyte for comparison. Overlays of the voltammograms for both cases, along with a standard addition plot of Cd (II) concentration versus peak area, are shown in Figures 5.10a and b respectively.

In both instances, the Cd (II) was not quantitatively detected on the electrode until a concentration of 150 μgL^{-1} was added, with the calibration plot becoming linear from approximately 250 μgL^{-1} over a 50 – 500 μgL^{-1} range. However the signal for the cadmium peak was almost tripled at a cadmium concentration of 500 μgL^{-1} when the antimony was present, with peak currents of 6.5 µA and 2.5 µA observed with and without antimony respectively. There was an overall positive shift in the peak position of ca. 25 mV in the Sb-modified BDD voltammetry, with the cadmium peak reaching a maximum at ca. -0.774 V vs. SCE compared to a potential of ca. -0.802 V vs. SCE without the antimony.

The shape of the cadmium peak remained the same in both situations, along with the detection limit of 150 μgL^{-1}. This is possibly due to the inability of Cd^{2+} to deposit onto the electrode surface in the highly acidic medium of pH 1, as Cd^{2+} has been observed on bare BDD at lower concentration levels in previous research under less acidic experimental conditions . The effect of the cadmium addition [56-58] on the antimony peak was evident

in the immediate decrease of the antimony peak from the first 50 μgL^{-1} cadmium addition however.

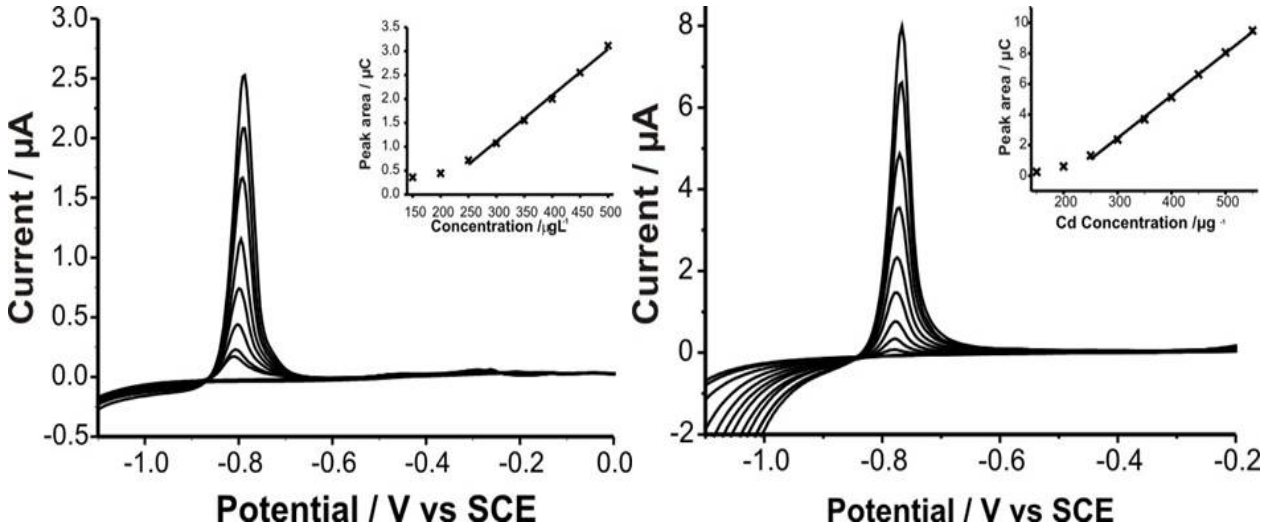


Figure 5.10:

a) *Overlay of LSVs at a bare BDD electrode in 0.1 M HCl following the standard additions of Cd^{2+} over a 50-500 μgL^{-1} concentration range. Stirred deposition at -1.1 V for 120 s, scan rate 50 mVs^{-1}. Inset: Calibration plot of peak area versus Cd concentration*

b) *Overlay of LSVs at a Sb-modified BDD electrode in 0.1 M HCl containing 1mgL^{-1} Sb following the standard additions of Cd^{2+} over a 50-550 μgL^{-1} concentration range. Stirred deposition at -1.1 V for 120 s, scan rate 50 mVs^{-1}. Inset: Calibration plot of peak area versus Cd concentration*

5.3.2.3 Linear sweep ASV of lead on the bare BDD and Sb-BDD electrodes

The 50 μgL^{-1} additions of Pb(II) to both the bare BDD and Sb-BDD gave a stripping peak from the first 50 μgL^{-1} addition and linear calibration plot through to 500 μgL^{-1}. These are shown in Figures 5.11a and b

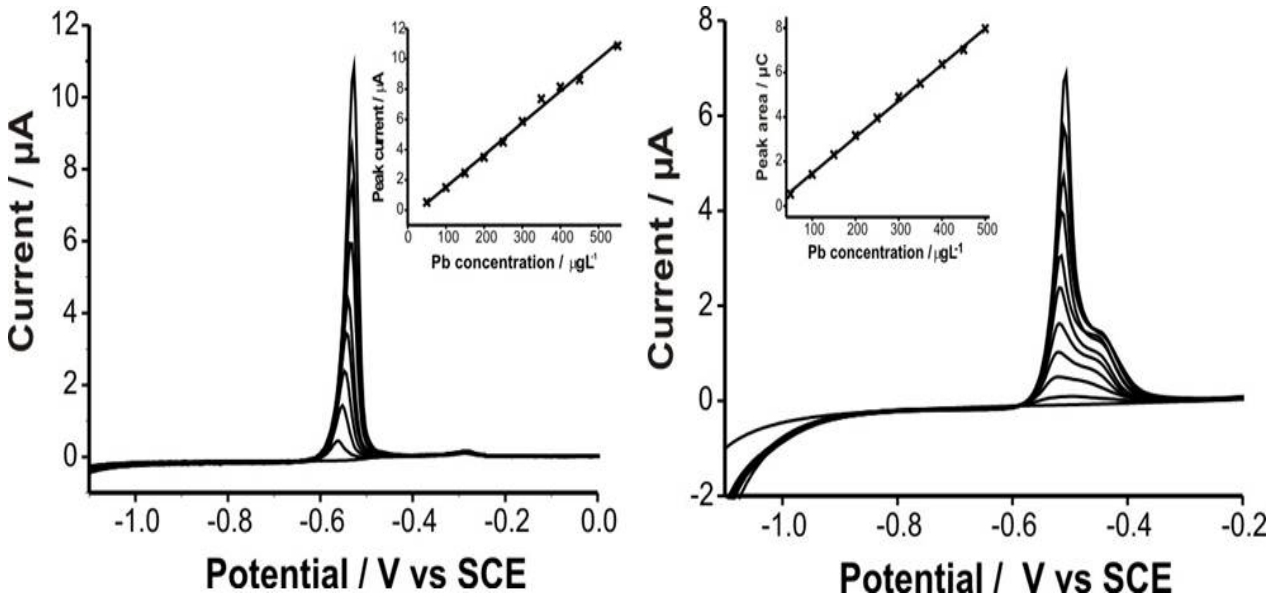


Figure 5.11:

a) *Overlay of LSVs at a bare BDD electrode in 0.1 M HCl following the standard additions of Pb^{2+} over a 50-550 μgL^{-1} concentration range. Stirred deposition at -1.1 V for 120 s, scan rate 50 mVs^{-1}. (Inset): Calibration plot of peak area versus lead concentration*

b) *Overlay of LSVs at a Sb-modified BDD electrode in 0.1 M HCl containing 1mgL^{-1} antimony following the standard additions of Pb^{2+} over a 50-500 μgL^{-1} concentration range. Stirred deposition at -1.1 V for 120 s, scan rate 50 mVs^{-1}. (Inset): Calibration plot of peak area versus lead concentration*

On the bare BDD, in 0.1 M HCl, a single peak was observed at ca. -0.545 V vs. SCE. The corresponding peak area calibration plot for the additions was linear (R^2 0.994) and gave a limit of detection (3σ) [55] of 41.8 μgL^{-1}.

In the presence of antimony however, the lead stripping peak has a definite shoulder, centred approximately 50 mV positive of the main peak. The presence of the shoulder or second merged peak is indicative of alloying between the lead and antimony. Alloying between these metals is well documented [18-20, 59], with the two forming a strong and durable material. Due to the co-deposition of the lead and antimony it is possible that the

stripping of Pb and Pb/Sb alloy is being observed in this double peak. A calibration plot of the whole peak area versus lead concentration gives a highly linear plot over the 50 – 500 μgL^{-1} range (R^2 0.999) and a limit of detection of 18.5 μgL^{-1}. Again, an overall positive shift in the lead peak of approximately 30 mV was observed in the presence of antimony.

5.3.2.5 LSASV of Cd and Pb simultaneously detected on the bare BDD and Sb-BDD

Following the detection of lead and cadmium on bare and Sb-BDD individually, the simultaneous detection of the two analytes was attempted. First, 50 μgL^{-1} additions of both Pb^{2+} and Cd^{2+} were made to the 0.1 M HCl solution, and deposited at -1.1 V for 120 s under stirring as before. An overlay of the subsequent voltammograms are shown in Figure 5.12a, in which it is evident that only one peak corresponding to the lead is observed. This is consistent with the observations in $HClO_4$ described above in the bismuth set of results. The calibration plot of lead concentration versus peak area is linear over the 50 – 500 μgL^{-1} range (R^2 0.997) and has a limit of detection of 25.7 μgL^{-1}.

In the presence of 1 mgL^{-1} antimony in the 0.1 M HCl however, both the Cd (II) and Pb (II) were observed. The cadmium was detected from a concentration of 100 μgL^{-1} in the 50 -500 μgL^{-1} range giving a linear calibration plot (R^2 0.995) and a limit of detection of 38.1 μgL^{-1}. The peak potential was the same as previously observed in the antimony condition, ca. -0.774 V vs SCE. The lead was detected from the first 50 μgL^{-1} cadmium and lead addition, with a plot of the whole peak giving a linear calibration plot (R^2 0.997) over the 50-500 μgL^{-1} range, and a limit of detection of 25.4 μgL^{-1}. Again, two convoluted peaks were observed for the lead, at ca. 90 mV apart, with the dominant peak in the same position, ca. -0.510 V vs SCE as in the previous lead and antimony condition. Further, the sensitivity of the lead detection was improved by the antimony modification, with a peak current of 11.67 µA observed in the presence of antimony compared to 8.92 µA without antimony at 500 μgL^{-1} of lead and cadmium.

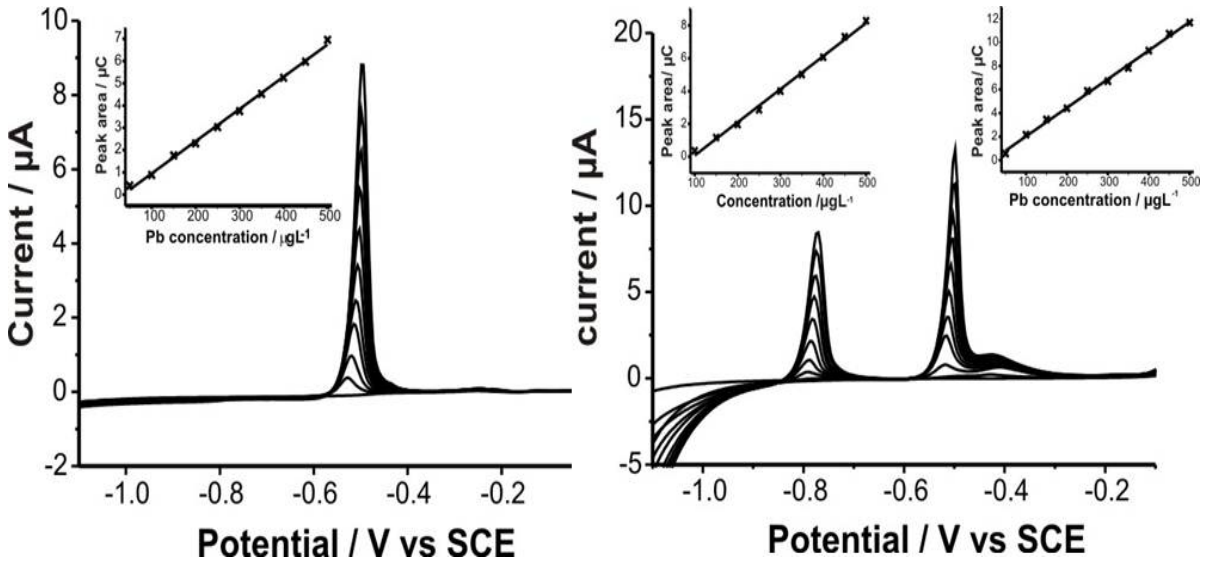


Figure 5.12:

a) *Overlay of LSVs at a bare BDD electrode in 0.1 M HCl following the standard simultaneous additions of Cd^{2+} and Pb^{2+} over a 50-500 μgL^{-1} concentration range. Stirred deposition at -1.1 V for 120 s, scan rate 50 mVs^{-1}. (Inset): Calibration plot of peak area versus lead concentration*

b) *Overlay of LSVs at a Sb-modified BDD electrode in 0.1 M HCl containing 1mgL^{-1} Sb following the standard simultaneous additions of Cd^{2+} and Pb^{2+} over a 50-500 μgL^{-1} concentration range. Stirred deposition at -1.1 V for 120 s, scan rate 50 mVs^{-1}. (Inset): Calibration plot of peak area versus cadmium and lead concentration*

5.4. Conclusions

The use of bismuth or antimony to modify boron doped diamond electrodes for improved simultaneous detection of cadmium and lead has been presented. Bi-modified boron doped diamond electrodes have been presented as a promising and reliable analytical candidate for the detection of low concentration heavy metals. The comparison of a bare BDD electrode and bismuth modified electrode has shown that the presence of bismuth allows the detection of lead to a 10 fold lower detection limit of 1.9 μgL^{-1}, and a 3 fold increase in peak current than the unmodified BDD electrode. Furthermore, cadmium may be simultaneously

detected on the bismuth array to a low detection limit of 2.3 μgL^{-1}, yet is not detected at all on the bare BDD electrode, even at relatively high concentrations of 200 μgL^{-1}. Further comparison of the nano Bi-BDD electrode with a bulk bismuth electrode confirms the positive influence of bismuth on the detection of cadmium. The performance of the Bi-BDD was much better than the BBiE however, indicating the benefits of a nanoparticle array as opposed to a polycrystalline bulk surface.

In this preliminary investigation, the detection of lead and cadmium as individual analytes was not improved by the presence of antimony, particularly evident in the case of cadmium, in which the metal remained undetectable to concentrations of 150 μgL^{-1} present. The low concentration of antimony did improve simultaneous detection of the cadmium and lead however, giving two well separated stripping peaks, compared to the bare BDD condition in which cadmium was not detected even at high concentrations of 500 μgL^{-1}.

This investigation has shown that a random nanoparticle array bismuth modified BDD electrode possesses many attractive properties and holds great potential for further development as a robust, sensitive and reliable electroanalytical tool. Analytically, the system offers the advantages of a simple and reproducible technique, a readily renewable Bi-modified electrode, a marked and clear separation of the analyte stripping peaks, limits of detection comparable to mercury electrodes, and is non-toxic and environmentally benign.

Although the detection limits were not necessarily improved using the Sb-BDD electrode, the low antimony concentration of 1 mgL^{-1} (8.21 μM), used in this investigation, did enhance the electroanalytical ability of the BDD electrode. Further research using higher concentrations of antimony that are comparable to other modified electrode systems, such as bismuth (0.1mM) and mercury film electrodes (>0.1 mM), is therefore necessary to discern the full capabilities of this antimony modified electrode. Unlike bismuth the use of antimony in this manner is very new to the field of metal electroanalysis, and therefore poses more questions with regard to diversity of application and enhanced metal deposition.

The in-situ EC-AFM results obtained, particularly in the staged process, have demonstrated an ability to control bismuth particle size on the BDD surface, an interesting feature of the electrode that has yet to be explored. This modified electrode has great potential for optimisation, and many experimental parameters have yet to be explored, therefore more detailed investigations are required to discover the true prowess of this new electrode. In the following Chapters BDD is used as a substrate for nickel nanoparticle modification, applying the system to the determination of various organic analytes.

5.5. References

[1] R.G. Compton, C.E. Banks, *Understanding voltammetry,* 1st edition, World Scientific, Singapore, **(2007)**.

[2] J. Wang, *Analytical electrochemistry,* 2nd edition, Wiley-VCH, New York ; Cambridge, **(1994)**.

[3] J.C. Ball, R.G. Compton, *J. Phys. Chem. B* **(1998)** 102, 3967.

[4] M. Branica, L. Sipos, S. Bubic, S. Kozar, *Natl. Bur. Stand. (U. S.), Spec. Publ.* **(1976)** 422, 917.

[5] A. De Santis, J. Marquez, L. Linares de Monsalve, *Ciencia* **(2005)** 13, 302.

[6] V.P. Gladyshev, S.V. Kovaleva, N.A. Khramtsova, *J. Anal. Chem.* **(2001)** 56, 443.

[7] S. Glodowski, Z. Kublik, *Anal. Chim. Acta* **(1979)** 104, 55.

[8] I. Karai, K. Fukumoto, S. Horiguchi, *Osaka City Med. J.* **(1980)** 26, 39.

[9] G. Mamantov, P. Papoff, P. Delahay, *J. Am. Chem. Soc.* **(1957)** 79, 4034.

[10] Z. Stojek, Z. Kublik, *J. Electroanal. Chem.* **(1979)** 105, 247.

[11] A. Economou, P.R. Fielden, *Analyst* **(2003)** 128, 205.

[12] J. Wang, J. Lu, U.A. Kirgoz, S.B. Hocevar, B. Ogorevc, *Anal. Chim. Acta* **(2001)** 434, 29.

[13] G.G. Long, L.D. Freedman, G.O. Doak, *in Encyclopedia of chemical technology,* R.E. Kirk and D.F. Othmer (Eds.), Wiley, New York, **(1978),** p. 912-937.

[14] A. Economou, *TrAC, Trends Anal. Chem.* **(2005)** 24, 334.

[15] S.B. Hocevar, I. Svancara, B. Ogorevc, K. Vytras, *Anal. Chem.* **(2007)** 79, 8639.

[16] K. Tyszczuk, M. Korolczuk, M. Grabarczyk, *Talanta* **(2007)** 71, 2098.

[17] Y.Q. Tian, N.B. Li, H.Q. Luo, *Electroanalysis* **(2009)** 21, 2584.

[18] A.A.A. Azim, K.M. El-Sobki, A.A. Khedr, *Corros. Sci.* **(1976)** 16, 209.

[19] S. Brinic, M. Metkos-Hukovic, R. Babic, *J. New Mater. Electrochem. Syst.* **(2005)** 8, 273.

[20] R.D. Prengaman, *J. Power Sources* **(2006)** 158, 1110.

[21] L.-. Chen, J.-. Yang, *Bull. Environ. Contam. Toxicol.* **(2007)** 78, 459.

[22] R. Poon, I. Chu, P. Lecavalier, V.E. Valli, W. Foster, S. Gupta, B. Thomas, *Food Chem. Toxicol.* **(1998)** 36, 21.

[23] L.K. Shpigun, V.K. Lunina, *J. Anal. Chem.* **(2003)** 58, 983.

[24] E.A. McGaw, G.M. Swain, *Anal. Chim. Acta* **(2006)** 575, 180.

[25] V. Rehacek, I. Hotovy, M. Vojs, F. Mika, *Microsyst. Technol.* **(2008)** 14, 491.

[26] J. Wang, *Electroanalysis* **(2005)** 17, 1341.

[27] A. Merkoci, M. Vasjari, E. Fabregas, S. Alegret, *Mikrochim. Acta* **(2000)** 135, 29.

[28] H. Nirmaier, M. Lauer, G. Henze, *Electroanalysis* **(1998)** 10, 326.

[29] J. Konvalina, E. Khaled, K. Vytras, *Collect. Czech. Chem. Commun.* **(2000)** 65, 1047.

[30] D. Demetriades, A. Economou, A. Voulgaropoulos, *Anal. Chim. Acta* **(2004)** 519, 167.

[31] R.T. Kachoosangi, C.E. Banks, X. Ji, R.G. Compton, *Anal. Sci.* **(2007)** 23, 283.

[32] X. Du, W. Gong, Y. Zhang, M. Wang, S. Wang, J. Anzai, *Sens. Lett.* **(2007)** 5, 572.

[33] J. Kruusma, C.E. Banks, R.G. Compton, *Anal. Bioanal. Chem.* **(2004)** 379, 700.

[34] A. Manivannan, R. Kawasaki, D.A. Tryk, A. Fujishima, *Electrochim. Acta* **(2004)** 49, 3313.

[35] C. Prado, S.J. Wilkins, F. Marken, R.G. Compton, *Electroanalysis* **(2002)** 14, 262.

[36] R.G. Compton, J.S. Foord, F. Marken, *Electroanalysis* **(2003)** 15, 1349.

[37] C.M. Welch, M.E. Hyde, C.E. Banks, R.G. Compton, *Anal. Sci.* **(2005)** 21, 1421.

[38] C.M. Welch, A.O. Simm, R.G. Compton, *Electroanalysis* **(2006)** 18, 965.

[39] Q. Chen, M.C. Granger, T.E. Lister, G.M. Swain, *J. Electrochem. Soc.* **(1997)** 144, 3806.

[40] C.M. Welch, R.G. Compton, *Anal. Bioanal. Chem.* **(2006)** 384, 601.

[41] F.W. Campbell, R.G. Compton, *Anal. Bioanal. Chem.* **(2010)** 396, 241.

[42] L. Balan, D. Burget, *Eur. Polym. J.* **(2006)** 42, 3180.

[43] J. Fang, K.L. Stokes, J. Wiemann, W. Zhou, *Mater. Lett.* **(2000)** 42, 113.

[44] Y.F. Kargin, S.N. Ivicheva, E.Y. Buslaeva, T.B. Kuvshinova, V.D. Volodin, G.Y. Yurkov, *Inorg. Mater.* **(2006)** 42, 487.

[45] R.N. Grass, W.J. Stark, *J. Nanopart. Res.* **(2006)** 8, 729.

[46] M. Pourbaix, *Atlas of electrochemical equilibria in aqueous solutions,* 2nd English edition, National Association of Corrosion Engineers ; Brussels : CEBELCOR, Houston, Tex : Brussels, **(1974)**.

[47] H.R. Pohl, H.G. Abadin, J.F. Risher, *Met. Ions Life Sci.* **(2006)** 1, 395.

[48] L. Barbu, E. Gheorghe, *Rev. Fiz. Chim.* **(2007)** 42, 27.

[49] S.B. Hocevar, I. Svancara, K. Vytras, B. Ogorevc, *Electrochim. Acta* **(2005)** 51, 706.

[50] G. Kefala, A. Economou, A. Voulgaropoulos, M. Sofoniou, *Talanta* **(2003)** 61, 603.

[51] E.E. Finney, R.G. Finke, *J. Colloid Interface Sci.* **(2008)** 317, 351.

[52] M.Y. Abyaneh, M. Fleischmann, *J. Electroanal. Chem.* **(2002)** 530, 89.

[53] N. Spataru, X. Zhang, T. Spataru, D.A. Tryk, A. Fujishima, *J. Electrochem. Soc.* **(2008)** 155, B264.

[54] J.S. Foord, W. Hao, K. Eaton, *Phys. Status Solidi A* **(2005)** 202, 2116.

[55] C.M.A. Brett, A.M.O. Brett, *Electroanalysis,* Oxford University Press, Oxford, **(1998)**.

[56] O. El Tall, N. Jaffrezic-Renault, M. Sigaud, O. Vittori, *Electroanalysis* **(2007)** 19, 1152.

[57] C. Babyak, R.B. Smart, *Electroanalysis* **(2004)** 16, 175.

[58] C.E. Banks, M.E. Hyde, P. Tomcik, R. Jacobs, R.G. Compton, *Talanta* **(2004)** 62, 279.

[59] A.A. Jenkins, W.C. Maskell, F.L. Tye, *J. Power Sources* **(1987)** 19, 75.

Chapter 6

Electrochemical non-enzymatic glucose sensors

The work presented in this chapter has been published in

International Journal of Electrochemical Science, **(2010),** 5, 1246

In this chapter an overview of glucose sensors is presented, with specific focus on the promise of non-enzymatic electrochemical glucose sensors. The mechanisms for catalysis are evaluated, and the future of the systems discussed. The review chapter addresses the merits and shortfalls of non-enzymatic electrodes with respect to their commercially available enzymatic counterparts, in anticipation for the following chapter in which a non-enzymatic nickel modified boron doped diamond electrode is applied to glucose analysis.

6.1. Introduction

The clinical conditions of diabetes mellitus are well known and well understood, yet remain a growing concern as the prevalence of the disease increases worldwide at an alarming rate. A number of life-threatening and life-impeding conditions greatly affect the diabetic community, resulting in a much greater risk of cardiac, nervous, renal, ocular, cerebral and peripheral vascular diseases. It was estimated that 2.8 % of the world population was affected by diabetes in 2000, approximately 171 million people [1]. By 2030 however, this is projected to more than double, with 366 million people suffering from the disease globally [1]. Treatment has become a far more sophisticated science, with self-testing

becoming increasingly more compact and accurate, and continuous glucose monitoring now obtained from practical commercial sensors. Glucose sensors are therefore a highly active area of sensor research, and accordingly they account for approximately 85% of the biosensor industry [2].

Sensitive and selective glucose sensors are not only relevant for use in blood sugar monitoring, but also in the food industry, bio-processing and in the development of renewable, sustainable fuel cells. Non-enzymatic glucose electrodes used in direct oxidation show considerably greater sensitivity, with oxidation currents as high as mA mM^{-1} cm^{-2} now being reported [3]. However, the superior selectivity and relative non-toxicity of enzyme based electrodes has retained the focus of commercially available glucose sensors on enzymatic systems.

Over the past decade the development of non-enzymatic glucose sensors has risen at a considerable rate. The fabrication of a wide variety of nanomaterials has introduced a plethora of selective and highly responsive glucose sensors. In 2005 Park et al [4] published an excellent and authoritative review regarding the development of non-enzymatic glucose sensors. Yet, in the 5 years since, over 80 glucose sensors have been reported (Tables 1, 2 and 3), and a further 60 publications report possible non-enzymatic materials that may be developed and used for glucose sensing. Research into this area of sensing is therefore evidently in full force, and in this review we hope to assess the current situation with respect to the practical application of non-enzymatic glucose sensors we note. In 2008 two extensive critical reviews of *enzymatic* electrochemical glucose sensors were published by Heller and Feldman [5] and by Wang [2]. As such, enzymatic systems will be briefly discussed herein, but the reader is encouraged to read the latter two reviews for more substantial understanding and detail.

6.2. Enzymatic glucose sensors

Enzymatic glucose sensors dominate the biosensing industry, particularly with the ever advancing development of self-testing and continuous blood glucose monitoring. The first enzymatic glucose sensors were introduced by Clark and Lyons in 1962 [6], in which oxygen consumption was monitored based on the catalytic oxidation of glucose in the presence of oxygen. Problems with varying amounts of background oxygen led to further development of the oxygen sensor by Updike and Hicks [7] which corrected for background oxygen levels. The first amperometric enzyme glucose sensor was developed in 1973 [8], in which the anodic production of hydrogen peroxide was analysed instead of the highly variable oxygen reduction current. Since this ground work the field of glucose sensors has progressed rapidly with increasingly innovative, efficient, and superior electrochemical technology being developed every year.

Originally, and until relatively recently, the enzyme glucose 1-oxidase (GOx) was the main catalytic component used in enzymatic biosensors. It was described as the 'ideal enzyme' for glucose oxidation in the review by Wilson and Turner [9] in 1992, owing to a relatively high selectivity, sensitivity and stability, compared to other enzymatic materials. The key component of the large protein molecule is the redox centre, flavin adenine dinucleotied (FAD). The flavin group is reduced on interaction with glucose, thus producing the redox product of glucolactone, in accordance to Eq. 6.1.

$$\mathrm{GOx(FAD)} + \mathrm{glucose} \rightarrow \mathrm{GOx(FADH_2)} + \mathrm{glucolactone} \qquad (6.1)$$

This redox centre is deep within the enzyme however, protected by a thick protein layer. As such electron transfer to the active centre is a major limiting factor, and the cause for complicated electron transfer mechanisms. To date, three approaches are in place to oxidise the reduced $FADH_2$ centre, catalytically regenerating it either by reducing naturally present oxygen, reacting with a mediator, or direct oxidation by the electrode. As such, enzymatic

glucose sensors are discussed with respect to their regeneration mechanism, as will be observed in the following sections. They are also summarized in Figure 6.1.

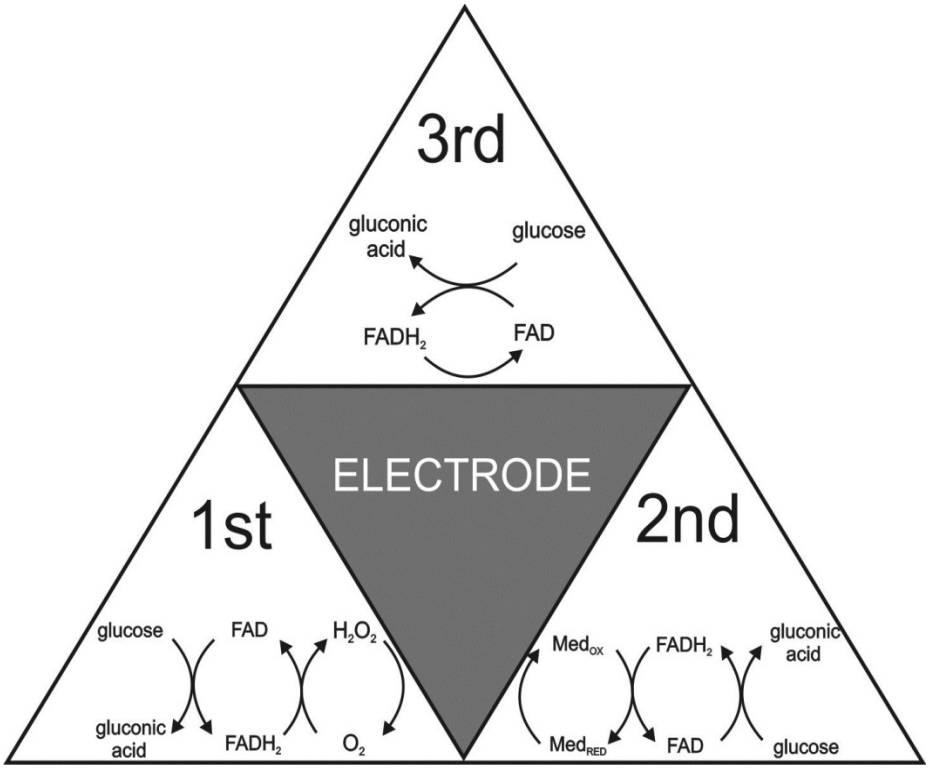


Figure 6.1: *Summary of enzymatic glucose oxidation mechanisms, presented as first, second and third generation sensors*

6.2.1 First generation enzymatic glucose sensors

First generation glucose biosensors are dependent on the presence of oxygen as a co-substrate to ensure the catalytic regeneration of the FAD centre. The consequent reaction is shown in Eq. 6.2, and is the immediate process to follow Eq. 1 above.

$$\mathrm{GOx(FADH_2)} + \mathrm{O_2} \rightarrow \mathrm{GOx(FAD)} + \mathrm{H_2O_2} \qquad (6.2)$$

The original Clark oxygen electrode used depletion of oxygen as a guide to glucose oxidation, the approach used in the fabrication of the first commercial glucose biosensor by Yellow Spring Instrument Company in 1975. Two years prior to this however, an amperometric approach to glucose determination was proposed by direct measurement of the hydrogen peroxide produced [8]. This offered a more simple, precise and selective

approach to blood glucose testing as interference by background oxygen was eliminated, and the sensing of hydrogen peroxide at the anodic potential of 0.6V vs. SCE, gave a current directly proportional to the glucose concentration. The oxygen was regenerated in the oxidation of the peroxide, thus replenishing the oxygen electron mediator.

First generation glucose electrodes face two major problems however; the presence of electroactive interference species in the blood and the dependence on free oxygen as a catalytic mediator. The former problem is addressed more thoroughly in Section 4 of this review, but in short the potential range at which hydrogen peroxide is oxidised coincides with the oxidation potential of numerous compounds found in blood. These are listed in Table 4, alongside their normal human blood levels. Furthermore, the frequent use of a modified platinum electrode leaves the sensor open to fouling by blood proteins and adsorptive inhibition by chloride ions. As such various approaches to avoid interference effects have been undertaken and these are discussed later on.

The oxygen dependence of first generation enzyme glucose sensors is a problem specific to this generation. The errors surrounding this high dependence on oxygen to mediate regeneration of the catalytic centre are quite significant, as oxygen levels can vary considerably. There is an oxygen limitation in which there is quite simply not enough oxygen available in a real blood sample to efficiently maintain glucose oxidation, thus this oxygen deficit has a great impact on accurate determination of glucose levels. A number of ways to address this deficit have been suggested and demonstrated, yet all involve overcomplicating the fabrication method and enlarging the overall sensor. Approaches include the use of a two-dimensional cylindrical electrode which doubles the oxygen input relative to the glucose input [10], the use of films that limit specific diffusion, allowing more oxygen relative to glucose through the film [11], and also the use of oxygen rich electrode materials which act as an internal source of oxygen for the reaction [12,13].

6.2.2 Second generation enzymatic glucose sensors

Due to the major problem of oxygen dependence observed in first generation enzymatic glucose sensors, the use of alternative co-substrates was introduced. Synthetic, electron-accepting mediators are utilised to facilitate electron transfer, with their consequent re-oxidation by the electrode resulting in a quantifiable amperometric current. A number of non-physiological mediators have been reported including ferrocene derivatives [14,15] and ferricyanide [16] of which most commercial sensors use, quinones [17,18] and transition-metal complexes [19]. Each of these mediators possess a number of essential attributes that idealise them for enzymatic glucose analysis. These include a low molecular weight and insoluble nature so as to effectively diffuse without complexing, a reversible or quasi-reversible properties, a suitably lower redox potential to avoid oxidation of interfering species, a high stability and resistance to forming side compounds, and a low toxicity (particularly where in vivo use would be required).

Unfortunately, problems still remain when using a mediator. Being small, diffusive molecules, maintaining the presence of the mediator near the electrode and enzyme surface is very difficult, particularly over relatively prolonged use, thus requiring elaborate and complicated methods of tethering the mediator to the two entities [16-20]. Although the mediator ideally reacts with the enzyme at a considerably faster rate than oxygen, the possibility of dissolved oxygen also competing with the mediator is highly likely, thus reducing the efficiency of the system and causing a build-up of hydrogen peroxide. It is also possible for the mediator to react with interference species present in the blood, further affecting the accuracy and efficiency of the analytical system.

In recent years, the most innovative enzymatic glucose sensor to have been developed is that developed by Heller et al with Abbott Diabetes Care [20]. The FreeStyle blood glucose monitoring system uses glucose dehydrogenase (GDH) as the enzyme as opposed to GOx, and an osmium redox mediator. The mediator is chosen in particular due

to its substantially negative formal potential of 0 to -0.2 V vs. Ag/AgCl, thus allowing a system of two parallel facing working and counter electrodes merely 50 μm apart. The oxidised Os^{3+} is thus unable to be reduced by the positively poised Ag/AgCl counter electrode, and current does not pass between the two electrodes directly. As such an astonishingly small sample size of 0.3 μL may be used, and effective bulk electrolysis of the glucose is achieved [20]. The continuous glucose monitoring system, FreeStyle navigator, more recently commercialised in 2007, utilises a very new patented technology of wired enzymes [20-22]. GOx is once again selected as the oxidising enzyme, and is 'wired' to the electrode surface using a redox hydrogel consisting of a polymer bound osmium redox mediator. It is a non-diffusive approach which addresses one of the main issues of second generation enzymatic glucose sensors [20].

6.2.3 Third generation enzymatic glucose sensors

Third generation enzymatic glucose sensors involve direct electron transfer between the enzyme and the electrode, without the need for natural or synthetic mediators. This is an ambitious type of enzymatic glucose sensor, yet in recent years it has become increasingly realistic. Achieving mediator free electron transfer between the electrode and redox enzyme is of great fundamental interest. It would be a more perfect system, as the complications of tailored mediators would be avoided, and selectivity and sensitivity could be very high and unhindered.

As mentioned previously, the biggest difficulty in achieving direct electron transfer between the electrode and enzyme is the thick protein in which the redox active centre is embedded. Mediators and glucose access this centre by means of diffusion and penetration of the 3D molecular network, yet this is not possible at a perfect planar electrode. In recent years however, rapid advancement in the development of nano and porous materials have grossly increased electrode surface areas and dynamics [23-25]. Mesoporous electrode

materials are of particular interest [23,24], offering an electrode surface that entraps and encompasses the enzyme. As such direct electron transfer from enzyme to electrode can occur, and a current corresponding to enzyme oxidation may be directly observed, without the complications of mediators, the intrusion of electroactive interferences, or the dependence on dissolved oxygen. This does not necessarily resolve the interference effects of dissolved oxygen competing with the electrode to regenerate the enzyme, but the impact can be considerably lower.

Other approaches reporting the mediator-free oxidation of GOx and other enzymes include the use of an over-oxidised boron doped diamond electrode (BDDE) [26] in which the surface carboxyl groups covalently bond to the enzyme through glutaraldehyde, over-oxidised TTF-TCQN[1] salts in a tree-like crystal growth on a platinum electrode [27], and an electro-conductive screen printed polymer membrane [28], though the latter may be deemed a second generation enzyme electrode given that the poly(pyrrole) essentially mediates electron transfer.

6.2.4 The advantages and disadvantages of enzymatic glucose electrodes

Overall, enzymatic glucose sensors remain a balance of advantages versus disadvantages of which both are significant. Despite dominating the glucose sensor industry, enzymatic systems have a number of critical flaws. First generation sensors suffer a high oxygen dependency, and are therefore immediately unsuitable for practical and reliable analytical use. Furthermore, their sensory ability is highly impacted by the presence of other electroactive interferences in the sample that are always commonplace in real blood samples. To overcome this, second generation sensors have utilized synthetic mediators as opposed to oxygen, achieving oxygen independence and a lower amperometric potential thus avoiding some electroactive interferences. In compensating however, the electrodes have become even more elaborate, and complicate mass production of a reproducible

[1] poly(pyrrole)/tetrathiafulvalene-tetracyanoquinodimethane

sensor. Finally, third generation sensors are still in their infancy, yet evidence for working based on nano mesoporous electrode surfaces shows some promise [23-25].

Stability issues that surround enzymatic systems in all fields of science also hinder the development and application of enzymatic glucose sensors. Despite numerous attributes with respect to relative stability, GOx is still constrained to pH ranges of 2-8, temperatures below 44ºC [9,29,30], and ambient humidity levels [29,30]. Ensuring the stability of immobilized enzyme and mediator electrodes requires considerable attention, with elaborate fabrication processes of electropolymerisation [30], covalent cross-linking at a pretreated surface [31], sol-gel entrapment at the electrode surface [32], or even the electrochemical 'wiring' of enzymes to mediated polymer chains [20-22], ensuring greater fabrication costs lower reproducibility, and short-term stability. As diabetes continues to rise in developing countries, such high cost fabrication processes and short shelf-life of sensors become less viable.

Despite these problems, enzymatic glucose sensors remain commercially unchallenged. This is understandable given the high selectivity of the enzyme towards glucose. Fabrication by mass production has been possible, allowing for single-use disposable electrodes, due to the possibility of screen printing electrodes. Screen printed carbon electrodes are produced from a complex mixture of mediators, enzyme and conductive carbon with binders and stabilizers, such that the mediator is bound to the electrode surface along with the enzyme, and can still mediate electron transfer. The method was introduced in the 1990's by a number of groups [33,34].

6.3. Non-enzymatic glucose sensors

The use of non-enzymatic electrodes as glucose sensors potentially promises a fourth generation to analytical glucose oxidation. Instead of facilitating the needs of a fragile and relatively difficult enzyme however, non-enzymatic electrodes strive to *directly* oxidise

glucose in the sample. This is an ideal system that was first investigated a century ago by Walther Loeb [35] who electrochemically oxidised glucose in sulphuric acid at a lead anode. This occurred long before to the fabrication of the Clark oxygen electrode [6], though extensive research into the non-enzymatic approach actually coincided with enzymatic development [36,37]. Despite decades of research into non-enzymatic systems however, the problems associated with this approach have prevented the practical application of the sensors. This is mostly due to a lack of selectivity at the electrode, but also the slow kinetics of glucose oxidation at many 'bare' electrodes, fouling of the electrode by real sample constituents, and the limited number of systems that are applicable to physiological pH.

The following tables list most non-enzymatic glucose sensors and their electroanalytical properties reported in scientific literature upto early 2010. These tables are all presented with respect to electrode type, sensitivity, linear range, limit of detection and publication year. Table 1 lists the non-enzymatic glucose sensors that use fixed potential amperometric analysis, as would be used in physiological applications. Limits of detection are generally within the realm of blood glucose concentration (i.e. 2-10 mM), sensitivity varies with respect to surface structure and the catalyst used, with the development of nano-dimensioned materials in the last decade coinciding with a sudden surge in non-enzymatic systems.

Table 1: *Non-enzymatic glucose sensors that have only used fixed potential, chronoamperometric methods for electrochemical determination. Abbreviations are given at the foot of the table*

Electrode composition	Sensitivity (mA mM^{-1} cm^{-2})	Linear Range (mM)	LOD (µM)	Year	Ref.
POROUS LAYERS					
Ni film Au nanoporous	5.1	$1x10^{-3}$ - 10	not given	2009	[38]
Pt nanoporous	0.642	0.1 - 1.5	not given	2008	[39]
Pt nanoporous	0.291	1.0 - 10	not given	2008	[40]
Pt-Ir nanoporous	0.0937	1.0 - 10	not given	2008	[41]
Au 3D GFE[a]	0.0466	$5x10^{-3}$ - 10	3.2	2008	[42]
Pt nanoporous	0.0375	0.05 - 30	50.0	2008	[43]
Au porous	0.032	2.0 - 20	2.0	2007	[44]
Pt InvOp[b]	0.0313	$1x10^{-3}$ - 10	0.1	2005	[45]
Au macroporous film	0.0118	2.0 - 10	5.0	2007	[46]
C OM[c]	0.0108	2.5 - 5.0	20.0	2007	[47]
PtPb nanoporous on Ti	0.0108	1.0 - 16	not given	2008	[48]
Pt nanoporous	0.0017	1.0 - 10	97.0	2007	[49]
Pt nanoporous	0.00083	not given	not given	2008	[50]
NANOTUBES					
Pt-NC[d]-CNTs[e]	0.28	$2x10^{-4}$ - 12	0.2	2009	[51]
Cu nps/SWCNTs/GC	0.256	$5x10^{-4}$ - 0.5	0.3	2004	[52]
C SWCNT films	0.2486	0.01 - 2.16	10.0	2007	[53]
Pd-SWNTs	0.16	0.5 - 17	0.2	2009	[54]
Ni (II)-Qu[f]-MWCNT-IL[g]	0.0369	$5x10^{-3}$ - 2.8	1.0	2009	[55]
CuS2-nanocrystal-CNTs	0.035	$1x10^{-3}$ - 12	1.0	2009	[51]
MnO2/MWNTs	0.03319	0.01 - 28	not given	2008	[56]
PtRu/MWNTs	0.02826	1.0 - 15	25.0	2008	[57]
PtPb nps/MWCNT	0.0178	up to 11	1.8	2007	[58]
Cu-CNTs-GCE	0.01776	$7x10^{-4}$ - 3.5	0.2	2007	[59]
Pt/MWCNTs	0.01183	1.0 - 9 & 9 - 23	50.0	2008	[60]
PtRu/MWNT–IL/GC	0.0107	0.2 - 15	50.0	2009	[61]
SnO2-NC-CNTs	0.0099	$3x10^{-3}$ - 12	3.0	2009	[51]
CuS nanotubes	0.00784	0.05 - 5.0	not given	2008	[62]
Cu2O/MWCNT	0.00653	$5x10^{-5}$ - $5x10^{-3}$	0.1	2009	[63]
C MWCNTs	0.00436	$2x10^{-3}$ - 11	1.0	2004	[64]
Au NTA [h]	0.00113	1.0 - 42.5	10.0	2009	[65]
Pt-NTA	0.0001	2.0 - 14	1.0	2005	[66]
Pt-MWCNTs	not given	1.0 - 26.5	not given	2007	[67]
CoOx/MWCNT/GC	not given	0.15 - 5.0	70.0	2008	[68]
NANOPARTICLE					
Ni-BDD	1.04	0.01 - 10	2.7	2010	[69]
Ni nps on CFP [i]	0.4204	$2x10^{-3}$ - 2.5	1.0	2009	[70]

Cu nps/SWCNTs/GC	0.256	$5x10^{-4}$ - 0.5	0.3	2004	[52]
Ni mod CILE [j]	0.202	0.05 - 23	6.0	2009	[71]
Au nps ITO [k]	0.1835	$4x10^{-3}$ - 0.5	5.0	2009	[72]
Au nps on 3DSN [l]	0.179	$7.5x10^{-5}$ -$7.5x10^{-4}$	0.1	2006	[73]
Pt nps	0.1377	0.2 - 3.2	5.0	2007	[74]
Pt-xGnP [m]	0.0615	up to 20	1.0	2008	[75]
CuS2-nanocrystal-CNTs	0.035	$1x10^{-3}$ - 12	0.0	2009	[51]
PtPb nps/MWCNT	0.0178	up to 11	1.8	2007	[58]
Ni/GC-PtNPs-HT [n]	0.00144	up to 8	15.0	2007	[76][77]
NANOSTRUCTURES					
Ni/Ti nano	7.32	0.05 - 0.6	1.2	2008	[3]
Ni NWA[o]	1.043	$5x10^{-4}$ – 7.0	0.1	2009	[78]
CuO-NFs-GC	0.4313	$6x10^{-3}$ - 2.5	0.8	2009	[79]
CuO nanosphere/Nafion	0.40453	up to 2.55	1.0	2008	[80]
Cu nanobelt	0.0798	0.01 – 1.13	10.0	2009	[81]
Pt - 3D DPNs [p]	0.0121	1.0 - 20	1.2	2008	[82]
PtPb NWA	0.01125	1.0 - 11	8.0	2008	[83]
C BDD nanoforest	0.0081	up to 7.0	0.2	2009	[84]
Pt nps CNFs[q]	0.00052	2.0 – 20	not given	2010	[85]
CuO nanowires	0.00049	$4x10^{-4}$ - 2.0	0.049	2008	[86]
CuO nanorod	0.00045	0.01 - 0.1	1.2	2008	[87]
UNMODIFIED SURFACES					
Ni foil	0.67	0.01 - 10	1.8	2010	[69]
C graphite pencil	not given	$5.5\ x10^{-3}$ – 0.044	0.1	2009	[88]
INTERCALATED/IMPLANTED					
IrO2 in PbO2 matrix	$8.30\ x10^{-9}$	0.1 - 20	50.0	1997	[89]
Cu implanted BDD	not given	1.0 - 5.0	not given	2006	[90]
Cu/SAMs [r]	not given	$3x10^{-3}$ - 10	0.7	2006	[91]
Cu-TO[s]	not given	$2.5x10^{-4}$ - 8.0	0.1	2009	[92]
CHEMICALLY MODIFIED SURFACES					
Ni powder MCC [t]	$4.00\ x10^{-5}$	$5x10^{-4}$ - 5.0	0.1	2005	[93]
Ni(II)-curcumin	not given	$1x10^{-3}$ - 10	0.1	2006	[94]
Ni-Al-NO3 ldh [u]	not given	$7x10^{-4}$ -1.2	0.5	2009	[95]
NiCu/GC	not given	1.0 - 9.0	0.8	2009	[96]

List of abbreviations: a- gold film electrode, b- inverse opal, c- ordered mesoporous, d- nanocube, e-carbon nanotubes, f-quercetin, g- ionic liquid, h- nanotube array, i- carbon fiber paste, j- carbon ionic liquid electrode, k- indium tin oxide, l- three dimensional silicate network, m- exfoliated graphite, n- hydrothermal, o- nanowire array, p- dendritic platinum nanostructures, q- carbon nanofibers, r-self assembled monolayers, s- titanate, t- modified carbon ceramic, u- layered double hydroxide

In the medium of fixed potential amperometry coupled with flow injection analysis (FIA) and liquid chromatography (LC), non-enzymatic glucose sensors were found to be sensitive and durable electrodes, with the problems of selectivity and electrode fouling addressed by the use of chromatographic stages. These are shown in Table 2, and it can be seen that the limits of detection are considerably lower, and the electrodes are generally less elaborate.

Table 2: *Non-enzymatic glucose sensors that have used fixed potential, chronoamperometric methods for electrochemical determination coupled with separation stage such as liquid chromatography and flow injection analysis*.

Electrode composition	**sensitivity (mA mM^{-1})**	**Linear Range (mM)**	**LOD (μM)**	**Year**	**Reference**
POROUS OR INTERCALATED LAYERS					
Cu nanoporous	220	0.01 - 0.5	40.0	2009	[97]
Cu implanted BDD	6.4 x10^{-3}	0.001 - 0.05	1.50	2004	[98]
Ni implanted BDD	2.8 x10^{-3}	0.001 - 0.05	0.67	2004	[98]
Ni–AuBPE[a]	3.12x10^{-4}	1x10^{-4} - 2.0	0.031	2009	[99]
Ni-NDC	not given	5x10^{-5} - 0.5	0.02	2003	[100]
NANO-TUBE/PARTICLE/STRUCTURE					
Cu/CNT	0.602	5x10^{-4} - 1.8	0.10	2009	[101]
Bi-modified/Pt	0.35	0.0011 - 1.2	1.10	1996	[102]
Cu mps Au elect.	not given	4x10^{-5} - 0.7	8.0 x10^{-7}	1997	[103]
Au nanofract. film	not given	up to 57.5	0.75	2006	[104]
METAL / UNMODIFIED					
Cu wire	37.9	0.01 - 1.0	5.0 x10^{-6}	1997	[105]
Cu electrode	2.30	0.001 - 0.05	10.0	2004	[98]
Ni electrode	1.60	0.001 - 0.05	91.0	2004	[98]
Cu RDE[b]	2.30x10^{-3}	not given	1.0 x10^{-3}	2001	[106]
Ni	not given	0.1 - 2.5	40.0	2007	[107]
Ag	not given	0.001 - 1.0	2.0 x10^{-3}	1991	[108]
Au	not given	0.001 - 1.0	0.03	1991	[108]
Cu	not given	1x10^{-4} - 0.1	0.03	1991	[108]
Ni	not given	0.001 - 1.0	0.20	1991	[108]
Ni BPE	not given	3 orders of mag.	0.48	2008	[109]
Pt	not given	1x10^{-4} - 0.1	0.20	1991	[108]
Ni wire	not given	not given	5.90 x10^{-7}	1990	[110]
Cu	not given	2x10^{-10} - 1x10^{-6}	2.00 x10^{-7}	1996	[111]
Cu	not given	not given	5.90 x10^{-5}	1994	[112]
Cu/Cu(OH)2	not given	not given	2.36 x10^{-5}	1994	[112]
Ni	not given	not given	1.77 x10^{-4}	1994	[112]

Ni/Ni(OH)2	not given	not given	5.90 x10^{-5}	1994	[112]
Ni-MCH	not given	not given	2.50 x10^{-5}	1994	[113]
Ni(III) oxide	not given	not given	0.0944	1986	[114]
Au	not given	6x10^{-4} - 10	0.50	1988	[115]
Au with Nafion	not given	not given	0.025	1989	[116]
Pt	not given	0.02 - 0.5	20.0	2002	[117]
CHEMICALLY MODIFIED ELECTRODE					
Cu2O/CPE	0.215	not given	1.18 x10^{-6}	1991	[118]
Co/GC	0.01	5x10^{-4} - 0.5	5.31 x10^{-6}	1992	[119]
Ni-CME[c]/GC	8.60x10^{-3}	0.005 - 0.5	5.90 x10^{-6}	1995	[120]
RuOx-RuCN mv[d]	6.20x10^{-3}	0.3 - 20	40.0	2005	[121]
Ru02	6.30x10^{-4}	from 1x10^{-6}	1.60 x10^{-5}	1990	[122]
Ni tetra ruth porph	not given	0.0025 - 1.0	0.36	2005	[123]
Eastman-AQ[e]/Ni(II)	not given	0.010 - 50	5.00	1991	[124]
Cu- coated	not given	6.2x10^{-5} - 0.4	1.20 x10^{-6}	1989	[125]
Ni-CME GC	not given	0.0025 -0.1	2.50 x10^{-6}	1991	[126]
Co-modified GC	not given	not given	2.36 x10^{-4}	1994	[112]
Cu-modified GC	not given	not given	2.07 x10^{-4}	1994	[112]
Ni-modified GC	not given	not given	5.90 x10^{-5}	1994	[112]
ALLOY					
Ni-Ti alloy	2000	not given	5.00 x10^{-8}	1999	[127]
Ni-Cr-Fe	36.6	1x10^{-4} - 0.5	1.00 x10^{-6}	1993	[128]
Ni-Cr	30.0	1x10^{-4} - 1.0	5.00 x10^{-7}	1993	[129]
Ni-Cu	27.7	0.001 - 0.5	1.50 x10^{-5}	1993	[128]
Ni-Ti alloy	19.6	1x10^{-4} - 1.0	5.00 x10^{-5}	1994	[130]
NiCr	not given	0.001 - 1.0	0.033	2001	[131]
ELECTROCHEMICALLY DEPOSITED					
Cu oxide-CP	1000	1x10^{-8} - 1x10^{-6}	3.00 x10^{-6}	1994	[132]
Ni(OH)2/GC	13.80	not given	3.40	2009	[133]
Au /Cu bimetallic	0.24	4 orders of mag.	4.00 x10^{-6}	1998	[134]
Au-Ni(OH)2	0.0277	6x10^{-5} - 0.7	1.50 x10^{-6}	1999	[135]
Co/GC	not given	3x10^{-4} - 3.0	0.30	2003	[136]
Ni(CN)2 on Au	not given	6x10^{-5} - 0.2	3.30 x10^{-6}	2001	[137]
POLYMER AND COMPOSITE					
NiOx polymeric	0.27	0.1–1000	56.0	2002	[138]
Cu2O-CCE	2.56x10^{-3}	up to 5.0	8.00 x10^{-5}	1997	[139]
PVdF/PAPBA[f]-NFM [g]	2.00x10^{-3}	0.1 - 16	100	2007	[140]
Au /Nafion	2.34x10^{-4}	5.0 - 60	1200	2001	[141]
Cu/p-1-NAP[h]/GC	not given	0.001 - 0.5	5.00 x10^{-5}	2003	[142]
NiO-CP	non given	0.001 - 1.0	0.30	2007	[143]
PEG/Cu2O CPME	not given	0.001– 0.05	0.12	2007	[144]
Cu ions/p-1-NAP	not given	0.001 - 0.3	8.00 x10^{-5}	1999	[145]

List of abbreviations: a- barrel plated electrode, b-rotating disk electrode, c- chemically modified electrode, d-multivalent, e-anthraquinone, f- poly(vinylidene fluoride) poly(aminophenylboronic acid), g- nanofiborous membrane, h- poly-1-napthylamine

Table 3 lists the non-enzymatic electrodes that have used variable potential amperometric methods in their analytical approach such as potential sweep and pulsed voltammetry, therefore again losing the imposed selectivity and increased sensitivity of the FIA and LC.

Table 3: *Non-enzymatic glucose sensors that have used sweeping potential methods such as linear sweep, cyclic and square wave voltammetry for electrochemical determination.*

Electrode composition	sensitivity (mA mM^{-1} cm^{-2})	Linear Range (mM)	LOD (mM)	Year	Reference
POROUS/NANOTUBE/NANOPARTICLE/NANOSTRUCTURED					
Au nps on thin Au	0.16	0.5 - 8	0.50	2006	[146]
Au nano/Ti	0.14	1.0 - 15	0.0148	2009	[147]
Au nanowire array	0.04	0.1– 20	0.003	2009	[148]
Au nps on NH2-HSM[a]	0.0025 *	0.2 - 70	0.10	2007	[149]
Au-chitosan nps	not given	0.4 - 10.7	0.37	2009	[150]
BOx[b] nps MWCNTs	not given	1.5 $x10^{-3}$ - 0.26	8.00 $x10^{-4}$	2009	[151]
PdNPs func-CNTs	not given	5.0 $x10^{-4}$ - 0.04	9.00 $x10^{-5}$	2009	[152]
Au nps DHP[c] film/GC	not given	0.09 - 9.9	0.01	2007	[153]
METAL/UNMODIFIED					
C BDND[d]	0.1525	0.25 - 12	0.025	2009	[154]
C BDD micro & nano	0.1019	0.25 -10	25.0	2009	[155]
Ni DLC[e]	not given	1 $x10^{-3}$ - 0.45	not given	2009	[156]
BDD	not given	0.5 - 10	0.50	2005	[157]
Ni-BDD	not given	not given	not given	2009	[158]
ELECTROCHEMICAL MODIFICATION					
Au-chitosan nps	not given	0.4 - 10.7	0.370	2009	[150]
Ni/1-NAP [f]	not given	0.04–1.0	6.00 $x10^{-3}$	2004	[159]
NiOx PANI [g]	not given	1.0 - 100	not given	2007	[160]
POLYMER AND COMPOSITE/OTHER					
MIP Au	16.5 *	5 $x10^{-3}$ - 0.12	2.0 $x10^{-6}$	2009	[161]
Au-chitosan nps	not given	0.4 - 10.7	0.37	2009	[150]
Ni/1-NAP	not given	0.04 – 1.0	6.00 $x10^{-3}$	2004	[159]
CoPcTS [h]	not given	0.25 - 20	0.10	2008	[162]
MIP[i] Au/o-PDA [j]	not given	0.1 - 20	0.05	2001	[163]
Au nps DHP film/GC	not given	0.09 - 9.9	0.01	2007	[153]

List of abbreviations: a- amine functioned hexagonal mesoporous SiO_2, b- boron oxide, c- dihexadecyl hydrogen phosphate, d- boron doped nano diamond, e- diamond-like carbon, f- poly-1-napthylamine, g- polyanaline, h- cobalt (II) phthalocyanine tetrasulfonate, i- molecularly imprinted, j-phenylendiamine

* - these values are in units of mA mM^{-1}

Direct non-enzymatic electro-oxidation of glucose varies considerably depending on the electrode material used. Electrocatalytic processes are key to glucose oxidation, as it is otherwise a kinetically very slow process that would produce no discernable faradaic current at most commercial electrodes. This explains why direct glucose oxidation often does not adhere to scan rate dependent voltammetry, indicating a non-diffusion controlled process [4,164]. A number of electrode materials have been used over the past 60 years; some are more frequently used than others. The following sections discuss the electro-oxidation process for glucose at a number of electrodes, namely platinum, gold, nickel, copper and carbon electrodes.

6.3.1. The mutarotation of glucose

Glucose has three aqueous isomers denoted α-glucose (α-G), β-glucose (β-G) and γ-glucose (γ-G) shown in Figure 6.2.

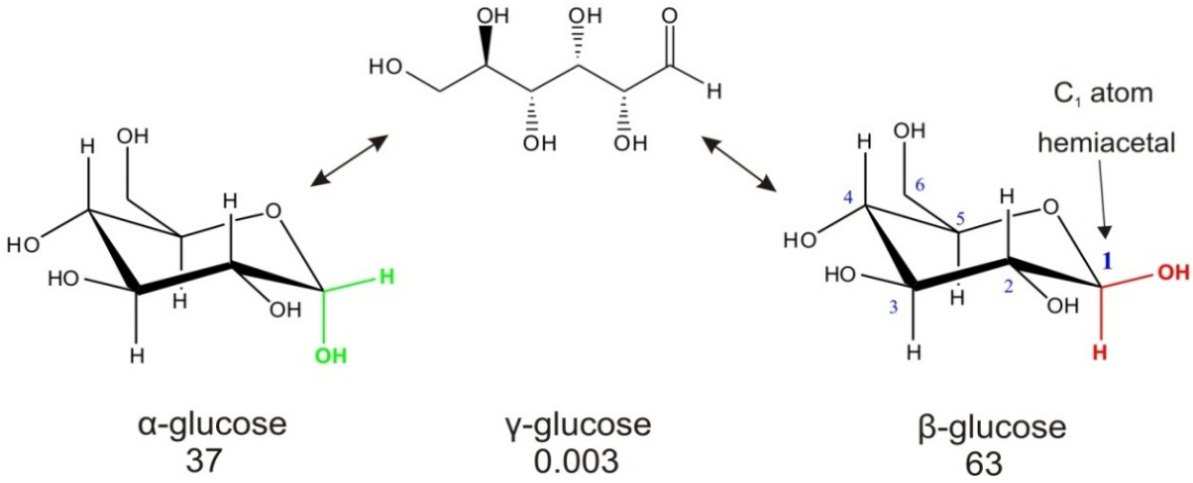


Figure 6.2: *The interconversion of glucose anomers (α, β and γ) and their relative ratio at pH 7. The hemiacetalic C_1 atom is highlighted to indicate the difference between the two anomers*

The former two species are the most abundant in solution, and correspond to cyclic hemiacetal forms. γ-G is an intermediate between the two cyclic groups, and corresponds to a linear, free-aldehyde form of the compound. When at equilibrium in water at room

temperature these isomers are present in the ratio of 37:63:0.003 for α, β and γ respectively [165], thus indicating that glucose is most stable in its cyclic form.

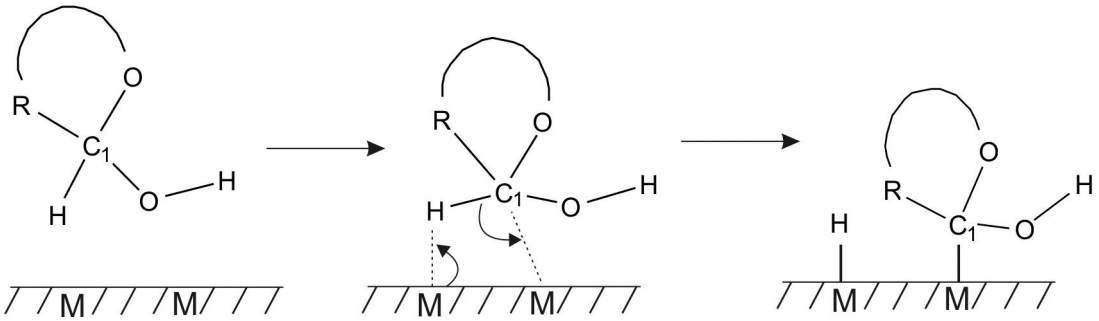
The enzymes GOx and GDH are anomer specific, responding only to β-G and as such an awareness of the ratio of α to β glucose in the blood is necessary. Glucose interconverts between the α and β form until a thermodynamic equilibrium is established. In water at pH 6.8 this can take over 2 hours at room temperature (ca. 24ºC) [166], and blood is found to have approximately the same ratio of glucose anomers as in water [167]. Mutarotation follows first order kinetics, the rate of interconversion increasing with temperature, yet the process is very slow, and even at temperatures of 45 ºC the ratio of α to β only shifts to ca 40:60 after equilibrating. As the cells uptake β-G in the blood for use in glycolysis, the equilibrium is actually maintained by mutarotases [168], enzymes secreted at the kidneys and liver that accelerate the interconversion of α to β glucose. As such, changes in temperature when conducting in-vitro analysis of blood is not a concern. The rate of mutaroation is acid base catalysed however, with alkaline solution shown to favour β-G in a 20:80 ratio of the anomers [165]. As such, the pH of a solution is highly important when conducting glucose tests that are to reflect the whole blood glucose concentration, as the physiological ratio of α to β glucose can shift significantly. Furthermore, an anomeric effect has been observed for glucose in which β-G is oxidised at a faster rate than α-G, suggesting a preferred orientation for glucose adsorption on platinum electrodes [165,169].

6.3. 2 Theories of non-enzymatic electrocatalysis

Non-enzymatic electrocatalysts come in a number of forms, specifically; metals (e.g. Pt, Au), metal oxides/ semiconductors (e.g. $Ni(OH)_2$, $RuO_{2,}$), alloys (e.g. PtPb, PtRu), complexes (e.g. cobalt phthalocyanine) and carbon based (e.g. carbon nanotubes, boron doped diamond). Apart from the latter all the catalysts listed are dependent on a transition metal centre. The process of electrocatalysis is generally observed to occur via the adsorption of the analyte to the electrode surface, a process that presumably involves the d-

electrons and d-orbitals of the metal substrate that allows it to form a suitable bond with the adsorbate [170]. This bond is required to form and break in the midst of the catalytic process, and as such a bond of intermediate strength would be ideal, so as not to limit adsorption or hinder desorption at any stage. The bond strength is dependent on the Gibbs energy of adsorption. Alternatively a change in bond strength may be imposed by a change in the metal oxidation state, which might alter the adsorbate-metal interaction and encourage desorption of the product [170].

The geometry of the electrode is also highly important, as is evident in numerous single crystal studies of glucose oxidation [171,172] and other organic molecules [170]. Pletcher suggested the catalytic process may occur via a concerted step, i.e. the process of hydrogen abstraction occurs simultaneously to the adsorption of the organic species. Indeed, the rate determining step in most glucose electro-oxidation experiments is deemed the removal of the hemiacetalic hydrogen atom [173] (see Figure 6.2), and the chemisorption of the analyte is generally considered to occur simultaneously. This would mean that adjacent metal active sites would be occupied by a single adsorbate at any time, in accordance with Scheme 6.1. As such, in the fabrication and study of electrocatalysts both electronic and geometric factors must be considered, so as to fully exploit the kinetic enhancements offered by well-spaced adsorption sites and increased surface area.



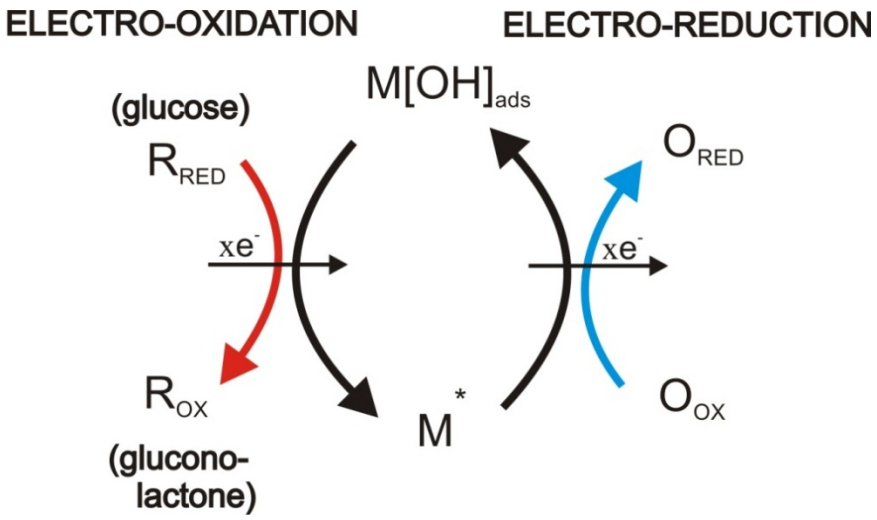
Scheme 6.1: *An illustration of the concentric adsorption theory with adjacent adsorption sites as proposed by Pletcher [44]*

The proposal of active transition metal centres across the electrode only explains the adsorption process onto the surface however, but fails to consider the oxidative role of hydroxyl radicals. It has been evident in numerous publications; [172-176] that electro-oxidation of glucose and many other organic molecules coincides with the onset of adsorbed OH_{ads}. Burke [177] discussed the importance of this hydrous oxide layer on the electrocatalytic process, and proposed the 'Incipient Hydrous Oxide Adatom Mediator' model (IHOAM). This was based on the observation that 'active' surface metals atoms undergo a premonolayer oxidation step that forms an incipient hydrous oxide layer of reactive OH_{ads} that mediate oxidation and inhibit reduction of kinetically slow electrode reactions. The active sites of the electrodes surface are considered to have a low lattice co-ordination value (LCN), and as such lack normal lattice stabilization energy. This occurs frequently across a polycrystalline surface at discontinuous areas such as grain boundaries and edges, and also across the surface generally due to direct exposure to the solution relative to the bulk crystal structure. Due to a lack of stability they are more reactive, and thus undergo premonolayer oxidation at lower potentials than thermodynamic surface oxidation predicts.

The catalytic importance of the active OH_{ads} layer was well known with respect to small organic compound oxidation, as the formation of the hydrous species was recognised as a fast, pre-oxidation step following chemisorption of the glucose molecule [164,169,174,178]. The hydrous premonolayer then mediates oxidation of the adsorbed species at potentials considerably lower to normal. This process is illustrated in Scheme 6.2.

Both the activated chemisorption model [170] and the IHOAM model [177] will be considered in the following sections regarding each main metal electrode individually. It seems that the IHOAM model is most apt for enhanced catalysis of the platinum group metals (i.e. platinum, ruthenium, iridium and palladium) and gold. This is possibly due to the majority of research regarding non-enzymatic electrocatalysis involving these metals

however. The hydroxyl group undoubtedly plays a role in the electrocatalysis of glucose at nickel and copper electrodes too, as seen later on, however in these cases an incipient hydrous premonolayer is not formed to induce catalysis, but an oxidation state change of the metal hydroxide.



Scheme 6.2: *A schematic of the IHOAM model in which* M^* *is the reductive metal adsorption site, and* $M[OH]_{ads}$ *is the oxidising adsorbed hydroxide radical. The scheme shows how both oxidative and reductive process are catalysed by the metal surface*

6.3.3 Nanomaterials in glucose sensors

Recent advances in the development of glucose sensors, enzymatic and non-enzymatic, revolve around the increase in the synthesis of nanomaterials. Nanoporous and microporous materials have raised particular interest, as is evident in Tables 1, 2 and 3, for non-enzymatic glucose sensors alone. Porous materials offer surfaces with a high surface to volume ratio. As such they have made an impact on several industries such as microelectronics, clean energy, environment, petroleum and gas, manufacturing and agriculture. A selection of nanostructured materials that have been used in non-enzymatic glucose sensing are shown in Figure 3.

For platinum and gold electrode the activity of the electrode is often considered in terms of its roughness factor, in which the greater the surface roughness, the greater the electrochemical activity. This is directly related to the need for active sites for adsorption as discussed by Pletcher [170] previously. Nanoscopic electrode materials impose a very high active surface area that is significantly greater than the geometric surface area, which is ideal for a kinetically controlled, surface bound reaction such as glucose oxidation. The active surface area of a porous platinum electrode has been shown to be up to 600 times greater than a planar polycrystalline platinum electrode [39], and as such kinetically diffusive interference reactions are negligible relative to the adsorptive reactions.

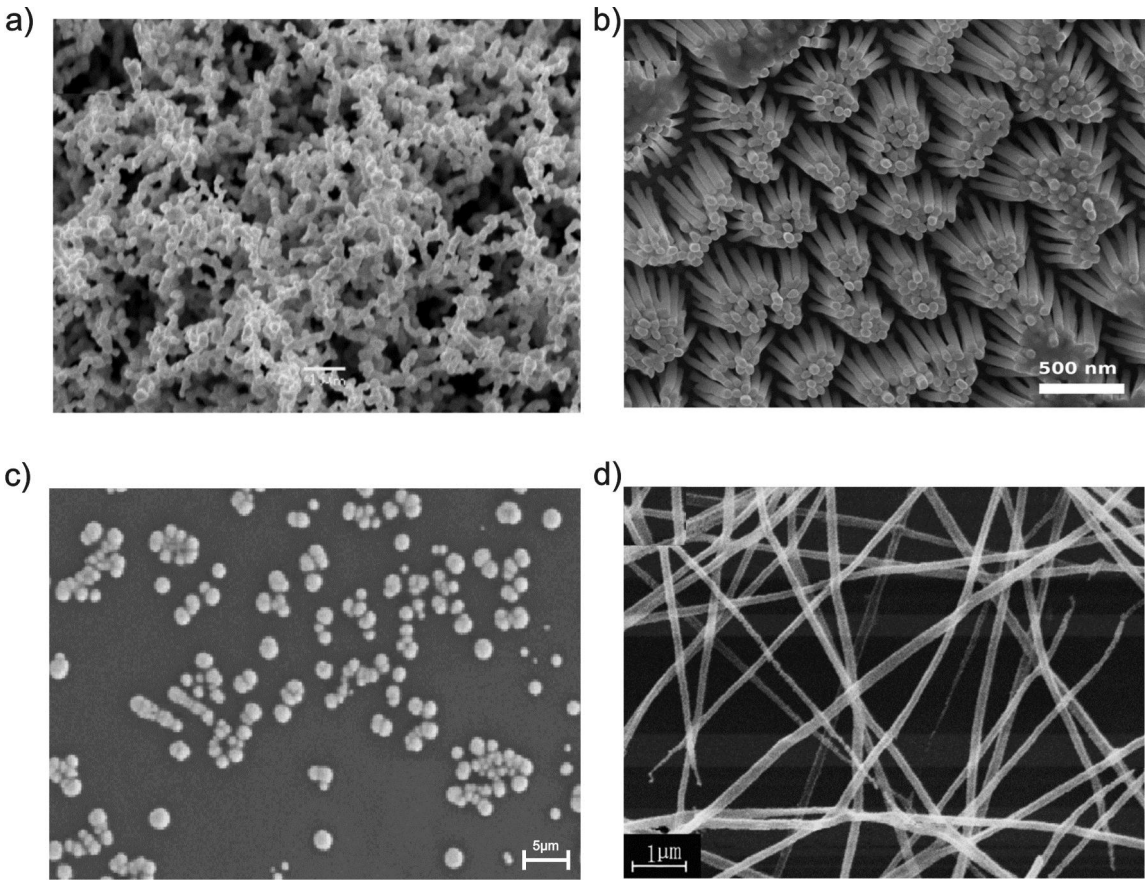


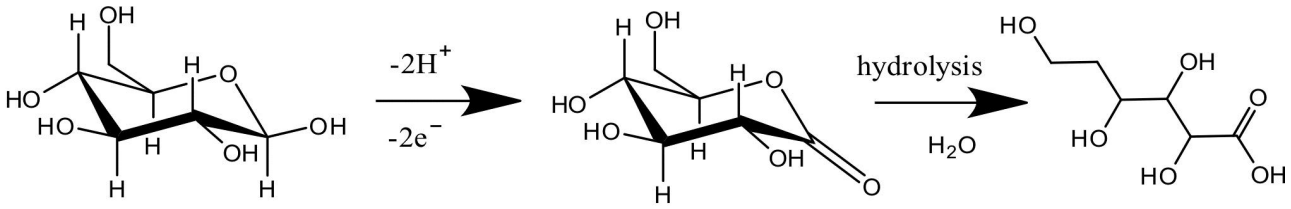
Figure 6.3: *A selection of nanostructured nonenzymatic electrode materials. a) PtPb nanoporous (from [77]), b)Au nanowire array (from [93]), c) Ni microparticles on BDD (from [106]) and d) CuO nanofibers (from [248]).*

The introduction of carbon nanotubes to enhance electrocatalysis also demonstrates the advantages posed by increasing surface area. Due to the intrinsic electronic properties of carbon nanotubes, modifying a planar electrode with the material produces a carbon electrode surface that is essentially porous, offers a very high surface area, and is very diverse with respect to modification and range of application. The use of surface modified carbon nanotubes is significant in the literature, as can be seen in Table 1 in which 20 electroanalytical reports of glucose electro-oxidation using carbon nanotubes are reported. Here we see carbon nanotubes decorated with nanoparticles of platinum [51,60], bimetallic platinum [51,57,58], copper [52,63] and nickel [55], all reporting a doubly enhanced response due to the carbon nanotubes and metal nanoparticles.

6.3.4 Platinum electrodes

6.3.4.1. Mechanism of glucose oxidation at platinum

A large amount of the work first investigating the direct electro-oxidation of glucose was performed at platinum electrodes [164,169,174,178-182]. Researchers have explored the behaviour of glucose at a platinum electrode in acid [179], neutral [164,178,180,181] and alkali [164] conditions.



Scheme 6.3: *The 2e⁻ oxidation of glucose to gluconolactone and further hydrolysis to gluconic acid*

A common conclusion from a number of authors was that the sole product of oxidation is gluco-δ-lactone, which hydrolyses to gluconic acid on standing, regardless of the solution pH (Scheme 6.3) [164,174]. However, spectrochemical evidence regarding intermediate adsorbates has frequently disagreed, suggesting reduced CO_2, CO_{ads} and fragments of the glucose molecule to also be present as oxidation products [169,181].

The cyclic voltammetry of glucose at a platinum electrode is reflective of the three distinct areas associated with platinum voltammetry, though it may vary significantly depending on electrolyte and temperature conditions. Investigation by Vasil'ev et al [164,174] and numerous other authors [169,172,178-182] all conclude that in the anodic sweep three oxidation peaks are observed. A typical cyclic voltammogram of glucose on a platinum electrode at pH 7 is shown in Figure 6.4 (edited from ref [182]) with each peak numbered, including the two cathodic oxidation peaks 4 and 5.

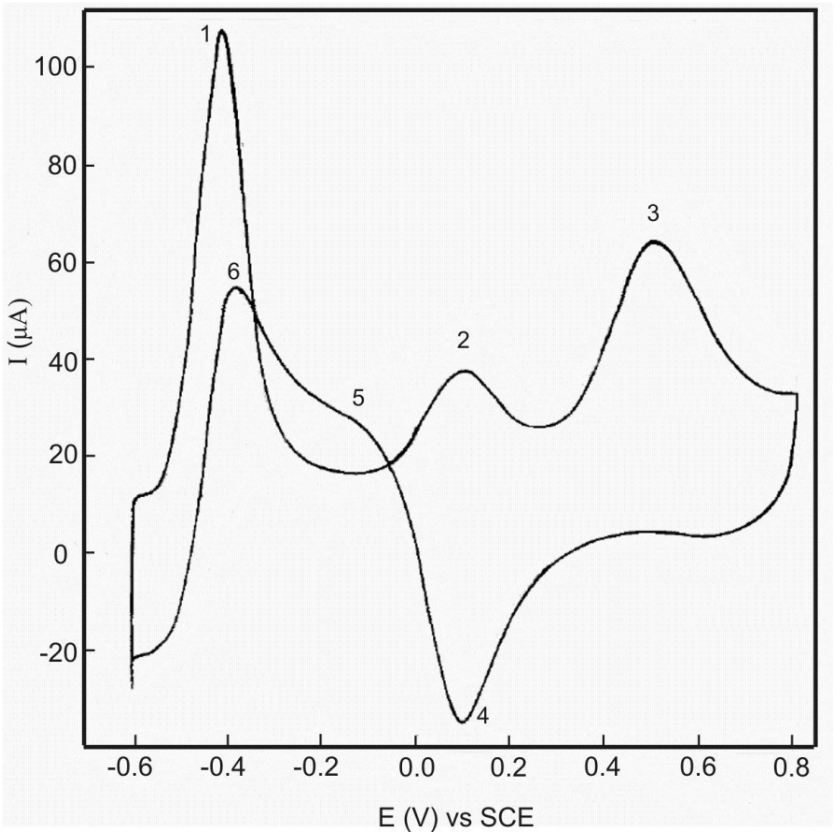


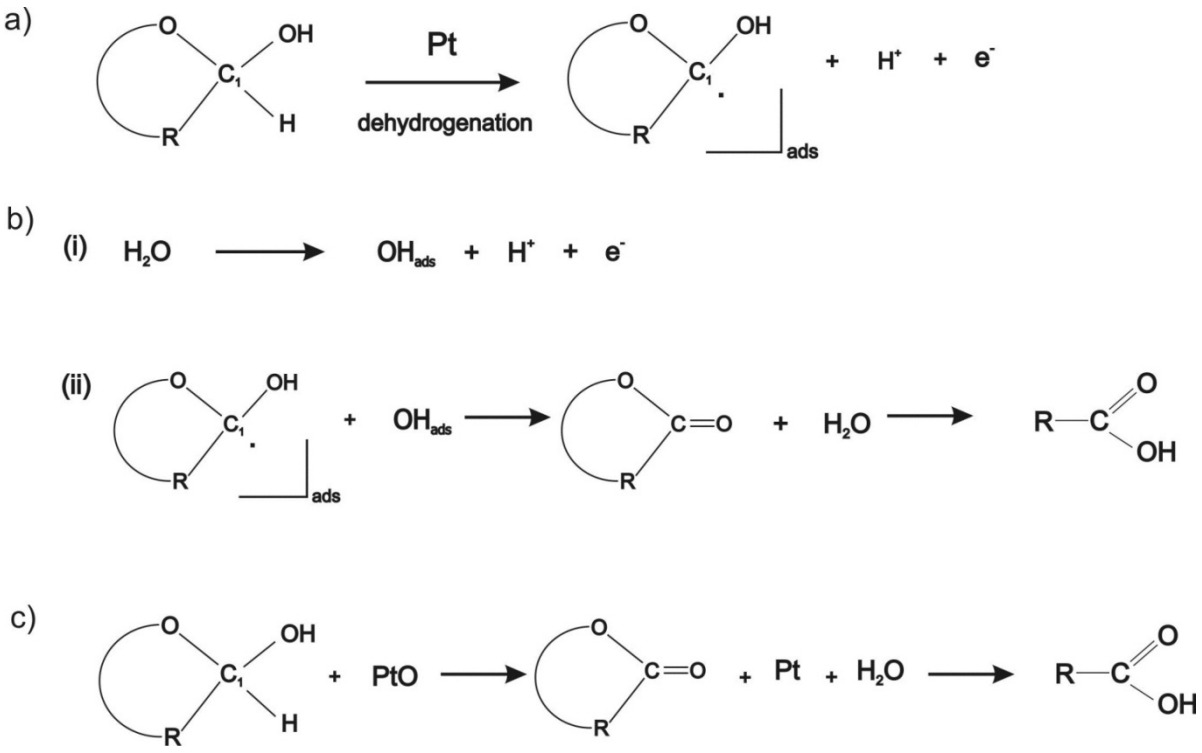
Figure 6.4: *Typical cyclic voltammogram of glucose oxidation (0.1M) taken at 30°C on a bright platinum electrode in pH 7 phosphate buffer (0.2 M). Edited from Figure 7 in reference [64].*

Platinum and platinum group metals electrocatalyse glucose oxidation in a manner that is, for the most part, analogous to the electro oxidation of methanol, methanal and methanoic acid [164,174,175,183,184]. Scheme 6.4 illustrates the three oxidation mechanisms associated with each potential region of the platinum electrode. The three mechanisms are as follows:

Peak 1 – The chemisorption and dehydrogenation of glucose in the *hydrogen region.* This initial step is the dehydrogenation of the glucose molecule at the hemiacetalic carbon 1 atom (C_1) [169], and adsorption of the glucose molecule onto the platinum surface (Sch. 6.4a). This occurs in the potential region of > 0.3 V vs. RHE, with the removal of the first hydrogen atom considered the rate determining step [164,173].

Peak 2 – Electro-oxidation of the chemisorbed species occurs in the *double layer region* spanning <0.3 to <0.6 V vs. RHE. At increasingly anodic potentials, the abundance of OH_{ads} species increases, as the fast dissociation of water reaction (b(i)), and subsequent adsorption of the hydroxide anion occurs. In accordance to the IHOAM model, the incipient hydroxide is catalytic to the oxidation of the adsorbed glucose, thus accelerates electro oxidation by following reaction b(ii). Thus the maxima for Peak 2, and surface bound glucose oxidation is observed at the potential onset for pre monolayer oxygen adsorption on platinum [164,174,177,178].

Peak 3 – The *oxygen region* from ca. >0.7 V vs. RHE to the onset of bulk oxygen evolution. Here the platinum surface is covered by a monolayer of adsorbed oxygen, initially inhibiting glucose oxidation as OH_{ads} is desorbed and replaced by less catalytically active O_{ads}. However, as soon as a suitable PtO film has formed, direct catalytic oxidation of the bulk glucose solution may occur. This is observed experimentally as the reaction kinetics become diffusion controlled rather than surface bound [179,180], and inhibition of the reaction is now observed as other oxy-compounds are formed at the platinum instead of platinum oxide. This reaction is shown in Scheme 6.4c, and is followed by the immediate regeneration of the PtO layer.



Scheme 4: *A possible mechanism for the oxidation of glucose at a platinum electrode.*

a) Glucose is adsorbed onto the platinum surface following hydrogen abstraction at the C_1 position. This dehydrogenation process is observed in peak 1 of Figure 6.4.

b) (i) the dissociation of water to produce hydroxide anions

(ii) the subsequent oxidation of adsorbed glucose by the adsorbed hydroxide ions

c) Oxidation of glucose by PtO in the oxygen region of the scan in Figure 6.4, peak 3

In the above approach it is assumed that the glucose oxidation pathway follows Scheme 6.3, i.e. glucose to gluconolactone to gluconic acid. However spectrochemical evidence of glucose oxidation suggests otherwise. Bolzan et al [181] used online mass spectrometry to explore the oxidation intermediates and products observed during glucose oxidation on platinum. They found that CO_2 was formed in the hydrogen region from the hemiacetalic C atom, via decarboxylation of a gluconate intermediate. In the double layer region a number of strongly adsorbed intermediates are formed bound at the C1 and other C atoms which

then oxidise to CO_2. Beden et al [169] used Fourier transform infrared reflectance spectroscopy (FTIRS) to discern the structures of the adsorbed intermediates. They claimed that in the double layer region the dehydrogenated glucose species was adsorbed as the gluconate bound at one or two oxygen atoms, but at E< 0.6 V the intermediate was adsorbed gluconolactone. The latter investigation again stressed the importance of 'active' OH^- anions in the vicinity of electrode surface to drive the double layer oxidation by breaking the C-O-C bond. However, Beden makes no claim to have observed the formation of CO_2 at the surface.

Skou [179] investigated the oxidation of glucose in the PtO region (i.e. Peak 3) in both acidic and neutral conditions. It was observed that relative to the blank solution, surface oxide formation was inhibited in the region of Peak 2, presumably due to the presence of adsorbed glucose, yet a large oxidation peak (Peak 3) was observed at higher anodic potentials. The peak current of Peak 2 was found not to alter with increasing scan rate, yet Peak 3 was scan rate dependent.

6.3.4.2. Disadvantages of platinum electrodes

The oxidation of glucose on platinum strongly depends on the electrolyte conditions, particularly the nature and the concentration of the ions present [182]. This is due to the dependence of glucose adsorption on the availability of the platinum surface. Competitive adsorption by other anions, especially true of phosphate anions [164,182], the extent of hydrogen and hydroxide adsorption, and the isomeric structure of the glucose molecule (i.e. α, β or γ glucose) [165] all influence the extent of glucose chemisorption, and therefore the extent of glucose oxidation. The HPO_4^{2-} anion (pKa 12.48 at 25ºC) is the most abundant at pH 7.7 to pH 12.03 and is also has the greatest affinity for adsorption onto platinum out of the phosphate anions. It is therefore necessary to consider the competitive adsorption of the anion when investigating glucose electro-oxidation on platinum in neutral phosphate buffers that do not reflect human blood conditions [182,185].

Because of the dependence of glucose oxidation on the degree of adsorption to the electrode surface, direct proportionality between the oxidation current and glucose concentration is lost as soon as the electrode surface is saturated. This is a limiting factor for platinum electrodes, as the linear range for glucose oxidation becomes dependent on the electrode surface area, and this is over the physiological glucose concentration range of 2 to 30 mM. Furthermore, the activity of the platinum electrode largely dictates the extent of the catalytic current for glucose, and is difficult to reproduce from one experiment to the next [164]. The electrode surface structure is paramount to the electroactivity of platinum towards glucose oxidation, and a number of other small organic molecules. Adsorption sites vary across various single crystal and polycrystalline surfaces thus greatly altering adsorption and surface activity, and therefore the fundamental kinetics of glucose oxidation at platinum. The onset and degree of catalytic activity therefore varies depending on surface structure, as researchers have observed [170,172,174].

One of the biggest drawbacks of using platinum electrodes however, especially in the physiological condition, is its tendency to undergo poisoning from so many species. Within physiological solutions numerous species exist that immediately inhibit the electroactivity of platinum. One of the most significant constituents is chloride anions, which strongly chemisorb to the surface of platinum and thus render the surface inaccessible to glucose, hydrogen, and hydrous oxide, particularly in acidic solutions [164]. Other organic compounds also severely reduce the ability of platinum, in particular amino acids and other blood based proteins, and electroactive compounds such as uric acid (UA), ascorbic acid (AA) and acetaminophen (AP), which also strongly adhere to the surface and react. However, even in the absence of the extraneous species, platinum can undergo self-poisoning during the oxidation of glucose, simply due to the adsorption of the oxidation products and intermediates [169,181]. Essentially the surface of a platinum electrode is non-selective to what adsorbs onto it, and as such, poorly diffusive molecules such as glucose, cannot compete for electroactive surface over any length of time.

Finally, the significant cost of platinum far outweighs its practical use in disposable glucose sensors, and without a doubt their application would vastly increase the cost of the overall product. This is a factor that cannot be ignored in the search for practical, non-enzymatic glucose sensors, as the prevalence of the disease rapidly increases in economically poor areas of the world, and the enzymatic alternatives are screen printed carbon based electrodes.

6.3.4.3. Recent advances in platinum electrode fabrication

From Table 1 it is evident that despite the drawbacks associated with the platinum electrode discussed above, the electrode material has been persistently used, and in recent years, quite successfully. The introduction of nano dimensions to electrode materials seems key to their successful application, with nanoporous [39,40,43,45,49,50], nanoparticle [74,75] and other nanostructured [51,66] platinum, electrodes emerging. The latter publications report enhanced amperometric detection that avoids electroactive interference due to the increased roughness factor of the electrode surface, as discussed in section 3.1.2.

A platinum iridium (Pt-Ir) nanoporous material was found to give a very strong and sensitive response to the amperometric oxidation of glucose [41], despite the presence of the electroactive interferences AA, UA and AP, and also a high concentration of chloride anion. This is in part due to the cathodic shift in optimum amperometric current to 0.1 V vs. Ag/AgCl, a potential at which the interferences are not active. The shift is attributed to the enhanced catalysis imposed by the iridium. Another platinum bimetallic porous electrode reported by Wang et al [48] reports improved sensitivity and reduced poisoning effect from Cl^-, as well as a much lower amperometric potential of -0.08 V vs. Ag/AgCl. A comparable sensitivity from a PtPb nanowire array was also reported in 2008 [83] by operating effectively at a negative potential of -0.2 V vs. SCE, again reducing the effect of unwanted electroactive interference species. Platinum nanotubule arrays [66] were reported prior to this in 2005, and shown to discriminatively enhance the catalytic response to glucose,

though the sensitivity was much less than has been observed at porous platinum electrodes. Overall, the introduction of nano materials to electrode fabrication has led to an improvement in the development of platinum electrodes, particularly with respect to a resistance to fouling and the effect of interference species.

6.3.5 Gold electrodes

6.3.5.1 Mechanism of glucose oxidation on gold electrodes

Gold electrodes are very weak chemisorbers due to filled d orbitals, yet display a higher electroactivity towards glucose oxidation than platinum, and have therefore also been greatly researched as non-enzymatic glucose sensors. The electrocatalytic behaviour of gold is highly complex however, and despite numerous investigations, the exact mechanism for glucose oxidation at gold remains undetermined, though a variety of mechanisms have been proposed [173,174,176,177,186,187]. Vasil'ev et al [174] claimed the process to be the same as on platinum electrodes in which the C_1 hydrogen atom was first detached, and adsorbed OH species then further oxidised the adsorbed intermediate to form gluconic acid. A number of researchers disagree with this however [173,176,181,186] due to the different pH dependence, position of anodic peaks, the potential onset of glucose oxidation, and the much reduced level of self-poisoning and adsorbate poisoning on gold.

The catalytic component of gold electrode is believed to be hydrous gold oxide, AuOH, which is formed by the chemisorption of hydroxide anions to the gold surface. This effect is more pronounced at higher pHs, and occurs in the region of pre-monolayer oxidation of the gold surface [174,177]. Anodic sweeping voltammetry over a range of pHs found that at pH < 3 glucose could not undergo oxidation until the gold surface was suitably oxidised. At pH>4 however, the onset of glucose oxygen shifts cathodically, and is observed on the non-oxidised surface. Thus Vasil'ev et al [174] concluded that chemisorbed OH_{ads} particles take part in the slow step of glucose oxidation, explaining the pH dependence of the catalysis. This is also supported by the IHOAM model [177] of

electrocatalysis, in which Burke stipulates that the electrocatalytic nature of gold is due to the hydroxide pre-monolayer formation.

$$H_2O \rightarrow OH^- + H^+ \quad (6.3)$$

$$Au + OH^- \rightarrow AuOH_{ads} \quad (6.4)$$

This process occurs at potentials of ca. -0.1 to 0.3 V vs. SCE depending on the surface structure of the gold electrode. Unlike platinum however, a chemisorption process is not evident, and therefore possibly occurs at the hydroxide surface, and is followed by rapid oxidation of adsorbed glucose by the adsorbed hydroxide anions. Investigations using fructose and sodium gluconate, both lacking the labile C_1 hemiacetalic hydrogen, have found that their oxidation is inhibited at a Au(100) surface in pH 7.4 in the double-layer potential region (i.e-0.6 to 0.6 V vs. SCE) [171,173,183]. The latter investigation by Hsiao et al also observed the deuterium labelled glucose versus normal glucose, and confirmed that the removal of the hemiacetal hydrogen was in fact the rate determining step of the reaction, as was previously observed for platinum. This strongly suggests that the hemiacetalic hydrogen is essential to the initial glucose oxidation on gold, and an adsorbed radical intermediate is observed prior to glucose oxidation [173,174].

FTIR and H_1NMR investigations showed gluconic acid, via gluconolactone, to be the sole product at potentials cathodic of the gold oxidation to higher oxides (i.e. Au_2O_3). It is possible that further oxidation of glucose occurs at these highly anodic potentials, as CO_2 has been observed as a product suggesting C-C bond cleavage [181]. Also the response of sodium gluconate on single crystal Au(100) gives two strong oxidation peaks rather than the three observed for glucose, indicating the most cathodic peak to be the formation of the gluconic acid [171,173], or at least due to hemiacetalic carbon.

Rotating disk experiments at a polycrystalline gold electrode [173] showed a curious decrease in peak current with increasing rotation rate suggesting competitive adsorption of intermediates with impurities and the further oxidation of the adsorbed intermediates on

gold electrode, which gave rise to the high oxidation currents. Larew et al [176] indeed believed that oxidation above gluconolactone occurs at gold electrodes depending on glucose concentration and electrode potential. They proposed four processes regarding the latter two parameters. First, at high glucose concentrations a 2 electron step oxidation to gluconic acid occurs. Second, gluconic acid is the product of a low glucose concentration but at a potential lower than -0.35 V. The third observation was at low glucose concentrations but potentials greater than -0.35 V, the oxidation involved more than 2 electrons. Here it was postulated that an oxidative cleavage between carbon atoms 1 and 2 may occur, as well as the oxidation of carbon atom 6. Finally, the fourth observation, to satisfy an even greater oxidative current, was the possible formation of an endiol intermediate. However, mass spectrometry investigations indicate CO_2 is not formed until the onset of higher gold oxides [181] therefore oxidation is unlikely to proceed to C-C bond cleavage within the double-layer region.

As with platinum, the mechanism of glucose oxidation on gold also depends on the gold surface structure. Significant differences in voltammetry have been observed on single crystal gold electrodes of varying crystallographic planes, and these in turn differ greatly to the process observed on polycrystalline gold [171,173,174]. The dependence on surface structure indicates a dependence on adsorption sites and surface activity, and therefore supports the activated chemisorption model [170]. On the other hand, gold is a poor chemisorber, and as such it would be deemed a very poor catalyst with respect to the latter model. Recently Burke proposed an alternative view of gold electrode surface, suggesting that its electrocatalytic behaviour arises from metastable surface states (MMS) [186]. These metastable states function as electrocatalytic redox mediators, and allow the oxidation of the surface by an active hydrous layer at a much reduced potential relative to usual monolayer oxide. This is once again the basis of the IHOAM model, but it further illustrates the dependence of gold electrocatalysis on the activity of the electrode surface

and thus provides some explanation for the difference in single crystal catalysis, and the recent enhancements by nanomaterials.

6.3.5.2 Disadvantages of gold electrodes

Pure gold electrodes are more selective than platinum electrodes, yet still exhibit an affinity for the adsorption of chloride ions in neutral conditions [174]. It was observed that in neutral phosphate buffer solutions, glucose electro-oxidation rate decreases proportionally to the chloride ion concentration, with the strongest effect observed at less positive potentials. This is believed due to the displacement of adsorbed chloride ions by adsorbed oxygen at higher potentials on the gold surface [174]. Despite a significant decrease in sensitivity to glucose when in the presence of chloride anions, the gold electrode maintains a directly proportional signal to glucose concentration over a broad linear range [174]. Alkaline conditions practically eliminate the effect of chloride, even at physiological levels of the anion. The presence of various anions were found to be inhibitory to glucose oxidation on gold electrodes in acidic media, in particular strongly adsorbed anions such as chlorides, sulfides and phosphates [187]. The investigation found that the acidic media did not inhibit glucose oxidation, and that in the absence of the adsorbing interfering species glucose oxidation readily occurs on gold in acid. Amino acids, however, almost completely inhibit the gold electrode surface, preventing electro-oxidation in both neutral and alkaline conditions, and as such a semi-permeable membrane across the electrode surface would need to be employed to protect against fouling.

Again, the cost effectiveness of using gold materials in the fabrication of disposable electrodes must be considered. As with platinum electrodes, the high cost involved is a significant disadvantage to using gold or gold modified electrodes in this application. Gold electrodes therefore remain as unsuitable to glucose biosensor applications as platinum electrodes, unless used in suitably small quantity as is possible in the fabrication of nanomaterials.

6.3.5.3 Recent advances in gold electrodes

Similarly to platinum, advances in gold electrodes have tended towards the use of nanomaterials in recent years. Porous and nanofractured gold surfaces [42,44,46,104,147], gold nanoparticles [72,73,146,149,150,153] and gold nanotubes and nanowires [65,148] have all been utilised in the past 5 years to increase the active surface area of the electrode and enhance electro-oxidation.

Bai et al [42] fabricated a unique electrode material described as a three dimensional gold film electrode (3DGFE). The electrode was found to be highly catalytic towards glucose relative to other gold porous electrodes, and was able to operate effectively at a negative potential of -0.3 V vs. SCE in a NaCl electrolyte. As such the electrode observed no interference from AA, UA or AP, and also proved to be unaffected by the presence of chloride anions in the solution. A similar response was obtained by a highly porous polycrystalline gold electrode treated by an amalgamation process [46]. Again the operating potential for glucose detection could occur at a more negative potential of -0.1 V vs. SCE, thus avoiding electroactive interference species.

Gold nanoparticles seem to have had the greatest impact on enhancing glucose electro-oxidation currents, as we observe almost a tenfold increase in sensitivity relative to porous electrodes (see Tables 1 and 3). Traditionally, gold nanoparticles are synthesised chemically with stabilisers such as thiol or chitosan so help retain the particulate structure. However, the use of electrochemical approaches [188,189], or seed mediated growth techniques allow the fabrication of pure gold particles without the catalytically hindering effect of the stabilising molecules. In 2009 Ma et al [72] electrochemically fabricated a gold nanoparticle (Au np) modified indium tin oxide (ITO) electrode, forming a gold nanoparticle array ranging from 20 to 60 nm in diameter. The Au np ITO electrodes were applied to nonenzymatic glucose sensing, and observed a high sensitivity of 183.5 $\mu A\ mM^{-1}$, though the linear range did not encompass the physiological level of glucose. A high response to glucose was also observed from a sol-gel fabricated Au np modified silicon

network electrode [73] in which a sensitivity of 0.179 nA cm^{-2} nM^{-1} was achieved. In the latter work, the sensitivity of glucose catalysis on gold with respect to particle size and surface orientation was again demonstrated, as the greater variety of crystal planes in the enlarged gold nanoparticles encouraged earlier onset of glucose oxidation, and improved catalytic activity at a lower potential [73]. These results mirror the metastable surface states theory by Burke [177,186], indicating that a higher degree of surface active sites such as grain boundaries and crystal defects, result in the earlier onset of surface oxidation, thus mediating electrocatalysis at a significantly lower potential.

A further improvement to the catalytic effect of gold was found by the addition of ad-atoms to the gold surface. Metals including Ag [190], Hg, Cd, Cu and platinum group metals Ru, Pd, Ir and Pt [191] have all been deposited on gold surfaces, with silver and mercury only displaying catalytic improvement. Silver underpotential deposition (UPD), forming a 1/3 monolayer across the gold surface was found to greatly improve catalysis, shifting the oxidative response of single crystal gold ca. 0.2 V to more cathodic potentials [190,191]. Such a pronounced negative shift can have significant benefits with regards to avoiding interference effects, as has been observed on bimetallic platinum electrodes [41,48,83].

6.3.6 Nickel electrodes

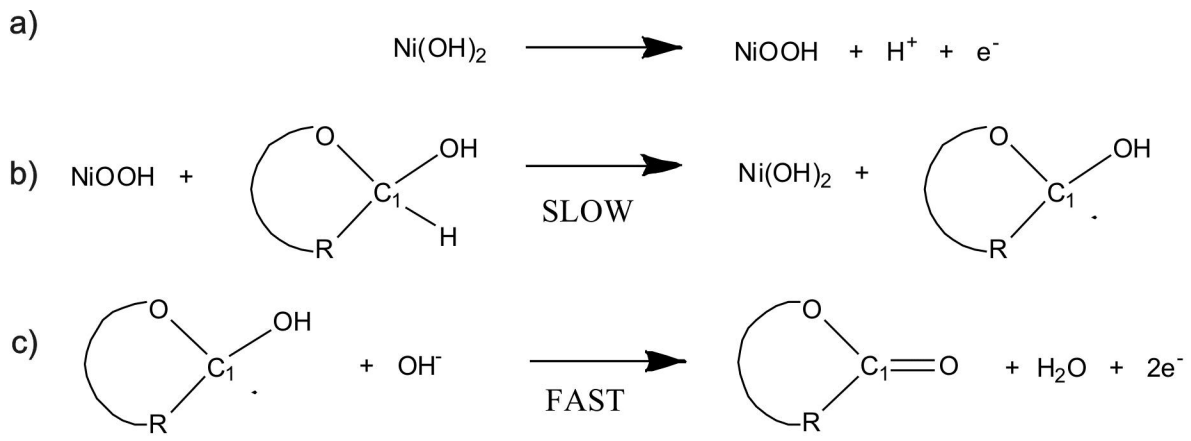
6.3.6.1 Mechanism of glucose oxidation on nickel electrodes

Nickel electrodes have been extensively explored as catalysts of organic compound oxidation in an alkaline medium. Fleishmann at al [192] published a thorough investigation into the behaviour of a nickel anode on the electro-oxidation of numerous organic materials, including glucose. It was established, in agreement with a number of other works [193-195], that the catalytic component is a Ni(III) oxyhydroxide species, the oxidized partner to the $Ni(OH)_2$/NiOOH redox couple. This is a surface bound change of the nickel oxidation state, and may be simply represented by the equation:

$$Ni(OH)_2 \rightarrow NiOOH + H^+ + e^- \quad (6.5)$$

Immersion of a nickel electrode, or electrodeposited $Ni(OH)_2$ electrode, into an alkaline electrolyte leads to the formation of two crystallographic species, the hydrated α- $Ni(OH)_2$ and anhydrous β-$Ni(OH)_2$ [192,196,197]. The β species is the more stable of the two with a structure of nickel octahedrally coordinated to eight oxygen atoms. The hydrated α structure however is much less crystalline, and has water molecules intercalated between the layers of NiO_2 that form the $Ni(OH)_2$ crystal structure.. On electro-oxidation of the nickel hydroxides, two corresponding oxyhydroxide species are formed, γ-NiOOH and β- NiOOH. The former γ structure is relatively unstable, and when oxidised to the oxyhydroxide in an alkaline medium, ionic species intercalate the layers along with water. It can be considered to have the general formula of $A_xH_y(H_2O)_zNiO_2$ (x,y < 1), in which A represents an alkali ion [193,197]. On deposition of the $Ni(OH)_2$ the α and β species are present in non-stoichiometric amounts. Potential cycling of the nickel in strong alkali leads to ageing of the material however, characterised by a potential shift to more anodic values [197-199] and an enrichment of the $Ni(OH)_2$ layer.

As with platinum and gold previously, the rate determining step of glucose oxidation at nickel oxy hydroxide is the abstraction of the hydrogen atom at the C_1 atom. This is supported by the rate constant order for amine oxidation at nickel anodes, in which the rate constant decreased in the order of primary>secondary>tertiary [192]. A rate determining step that involved electron transfer would give rise to the reverse order, as an electron is more easily lost from a tertiary amine. Oxidation of all small organic molecules at the nickel electrode occurs immediately after the formation of the Ni(III) species and forms a radical intermediate [192], which in turn reacts with active hydroxyl radicals in the NiOOH surface, as per Scheme 6.5.



Scheme 6.5: *A suggested mechanism for the oxidation of glucose at a $Ni(OH)_2$ electrode*

a) $Ni(OH)_2$ is oxidised to catalytically active NiOOH

b) Glucose undergoes hydrogen abstraction at the surface to form a radical intermediate and reforming the $Ni(OH)_2$ species

c) Hydroxyl anions in the solution rapidly complete the oxidation of the organic radical intermediate to form gluconolactone

The reaction product of electro-oxidation with the Ni(III) catalyst is still believed to form a gluconolactone and subsequently gluconic acid (Scheme 6.3). The adsorption of the intermediate is unconfirmed however, as bulk oxidation of glucose seems to occur rather than surface constrained oxidation, as shown by the linear proportionality of peak current to square root of scan rate [3]. Furthermore, repeated cyclic voltammograms of glucose on nickel electrodes show no fouling due to adsorbed intermediates or other species [69,70,199].

It has been proposed that electro-oxidation of organic molecules at NiOOH involves the reaction of 'trapped' hydroxyl radicals in the nickel surface [192]. These are due to the mixed valent and hydrated higher oxide products of Eq. 6.5 which are described above to contain alkali ions and water molecules [193,197]. The consumption of the catalytic NiOOH species is evident from cyclic voltammetry of glucose additions as shown in Figure 6.5 (from [69] and discussed in Chapter 7).

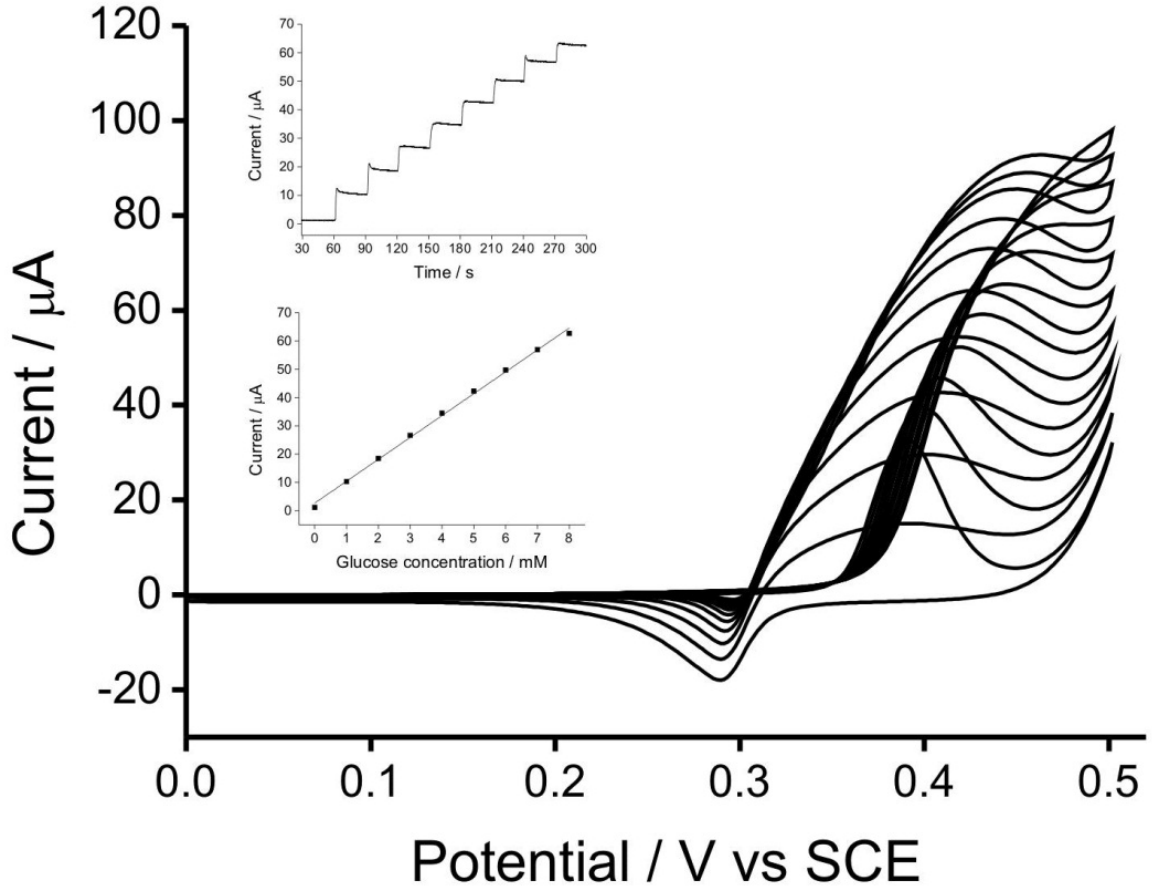


Figure 6.5: *Overlay of CVs following 1 mM additions of glucose to a 1M KOH solution at a Ni microparticle modified boron-doped diamond electrode. In-set: a) amperometric plot of 1 mM glucose additions under constant stirring in 1 M KOH held at 0.48 V and b) the corresponding calibration plot of current vs. glucose concentration. Used with permission from reference [106].*

The $Ni(OH)_2$ modified boron doped diamond electrode shows two distinct redox peaks corresponding to Eq. 5 in the 1 M KOH medium. However, on 1 mM glucose additions the anodic peak is observed to significantly increase, yet the cathodic peak decreases. This is due to the catalytic regeneration of the $Ni(OH)_2$ species by oxidising the glucose, and as such a relatively smaller current is generated by electrochemical reduction. Furthermore, the continued catalytic oxidation of the glucose is observed in the negative scan also, until the surface reduction potential is reached and the surface becomes

electrocatalytically inactive again. This has been observed in almost all cases of $Ni(OH)_2$ electrocatalysis.

The apparent bulk oxidation of glucose at nickel modified electrodes is possibly due to the bulk presence of the catalytic surface species. Unlike at gold and platinum, the surface is not gradually oxidised with a hydrous pre-monolayer which eventually forms the oxide monolayer, but instead is immediately oxidised to an oxyhydroxide state at a specific potential. The loss of electrons at the surface to produce the Ni(III) species seems to instantly activate the nickel electrode indicative of strong oxidant, with suitable empty d-orbitals to rapidly adsorb the organic analyte. The very high oxidation current produced does suggest that perhaps a more than two electron oxidation of glucose is occurring, yet the shift in the peak with each addition is more indicative of a rapid and prolonged oxidation cycle, and possibly a gradual change in local pH of the electrode surface during the anodic sweep.

6.3.6.2. Disadvantages of nickel electrodes

Nickel electrodes seem to be the most sensitive of the non-enzymatic electrode materials (see Table 1) with sensitivity reported as high as mA mM^{-1} cm^{-2} in a number of publications [3,38,69]. However they have a number of drawbacks that currently prevent their application to biosensing. Most significant is their inability to function in the physiological condition of approximately pH 7. NiOOH catalysis is highly dependent on the concentrated presence of OH^- anions, as demonstrated by the positive shift of the redox couple and significant decrease in peak currents as pH is decreased [199]. Nickel electrodes have not been reported in this capacity in either pH neutral or acid conditions, and as such their use in glucose sensing is very limited. This is not the case for fuel cells and the food industry however, in which the electrolyte medium is of no consequence to the result, and the higher the catalytic current the better.

Although nickel has proved to be unaffected by chloride ions [70], does not undergo electrode fouling if on a suitable electrode substrate [69,70], and has also shown a promising long term stability, selectivity remains a huge problem. In Fleishmann's [192] investigation of nickel electrodes he found that all the small organic molecules oxidised at the same potential, immediately after the formation of NiOOH. Although most of the analytes explored in that research would not be present in blood (see Table 4), one major oxidisable component often present is ethanol. Nickel electrodes oxidise ethanol comparably to glucose as demonstrated in a number of papers [192,198-202], thus the presence of even low alcohol levels in the blood could affect blood glucose determination. Furthermore, the oxidation potential would be indiscriminate against electroactive interferences such as AA, UA and AP at the fixed potential of amperometric detection, and thus the electrochemical determination would be compromised. This does not also consider a number of other sugars that could potentially be present in the blood depending on the patient's medication.

6.3.6.3 Recent advances in nickel electrodes

Although not dependent on adsorption to the electrode surface, the surface coverage of NiOOH is essential for efficient and rapid glucose oxidation, and as such a high surface area is preferable. As has been the case for platinum and gold above, the introduction of nanomaterials has shown a significant increase in reported sensitivity and resistance to interference species. Nickel electrodes report the highest current densities for glucose oxidation as shown in Tables 1-3. Hydrothermally fabricated nickel nanoflakes on a titanium support are reported to have a current density of 7.32 mA mM^{-1} cm^{-2}, the highest value reported [3]. In the same region of sensitivity, we see 5.07 mA mM^{-1} cm^{-2} at a nickel film modified nanoporous gold electrode [38], apparently giving a signal 340 times greater than an equivalent nickel film modified polished gold electrode. The simple electrodeposition of nickel/nickel hydroxide onto a boron doped diamond substrate also

proved an effective electrocatalytic electrode [69], observing a high sensitivity of 1.04 mA mM^{-1} cm^{-2}, and offering a very simple and reproducible fabrication method.

Ionic liquid pastes have recently incorporated nickel nanomaterials to combine the high rates of electron transfer of the carbon ionic liquid electrode (CILE) with the electrocatalytic effect of nickel hydroxide [71]. The composite electrode offered extraordinary stability, and was easily renewed by light polishing on smooth paper. Different voltammetric behaviour was observed however, in which both the anodic and cathodic peak currents increased with glucose addition, instead of the expected decrease of the cathodic peak. This was also observed at a metallic nickel electrode by Zhao et al [107], and ascribed to the Ni(II)/(III) redox couple serving a double function of electronic medium and catalyst, simultaneously, though what this quite means is unclear. It was not a behaviour observed on another ionic liquid paste electrode described by Zheng et al [55] either, which utilised a multiwall carbon nanotubes (MWCNTs) ionic liquid paste electrode (IL-PE) modified by a nickel (II) quercetin complex.

6.3.7 Copper electrodes

6.3.7.1 Mechanism of glucose oxidation on copper

Copper electrodes are often considered in the same way as nickel electrodes with respect to organic molecule electro-oxidation. They too catalyse oxidation by reducing the M(III) centre to M(II) (where M = Ni or Cu), however a distinct redox couple for the Cu(II)/(III) surface process is not clearly evident as it is for most nickel electrodes. Fleischmann et al [203] claimed that the copper II/III transition occurs at potentials of 0.65 V vs. SCE in 0.1 M KOH, too close to bulk oxygen evolution to be studied in detail, but there was clear indication of the presence of Cu(III) in the apparent charge under the peaks. The other redox peaks for copper are clearly defined however, with the oxidation to Cu(I) and Cu(II) states, and the corresponding reduction evident in voltammetric studies [111,118,132,204-206].

Kano et al [111,132] investigated the catalytic mechanism for glucose oxidation, and found that a bare copper electrode in 0.15M NaOH was insensitive to carbohydrates. However, a copper (II) oxide electrode responded to the glucose presence with an irreversible oxidation peak. This peak observed a steady-state type of behaviour at scan rates of 0.1 Vs^{-1} or slower, yet at higher scan rates a definitive peak emerged, suggesting a decreased contribution by a chemical process [111]. The same investigation observed the response of a Cu(I) oxide and $Cu(OH)_2$, and found both to be inactive towards glucose oxidation, thus concluding CuO is necessary to observe catalysis. CuO suspended in a solution of NaOH did not catalyse electro-oxidation however, thus suggesting the catalytic component is likely to be a higher oxide such as CuOOH, as is observed for nickel.

Based on comparative RDE experiments of glucose, sorbitol and xylose, Kano et al proposed a 12 electron oxidation of glucose in which the copper oxide facilitates six, two-electron step oxidations to produce formic acid [132]. The complete oxidation of glucose at the copper electrode, and similarly at the nickel electrode, would certainly explain the significantly greater electro-oxidation currents observed relative to platinum and gold. Xie et al [118] proposed a mechanism akin to those previously suggested, in which active hydroxyl radicals and the carbohydrate adsorb onto the electrode surface simultaneously, and at adjacent active sites. This is followed by the rate determining concerted step in which the adjacent OH_{ads} abstracts the α-hydrogen atom, and the organic radical is further oxidised by OH^- species to the acid product. Despite this research, the electro-oxidation mechanism for glucose on copper remains controversial.

In an experiment by Watanabe et al [90] comparing Cu-BDD and copper electrodes, peak shaped voltammograms were only observed in response to the presence of glucose. Furthermore, the cathodic current of the CV for the Cu-BDD electrode overlayed the anodic current, yet this was not so on the bulk copper electrode. This was believed due to a difference in diffusion domains in which the implanted copper centres of the Cu-BDD electrode imposed a microarray diffusion pattern, whereas the copper electrode had planar

diffusion. As such the copper electrode showed a linear relationship with the square root of scan rate, confirming diffusional control of the response, but the Cu-BDD electrode did not.

6.3.8 Alloys and bimetallic systems

Non-enzymatic electrocatalytic electrodes employing bimetallic systems have been emerging in the form of alloys [96,130,131,206] or metal adatoms [190,191,207,208], to offer electrodes of highly desirable electronic and catalytic properties. Vasil'ev et al [174] commented on the improved electro-oxidation of organic compounds at alloyed platinum electrodes, stating they observed the highest catalytic activity toward small organic molecules. Metal adatoms on electrode substrates, and alloy/bimetallic systems have therefore been the focus of much electrocatalytic research.

The attraction of bimetallic systems stems from the anticipation of a synergistic electronic response, in which the catalytic benefits of each component combine to form a 'super' catalyst [96,206]. Pletcher [170] observed that partial coverage of electrodes, such as platinum and gold, by other metal atoms could greatly enhance catalysis and improve long term activity of the system. An example of the selective poisoning effect of lead adatoms of a platinum surface demonstrates the catalytic enhancement of adatoms, in which the oxidation of formic acid is improved, and long term activity sustained [207,208]. This was proposed to be due to the partial coverage on the electrode such that the lead atoms interact with two platinum sites, thus forming a surface of pairs of platinum atoms. This is due to the imposed limited active sites across the electrode surface, such that unwanted, poisoning side reactions cannot also take place [170].

A variety of Pt-based bimetallic materials (Au, Pb, Bi, Pb and Tl) have been fabricated with the goal of improving the sensitivity and selectivity of the electrodes towards the electro–oxidation of glucose [48,61,208,209]. The success of bimetallic systems such as PtPb [48,83] and PtIr [41] porous electrode in recent years have already been discussed earlier, again having the advantage of reducing the overvoltage for glucose

oxidation to negative potentials. Aoun et al [210,211] explored the benefits of silver adatoms on single-crystal gold, and observed a marked decrease in oxidation potential that may improve the selectivity and resistance to interferences species across the electrode.

6.3.9 Carbon based electrodes

Numerous new carbon based electrodes or carbon based modifications to electrodes have emerged over the past decade for use in electrocatalysis, including glucose oxidation. Carbon electrodes have been explored as potential electrodes for direct glucose oxidation for a long time however, with the fabrication of carbon based, screen printed enzymatic electrodes revolutionising finger-stick electrodes in the early 1990s, allowing for mass production and lower cost sensor fabrication [33,34]. Generally carbon substrates are used due to their electronically conductive, yet electrocatalytically inert properties. Glassy carbon electrodes were investigated by Vasil'ev et al [174] in 1985, and found to produce a slight anodic current in response to glucose. This was completely inhibited by the introduction of physiological levels of chloride ions however, thus rendering the electrode nonviable in terms of sensing.

Over the past decade the emergence of carbon-based nanostructured materials such as carbon nanotubes (CNTs), doped diamond-like materials, and most recently graphene electrode materials has opened new doors to improving electrochemical glucose sensing. These materials have great promise in biosensing applications due to their ease of modification and functionalization, good conductivity, biocompatibility and in some cases, very high surface area. This is particularly so of carbon nanotubes (CNTs), finding application in both enzymatic and non-enzymatic sensors [101,212,213]. These carbon based electrodes are frequently used as inert substrates, but recent publications also claim that they are directly electrocatalytically active. The following subsections explore boron doped diamond electrodes (BDD), single and multiwall carbon nanotubes (SWCNT and

MWCNT) electrodes and other novel electrode materials, such as graphene, as non-enzymatic electrocatalytic glucose sensors.

6.3.9.1 Boron doped diamond (BDD)

BDD electrodes have found increasing application to electroanalysis over the past 25 years [214-222], including in the oxidation of organic materials. As a substrate electrode for modification, BDD electrodes have been found to be particularly ideal, owing to a very low capacitative current relative to metal and other carbon electrodes, a highly inert surface and therefore resistance to fouling, and with respect to glucose, a pronounced lack of electrochemical activity [69,223].

A high resistance to electrode fouling is key to the application of BDD towards waste water treatment, as the electrode is durable and resistive to a number of common fouling ionic species such as chloride. It and also has a very large potential window, both cathodically and anodically, due to high oxygen and hydrogen over potentials. Metal modification, by chemical modification [223], metal ion implantation [90,98,224] or electrochemical modification [69,199,225-228], has allowed BDD electrodes to respond to numerous organic analytes effectively and sensitively whilst maintaining low poisoning effects, resilience to harsh experimental conditions and very low background currents.

Despite BDD electrodes being mostly noted far a lack of response to glucose [69,90,98,158,224] the direct oxidation of glucose at an unmodified BDD electrode has also been reported [84,155,157]. The first report was in 2005 by Lee and Park [157] in which a commercially bought polycrystalline BDD electrode was hydrogen flame annealed prior to experimentation, and used without further modification to oxidise glucose in an alkaline solution. The CV gave an oxidation peak at 650 mV vs. Ag/AgCl for both the forward and reverse scan, in a manner akin to the oxidation of polyamines [229]. In the latter work regarding polyamines it was postulated that the reaction mechanism involved a reaction between adsorbed hydroxyl radicals and adsorbed polyamines, occurring at surface

adsorption sites across the BDD electrode. The adsorbed hydroxyl and organic species undergo an anodic oxygen transfer, and the organic compound is oxidised to an intermediate. This is shown in Equation 6.6 in which the electrode adsorption sites are represented by M( ), M' represents a possibly different adsorption site, and R represents the organic analyte.

$$\mathrm{M}(\mathrm{O}H^{*}) + \mathrm{M}'(\mathrm{R}) \rightarrow \mathrm{M}(\,) + \mathrm{M}'(\mathrm{RO}) + \mathrm{H}^{+} + e^{-} \qquad (6.6)$$

The organic intermediate was speculated to remain adsorbed on the BDD electrode surface, due to the decrease in the reverse sweep oxidation, and the gradual decrease in peak current over 40 consecutive scans. However, the electrode fouling is to a very small extent relative to other metal electrodes such as platinum and gold, and the current response is readily renewed by simply rinsing the electrode in water.

In Zhao's work [155] the as-prepared microcrystalline and nanocrystalline BDD electrodes reportedly exhibit a high sensitivity and stability, good reproducibility and selectivity over a glucose range of 0.25 to 10 mM in sodium hydroxide solution. The response is surface bound, showing a non-linear response to the square root of scan rate. It is observed to have a rapid increase in peak current at slower scan rates, but at sweep rates over 50mVs^{-1} the peak current is limited and plateaus. This is suggested to be due to slow desorption kinetics of the products at the electrode surface, in which the electro-oxidation products do not desorb fast enough to relinquish active sites, thus desorption becomes the peak current limiting factor [155,229]. At sufficient scan rates however, the rate of desorption is exceeded and a maximum peak current is observed.

The BDD electrode response was found to vary from one electrode to the next, indicating an intrinsic difference in the BDD morphology that gave a varied response to the same glucose concentration. Zhao et al [155] suggest the electrode active sites are in fact the boron atoms heterogeneously dispersed throughout the thin film. They propose adsorption to these electroactive sites, and the subsequent oxidation on the electrode by

adsorbed hydroxyl radicals at other surface sites, a theory that indeed supports the varied electroactivity across the different batches of electrodes, and has also been suggested by Koppang et al with regard to the BDD oxidation of polyamines [229].

The effect of electroactive species interferences species UA and AA, were explored by Lee [157] and Zhao [155] on their respective bare BDD electrodes. At AA and UA concentrations as high as 0.5 mM, the oxidation peaks were found to be distinguishable from the glucose peak, and pose no real interference to glucose determination. The electrodes were also utilised in the analysis of glucose in a real blood sample in alkaline solution [154], and a comparable results was obtained.

In both cases, the linear range of the electrode was limited to values up to 10 mM however, a major limitation in the practical use of bare BDD electrodes. The key aspect of the BDD electrode reported in Lee and Park's research is the use of hydrogen flame treatment to maintain the hydrogen termination of the diamond surface. At highly anodic potentials carboxyl functionalities are known to form and decrease the conductivity of the BDD electrode [230]. Consequently the glucose signal is lost at the oxidised BDD surface.

It does remain that BDD electrodes have otherwise shown inactivity towards glucose without first undergoing metal-modification [69,90,98,158,223,224]. This is possibly due to the surface termination of the electrode, as implied by the inactivity of the oxidised BDD electrode towards glucose [157]. The as-prepared microcrystalline BDD electrode described by Zhao [155] also lacked a response to glucose following acid treatment, yet the nanocrystalline BDD electrode maintained a good response despite 30 minutes of treatment in hot aqua regia. Thus there is also a strong indication that the surface structure with regard to diamond size, grain boundaries and distribution of boron atoms, has a large effect on the electrochemical activity of the doped diamond electrode. This theory is greatly supported by the recent work of Luo et al [84] in which a boron-doped diamond nanoforest (BDDNF) was fabricated and applied to glucose determination. Relative to a planar BDD

electrode, the BDDNF gave a well-defined current response to the glucose, a vast improvement that suggests a strong dependency on the surface structure of the electrode.

All the unmodified BDD electrodes used in direct glucose oxidation discussed here have shown selective determination of the analyte in the presence of ascorbic acid and uric acid. This is in part due to a significant difference in peak potential, in which in all three publications [84,155,157] the interferences respond at approximately 100 to 300 mV vs. SCE, whereas the glucose has a peak current at approximately 600 mV vs. SCE. However, in each case the linear range of each electrode does not exceed 10 mM, which is a major issue with regard to developing a viable biological glucose sensor. The sensitivity of the electrodes is also lower than at metal modified electrodes, including metal modified BDD electrodes [69], observing values of 101.9 μA mM^{-1} cm^{-2} on the BDND [155] and merely 8.1 μA mM^{-1} cm^{-2} on the BDDNF electrode [84]. These are very recent publications however, and it is therefore evident that nanocrystalline and nanostructured boron doped diamond materials hold a lot of promise as viable, reusable glucose sensors for diabetes.

6.3.9.2 Carbon nanotubes

Carbon nanotubes (CNTs) are also a relatively new carbon based electrode material that offers alternative electroactivity to conventional carbon surfaces. CNTs have found substantial application to electroanalysis of a wide variety of analytes, most frequently in the modification of planar electrodes, increasing surface roughness, porosity and compatibility to biological substances. The cylindrical graphene sheets of nano dimensions are highly conductive, and substantially increase the surface area of a planar electrode whilst retaining high chemical and physical stability. In Table 1 multiwalled and single walled carbon nanotubes (MWCNTs and SWCNTs) are shown to have been used alone [53,64] but most frequently in conjunction with other catalytically active metals [52,55-57,59-61,85,231,232].

As mentioned in Section 6.2.4, carbon nanotubes have shown promise in glucose sensing in the development of third generation enzymatic glucose sensors [233,234]. When immobilised with GOx, the carbon material does not require a mediator or oxygen to facilitate glucose oxidation, and as such is believed to allow for direct electron transfer between the enzyme and electrode [233]. Furthermore, the CNT modified electrodes have shown greater long term stability than is observed on a modified glassy carbon electrode [234], due to the strong adherence of the enzyme to the carboxylated open ends of the nanotubes [233].

Non-enzymatic and unmodified carbon nanotubes have been also been successfully used in glucose detection, as reported by Ye et al [64]. A well-aligned MWCNTs electrode was fabricated on a tantalum substrate grown on a thin layer of cobalt catalyst. In alkaline conditions, and clear faradaic response to the presence of glucose was observed at 0.42 V vs. Ag/AgCl, and a diffusion-controlled process was indicated by the linearity of the square-root of scan rate vs. peak current plot [64]. The cobalt present in the fabrication process was found to contribute approx. 14% of the glucose response however, but the bulk of the response was considered to be due to the CNTs. Although the CNTs gave a good, linear response to glucose to levels of 11 mM, even in high concentrations of chloride, the chronoamperometric response to interference species, AA and UA, was considerable, accounting for 25 % of the current response relative to glucose. This is possibly due to the lower overpotential of 0.4 V vs. Ag/AgCl used with the CNTs compared to the ca. 0.6 V potential applied to the BDD electrodes, in which the interfering species oxidized at lower potentials to glucose. Wang et al [53] fabricated free standing SWCNT films in a more recent investigation, in which carbon nanotubes were spread of a glass substrate and bound to the surface using Nafion. In this instance the CV showed an increase in current from approximately 0.5 V vs. Ag/AgCl, though no discernable peak was produced. The linear range was also limited, deviating at the very low concentration of 2.16 mM.

The nanotubes subsection of Table 1 includes numerous CNTs-based electrodes that have been modified with various catalytic metals, most of which have been discussed previously. Sensitivity at best is reportedly 280 μA mM^{-1} cm^2 for a platinum nanocube doped CNTs electrode [51], and linear ranges rarely exceed 15 mM. Platinum and platinum group bimetallic nanoparticles have been successfully distributed on CNTs in a number of publications, and have offered a catalytic response without the issues of electrode fouling [51,57,58,60,67,85].

A number of metal oxides have been used in conjunction with carbon nanotubes to produce electrocatalytic glucose sensors [51,56,63,68,87,235]. MnO_2 was coupled with carbon nanotubes in 2008 by Chen et al [56] in a novel non-enzymatic glucose sensor, which showed a wide linear range to 28 mM and a reasonable sensitivity of 33.19 μAmM^{-1} cm^{-2}. The alternative metal oxide displayed a high tolerance to electrode fouling too, exhibiting no interference from chloride ions or common electroactive interference species. Most notably the MnO_2 caused a substantial negative shift of the anodic peak potential to +0.1 and +0.4 V vs. Ag/AgCl, a shift of over 200 mV relative to the unmodified MWCNTs. Two oxidation peaks were observed in the anodic sweep of the MnO_2/MWCNTs electrode before glucose addition, the first assigned to the Mn(II) to MnO_2 oxidation, and the second to the MnO_2 to MnO_4^{2-} process. Both peaks significantly increased on addition of glucose, and as such it was suggested that the both Mn(II) and Mn(IV) were involved in the electrocatalytic process [56]. CuS_2 and SnO_2 were deposited on double wall carbon nanotubes, though the latter gave a relatively poor response to glucose and H_2O_2, and the CuS_2 was only marginally better. The latter experiment did strongly emphasize the catalytic nature of copper towards glucose oxidation however, as the SnO_2 was speculated to be most active due to the presence of more active sites, yet this was evidently not the case.

Overall, carbon nanotubes have been shown to offer a good base for simple modification, to allow for deposition of less material, yet still offer high catalytic response and electron transfer. Furthermore, unmodified CNTs are directly responsive to glucose,

and unaffected by interfering species and chloride, as well as resistant to surface fouling. However, a major limitation lies in the linear range of both modified and unmodified CNTs, as the latter do not exceed 10 mM and the former rarely surpass a 15 mM maximum.

6.3.9.3 Graphene and carbon nanofibres

A graphene nanosheet (GNS) is the basic structural component of graphite, carbon nanotubes, fullerenes and carbon nanofibres. It is a planar 2D layer, a single atom thick, of sp^2 hybridised carbon, and was first fabricated and discussed in 2004 by Novoselov et al [236]. It was long believed that graphene could not exist in its free-state, due to thermodynamic instability, instead preferring to form more stable, curved structures. However, on successful fabrication by exfoliating small flat elevated areas of highly oriented pyrolytic graphite (HOPG), the unique electrochemical properties of the material were discovered [236]. GNS is unique as theoretically it is a zero bandgap semiconductor [236] therefore has very high conductivity akin to that of metal, a property unknown to films of such thickness. The new carbon structure is therefore considered to possibly offer a new wave of electrocatalytic abilities, particularly in combination with metallic nanoparticles [237]. That said, work by Pumera [238] rightly suggests this excitement might be tempered with caution.

Recent advancements in the preparation of graphene have allowed experimental studies of graphene to rapidly progress, and as such the last two years have seen a surge in graphene based catalysts. With regard to glucose oxidation, experiments thus far have focused on enzymatic systems, in which GOx is immobilised on the surface [239-243], along with nanoparticles of platinum and gold. As yet there have not been any non-enzymatic studies regarding graphene based electrodes however. That said, the attempted step from enzymatic to non-enzymatic approaches can be anticipated. It has been speculated that sp^2 carbon plays an important role in the electrochemical detection of organic compounds, due to the low potential at which the hydroxyl radical may be formed at

the surface sites [229]. As such there is further indication that non-enzymatic glucose sensing might be possible at graphene thin layers.

In a variation on graphene, carbon nanofibres (CNFs) are finding increasing application to biosensors, including enzymatic glucose sensors. Carbon nanofibres are composed of well-arranged graphite layers that are organised into cylindrical structures to give highly conductive nanowires. Unlike carbon nanotubes, the fibres are not hollow, and expose the edges of the graphene plane rather than the basal plane surface, thus they have a very large active surface area and a very conductive [244]. In the past 4 years, carbon nanofibres have been modified with enzymes to produce successful glucose biosensors with superior performance to modified carbon nanotubes. Non-enzymatic CNF electrodes have also been developed recently however. Rathod et al [85] modified the CNFs with a fine distribution of platinum nanoparticles, and analysed glucose under physiological conditions (pH 7), though the platinum modified MWCNTs proved to be a better sensor. This surprising result was attributed to a relatively lower level of platinum doping and accessibility of particles for glucose oxidation due to the larger size of the CNFs used, as well as the effect of coating the surface with an insulating Nafion layer [85]. Liu et al [70] developed a renewable nickel nanoparticle loaded carbon nanofiber paste electrode, in which a wide linear range of 2μM to 2.5 mM was observed, and a sensitivity of 420.4 μA mM^{-1} cm^{-2}.

6.4. Electroactive interferences and electrode fouling

Two major problems of the amperometric glucose sensing is the presence of other electroactive interferences in the blood and electrode fouling. The moderately high anodic potential used to oxidise glucose also oxidises these interferences, thus giving an amperometric current that overestimates the blood glucose value. This also applies to non-enzymatic glucose sensors, in which selectivity is even less, and electro-oxidation reactions are enhanced. The overestimation of blood glucose levels might have life threatening

consequences, as hypoglycaemia can be masked or even be induced by inappropriate administration of insulin, thus leading to a hypoglycaemic coma or even death. A number of compounds found in human blood can interfere with the glucose determination. These are listed in Tables 4 and 5 and discussed in the following sections.

Table 4: *Possible electroactive and fouling components of blood and their relative concentrations*

Compound	Blood conc. (mM)[a]	Compound	Blood conc. (mM)
Natural interferents		**External influences**	
Uric acid	0.18 - 0.42	Acetaminophen	0 - 0.2
Ascorbic acid	0.023 - 0.085	Salicylate	0 - 2.2
Bilirubin	up to 0.02	Alcohol (ethanol)	0 - 65
L-Cystine	0.003 - 0.015	L-Dopa	varies
Chloride	98-106	Tolazamide	varies
Protein	6 - 8.4 gm/dL		

Values obtained from Merck manual of medical information [245], a – unless state otherwise

6.4.1 Naturally occurring interferences

Ascorbic acid (AA) and uric acid (UA) (Figures 6.6a and b) are two electroactive species naturally occurring in blood that cause the most electrochemical interference during glucose sensing. Like glucose they are strong reducing agents, therefore readily oxidise at moderate electrode potentials. AA is commonly known as vitamin C, and although concentrations in blood vary on dietary intake, normal blood concentrations are ca. 0.02 and 0.08 mM [245]. UA is present as the final metabolite of purine, and is present in the blood as an antioxidant at concentrations of ca. 0.18 to 0.42 mM. Ever present, most recent papers of the past decade focus on these two main electroactive interference compounds when testing the practical application of the sensor, be it enzymatic or non-enzymatic.

Cysteine (Figure 6.6c) has been named as an electroactive interference with regard to glucose sensing by a number of researchers [134,246-249], and is present in the blood at very low concentrations of 3 to 15 μM. Dopamine (Figure 6.6d) is also present at low levels naturally, and is known to oxidise at similar potentials to glucose [47,95,107] thus often considered a natural interference.

As can be seen in Table 4, the concentrations of the interferences are found in sub millimolar concentrations, which is considerably lower (ca. 250 times) than the blood glucose concentration of 3-8 mM (optimally). This can arise if the interferences react in a diffusion controlled manner whereas the glucose is subject to kinetic limitations at the potential of interest.

6.4.2 Pharmacological interferences

A number of drugs, ranging from commonly used to highly specific, have been shown to interfere with blood glucose determination. The most damaging of these is acetaminophen (AP) (Figure 6e), a constituent of paracetamol and therefore commonly used and of a variable concentration in the blood, with therapeutic levels of up to 0.2 mM. Similarly, salicylic acid (Figure 6f), a component of aspirin, may also be present in the blood at an interfering level, though actual interference by salicylates has not been generally reported at enzymatic glucose sensors. Another common interference species is dopamine, naturally occurring in low concentrations, yet found in certain food stuffs and administered as a drug in the form of its precursor L-DOPA.

Finally one other recognised interfering chemical that has had variable effects on GOx based sensors is ironically Tolazamide (Figure 6.6g), a sulphonamide based drug used to lower blood glucose levels in Type 2 diabetics. These are all chemicals from drugs known to interfere with enzymatic blood glucose sensors, yet potential interference of many drugs that is yet unknown must always be considered, especially as new chemicals and compounds are always being produced in the pharmaceutical industry. The impact of these

chemicals on non-enzymatic glucose sensors is much less researched, as non-enzymatic blood glucose monitoring systems have yet to be introduced. As such, the impact of so many drugs needs to be determined, especially as electro-oxidation at non-enzymatic systems is most frequently not selective and produces a greater oxidative current response.

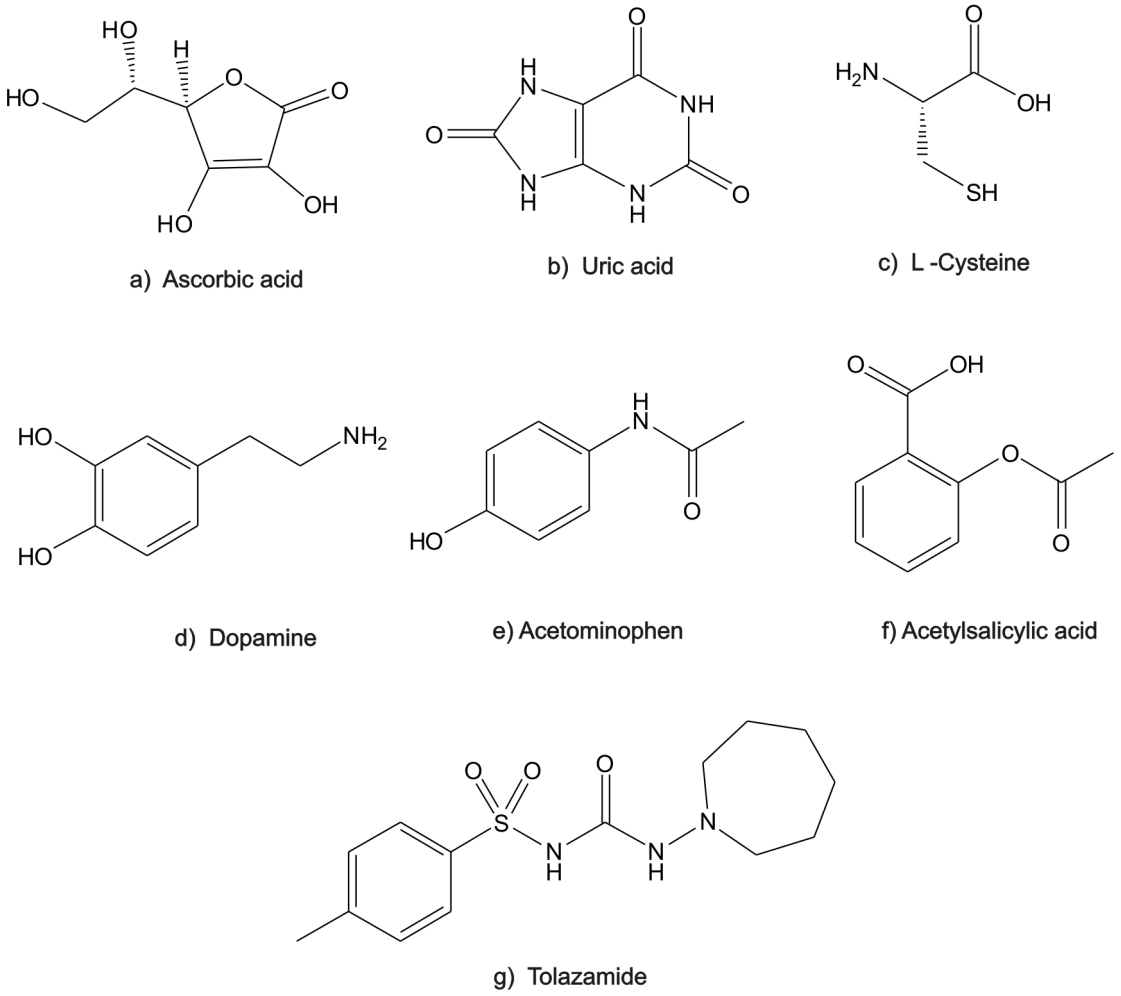


Figure 6.6: *The chemical structures of various known electroactive interferences species. a) Ascorbic acid, b) uric acid, c) L-cysteine, d) dopamine, e) acetaminophen, f)acetylsalicylic acid and g) Tolazamide*

6.4.3 Proteins and chloride anions

Interferences also include proteins, of which there are can be up to 84 g/L in the blood, which readily adsorb and cause inhibitory electrode fouling, particularly on platinum and gold electrodes [164,174]. High concentrations of triglycerides in the blood can have a similar effect, competing with glucose in the sample volume, thus lowering the glucose

oxidation signal. Chloride anions greatly interfere with platinum electro-oxidation signals, as the chloride strongly chemisorbs irreversibly onto the platinum surface, and thus inhibits catalysis [164,174]. Chloride concentration is relatively high in the blood, with a concentration of approximately 100 mM, and thus its poisoning influence cannot be deemed negligible.

Phosphate buffers, in which much of the pH neutral experimentation is performed, are believed to have a somewhat interfering effect themselves on platinum electrodes [174,185]. Although not an interference present in blood samples, the effect of phosphate anions is not to be disregarded, as many preliminary experiments are performed in the buffer solution giving an idea of the electrode response in a real sample.

6.4.4 Non-glucose sugars

Although glucose is the main carbohydrate found in blood, a number of other mono and polysaccharides, listed in Table 5, may be present that can severely interfere with glucose analysis [250]. Despite their much higher selectivity towards glucose relative to non-enzymatic systems the presence of non-glucose sugars in the blood has proved problematic for enzymatic sensors, as particular non-glucose sugars are catalysed alongside glucose by the various types of enzyme in sensors. [250]. This can provide a gross overestimate of blood glucose level and is a life threatening error to impose.

Table 5: *Non-glucose sugars that are known and possible signal interferences in sensing*

Sugars	**Source**	
Know interferences		**Possible interferences**
Maltose	food, immune globulins, perineal dialysis	Mannose
Galactose	food	Lactose
Xylose	malabsorption testing	Ribose
Icodextrin	perineal dialysis	Arabinose

In 2003 a medical device alert was issued for glucose monitoring systems that used glucose dehydrogenase (GDH)-pyrroloquino-linequinone (PQQ) enzymatic test strips. The interference sugars were identified to be icodextrin and maltose, the former a polymer of glucose consisting of 10 to 250 glucose units, and the latter, a metabolite of icodextrin consisting of two glucose units. Icodextrin is used in an ever increasing demand for peritoneal dialysis in the treatment of chronic kidney disease.

On the death of a number of patients investigation into the effects of non-glucose sugars on blood glucose determination led to monosaccharide's, galactose and xylose, to also be determined to be interferences for blood glucose monitoring systems that were based on glucose dye oxidoreductase and GDH-PQQ enzymatic test strips. These sugars GOx based test strips have also shown interference by galactose and maltose [250] electrode resulting in an overestimation of blood glucose levels, though they are generally considered to not be susceptible to non-glucose sugar interference. Only systems based on GDH-nicotinamide adenine dinucleotide (GDH-NAD), or GDH-flavin adenine dinucleotide (GDH-FAD) are free of these interferences.

6.4.5 Alcohol

One major concern for the application of non-enzymatic glucose sensors is the potential interference of alcohol. A similar catalytic response by many metallic, non-enzymatic electrodes to alcohol is a major issue, as many of the electrodes presented as possible glucose sensors have also been applied to alcohol sensing in similar circumstance [76,198,251-254]. Direct alcohol fuel cells that frequently employ ethanol, are based around similar electrode systems to non-enzymatic glucose electrodes. In fact, a number of potential glucose sensors are suggested in glucose fuel cells, due to the high oxidative current produced at certain catalytic metals.

6.4.6 Methods to overcome interference effects

In industry and laboratory based testing, FIA and HPLC systems can be used to separate different sugars and alcohols prior to oxidation at the non-enzymatic electrode, thus avoiding the issue of interferences, as shown in Figure 6.7. This is not possible for blood glucose sensors however, as chromatographic systems are not viable in terms of self-testing using in-vitro handheld glucose meters, and they are certainly incompatible for in-vivo analysis.

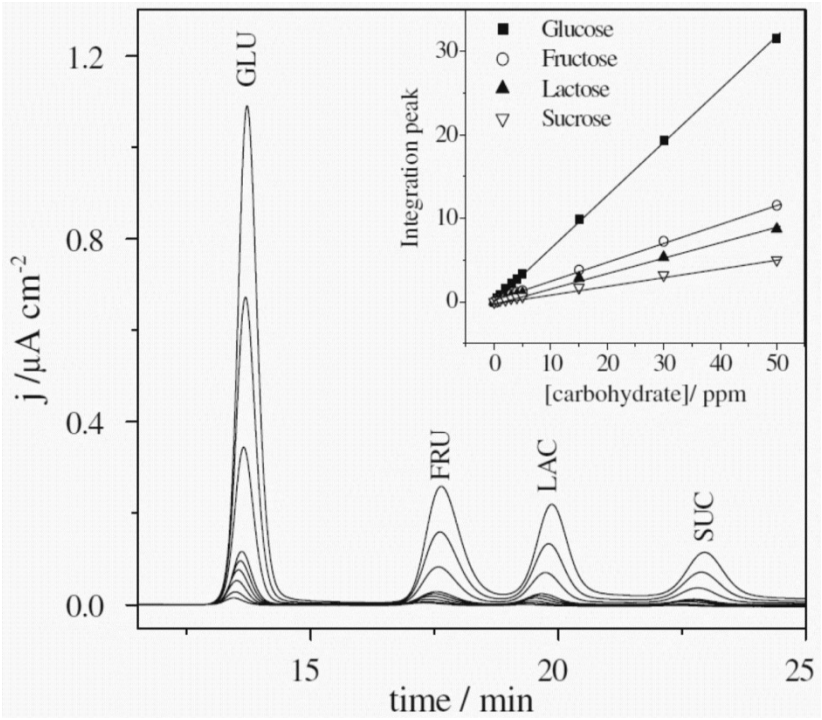


Figure 6.7: *The determination of different sugars using HPLC methods. Amperometric detection was performed using a nickel hydroxide modified electrode. The solutions were passed through chromatographic column. Eluent: NaOH 0.1 M, flow rate: 1.0 mL min^{-1}, electrode potential 0.45 V vs.Ag/AgCl. From reference [225]*

A number of approaches have been taken to overcome the problem of interferences. These include the use of permselective coatings such as Nafion [50,58,89,116] or electropolymerised films [12,249,255], reducing the overpotential for glucose detection to less anodic values at which the interferences are not oxidised [41,48,83,190,191], the use of

chromatographic stages prior to analysis (Table 2), and the specific fabrication of the electrode surface to enhance the kinetics of the slower, surface bound reaction.

The option to use a passive membrane that imparts chemical selectivity and size exclusion to retard the interfering species is the most well established approach. Permselectivity leads to a significant improvement of sensitivity, selectivity and stability of the electrochemical sensor. Nafion is a sulfonated tetrafluoroethylene copolymer, and imparts a negative charge that discriminatively prevents the transfer of anions and electrons, but allows the transport of cations. Their application to biosensors has been extensive [50,58,89,116], as they are an effective way of preventing electrode fouling and imposing some selectivity for glucose catalysis [249]. Undesirable anions such as organic acids (AA, UA), chloride anions and phosphate anions can be suitably repelled by the charge exclusive Nafion film, which greatly limits their transport to the electrode surface. Electropolymerised permselective coatings, such as polyphenol and overoxidised polypyrole, impart size exclusion as well as charge repulsion, so that macromolecules such as proteins are unable to foul the electrode surface. Electropolymerization offers several advantages as well, such as the simplicity of the experimental setup, ease of control and capability to address the modification solely on the device sensor [249,256].

Reduction of the oxidation overpotential to values cathodic of the interference oxidation is another option. Generally metal and metal oxide electrodes oxidise glucose at potentials of 0.4 to 0.7 V vs. SCE. This is a relatively high potential, and is therefore capable of oxidising a number of available species. The glucose active overpotential of gold electrodes has been successfully reduced by modification with partial monolayers of adatoms such as silver [48,190]. Oxidation peak potentials of ca. -0.5 V vs. Ag/AgCl were observed on the 1/3 Ag monolayer on Au(100) electrode. This was also observed for a porous PtPb electrode [48] in which the overpotential was reduced to -0.08V vs. Ag/AgCl and successfully avoided interference from AA, UA and AP.

In this latter case, the structure of the electrode may also have played a part in improving electroselectivity towards glucose. As discussed in the previous section, the surge in fabrication of nanomaterials has led to a dramatic increase in viable non-enzymatic glucose sensors. The nano dimensions of a sensor would theoretically aide the sluggish kinetics of the electro-oxidation of glucose, by enhancing surface bound reactions and making no difference to mass transport limited electrode processes such as AA oxidation. This has been observed in a number of publications of late, and has demonstrated that a reduction in oxidation potential is not necessarily needed [45,84,257].

6.5. The requirements of glucose monitoring

Blood glucose monitoring (BGM) is one of the main applications of glucose sensors. Three commercial and clinical systems are presently in place, all involving enzymatic approaches. One accurate approach is known as the hexakinase method, but it is a lab based approach and not viable for portable, self-testing BGM. The other methods, as discussed in Section 6.2, involve enzymatic electrochemical glucose sensors based on either glucose oxidase or glucose dehydrogenase as their catalytic component. However a number of factors affect BGM that need addressing and overcoming as the technology evolves.

At present the main method of monitoring blood glucose levels is to self-test a blood sample taken from a finger prick or similar. This has been the established method for a long time, and allows the patient to take a sample reading of their blood glucose levels at various points throughout the day. Having an in-vitro system also allows for more liberties with respect to the electrode set-up, in that biological considerations such as immune response and toxicity are negligible. Another approach to blood glucose monitoring is the use of in-vivo glucose sensors for continuous glucose sensing. This approach would give glucose concentrations in real time, and provide a better overall understanding of blood glucose fluctuations.

6.5.1 In vitro glucose monitoring: Single point 'fingerstick' glucose sensors

At present fingerstick glucose sensors are disposable, screen printed enzyme electrode strips, and are produced by a variety of companies including Abbott Diabetes Care [258], AccuChek [259], LifeScan [260] and Bayer [261]. The fabrication process for these disposable sensors involves mass production of a complex mixture of enzymes, mediators and stabilisers which is screen printed in a thick film onto a suitable substrate. The electrode system is self-contained with a working and reference electrode, and as such a small blood sample should cover the entire set up and provide its own electrolyte. Blood samples range from 0.3 to 1.5 μL for modern testing strips, considerably less than the 3 to 10 μL samples required merely 10 years ago [262] thus indicating the rapid advancement and sophistication of fabrication methods and biosensor technology.

Table 6 lists the commercially available single use fingerstick strips of four of the companies involved in their production. The table compares the electrochemical assay, glucose range, temperature and humidity dependence, sample size and testing time.

As can be seen, only the LifeScan Onetouch employs the glucose oxidase enzyme in its sensor. GDH based enzyme electrodes have gradually replaced GOx systems in the past decade due to the error imparted by variable oxygen levels on the latter approach. GDH enzymes are not influenced by oxygen, yet are less substrate specific and stable. The substrate specify issues of GDH-PQQ were of particular concern at the turn of the 20th century, as discussed in Section 6.4.3 with regard to possible overestimations of blood glucose in patients receiving treatments such as peritoneal dialysis. In 2006 Tsujimura et al [16] reported a novel FAD dependent glucose dehydrogenase (GDH-FAD) enzyme, which was used in collaboration with a ferricyanide mediator. The resulting sensor gave a linear range of 5-30 mM, a highly selective amperometric response to glucose, was insensitive to oxygen, and also showed negligible response to other saccharides. This is employed by Abbott in their most recent Freestyle strip range [20].

Table 6: *Commercially available glucose sensors for single use, in vitro analysis*

Manufacturer	Model	Range (mM)	Enzyme	Sample size (µL)	Test t (s)	Oper. T	Oper. humid	Haematocrit	Mediator
Lifescan	OneTouch UltraEasy	1.1 - 33.3	GOx	1	5	6– 44°C	10-90 %	30 - 55%	--
AccuChek	Aviva	1.0 - 30.0	GDH-PQQ	0.6	5	6 – 44°C	10-90 %	20 - 70%	$Fe(CN)_6^{3-}$
Abbott	FreeStyle Lite	1.1 - 27.8	GDH-FAD	0.3	5	4 - 40°C	5% to 90%	15 - 65%	$Os^{2+/3+}$
Bayer	Ascensia Contour	1.0 - 30.0	GDH-FAD	0.6	5	5 - 45°C	10 - 93%	--	$Fe(CN)_6^{3-}$

Although they are the only commercially available systems for BGM, enzyme based glucose sensors have numerous intrinsic flaws and numerous sources of errors. A recent review by Ginsberg [263] explores the factors affecting blood glucose monitoring, in which he identifies four main sources; strip factors, physical factors, patient factors and pharmacological factors.

Strip factors include the surface area coverage of enzyme in the sample wells, the use of a mediator which is unstable in the oxidised form and at high temperatures, and the detrimental effect of high temperatures and high humidity on the performance and lifetime of the strips. The thermal instability is problematic to fabrication as well as storage methods, and NAD centred GDH requires a more complicated oxidation system to GOx and PQQ [16]. With regard to physical factors, the effect of altitude and temperature were explored to test the accuracy of various test strips. It was found that altitude affected GOx based meters by 6-15 %, whereas the non-oxygen dependent GDH systems observed accuracy within 5%. On testing at a temperature of 8°C the accuracy of the five strips tested varied considerably, regardless of the enzyme base with errors of 5-7% either positively or negatively [263].

Patient error is more difficult to address, as it involves miss use of the glucose monitor, and variation in haematocrit, the ratio of red blood cells to plasma in the whole blood. The former can be resolved by appropriate design and instruction of the meter, yet the latter is the percentage level of red blood cells in the blood, which varies considerably. Serious errors in BGM arise from variable haematocrit levels, with studies showing an error as large as 40% at very low haematocrit [264]. Lab based laboratory tests monitor plasma glucose levels rather than whole blood, thus observing glucose levels generally 10-15% greater than in the whole blood. Self BGM cannot be as specific, and tests the whole blood, therefore needs to account for variable haematocrit in its design.

In a bid to reduce patient discomfort in sample acquisition blood sample sizes have vastly decreased and are now of sub microlitre volumes. However, on the reduction of the sample size, the margin for error by contamination is increased. As Ginsberg discusses [263], if the patient has not washed their hands a contamination of just 1 μg of glucose could raise the glucose reading of a 0.3 μL blood sample by 300 mg/dL. This is an error perhaps best addressed by educating patients rather than attempting to account for external surface contamination in the sensor. This is an approach that would suit addressing pharmacological errors also, as were discussed in Section 4 and include the use of prescription drugs and non-glucose sugar treatments.

The introduction of 'wired' enzyme electrodes by Heller et al completely altered the conventional approach to glucose sensing [19]. Heller et al presented an innovative design that used parallel facing carbon working electrode and Ag/AgCl counter electrode, merely 50 μm apart [20,22]. This reduced the electrode area, and produced a faster assay, as well as imposing a strict control on the sample volume. To overcome the problem of a large capacitance due to rapid electron shuttling between the facing electrodes, a wired enzymatic system was proposed that utilised an $Os^{2+/3+}$ redox mediator with a formal potential between -0.2 and 0.0 V relative to the Ag/AgCl counter electrode. As such, the oxidised mediator could only be reduced by the enzyme thus preventing a current to be passed within the

electrode cell. The very small sample volume also ensures the complete, rapid oxidation of glucose, as opposed to partial oxidation of glucose or mediator as observed in other designs; therefore a more accurate determination of blood glucose is possible.

6.5.2 In vivo glucose monitoring: Continuous glucose sensors

Single point fingerstick glucose sensors have significantly improved diabetes control and blood glucose management over the past four decades. However, a number of clinical trials have shown that tighter glycemic control is required to obtain a significant reduction in complications related to diabetes [265-267]. Although instantaneously accurate, intermittent in vitro blood testing does not give a suitable picture of glycemic behaviour, providing a static overview of a continually changing system. In particular the time spent in high or low glycemic episodes is grossly misrepresented, and as such a gradual deterioration in health is still observed. The answer to this problem is to increase the frequency of blood glucose sampling, without however, increasing the frequency of the painful and inconvenient fingerstick monitoring. Over the past five years continuous glucose monitors have emerged to achieve exactly this.

Continuous glucose monitors (CGM) are in vivo electrochemical sensors inserted into the subcutaneous tissue of the upper arm or stomach for a period a days. During this time the glucose level of the interstitial fluid is continually monitored with readings taken as frequently as every minute and calibrated daily by a fingerstick strip test. The amperometric signal is recorded and the data is transferred wirelessly to a receiver which then assesses the glycemic levels. The original CGMs were analysed retrospectively by health workers performing 3-day blind studies. In 2000 the first real time continuous glucose monitor was commercialised [268], yet the past decade has seen a significant improvement in CGM technology. Presently, three CGM systems are available on the market; the Freestyle Navigator (Abbot Diabetes Care), Guardian ® Real-Time (MiniMed), and DexCom Seven.

In a recent study [269] the numerical and clinical accuracy of the CGM systems were compared, concluding that the Navigator and Guardian had comparable numerical accuracy but the DexCom observed a 30% higher value.

CGM systems pose additional complications to the issues associated with in vitro testing. First, the electrode needs to be able to undergo constant, stable and accurate amperometric detection, without undergoing electrode fouling, deterioration of the surface, or saturation of the surface. Secondly, the electrode must be very small so as to achieve the least discomfort possible. Thirdly, they must be completely non-toxic, without the possibility of any leachable materials. Finally, the sensor must be biocompatible. That is to say, it must cause the minimal immune response, as inflammation of the insertion site and surrounding tissue will produce a misrepresentation of the blood glucose, and significantly increase the risk of biofouling [270].

One of the most successful CGMs currently in use is the Abbot Freestyle Navigator [266,269], and it accounts for the above complications in a number of innovative ways. It consists of a 0.6 mm wide plastic substrate in which the working, reference and counter electrodes are layered by screen printing [20]. On the carbon working electrode the wired enzyme technology is once again utilised, and is covered by a flux-limiting membrane. Unlike the strip technology, the CGM sensor uses a GOx-FAD enzyme centre. This is combined with an osmium redox mediator using a conductive hydrogel which binds the electroactive components to the sensor, yet allows for the diffusion of glucose, glucolactone and water soluble species [5,20]. One of the most important properties of the sensor is the bound redox mediator, which therefore renders the sensor non leachable. The use of $Os^{2+/3+}$ allows for the application of a low potential of just 0.04 V vs. Ag/AgCl. The CGM has been successfully administered for over 5 days in trials [266], and requires no more than a one-point calibration from a drawn sample once a day.

6.6. Requirements of non-enzymatic blood glucose sensors

The intrinsic instability of enzymes and oxygen limitation encountered in glucose monitoring strips are two persistent and significant problems with commercial, in-vitro glucose sensors. Elimination of the bio-component and dependence on oxygen is therefore a desirable advancement of glucose sensors, and is the reason practical and viable non-enzymatic glucose sensors that supersede modern, commercially available systems are so highly sought after. The list provided in Table 7 outlines the minimum requirements (in addition to the data in Table 6) of non-enzymatic glucose sensors if they are to compete or indeed replace the enzymatic industry. The main areas for concern are selectivity, which is evidently still a problem for enzymatic systems, and sensitivity in a specific media i.e. blood at pH ca. 7.4.

At present research regarding chemical interferences at non-enzymatic electrodes is positive, with increasing selectivity being observed with regards to AA and UA in particular [41,71,84,271]. Less research has been conducted into the effects of non-glucose sugars however [159,190,272]. Aoun found that a gold electrode single crystal electrode modified with a silver ad-layer gave a response dependent on the sugar structure [190]. Glucose is an aldose type sugar, along with galactose, xylose, ribose, arabinose and mannose to name a few. They are monosaccharides which possess one aldehyde group per molecule, and therefore they all possess a single hemiacetalic carbon atom. Aoun found that only the aldose type monosaccharides, and also the aldose disaccharides maltose and lactose, gave a significant oxidation current. Ketose type monosaccharides, in which the molecule has a single ketone group, did not oxidise at the modified gold electrode [190]. Choudhry et al [272] found a copper oxide screen printed electrode to have a modest selectivity for glucose over maltose, sucrose and fructose, with the latter not giving any response, and the former two, both containing a glucose molecule, gave oxidative responses at potentials 0.39 and 0.46 V more positive of the glucose response respectively.

Sensitivity is considerably greater at non-enzymatic electrodes, with enzymatic systems stating 'high currents' of approximately 5 $\mu AmM^{-1}cm^{-2}$ [30,243,273,274], relative to currents of generally 100 $\mu AmM^{-1}cm^{-2}$ or more reported at non-enzymatic sensors.

With regard to the ever-decreasing sample size, the potential for nano-dimensioned, non-enzymatic electrodes far exceeds the constraints of large macrosized enzymes, potentially allowing for even smaller sample sizes and higher sensitivity. The benefits of inorganic fabrication methods also compete favourably against biosensor fabrication, as the delicate nature of the enzyme need not be considered, thus allowing for more diverse, rapid and lower cost processes. This offers another advantage to non-enzymatic glucose sensing; the ability to reuse an electrode. The long term stability of non-enzymatic electrodes varies widely depending on the fabrication method. Yet sustained, relatively high sensitivity has been observed and non-enzymatic glucose electrodes and their renewable properties demonstrated [70,71,93,157]. This may have a more significant application to in-vivo glucose monitoring, though renewable and robust in vitro sensors would also be cost effective and practical.

Although not the case for all non-enzymatic electrodes discussed here, a large number require an alkaline medium to operate [59,69,96,190,275-278], and as such non-enzymatic electrodes face their greatest problem in biocompatibility. For the most part, this applies to nickel and copper electrodes, with the rapid development of carbon based non-enzymatic electrodes is moving towards more biologically compatible sensors.

6.7 Other applications of non-enzymatic glucose electrodes

Glucose electro-oxidation is not only useful to blood glucose monitoring but may be applied to other areas such as the food industry, industrial processes, and the development of fuel cells and batteries. Although they have a potential for use in the blood glucose industry, non-enzymatic sensors are possibly of greater use in non-physiological situations. This is

primarily due to their lower selectivity, as industrial systems have a greater opportunity to impose selectivity via chromatographic methods, or indeed they may involve 'clean' systems which do not contain interference species. The high electrocatalytic activity of non-enzymatic electrodes vastly outweighs that of their enzymatic counterparts, and as such they are potentially useful in the fuel cell industry. Furthermore, the intrinsic thermal stability, chemical resistance and long term sensitivity observed in a number of non-enzymatic systems place them in a better position for experimentally extreme environments.

6.7.1 Industrial processes

In their application as sensors, non-enzymatic glucose electrodes may find extensive application as sensors in bio-industrial processes. Such industry includes fermentation plants, in which strict environmental controls are in place for optimum production. The need for diverse and adaptable sensors with a good, stable performance in variable conditions is therefore required. Enzymatic systems require optimum conditions themselves, therefore are not always applicable to industrial processes. Other bioprocesses include large scale synthesis in the pharmaceuticals industry, in which a control on the formation and consumption of key analytes or reactants such as glucose is required. A number of enzymatic glucose sensors have been developed and used in monitoring fermentation processes [279-282], yet non-enzymatic electrodes have yet to be practically applied.

6.7.2 Quality control

In the food industry quality control of food and drink products is essential, and measuring the quantity of various sugars to validate the quality, maturity, authenticity and nutritional value of the product is of considerable importance. Unlike in-situ environments such as inside a fermentor or reactor, analytical assessment of final products can involve secondary

separation stages to enhance selectivity. The use of flow injection analysis, high pressure liquid chromatography and capillary electrophoresis is common in the food industry, yet a responsive, highly sensitive sensor is essential none the less. In Table 2 non-enzymatic electrodes have been applied in collaboration with these stages, and the considerably lower limits of detection demonstrate the high sensitivity of the electrodes towards the analyte [100,129,133,137,144,145]. Chromatographic stages are not always necessary however. Nonenzymatic glucose electrodes have been used to discriminatively determine aldose type sugars (e.g. glucose, xylose and galactose) versus ketose type sugars (e.g. fructose and sorbose) [190,272].

6.7.3 Fuel cells

In the controlled environment of a fuel cell, that is not restrained by the problems associated with physiological conditions, non-enzymatic glucose fuel cells are understandably under extensive investigation. As climate change an environmental issues take scientific precedence in the last decade, the search for renewable power sources that are carbon neutral are highly sought, and as glucose is readily harvested in natural sugars and produced as a by-product to photosynthesis, it is an ideal fuel source to replace fossil fuels. Furthermore, the desire to fabricate a biologically powered artificial organ such as a heart or pacemaker [180,283-287] has been as great as to develop a glucose sensor. Glucose, or indeed other saccharide fuel cells, may therefore one day replace batteries in portable devices to engines in vehicles.

In comparison to other fuel cells the lure of a glucose based system is the potential to derive power from a degradable biomass, than is non-toxic, non-flammable and readily and renewably available, thus obtaining a high energy output from a sustainable source. Furthermore, glucose theoretically has a very high energy density, with the capacity to release up to 24 electrons per glucose molecule on the basis of complete oxidation to CO_2

and H_2O [288]. The complete oxidation in a fuel cell would theoretically yield the processes in equation 6.7 at the anode and cathode, occurring at a formal potential of 1.23 V and releasing 2870 kJ mol^- in energy [289].

$$\begin{aligned} &\text{Anode} && C_6H_{12}O_6 + 24OH^- \rightarrow 6CO_2 + 18H_2O + 24e^- \\ &\text{Cathode} && 6O_2 + 12H_2O + 24e^- \rightarrow 24OH^- \\ &\text{Overall} && C_6H_{12}O_6 + 6O_2 \rightarrow 6CO_2 + 6H_2O \end{aligned} \qquad (6.7)$$

The potential energy stored in glucose is substantial, yet enzymatic, and most non-enzymatic electrodes only oxidize glucose to the glucolactone, a mere two electron process that yields 250 kJ of energy [289]. This will always be the case at enzymatic systems, yet non-enzymatic catalysts have the potential to fully oxidize glucose. It has already been claimed by Larew et al [176] that glucose may be oxidized beyond gluconolactone on a gold electrode, depending on the electrode potential and on the glucose concentration. Mass spectrometry has also been used and shown signs of CO_2 formation at potentials well into the oxide region for gold [181], and Kokoh et al. used HPLC to analyze the products, and observed not only glucolactone and gluconic acid, but products derivative of further glucose oxidized [290]. Applying a high potential would defeat the object of a fuel cell, yet considering the significant decrease in operating potential for the initial glucose oxidation at modified gold electrodes [42,190,191], the potential required to fully or more substantially oxidize glucose may be shifted also. Such an electrode was reported by Jin and Taniguchi [291]in 2007 using a silver modified gold electrode.

A number of non-enzymatic glucose fuel cells have now been reported on a range of electrode materials including silver modified gold [291], silver microfibers [292] platinum [293] and very recently carbonized nanofibres [294]. The application of non-enzymatic glucose electrocatalysts towards fuel cells is an extensive topic in itself, and a number of comprehensive reviews on the subject have been recently published [288,289].

6.8. Conclusions

It is evident that the field of non-enzymatic glucose sensing electrodes is developing rapidly given the vast number of publications observed in the past 10 years. The surge in interest and improved success no doubt coincides with the development of nanomaterials, allowing for higher surface areas, improved glucose oxidation kinetics, and better selectivity. However, it is also evident that much of the research surrounding non-enzymatic glucose sensors is becoming repetitive and greatly lacks innovative approaches beyond designing new nanomaterials. The fabrication of a variety of nanostructures and modification of relatively new electrode materials, though aesthetically pleasing in the publication, are posing no significant improvement relative to enzymatic electrode design. The sophisticated and innovative 'wired' enzyme design developed by Heller et al [19,20,295] over the past 20 years epitomises the idea of a new and exciting electrochemical approach, and it is a comparable advancement that is missing from non-enzymatic research. This advancement may depend on research into new carbon based materials, presently a very hot topic however. The technology involving carbon nanotubes, graphene, carbon nanofibres and doped diamond is certain to rapidly develop in the near future, possibly leading to a useful non-enzymatic glucose sensor.

Although there is a clearer understanding of the mechanisms of direct glucose oxidation at metals and carbon electrodes they remain uncertain, with frequent contradictions observed in the literature. As such a universally agreed mechanism for non-enzymatic glucose oxidation remains unresolved, and as such real modification of electrodes cannot proceed effectively without this basic understanding. Non-enzymatic glucose electrodes offer high sensitivity, the possibility of long term stability, a resistance to thermal implications, and a low cost, simple and reproducible fabrication method, and as such they require a renewed approach to their design and development. However, they have yet to achieve all the requirements of a viable blood glucose sensor as stipulated in Tables 6

and 7, and have some limitations to overcome before they supersede enzyme technology, though the goal of non-enzymatic glucose sensing is close to being realized.

6.9. References

[1] S. Wild, G. Roglic, A. Green, R. Sicree,H. King, *Diabetes Care* **2004** *27* 1047.

[2] J. Wang, *Chem. Rev.* **2008** *108* 814.

[3] Q. Yi, W. Huang, W. Yu, L. Li,X. Liu, *Electroanalysis* **2008** *20* 2016.

[4] S. Park, H. Boo,T. D. Chung, *Anal. Chim. Acta* **2006** *556* 46.

[5] A. Heller and B. Feldman, *Chem Rev* **2008** *108* 2482.

[6] C. L. C. Jr and C. Lyons, *Annals of the New York Academy of Sciences* **1962** *102* 29.

[7] S. J. Updike and G. P. Hicks, *Nature* **1967** *214* 986.

[8] G. G. Guilbault and G. J. Lubrano, *Anal. Chim. Acta* **1973** *64* 439.

[9] R. Wilson and A. P. F. Turner, *Biosens. Bioelectron.* **1992** *7* 165.

[10] D. A. Gough, J. Y. Lucisano,P. H. S. Tse, *Anal. Chem.* **1985** *57* 2351.

[11] J. C. Armour, J. Y. Lucisano, B. D. McKean,D. A. Gough, *Diabetes* **1990** *39* 1519.

[12] J. Wang and F. Lu, *J. Am. Chem. Soc.* **1998** *120* 1048.

[13] J. Wang, J. -. Mo, S. Li,J. Porter, *Anal. Chim. Acta* **2001** *441* 183.

[14] A. E. G. Cass, G. Davis, G. D. Francis, H. A. O. Hill, W. J. Aston, I. J. Higgins, E. V. Plotkin, L. D. L. Scott,A. P. F. Turner, *Anal. Chem.* **1984** *56* 667.

[15] A. Mulchandani and S. Pan, *Anal. Biochem.* **1999** *267* 141.

[16] S. Tsujimura, S. Kojima, K. Kano, T. Ikeda, M. Sato, H. Sanada,H. Omura, *Biosci. , Biotechnol. , Biochem.* **2006** *70* 654.

[17] M. G. Loughran, J. M. Hall,A. P. F. Turner, *Electroanalysis* **1996** *8* 870.

[18] K. Lau, S. A. L. de Fortescu, L. J. Murphy,J. M. Slater, *Electroanalysis* **2003** *15* 975.

[19] C. Taylor, G. Kenausis, I. Katakis,A. Heller, *J. Electroanal. Chem.* **1995** *396* 511.

[20] A. Heller and B. Feldman, *Acc. Chem. Res.* ACS in press.

[21] F. Mao and A. Heller, *Preparation of transition metal complexes with (pyridyl)imidazole ligands for use in enzyme-based electrochemical sensor,* **(2003)** 2002-143300; 2001-290537, p. 23.

[22] A. Heller, B. J. Feldman, J. Say, M. S. Vreeke,M. F. Tomasco, *Small volume in vitro analyte sensor.* **(1998)**, 98-US2652; 97-795767, p. 83.

[23] S. Wu, H. Ju,Y. Liu, *Adv. Funct. Mater.* **2007** *17* 585.

[24] S. Bao, C. M. Li, J. Zang, X. Cui, Y. Qiao,J. Guo, *Adv. Funct. Mater.* **2008** *18* 591.

[25] Y. Wang and F. Caruso, *Chem. Commun.* **2004** 1528.

[26] J. Wu and Y. Qu, *Anal Bioanal Chem* **2006** *385* 1330.

[27] F. Palmisano, P. G. Zambonin, D. Centonze,M. Quinto, *Anal. Chem.* **2002** *74* 5913.

[28] C. G. J. Koopal, A. A. C. M. Bos,R. J. M. Nolte, *Sens. Actuators, B* **1994** *18* 166.

[29] Roche LTD, *Accu Chek Aviva, http://www.accu-chek.co.uk,* 2010/03/16.

[30] J. Li and X. Lin, *Biosens. Bioelectron.* **2007** *22* 2898.

[31] B. Wu, G. Zhang, S. Shuang,M. M. F. Choi, *Talanta* **2004** *64* 546.

[32] K. Han, Z. Wu, J. Lee, I. Ahn, J. W. Park, B. R. Min,K. Lee, *Biochem. Eng. J.* **2005** *22* 161.

[33] S. A. Wring, J. P. Hart, L. Bracey,B. J. Birch, *Anal. Chim. Acta* **1990** *231* 203.

[34] J. D. Newman and A. P. F. Turner, *Anal. Chim. Acta* **1992** *262* 13.

[35] W. Loeb, *Biochem. Z.* **1909** *17* 132.

[36] H. Wroblowa, B. J. Piersma,J. O. Bockris, *J. Electroanal. Chem.* **1963** *6* 401.

[37] J. O. Bockris, B. J. Piersma,E. Gileadi, *Electrochim. Acta* **1964** *9* 1329.

[38] J. Huang, *Chem. Commun.* **2009** 1270.

[39] J. Huang, *Electroanalysis* **2008** *20* 2229.

[40] C. Chou, J. Chen, C. Tai, I. -. Sun,J. Zen, *Electroanalysis* **2008** *20* 771.

[41] P. Holt-Hindle, S. Nigro, M. Asmussen,A. Chen, *Electrochem. Commun.* **2008** *10* 1438.

[42] Y. Bai, W. Yang, Y. Sun,C. Sun, *Sens. Actuators, B* **2008** *B134* 471.

[43] Y. Lee, D. Park, J. Park,Y. Kim, *Sensors* **2008** *8* 6154.

[44] S. Cho and C. Kang, *Electroanalysis* **2007** *19* 2315.

[45] Y. Song, D. Zhang, W. Gao,X. Xia, *Chem. Eur. J.* **2005** *11* 2177.

[46] Y. Li, Y. Song, C. Yang,X. Xia, *Electrochem. Commun.* **2007** *9* 981.

[47] J. C. Ndamanisha and L. Guo, *Bioelectrochemistry* **2009** *77* 60.

[48] J. Wang, D. F. Thomas,A. Chen, *Anal. Chem.* **2008** *80* 997.

[49] S. Joo, S. Park, T. D. Chung,H. C. Kim, *Anal. Sci.* **2007** *23* 277.

[50] Y. J. Lee, D. J. Park,J. Y. Park, *IEEE Sens. J.* **2008** *8* 1922.

[51] Y. Myung, D. M. Jang, Y. J. Cho, H. S. Kim, J. Park, J. Kim, Y. Choi,C. J. Lee, *J. Phys. Chem. C* **2009** *113* 1251.

[52] K. B. Male, S. Hrapovic, Y. Liu, D. Wang,J. H. T. Luong, *Anal. Chim. Acta* **2004** *516* 35.

[53] J. Wang, X. Sun, X. Cai, Y. Lei, L. Song,S. Xie, *Electrochem. Solid-State Lett.* **2007** *10* J58.

[54] L. Meng, J. Jin, G. Yang, T. Lu, H. Zhang,C. Cai, *Anal. Chem.* **2009** *81* 7271.

[55] L. Zheng, J. Zhang,J. Song, *Electrochim. Acta* **2009** *54* 4559.

[56] J. Chen, W. Zhang,J. Ye, *Electrochem. Commun.* **2008** *10* 1268.

[57] L. Li, W. Zhang,J. Ye, *Electroanalysis* **2008** *20* 2212.

[58] H. Cui, J. Ye, W. Zhang, C. Li, J. H. T. Luong,F. Sheu, *Anal. Chim. Acta* **2007** *594* 175.

[59] X. Kang, Z. Mai, X. Zou, P. Cai,J. Mo, *Anal. Biochem.* **2007** *363* 143.

[60] L. Li and W. Zhang, *Microchim. Acta* **2008** *163* 305.

[61] F. Xiao, F. Zhao, D. Mei, Z. Mo,B. Zeng, *Biosens. Bioelectron.* **2009** *24* 3481.

[62] X. Zhang, G. Wang, A. Gu, Y. Wei,B. Fang, *Chem. Commun.* **2008** 5945.

[63] X. Zhang, G. Wang, W. Zhang, Y. Wei,B. Fang, *Biosens. Bioelectron.* **2009** *24* 3395.

[64] J. Ye, Y. Wen, W. D. Zhang, L. M. Gan, G. Q. Xu,F. Sheu, *Electrochem. Commun.* **2004** *6* 66.

[65] Y. Zhou, S. Yang, Q. Qian,X. Xia, *Electrochem. Commun.* **2009** *11* 216.

[66] J. Yuan, K. Wang,X. Xia, *Adv. Funct. Mater.* **2005** *15* 803.

[67] L. Rong, C. Yang, Q. Qian,X. Xia, *Talanta* **2007** *72* 819.

[68] S. Buratti, B. Brunetti,S. Mannino, *Talanta* **2008** *76* 454.

[69] K. E. Toghill, L. Xiao, M. A. Phillips,R. G. Compton, *Sens. Actuators, B* **2010** *B147* 642.

[70] Y. Liu, H. Teng, H. Hou,T. You, *Biosens. Bioelectron.* **2009** *24* 3329.

[71] A. Safavi, N. Maleki,E. Farjami, *Biosens. Bioelectron.* **2009** *24* 1655.

[72] Y. Ma, J. Di, X. Yan, M. Zhao, Z. Lu,Y. Tu, *Biosens. Bioelectron.* **2009** *24* 1480.

[73] B. K. Jena and C. R. Raj, *Chem. Eur. J.* **2006** *12* 2702.

[74] Z. Cao, Y. Zou, C. Xiang, L. Sun,F. Xu, *Anal. Lett.* **2007** *40* 2116.

[75] J. Lu, I. Do, L. T. Drzal, R. M. Worden,I. Lee, *ACS Nano* **2008** *2* 1825.

[76] E. Scavetta, S. Stipa,D. Tonelli, *Electrochem. Commun.* **2007** *9* 2838.

[77] E. Scavetta, L. Guadagnini, A. Mignani,D. Tonelli, *Electroanalysis* **2008** *20* 2199.

[78] L. Lu, L. Zhang, F. Qu, H. Lu, X. Zhang, Z. Wu, S. Huan, Q. Wang, G. Shen,R. Yu, *Biosens. Bioelectron.* **2009** *25* 218.

[79] W. Wang, L. Zhang, S. Tong, X. Li,W. Song, *Biosens. Bioelectron.* **2009** *25* 708.

[80] E. Reitz, W. Jia, M. Gentile, Y. Wang,Y. Lei, *Electroanalysis* **2008** *20* 2482.

[81] T. Huang, K. Lin, S. Tung, T. Cheng, I. -. Chang, Y. Hsieh, C. Lee,H. Chiu, *J. Electroanal. Chem.* **2009** *636* 123.

[82] Q. Shen, L. Jiang, H. Zhang, Q. Min, W. Hou,J. Zhu, *J. Phys. Chem. C* **2008** *112* 16385.

[83] Y. Bai, Y. Sun,C. Sun, *Biosensors & Bioelectronics* **2008** *24* 579.

[84] D. Luo, L. Wu,J. Zhi, *ACS Nano* **2009** *3* 2121.

[85] D. Rathod, C. Dickinson, D. Egan,E. Dempsey, *Sens. Actuators, B* **2010** *B143* 547.

[86] Z. Zhuang, X. Su, H. Yuan, Q. Sun, D. Xiao,M. M. F. Choi, *Analyst* **2008** *133* 126.

[87] C. Batchelor-McAuley, G. G. Wildgoose, R. G. Compton, L. Shao,M. L. H. Green, *Sens. Actuators, B* **2008** *B132* 356.

[88] S. Y. Ly, *Curr. Anal. Chem.* **2009** *5* 59.

[89] W. Gorski and R. T. Kennedy, *J. Electroanal. Chem.* **1997** *424* 43.

[90] T. Watanabe, T. A. Ivandini, Y. Makide, A. Fujishima,Y. Einaga, *Analytical Chemistry* **2006** *78* 7857.

[91] J. Zhao, F. Wang, J. Yu,S. Hu, *Talanta* **2006** *70* 449.

[92] S. Tong, W. Wang, X. Li, Y. Xu,W. Song, *J. Phys. Chem. C* **2009** *113* 6832.

[93] A. Salimi and M. Roushani, *Electrochem. Commun.* **2005** *7* 879.

[94] M. Yousef Elahi, H. Heli, S. Z. Bathaie,M. F. Mousavi, *J. Solid State Electrochem.* **2006** *11* 273.

[95] M. Li, S. Xu, F. Ni, Y. Wang, S. Chen,L. Wang, *Microchim. Acta* **2009** *166* 203.

[96] M. Jafarian, F. Forouzandeh, I. Danaee, F. Gobal,M. G. Mahjani, *J. Solid State Electrochem.* **2009** *13* 1171.

[97] S. Sattayasamitsathit, P. Thavarungkul, C. Thammakhet, W. Limbut, A. Numnuam, C. Buranachai,P. Kanatharana, *Electroanalysis* **2009** *21* 2371.

[98] T. A. Ivandini, R. Sato, Y. Makide, A. Fujishima,Y. Einaga, *Diamond Relat. Mater.* **2004** *13* 2003.

[99] C. Tai, J. Chang,J. Zen, *Chem. Commun.* **2009** 6083.

[100] T. You, O. Niwa, Z. Chen, K. Hayashi, M. Tomita,S. Hirono, *Anal. Chem.* **2003** *75* 5191.

[101] X. Li, Q. Zhu, S. Tong, W. Wang,W. Song, *Sens. Actuators, B* **2009** *B136* 444.

[102] A. Struebing, G. Wittstock, R. Szargan,G. Werner, *Fresenius' J. Anal. Chem.* **1996** *356* 274.

[103] I. G. Casella, M. Gatta, M. R. Guascito,T. R. I. Cataldi, *Anal. Chim. Acta* **1997** *357* 63.

[104] W. Zhao, J. Xu, C. Shi,H. Chen, *Electrochem. Commun.* **2006** *8* 773.

[105] Z. -. Chen and D. B. Hibbert, *J. Chromatogr. , A* **1997** *766* 27.

[106] L. Nagy, G. Nagy,P. Hajos, *Sens. Actuators, B* **2001** *B76* 494.

[107] C. Zhao, C. Shao, M. Li,K. Jiao, *Talanta* **2007** *71* 1769.

[108] P. Luo, F. Zhang,R. P. Baldwin, *Anal. Chim. Acta* **1991** *244* 169.

[109] J. Sue, C. Hung, W. Chen,J. Zen, *Electroanalysis* **2008** *20* 1647.

[110] M. Goto, H. Miyahara,D. Ishii, *J. Chromatogr.* **1990** *515* 213.

[111] K. Kano, K. Takagi, K. Inoue, T. Ikeda,T. Ueda, *J. Chromatogr. , A* **1996** *721* 53.

[112] A. Stitz and W. Buchberger, *Electroanalysis* **1994** *6* 251.

[113] M. Uto, K. Kodama, K. Ishimori, Y. Kudo, S. Hoshi,M. Matsubara, *Anal. Sci.* **1994** *10* 835.

[114] R. E. Reim and R. M. Van Effen, *Anal. Chem.* **1986** *58* 3203.

[115] L. E. Welch, D. A. Mead Jr.,D. C. Johnson, *Anal. Chim. Acta* **1988** *204* 323.

[116] D. S. Bindra and G. S. Wilson, *Anal. Chem.* **1989** *61* 2566.

[117] J. C. Fanguy and C. S. Henry, *Analyst* **2002** *127* 1021.

[118] Y. Xie and C. O. Huber, *Anal. Chem.* **1991** *63* 1714.

[119] T. R. I. Cataldi, I. G. Casella, E. Desimoni,T. Rotunno, *Anal. Chim. Acta* **1992** *270* 161.

[120] T. R. I. Cataldi, E. Desimoni, G. Ricciardi,F. Lelj, *Electroanalysis* **1995** *7* 435.

[121] A. S. Kumar, P. Chen, S. Chien,J. Zen, *Electroanalysis* **2005** *17* 210.

[122] J. Wang and Z. Taha, *Anal. Chem.* **1990** *62* 1413.

[123] M. d. S. M. Quintino, H. Winnischofer, M. Nakamura, K. Araki, H. E. Toma,L. Angnes, *Anal. Chim. Acta* **2005** *539* 215.

[124] E. Wang and A. Liu, *J. Electroanal. Chem.* **1991** *319* 217.

[125] S. V. Prabhu and R. P. Baldwin, *Anal. Chem.* **1989** *61* 852.

[126] I. G. Casella, E. Desimoni,A. M. Salvi, *Anal. Chim. Acta* **1991** *243* 61.

[127] M. Morita, O. Niwa, S. Tou,N. Watanabe, *J. Chromatogr. , A* **1999** *837* 17.

[128] J. M. Marioli and T. Kuwana, *Electroanalysis* **1993** *5* 11.

[129] J. M. Marioli, P. F. Luo,T. Kuwana, *Anal. Chim. Acta* **1993** *282* 571.

[130] P. F. Luo and T. Kuwana, *Anal. Chem.* **1994** *66* 2775.

[131] M. I. Mora and J. M. Marioli, *J. Liq. Chromatogr. Relat. Technol.* **2001** *24* 711.

[132] K. Kano, M. Torimura, Y. Esaka, M. Goto,T. Ueda, *J. Electroanal. Chem.* **1994** *372* 137.

[133] M. Vidotti, C. D. Cerri, R. F. Carvalhal, J. C. Dias, R. K. Mendes, S. I. Cordoba de Torresi,L. T. Kubota, *J. Electroanal. Chem.* **2009** *636* 18.

[134] I. G. Casella, M. Gatta,E. Desimoni, *J. Chromatogr. , A* **1998** *814* 63.

[135] I. G. Casella, M. R. Guascito,T. R. I. Cataldi, *Anal. Chim. Acta* **1999** *398* 153.

[136] I. G. Casella and M. Contursi, *Anal. Bioanal. Chem.* **2003** *376* 673.

[137] I. G. Casella and M. Gatta, *Electroanalysis* **2001** *13* 549.

[138] H. Chung, H. Yang, W. Kim,J. Park, *Anal. Chim. Acta* **2002** *471* 195.

[139] T. R. I. Cataldi, D. Centonze, I. G. Casella,E. Desimoni, *J. Chromatogr. , A* **1997** *773* 115.

[140] K. M. Manesh, P. Santhosh, A. Gopalan,K. Lee, *Anal. Biochem.* **2007** *360* 189.

[141] W. Surareungchai, W. Deepunya,P. Tasakorn, *Anal. Chim. Acta* **2001** *448* 215.

[142] F. D'Eramo, J. M. Marioli, A. H. Arevalo,L. E. Sereno, *Talanta* **2003** *61* 341.

[143] X. Cheng, S. Zhang, H. Zhang, Q. Wang, P. He,Y. Fang, *Food Chem.* **2007** *106* 830.

[144] S. Dong, S. Zhang, X. Cheng, P. He, Q. Wang,Y. Fang, *J. Chromatogr. , A* **2007** *1161* 327.

[145] F. D'Eramo, J. M. Marioli, A. A. Arevalo,L. E. Sereno, *Electroanalysis* **1999** *11* 481.

[146] F. Kurniawan, V. Tsakova,V. M. Mirsky, *Electroanalysis* **2006** *18* 1937.

[147] Q. Yi and W. Yu, *Microchim. Acta* **2009** *165* 381.

[148] S. Cherevko and C. Chung, *Sens. Actuators, B* **2009** *B142* 216.

[149] J. Yu, S. Lu, J. Li, F. Zhao,B. Zeng, *J. Solid State Electrochem.* **2007** *11* 1211.

[150] D. Feng, F. Wang,Z. Chen, *Sens. Actuators, B* **2009** *B138* 539.

[151] Y. Wang, D. Zhang, W. Zhang, F. Gao,L. Wang, *Anal. Biochem.* **2009** *385* 184.

[152] X. Chen, Z. Cai, Z. Lin, T. Jia, H. Liu, Y. Jiang,X. Chen, *Biosens. Bioelectron.* **2009** *24* 3475.

[153] J. Zhao, J. Yu, F. Wang,S. Hu, *Microchim. Acta* **2007** *156* 277.

[154] J. Zhao, D. Wu,J. Zhi, *J. Electroanal. Chem.* **2009** *626* 98.

[155] J. Zhao, L. Wu,J. Zhi, *Analyst* **2009** *134* 794.

[156] G. Yang, E. Liu, N. W. Khun,S. P. Jiang, *J. Electroanal. Chem.* **2009** *627* 51.

[157] J. Lee and S. Park, *Anal. Chim. Acta* **2005** *545* 27.

[158] T. Watanabe and Y. Einaga, *Biosens. Bioelectron.* **2009** *24* 2684.

[159] R. Ojani, J. Raoof,P. Salmany-Afagh, *J. Electroanal. Chem.* **2004** *571* 1.

[160] X. Peng, W. Li, X. Liu,P. Hua, *J. Appl. Polym. Sci.* **2007** *105* 2260.

[161] C. Fang, C. Yi, Y. Wang, Y. Cao,X. Liu, *Biosens. Bioelectron.* **2009** *24* 3164.

[162] L. Ozcan, Y. Sahin,H. Turk, *Biosens. Bioelectron.* **2008** *24* 512.

[163] Z. Cheng, E. Wang,X. Yang, *Biosens. Bioelectron.* **2001** *16* 179.

[164] Y. B. Vasil'ev, O. A. Khazova,N. N. Nikolaeva, *J. Electroanal. Chem. Interfacial Electrochem.* **1985** *196* 105.

[165] F. Largeaud, K. B. Kokoh, B. Beden,C. Lamy, *J. Electroanal. Chem.* **1995** *397* 261.

[166] A. A. Rossini and J. S. Soeldner, *J. Clin. Invest.* **1976** *57* 1083.

[167] B. A. Bauer and E. S. Younathan, *Biochem. Med.* **1980** *24* 293.

[168] K. Ryu, C. Kim, C. Park,B. Choi, *J. Am. Chem. Soc.* **2004** *126* 9180.

[169] B. Beden, F. Largeaud, K. B. Kokoh,C. Lamy, *Electrochim. Acta* **1996** *41* 701.

[170] D. Pletcher, *J. Appl. Electrochem.* **1984** *14* 403.

[171] R. R. Adzic, M. W. Hsiao,E. B. Yeager, *J. Electroanal. Chem.*. **1989** *260* 475.

[172] G. Kokkinidis, J. M. Leger,C. Lamy, *J. Electroanal. Chem.*. **1988** *242* 221.

[173] M. W. Hsiao, R. R. Adzic,E. G. Yeager, *J. Electrochem. Soc.* **1996** *143* 759.

[174] Y. B. Vasil'ev, O. A. Khazova,N. N. Nikolaeva, *J. Electroanal. Chem.* **1985** *196* 127.

[175] V. S. Bagotskii and Y. B. Vasil'ev, *Electrochim. Acta* **1967** *12* 1323.

[176] L. A. Larew and D. C. Johnson, *J. Electroanal. Chem.* **1989** *262* 167.

[177] L. D. Burke, *Electrochim. Acta* **1994** *39* 1841.

[178] S. Ernst, J. Heitbaum,C. H. Hamann, *J. Electroanal. Chem.* **1979** *100* 173.

[179] E. Skou, *Electrochim. Acta* **1977** *22* 313.

[180] M. L. B. Rao and R. F. Drake, *J. Electrochem. Soc.* **1969** *116* 334.

[181] A. E. Bolzan, T. Iwasita,W. Vielstich, *J. Electrochem. Soc.* **1987** *134* 3052.

[182] M. F. L. De Mele, H. A. Videla,A. J. Arvia, *J. Electrochem. Soc.* **1982** *129* 2207.

[183] V. S. Bagotskii, Y. B. Vasilev,O. A. Khazova, *J. Electroanal. Chem.* **1977** *81* 229.

[184] T. Zerihun and P. Grundler, *J. Electroanal. Chem.* **1998** *441* 57.

[185] M. F. L. De Mele, H. A. Videla,A. J. Arvia, *Bioelectrochem. Bioenerg.* **1983** *10* 239.

[186] L. D. Burke, *Gold Bull.* **2004** *37* 125.

[187] M. W. Hsiao, R. R. Adzic,E. B. Yeager, *Electrochim. Acta* **1992** *37* 357.

[188] X. Dai and R. G. Compton, *Anal. Sci.* **2006** *22* 567.

[189] B. Yin, H. Ma, S. Wang,S. Chen, *J. Phys. Chem. B* **2003** *107* 8898.

[190] S. B. Aoun, G. S. Bang, T. Koga, Y. Nonaka, T. Sotomura,I. Taniguchi, *Electrochem. Commun.* **2003** *5* 317.

[191] S. Ben Aoun, Z. Dursun, T. Koga, G. S. Bang, T. Sotomura,I. Taniguchi, *J. Electroanal. Chem.* **2004** *567* 175.

[192] M. Fleischmann, K. Korinek,D. Pletcher, *J. Electroanal. Chem.* **1971** *31* 39.

[193] H. Bode, K. Dehmelt,J. Witte, *Electrochim. Acta* **1966** *11* 1079.

[194] R. S. Schrebler Guzman, J. R. Vilche,A. J. Arvia, J. Appl. *Electrochem.*

1978 *8* 67.

[195] J. F. Wolf, L. S. R. Yeh,A. Damjanovic, *Electrochim. Acta***1981** *26* 409.

[196] P. Oliva, J. Leonardi, J. F. Laurent, C. Delmas, J. J. Braconnier, M. Figlarz, F. Fievet,A. De Guibert, *J. Power Sources* **1982** *8* 229.

[197] H. Bode, K. Dehmelt,J. Witte, *Z. Anorg. Allg. Chem.* **1969** *366* 1.

[198] N. R. Stradiotto, K. E. Toghill, L. Xiao, A. Moshar,R. G. Compton, *Electroanalysis* **2009** *21* 2627.

[199] K. E. Toghill, L. Xiao, N. R. Stradiotto,R. G. Compton, *Electroanalysis* **2010** *22* 491.

[200] G. Jin, R. Baron, L. Xiao,R. G. Compton, *J.of Nanosci. Nanotech.* **2009** *9* 2719.

[201] Y. G. Lee and T. Chou, *Electroanalysis* **2003** *15* 1589.

[202] B. Ballarin, R. Seeber, D. Tonelli,A. Vaccari, *J. Electroanal. Chem.* **1999** *463* 123.

[203] M. Fleischmann, K. Korinek,D. Pletcher, *J. Chem. Soc. , Perkin Trans. 2* **1972** 1396.

[204] B. Miller, *J. Electrochem. Soc.* **1969** *116* 1675.

[205] M. A. Ghanem, R. G. Compton, B. A. Coles, A. Canals, A. Vuorema, P. John,F. Marken, *Phys. Chem. Chem. Phys.* **2005** *7* 3552.

[206] I. -. Yeo and D. C. Johnson, *J. Electroanal. Chem.* **2000** *484* 157.

[207] H. Angerstein-Kozlowska, B. MacDougall,B. E. Conway, *J. Electrochem. Soc.* **1973** *120* 756.

[208] I. Fonseca, L. Jiang,D. Pletcher, *J. Electrochem. Soc.* **1983** *130* 2187.

[209] M. Khalid, N. Wasio, T. Chase,K. Bandyopadhyay, *Nanoscale Res. Lett.* **2010** *5* 61.

[210] S. Ben Aoun and I. Taniguchi, *Chem. Lett.* **2008** *37* 936.

[211] S. Ben Aoun and I. Taniguchi, *Chem. Lett.* **2007** *36* 898.

[212] A. Guiseppi-Elie, N. K. Shukla,S. Brahim, *Nanobiosensors: Carbon nanotubes in bioelectrochemistry.*, **2007**, p. 27/1.

[213] F. Sheu and J. Ye, *Mater. Technol.* **2004** *19* 11.

[214] R. G. Compton, J. S. Foord,F. Marken, *Electroanalysis* **2003** *15* 1349.

[215] J. H. T. Luong, K. B. Male,J. D. Glennon, *Analyst* **2009** *134* 1965.

[216] K. Peckova, J. Musilova,J. Barek, *Crit. Rev. Anal. Chem.* **2009** *39* 148.

[217] C. H. Goeting, F. Marken, A. Gutierrez-Sosa, R. G. Compton,J. S. Foord, *Diamond Relat. Mater.* **2000** *9* 390.

[218] C. H. Goeting, J. S. Foord, F. Marken,R. G. Compton, *Diamond Relat. Mater.* **1999** *8* 824.

[219] C. H. Goeting, F. Marken, A. Gutierrez-Sosa, R. G. Compton,J. S. Foord, *New Diamond Front Carbon Technol.* **1999** *9* 207.

[220] C. H. Goeting, F. Jones, J. S. Foord, J. C. Eklund, F. Marken, R. G. Compton, P. R. Chalker,C. Johnston, *J. Electroanal. Chem.* **1998** *442* 207.

[221] A. J. Saterlay, S. J. Wilkins, C. H. Goeting, J. S. Foord, R. G. Compton,F. Marken, *J. Solid State Electrochem.* **2000** *4* 383.

[222] R. G. Compton, F. Marken, C. H. Goeting, R. A. J. McKeown, J. S. Foord, G. Scarsbrook, R. S. Sussmann,A. J. Whitehead, *Chem. Commun.* **1998** 1961.

[223] R. Uchikado, T. N. Rao, D. A. Tryk,A. Fujishima, *Chem. Lett.* **2001** 144.

[224] K. Ohnishi, Y. Einaga, H. Notsu, C. Terashima, T. N. Rao, S. Park,A. Fujishima, *Electrochem. Solid-State Lett.* **2002** *5* D1.

[225] C. Batchelor-McAuley, C. E. Banks, A. O. Simm, T. G. J. Jones,R. G. Compton, *Analyst* **2006** *131* 106.

[226] A. O. Simm, X. Ji, C. E. Banks, M. E. Hyde,R. G. Compton, *ChemPhysChem* **2006** *7* 704.

[227] K. E. Toghill, G. G. Wildgoose, A. Moshar, C. Mulcahy,R. G. Compton, *Electroanalysis* **2008** *20* 1731.

[228] K. E. Toghill, L. Xiao, G. G. Wildgoose,R. G. Compton, *Electroanalysis* **2009** *21* 1113.

[229] M. D. Koppang, M. Witek, J. Blau,G. M. Swain, *Anal. Chem.* **1999** *71* 1188.

[230] Q. Chen, M. C. Granger, T. E. Lister,G. M. Swain, *J. Electrochem. Soc.* **1997** *144* 3806.

[231] H. Zhu, X. Lu, M. Li, Y. Shao,Z. Zhu, *Talanta* **2009** *79* 1446.

[232] H. Cui, J. Ye, X. Liu, W. Zhang,F. Sheu, *Nanotechnology* **2006** *17* 2334.

[233] S. Sotiropoulou and N. A. Chaniotakis, *Anal. Bioanal. Chem.* **2003** *375* 103.

[234] S. G. Wang, Q. Zhang, R. Wang,S. F. Yoon, *Biochem. Biophys. Res. Commun.* **2003** *311* 572.

[235] L. Siegert, D. K. Kampouris, J. Kruusma, V. Sammelselg,C. E. Banks, *Electroanalysis* **2009** *21* 48.

[236] K. S. Novoselov, A. K. Geim, S. V. Morozov, D. Jiang, Y. Zhang, S. V. Dubonos, I. V. Grigorieva,A. A. Firsov, *Science* **2004** *306* 666.

[237] E. Yoo, T. Okata, T. Akita, M. Kohyama, J. Nakamura,I. Honma, *Nano Lett.* **2009** *9* 2255.

[238] M. Pumera, *Chem. Rec.* **2009** *9* 211.

[239] H. Wu, J. Wang, X. Kang, C. Wang, D. Wang, J. Liu, I. A. Aksay,Y. Lin, *Talanta* **2009** *80* 403.

[240] K. Zhou, Y. Zhu, X. Yang,C. Li, *Electroanalysis* **2010** *22* 259.

[241] C. Shan, H. Yang, D. Han, Q. Zhang, A. Ivaska,L. Niu, *Biosens. Bioelectron.* **2010** *25* 1070.

[242] T. T. Baby, S. S. J. Aravind, T. Arockiadoss, R. B. Rakhi,S. Ramaprabhu, *Sens. Actuators, B* **2010** *B145* 71.

[243] Y. Liu, D. Yu, C. Zeng, Z. Miao,L. Dai, *Langmuir* **2010** *26* 6158.

[244] V. Stavyiannoudaki, V. Vamvakaki,N. Chaniotakis, *Anal. Bioanal. Chem.* **2009** *395* 429.

[245] M. H. Beers, *The Merck manual of medical information*, Whitehouse Station, N.J. : Merck Research Laboratories, **2003**.

[246] T. J. Ohara, R. Rajagopalan,A. Heller, *Anal. Chem.* **1994** *66* 2451.

[247] H. Lei, B. Wu, C. Cha,H. Kita, *J. Electroanal. Chem.* **1995** *382* 103.

[248] I. -. Yeo and D. C. Johnson, *J. Electroanal. Chem.* **2001** *495* 110.

[249] A. Guerrieri, R. Ciriello,D. Centonze, *Biosens. Bioelectron.* **2009** *24* 1550.

[250] S. Mehmet, G. Quan, S. Thomas,D. Goldsmith, *Diabet Med* **2001** *18* 679.

[251] A. Abdel Aal, H. B. Hassan,M. A. Abdel Rahim, *J. Electroanal. Chem.* **2008** 17 *619*

[252] W. S. Cardoso, V. L. N. Dias, W. M. Costa*, et al*, *J. Appl. Electrochem.* **2009** *39* 55.

[253] I. Danaee, M. Jafarian, F. Forouzandeh, F. Gobal,M. G. Mahjani, *Int. J. Hydrogen Energy*, **2008** *33* 4367.

[254] J. Huang, W. Hwang, Y. Weng,T. Chou, *Thin Solid Films* **2008** *516* 5210.

[255] X. Chen, N. Matsumoto, Y. Hu,G. S. Wilson, *Anal. Chem.* **2002** *74* 368.

[256] F. Shang, Y. Liu, S. Hrapovic, J. D. Glennon,J. H. T. Luong, *Analyst* **2009** *134* 519.

[257] S. Park, T. D. Chung,H. C. Kim, *Anal. Chem.* **2003** *75* 3046.

[258] Abbott Diabetes Care, *http://www.abbottdiabetescare.co.uk*, , 2010/07/01.

[259] Accu-Chek, *http://www.accu-chek.co.uk/gb*, 2010/07/01.

[260] Lifescan, *http://www.lifescan.co.uk*, , 2010/07/01.

[261] Bayer Diabetes, *http://www.bayerdiabetes.com*, 2010/07/01.

[262] A. P. F. Turner, B. Chen,S. A. Piletsky, *Clin. Chem.* **1999** *45* 1596.

[263] B. H. Ginsberg, *J Diabetes Sci Technol* **2009** *3* 903.

[264] K. Wiener, *Diabet Med* **1991** *8* 172.

[265] J. S. Skyler, *Diabetes Technol. Ther.* **2009** *11* S5.

[266] R. L. Weinstein, S. L. Schwartz, R. L. Brazg, J. R. Bugler, T. A. Peyser,G. V. McGarraugh, *Diabetes Care* **2007** *30* 1125.

[267] B. W. Bode, S. Schwartz, H. A. Stubbs,J. E. Block, *Diabetes Care* **2005** *28* 2361.

[268] T. M. Gross, B. W. Bode, D. Einhorn, D. M. Kayne, J. H. Reed, N. H. White,J. J. Mastrototaro, *Diabetes Technol. Ther.* **2000** *2* 49.

[269] B. Kovatchev, S. Anderson, L. Heinemann,W. Clarke, *Diabetes Care* **2008** *31* 1160.

[270] G. S. Wilson and R. Gifford, *Biosens. Bioelectron.* **2005** *20* 2388.

[271] K. M. Manesh, J. H. Kim, P. Santhosh, A. I. Gopalan, K. Lee,H. Kang, *J. Nanosci. Nanotechnol.* **2007** *7* 3365.

[272] N. A. Choudhry, D. K. Kampouris, R. O. Kadara, N. Jenkinson,C. E. Banks, *Anal. Methods* **2009** *1* 183.

[273] M. H. Yang, B. G. Choi, H. S. Park, W. H. Hong, S. Y. Lee,T. J. Park, *Electroanalysis* **2010** *22* 1223.

[274] R. Szamocki, A. Velichko, F. Muecklich, S. Reculusa, S. Ravaine, S. Neugebauer, W. Schuhmann, R. Hempelmann,A. Kuhn, *Electrochem. Commun.* **2007** *9* 2121.

[275] Z. Liu, L. Huang, L. Zhang, H. Ma,Y. Ding, *Electrochim. Acta* **2009** *54* 7286.

[276] A. R. Stoyanova and V. T. Tsakova, *Bulg. Chem. Commun.* **2008** *40* 286.

[277] C. Xiang, Q. Xie,S. Yao, *Electroanalysis* **2003** *15* 987.

[278] I. G. Casella and M. Gatta, *J. Electrochem. Soc.* **2002** *149* B465.

[279] S. L. Brooks, R. E. Ashby, A. P. F. Turner, M. R. Calder,D. J. Clarke, *Biosensors* **1987** *3* 45.

[280] S. F. White, I. E. Tothill, J. D. Newman,A. P. F. Turner, *Anal. Chim. Acta* **1996** *321* 165.

[281] J. P. Favier, D. Bicanic, P. Helander,M. van Iersel, *J. Biochem. Biophys. Methods* **1997** *34* 205.

[282] M. P. Nandakumar, A. Sapre, A. Lali,B. Mattiasson, *Appl. Microbiol. Biotechnol.* **1999** *52* 502.

[283] R. F. Drake, M. C. Deibert, S. Matsuda, J. J. O'Connell,E. S. Nuwayser, *Implantable fuel cell for an artificial heart.*, **1968**, p. 216.

[284] S. K. Wolfson Jr., S. L. Gofberg, P. Prusiner,L. Nanis, *Trans. , Amer. Soc. Artif. Intern. Organs* **1968** *14* 198.

[285] J. Giner and G. Holleck, *Design considerations for an implantable fuel cell to power an artificial heart.*, **1972**, p. 283.

[286] S. P. Bessman and R. D. Schultz, *Trans. , Amer. Soc. Artif. Intern. Organs* **1974** *19* 361.

[287] J. R. Rao, G. J. Richter, F. Von Sturm,E. Weidlich, *Bioelectrochem. Bioenerg.* **1976** *3* 139.

[288] F. Davis and S. P. J. Higson, *Biosens. Bioelectron.* **2007** *22* 1224.

[289] S. Kerzenmacher, J. Ducree, R. Zengerle,F. von Stetten, *J. Power Sources* **2008** *182* 1.

[290] K. B. Kokoh, J. M. Leger, B. Beden,C. Lamy, *Electrochim. Acta* **1992** *37* 1333.

[291] C. Jin and I. Taniguchi, *Mater. Lett.* **2007** *61* 2365.

[292] P. Schechner, E. Kroll, E. Bubis, S. Chervinsky,E. Zussman, *J. Electrochem. Soc.* **2007** *154* B942.

[293] A. J. Appleby and C. Van Drunen, *J. Electrochem. Soc.* **1971** *118* 95.

[294] S. Prilutsky, P. Schechner, E. Bubis, V. Makarov, E. Zussman,Y. Cohen, *Electrochim. Acta* **2010** *55* 3694.

[295] C. Taylor, G. Kenausis,A. Heller, *"Wiring" of glucose oxidase within a hydrogel made with polyvinylimidazole complexed with [(Os-4,4'dimethoxy 2,2'-bipyridine) Cl]$^{+/2+}$,* **1996**,

Chapter 7

The non-enzymatic determination of glucose using an electrolytically fabricated nickel microparticle modified boron doped diamond electrode or nickel foil electrode

The work presented in this chapter has been published in

Sensors and Actuators B: Chemical, *147* **(2010)** 642

In this chapter a nickel modified boron doped diamond (Ni-BDD) electrode and a nickel foil electrode were used in the non-enzymatic determination of glucose in alkaline solutions. The nickel was electrodeposited onto the bare BDD electrode for 600s under stirring from a 1mM $Ni(NO_3)_2$ solution in 0.1M acetate buffer (pH 4.7). This was followed by repeat cycling in 1M potassium hydroxide for over 300 cyclic voltammograms to enrich the $Ni(OH)_2$ layers. SEM analysis of the electrodes found the Ni-BDD to be modified by a quasi-random microparticle assembly, with approximately 49.8 μg cm^{-2} of nickel present on the surface.

The $Ni(OH)_2$/NiOOH redox couple was used to electrocatalytically oxidise glucose in a highly quantifiable system that was resistant to fouling, reproducible and accurate. Using cyclic voltammetry and chronoamperometry, glucose was determined to limits of 2.7μM with a sensitivity of 1.04μA μM^{-1} cm^{-2} at the Ni-BDD electrode. The foil electrode was comparably sensitive achieving a limit of 1.8μM but a relatively lower sensitivity of 0.67μA μM^{-1} cm^{-2}.

These results are compared to those of non-enzymatic electrochemical sensors of comparable experimental parameters. The latter are tabulated and discussed, with a view to directly compare various other electrode abilities to the nickel BDD system.

7.1. Introduction

As discussed in the previous chapter the detection of glucose is a vital application of electrochemistry. Despite tremendous advancements in medicine, the prevalence of global diabetes is increasing at an alarming rate, with an estimated 5% of the world population expected to be affected by the condition by 2030 [1]. Electrochemical analysis of blood glucose levels has been the method of choice for decades now, since the arrival of the Clark oxygen electrode in the 1962 [2] and subsequent development by Updike et al in 1967 [3] for glucose detection. However, with an increasing demand for monitoring devices, particularly in poorer regions of the world, the need for lower cost, simply fabricated and environmentally robust electrodes is greater than ever.

The glucose detection industry is dominated by use of enzymatic electrodes, in which the enzyme glucose oxidase (GOx) has been predominantly used. It is a highly selective enzyme, and works at a wide range of pHs relative to other enzymes [4,5]. Enzyme modified electrodes, however, suffer from limited stability and variable sensitivity (due to problems with reproducibility) [4], requiring increasingly elaborate fabrication and immobilisation methods to overcome these boundaries [5]. The development of non-enzymatic glucose sensors is therefore an area of high interest in the scientific world with much focus on electrocatalytic metals and novel carbon materials as potential alternatives [6-24].

A number of metal electrode materials, namely platinum [6-8], copper [9-12], gold [13-16] and nickel [18-20], have been explored extensively in their application to catalytic oxidation of carbohydrates. These materials have all shown good sensitivity to glucose, well within the range of blood and urine sugar levels. Nickel electrodes were initially

studied by Fleischmann et al [17] in the early 1970's in an investigation of the electrocatalytic ability of the Ni(II)/(III) redox couple towards the electro-oxidation of small organic molecules. In his investigation, and later experiments by a number of researchers [17-20, 25] it was determined that the $Ni(OH)_2$, present at the electrode, is initially oxidized to the catalytically active NiOOH species, which subsequently irreversibly oxidizes small organic analytes.

Though the use of nickel electrodes in glucose detection has been reported numerous times over the past few decades [17-20, 26-28], the fabrication methods and electrode modifications have been quite elaborate, with the exception of a few simpler procedures [11, 17, 29,30]. The application of a nickel modified boron doped diamond electrode, towards the electrocatalytic oxidation of glucose, was briefly reported in 2001 by Uchikado et al [30]. This nickel BDD electrode was chemically modified however, and on a laboratory fabricated diamond electrode. The surface morphology of the nickel modified and unmodified boron doped diamond electrode therefore varied greatly to the electrodes presented herein. The results reported by Uchikado et al were highly promising however, and thus experiments to elaborate and further investigate the attributes of the nickel modified BDD electrode in the application of glucose oxidation have been performed.

The use of BDD as a substrate electrode is found to encourage the formation of a nano or microparticle array of metal deposits. As a substrate electrode for catalytic particles BDD has shown great promise, finding increasing application in the field, as well as other aspects of electrochemistry, over the past 15 years. The formation of a random microarray, as opposed to a film, has been reported to have at least as much catalytic ability as a continuous film or macroelectrode [51-54]. This is due to a higher surface area to volume ratio, significantly lower background capacitative current and excellent diffusional properties. In particular however, a considerably lower quantity of active material may be used when used in a micro-array form due to the overlap of diffusional regions that occurs at normal scan rates, imitating linear diffusion across the whole electrode surface [52-55].

Thus the use of nanoparticle-promoting BDD makes it an ideal substrate for nickel modification.

7.2. Experimental

Apparatus

All voltammetric measurements were recorded using an Autolab PGSTAT20 computer controlled potentiostat (EcoChemie, Utrecht, The Netherlands). A standard three-electrode configuration was used throughout, consisting of a boron doped diamond (BDD, diameter 3mm, Windsor Scientific, Slough, UK) working electrode, with a saturated calomel reference electrode (SCE) and graphite rod counter electrode. The BDD disk working electrode was incorporated into a custom built PEEK housing, equipped with a stainless steel piston to make electrical contact.

The nickel bulk electrode (nickel foil) was prepared from a nickel foil, 0.025mm thick (Goodfellow Advanced Materials, Surrey, UK) which was attached to a stainless steel piston and also incorporated into a custom built PEEK housing. The nickel foil electrode was prepared with the same surface area as the BDD electrode, to allow direct comparison to be made.

Scanning electron microscopy (SEM) was performed using a JEOL 6300 F instrument (FEG-SEM, tungsten filament as electron source, acceleration voltage 20keV). Energy dispersive X-ray (EDX) spectra analysis was performed simultaneously to the SEM image acquisition.

In-situ electrochemical atomic force microscopy (EC-AFM) was conducted on a MFP-3D stand-alone microscope (Asylum Research, Santa Barbara, CA) using TR-400 cantilevers from Olympus, in tapping mode. The software used for data acquisition and analysis was IGOR Pro 6.0 (Wavemetrics) with 3D imaging provided by Argyle- 3D imaging software.

Reagents and solutions

All chemicals were purchased from Sigma-Aldrich (Gillingham, UK), were of analytical grade and were used as received without any further purification. These were nickel (II) nitrate hexahydrate and alpha-D-glucose, anhydrous 96%. A standard 1 mM solution of nickel (II) nitrate was prepared in 0.1 M sodium acetate buffer solution (pH 4.7), the latter received as a 3 M biological standard solution from Aldrich, and diluted to 0.1 M using deionised water of resistivity not less than 18.2 $M\Omega cm^{-1}$ at 298 K (Millipore UHQ, Vivendi, UK). For the glucose oxidation experiments a standard 1.0 M solution of potassium hydroxide (ca. pH 14) was used, prepared using potassium hydroxide pellets purchased from BDH Laboratories (Poole, UK) in deionised water.

Experimental procedure

Prior to each set of standard glucose additions the surface of the BDD electrode was cleaned using a diamond slurry of 0.1 μm particle size, followed by sonication for 1 minute in ethanol/water and thorough rinsing using deionised water. This was also the procedure prior to modification by the nickel nanoparticles. The surface of the bulk nickel electrode was renewed via the same procedure prior to use. In addition to this, the electrodes were electrolytically cleaned by holding at +1V (vs. SCE) in 5M sulphuric acid, and cycling between 0 and 1V twice to ensure the complete removal of nickel.

Glucose electro-oxidation experiments were performed using cyclic voltammetry with a start and cathodic potential limit of 0 V and an anodic potential limit of ca. +0.5 V. Amperometric analysis was conducted at suitable oxidation potentials established from the cyclic voltammetry data, and was dependent on the concentration of glucose.

Ni-BDD formation

Nickel was deposited onto the BDD by cathodic reduction of a degassed 1mM $Ni(NO_3)_2$ solution in 0.1 M acetate buffer solution (pH 4.7) in which the BDD was held at -1.3 V for

600s under stirring. This was followed by removal of the modified electrode from the deposition solution to a non-degassed potassium hydroxide solution (1M). These parameters were established by a number of optimising experiments regarding deposition potential, deposition time and the modified electrode's response to glucose. It was found that the limits of detection were comparable for electrodes modified for 120s, 300s and 600s, yet the sensitivity of the electrode increased with greater modification. As such, nickel deposition was conducted for 600s under stirring.

7.3. Results and discussion

7.3.1. Characterisation of the nickel- microparticle modified BDD electrode and nickel foil electrode

7.3.1.1 Scanning electron microscopy (SEM), energy dispersive x-ray spectroscopy (EDX) and in-situ atomic force microscopy (AFM)

In Figure 7.1 scanning electron microscope (SEM) images of the a) bare BDD, b) Ni foil and c-f) Ni-BDD are shown. The Ni-BDD was modified in a de-aerated nickel (II) solution for 600s at -1.3 V (vs. SCE), and subsequently cycled 300 times over a potential range of 0 to 0.5V (vs. SCE) at a scan rate of 50 mVs^{-1} in an aerated 1M KOH solution. The electrode was then air dried and imaged. The representative images shown in Figure 1 are over the magnification range of 25 to 10000 μm^2 area.

From Figure 7.1c a random microparticle array can be seen, in which the nickel randomly deposited. Although not particularly evident in the images shown here, images presented in Chapters 4, 5 and 8 indicate that nucleation occurs in particularly active areas of the BDD electrode [42]. It is likely that nucleation occurred at the polycrystalline grain boundaries present across the diamond surface, as higher electrical activity has been demonstrated on these areas [55], but the prolonged deposition time caused some conglomeration of particles.

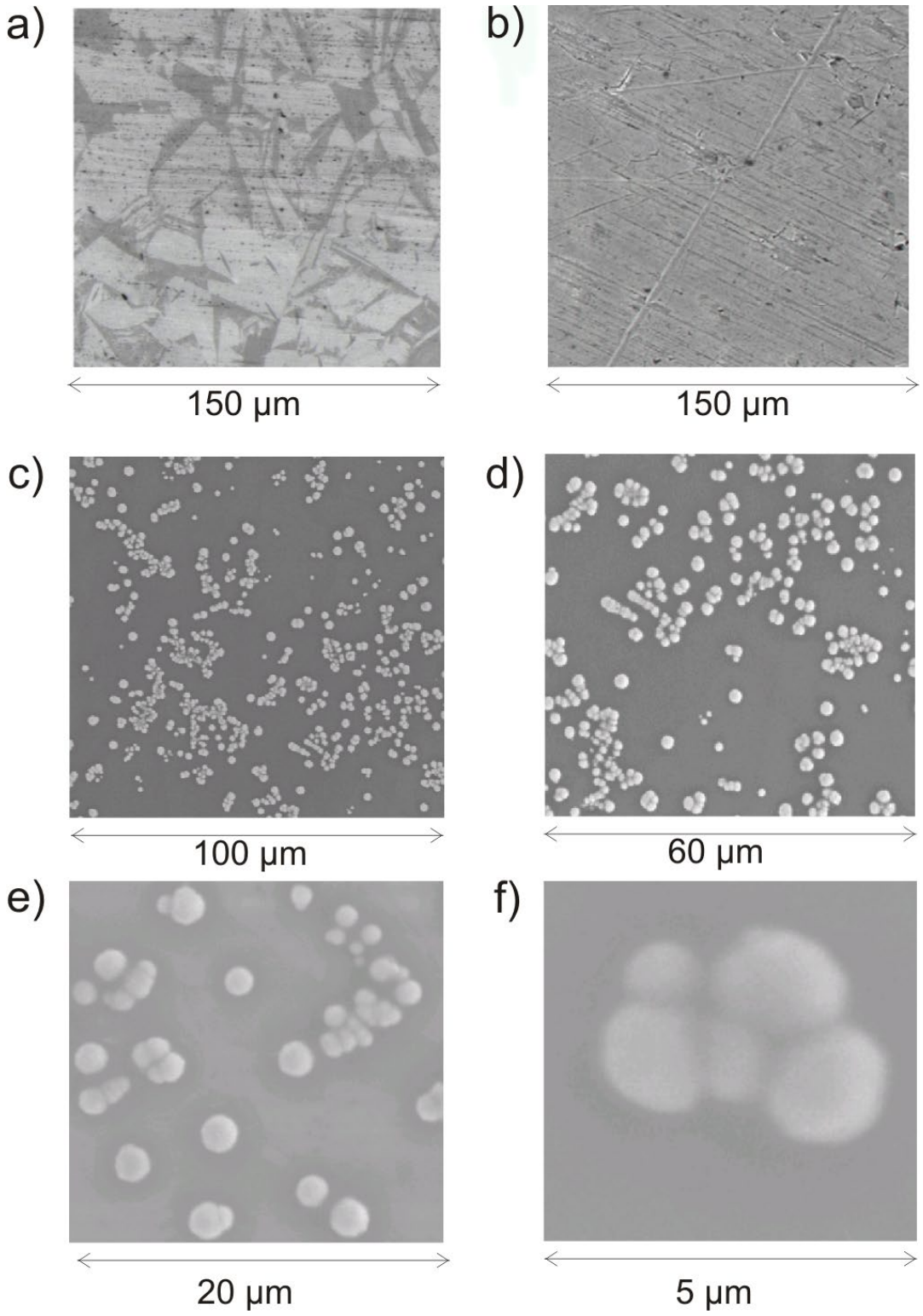


Figure 7.1: *SEM images of the a) bare BDD b) Ni foil and c-f) Ni-BDD electrode. The Ni-BDD was modified by electrochemical deposition of Ni(II) from a 1mM $Ni(NO_3)_2$ in 0.1 M sodium acetate buffer solution (pH 5) for* ***600 s*** *at -1.3 V (vs. SCE) under stirring and degassed.*

On increased magnification of the surface, hemispherical nano and microparticles of nickel are clearly observed. Calculations based on these images, and others (not shown), give an estimated nickel microparticle radius of 0.59 μm over a range of 0.05 to 1.9 μm. The average number of particles on the electrode was calculated to be approximately $1.2x10^{7}$ +/- $0.4x10^{6}$ particles cm^{-2}. From the images the average mass of a nickel particle was calculated to be 6.1 $x10^{-12}$ g, therefore the mass of nickel deposited was estimated between 22.9 μg cm^{-2} and 49.8 μg cm^{-2} depending on whether the material was deposited as $Ni(OH)_2$ or nickel metal respectively. The wide range in particle size suggests a progressive growth process stemming from continued nucleation of metallic nickel to the active BDD areas.

Energy dispersive x-ray (EDX) spectroscopic data for the Ni-BDD was acquired simultaneously to the SEM data and is shown in Figure 7.2. The EDX spectra of the bare BDD and nickel foil electrode were also obtained for comparison, though are not shown. Three peaks corresponding to the nickel were clearly observed at approx. 0.8, 7.5 and 8.2 keV in the modified BDD and nickel foil spectra only.

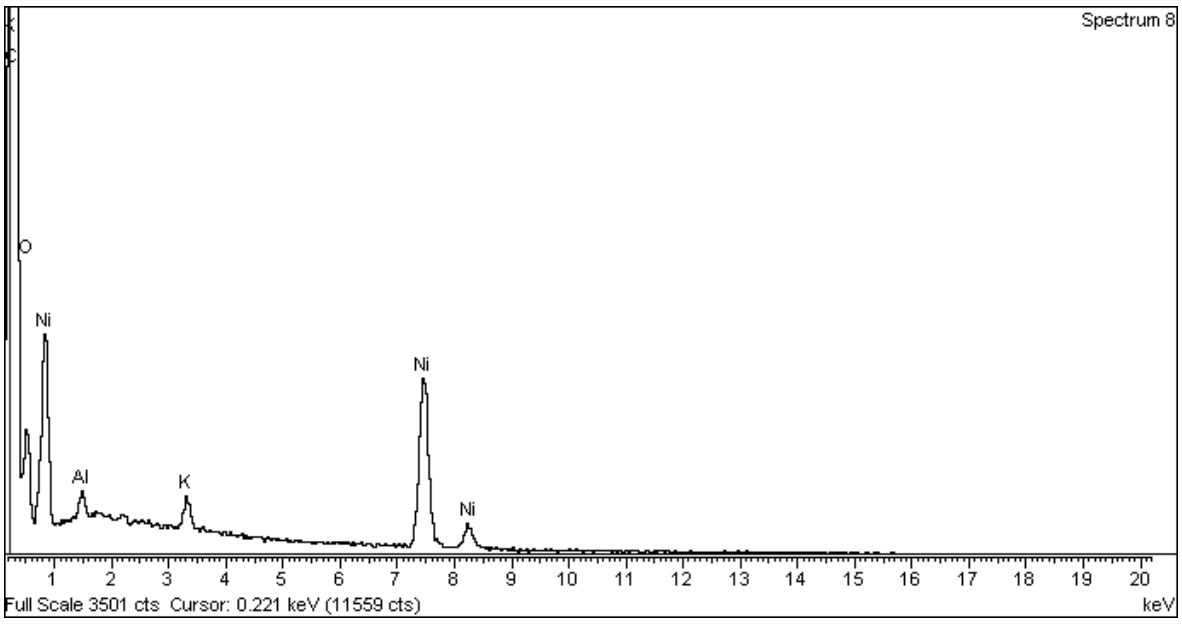


Figure 7.2: *EDX spectrum of the Ni-BDD showing the three indicative peaks for nickel*

In Figure 7.3, in-situ electrochemical atomic force microscopy (in-situ EC-AFM) images of the deposited nickel particles are shown.

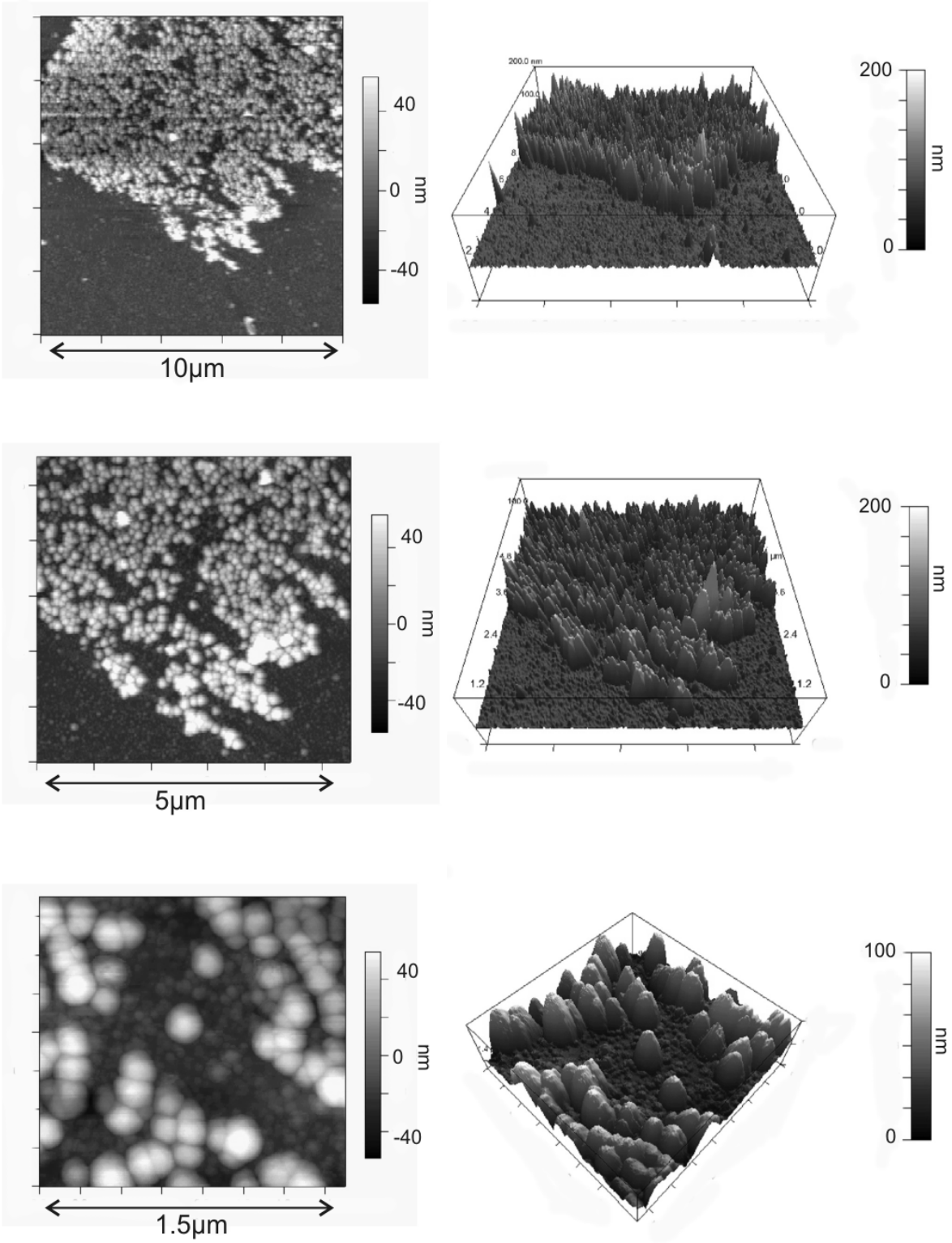


Figure 7.3: *In-situ EC-AFM images of a nickel modified BDD electrode. Nickel deposited at -1.2 V (vs. Ag/AgCl) for 180 s without stirring or degassing, from a 1mM $Ni(NO_3)_2$ in 0.1 M sodium acetate buffer solution (pH 5).*

The deposition time and experimental parameters differ to those preceding the SEM image acquisition, and subsequent glucose detection experimental conditions. The nickel was deposited from the same 1 mM $Ni(NO_3)_2$ in 0.1 M sodium acetate buffer solution, but without stirring or deaerating, and for a period of 180 s at -1.2 V (vs. Ag/AgCl) . Despite the much reduced deposition time, the formation of spherical nickel nanoparticles is still evident in active areas of the electrode surface.

The AFM data indicates that the average particle size is between 50 and 60 nm in height, which suggests deposition time has a considerable influence on the particle size. This is corroborated by other investigations presented in Chapters 4 and 8 in which nickel was deposited for 150s and 300s onto BDD producing nanoparticle arrays of 110 and 520 nm average nanoparticle diameter respectively [41].

7.3.1.2. Enrichment of the nickel hydroxide layer

The procedure used to modify the BDD electrode has been detailed in a number of publications [56-9], in which the nickel is electrochemically deposited from a $Ni(NO_3)_2$ solution. This procedure is known to deposit the nickel as both nickel metal and nickel hydroxide, as per the following equation:

$$NO_3^- + 7H_2O + 8e^- \rightarrow NH^+ \; 10OH^- \quad (7.1a)$$

$$Ni^{2+} + 2OH^- \rightarrow Ni(OH)_2 \quad (7.1b)$$

$$Ni^{2+} + 2e^- \rightarrow Ni^0 \quad (7.1c)$$

The deposition of nickel hydroxide leads to the formation of two crystallographic species; hydrated α-$Ni(OH)_2$ and anhydrous β-$Ni(OH)_2$. This is evident in Figure 7.4 in which an overlay of CVs taken during the enrichment process in 1M KOH is shown (BDD modification as in section 7.2). The initial scans show the presence of two oxidation peaks, the more cathodic corresponding to α-$Ni(OH)_2$ and the second, more anodic peak relating to

the β-$Ni(OH)_2$ species [57, 60, 61]. As the conditioning continues by potential cycling, the depth of the nickel hydroxide layer increases, and the oxidation and reduction peaks increase in peak height, the latter becoming a single peak predominantly consisting of the beta phase. Nickel hydroxide is known to age to the beta form when placed in strong alkali solutions and exposed to prolonged cycling over the oxidation and reduction potential range [57]. The figure shows every 30th scan, and the crystallographic phase is indicated in the positive scan.

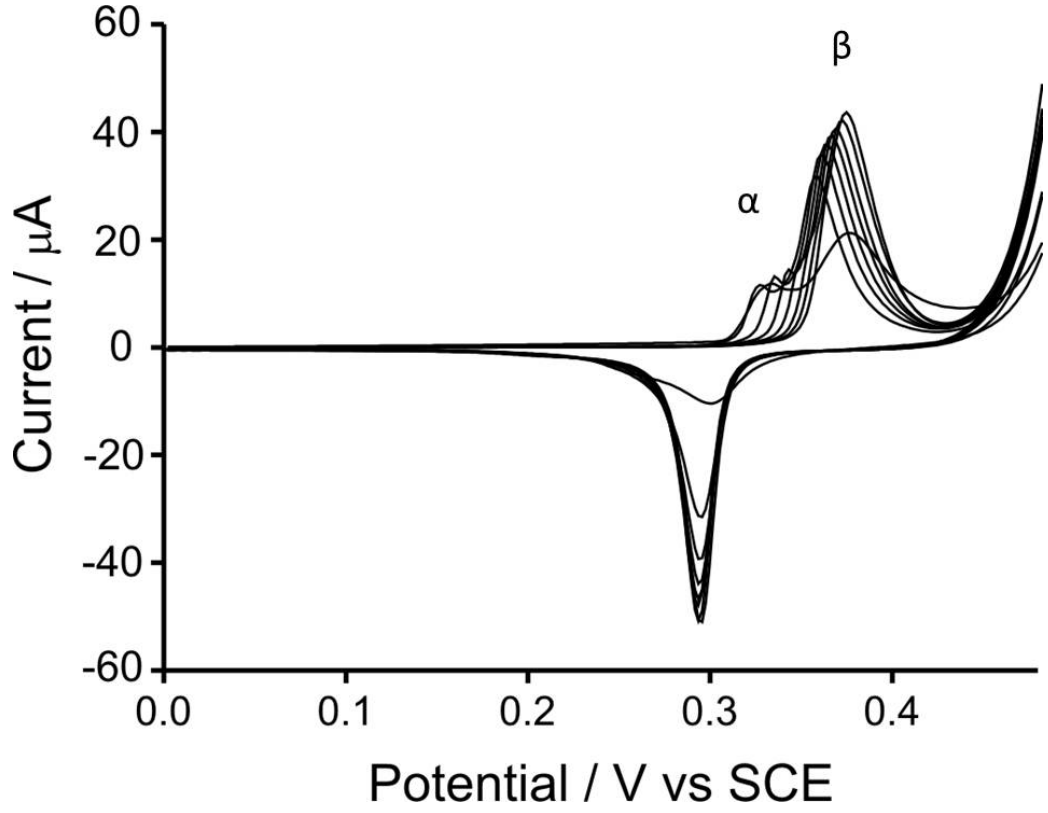


Figure 7.4: *Overlay of CVs taken during the nickel enrichment process. The Ni-BDD was modified at -1.3 V (vs. SCE) for 600s in a 1mM $Ni(NO_3)_2$. CV parameters: 50 mVs^{-1} scan rate, 1M KOH electrolyte, 300 consecutive cyclic scans in a non-degassed solution.*

Both the Ni-BDD and nickel foil electrodes were conditioned by potential cycling over 300 times between ca. 0 and 500 mV at 50 mVs^{-1} in 1M KOH, prior to electroanalytical use. This was to allow the enrichment of the $Ni(OH)_2$ species at the surface of the nickel, resulting in a thickening of the electrocatalytic layers. The number of

monolayers of $Ni(OH)_2$ present on the Ni-BDD and Ni-foil surfaces was calculated to comparable values of 19 +/- 2 and 22 +/- 2 respectively. This was based on the area under the reduction wave of NiOOH to $Ni(OH)_2$ providing the charge required to fully reduce the oxy hydroxide layer. The number of moles per square centimetre of NiOOH, Γ_o^*, was calculated using the equation $Q = nFA\Gamma_o^*$ [62], in which Q is charge, n the number of electrons, F is the Faraday constant, and A the surface area of nickel. The crystallographic value for a $Ni(OH)_2$ monolayer of $1.06x10^{-9}$ mol cm^{-2} was obtained from Bode et al [58]. Thus the nickel foil electrode, with a surface area of 0.07 cm^2, and a cathodic charge of $1.64x10^{-4}$ C, the number of monolayers is calculated to be 22.3.

With the Ni-BDD, the surface area of the nickel was estimated based on the SEM data to be between 0.01 and 0.025 cm^2, ca. 3-4 times less than the nickel foil. The average cathodic charge was determined as $2.03x10^{-5}$ C, which is eight times lower than the nickel foil, and calculates to 8.4 to 19.3 monolayers of $Ni(OH)_2$ using the higher and lower surface area estimates respectively. Based on the lower surface area estimate, the SEM and voltammetric data correspond well, and imply that the same degree of nickel enrichment is achieved during the same cycling procedure.

7.3.2 The electrochemical determination of glucose

Glucose concentration was determined from 1 M KOH solutions using cyclic voltammetry and chronoamperometry. In Figure 5 the Ni-BDD, modified for 600s at -1.3 V, in a stirred and degassed 1mM Ni(II) solution, is shown as an overlay of 10 CVs in which a series of 100 μM glucose additions have been made. The enhancement of the $Ni(OH)_2$ oxidation peak with each addition is evident, with an anodic shift in peak potential, as well as an increase in oxidative peak current, observed. Note that the reductive peak current decreases slightly on each addition, and does not undergo a potential shift. This is indicative of the irreversible oxidation of the glucose, and the catalytic conversion of the NiOOH back to $Ni(OH)_2$ prior to electrochemical reduction.

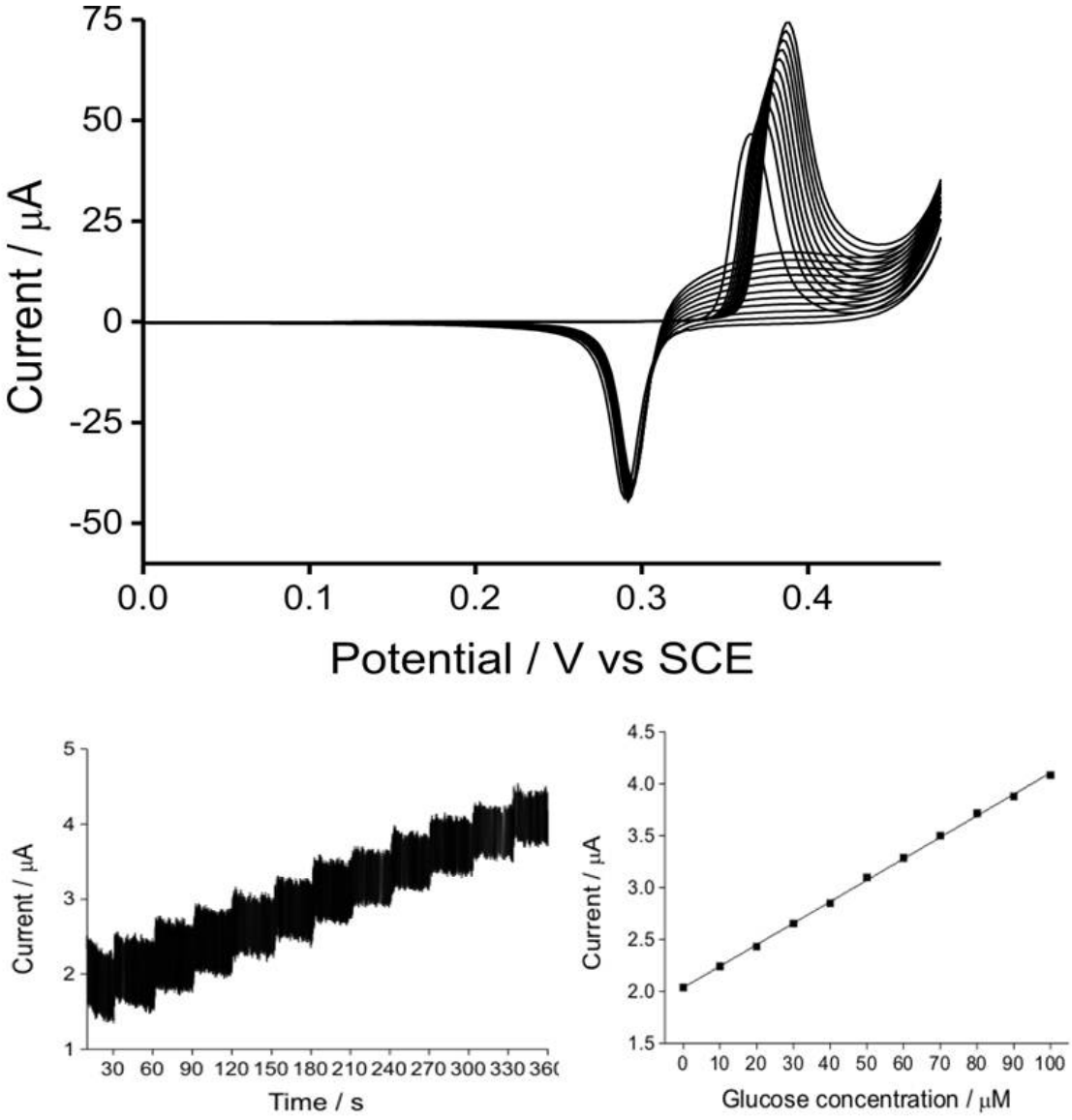


Figure 7.5: *Overlay of CVs following 100 µM additions of glucose to a 1M KOH solution at the Ni-BDD electrode. Below: left) amperometric plot of 10 µM glucose additions under constant stirring in 1 M KOH held at 0.48 V and right) the corresponding calibration plot of current vs. glucose concentration.*

Below the voltammograms of Figure 7.5 is a chronoamperometric analysis of glucose additions, and the corresponding calibration plot. The current vs. time plot shown corresponds to 10 µM glucose additions made to a 1M KOH solution under stirring. The systematic noise caused by the magnetic flea was easily removed by averaging the current

value over the 30s addition interval, thus providing a highly linear calibration plot of R^2 = 0.999. The limit of detection was calculated to be 2.7 µM using 3σ [63], and the sensitivity was determined to be 1.04 µA μM^{-1} cm^{-2}.

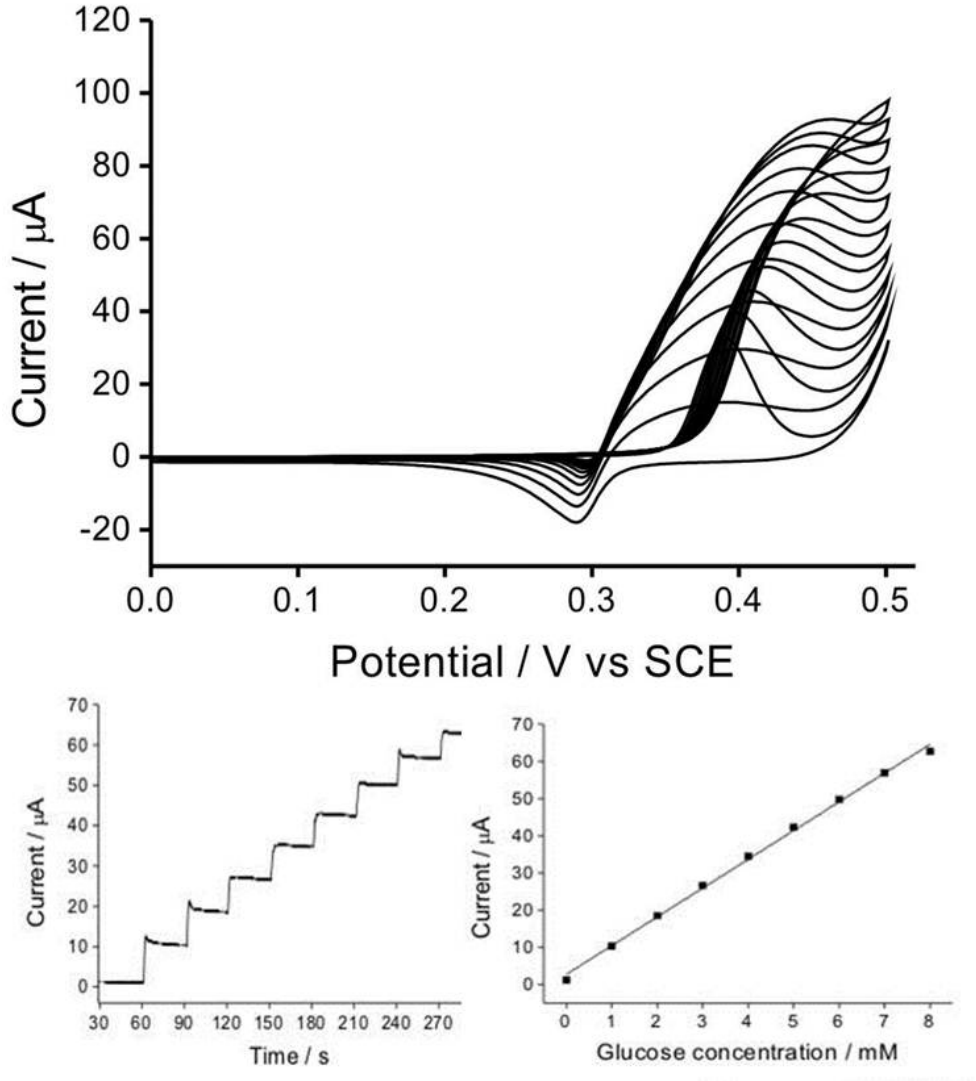


Figure 7.6: *Overlay of CVs following 1 mM additions of glucose to a 1M KOH solution at the Ni-BDD electrode (modified as in section 2.4). Below (left) amperometric plot of 1 mM glucose additions under constant stirring in 1 M KOH held at 0.48 V and (right) the corresponding calibration plot of current vs. glucose concentration.*

The Ni-BDD was used effectively over a linear range of 5 µM to 10 mM glucose concentration, without any electrode fouling or loss of sensitivity over the wide analytical range. Figure 7.6 shows the Ni-BDD's response to glucose concentrations over the 1-10

mM range, with a corresponding amperometric scan and linear calibration plot. This demonstrates that the Ni-BDD can detect high glucose levels akin to those present in blood, with average blood sugar levels between 3 and 8 mM in humans.

The Ni-BDD was directly compared to a nickel foil bulk electrode that was also conditioned for 300 CVs prior to analytical use (Figure 7.7).

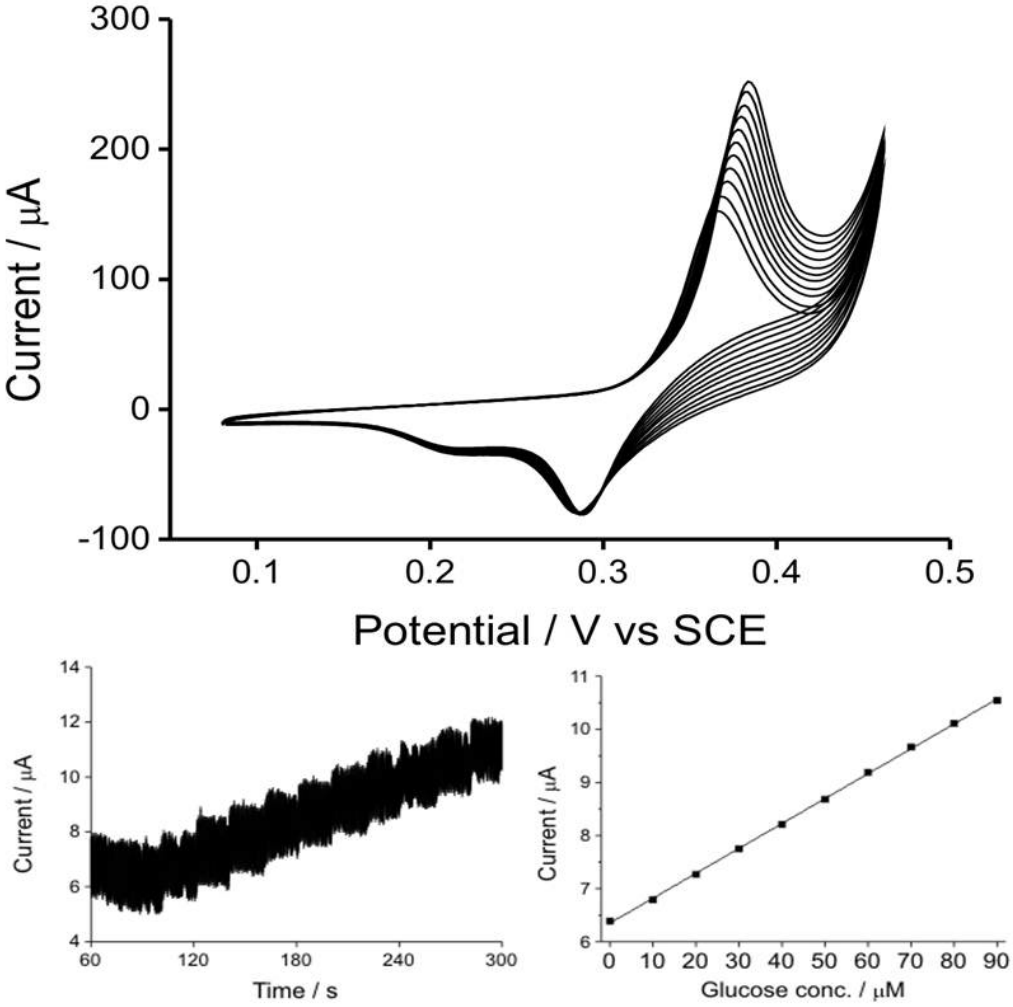


Figure 7.7: *Overlay of CVs following 100 μM additions of glucose to a 1M KOH solution at the Ni foil electrode. In-set: a) amperometric plot of 10 μM glucose additions under constant stirring in 1 M KOH held at 0.48 V and b) the corresponding calibration plot of current vs. glucose concentration.*

Figure 7.7 is a plot of 100 μM glucose additions comparable to the Ni-BDD data in Figure 7.5. The capacitative current for the nickel foil electrode, as well as the overall amount

$Ni(OH)_2$ is much greater than the Ni-BDD, owing to the macro nature of the electrode as well as the 400 times greater mass of nickel present on the bulk electrode. Consequently, the sensitivity is much lower than the Ni-BDD relative to the amount of nickel available, giving a value of 0.67 $\mu A\ \mu M^{-1}\ cm^{-2}$.

Once again, a potential shift to anodic values is observed with each addition of glucose. The reductive peaks are present in this instance as the reduction of the beta and gamma NiOOH species unlike at the Ni-BDD which was just the beta species. As with the Ni-BDD electrode, 1mM glucose additions using the nickel foil electrode was also performed (not shown). The linear increase of the oxidation peak was evident even to high concentrations of 10 mM glucose, as was the disappearance of the beta NiOOH reductive peak with the gamma remaining unchanged. This strongly supports that the catalytic species involved in the electro-oxidation of glucose and other small organic molecules, is the beta NiOOH, as has been extensively discussed in previous literature [17,18, 25, 60].

The amperometric analysis and corresponding calibration plot shown in-set of Figure 7.7 once again shows the analysis of 10 μM glucose additions, with an R^2 value of 0.998. From 3σ, a limit of detection of 1.8 μM was calculated, which is of a similar value to the Ni-BDD. The use of a nickel microparticle electrode may therefore be considered unnecessary as low detection limits can be achieved from a simple nickel foil system. Yet the voltammetry for the Ni-BDD, in which there is considerably less nickel present, is more consistent, giving similar cyclic voltammetry with only slight variation in the overall peak currents, approximately +/- 25 μA.

7.3.3 The application and reproducibility of the Ni-BDD electrode

To explore the application of the Ni-BDD towards the determination of an 'unknown' glucose concentration, amperometric, standard addition experiments were performed. Cyclic voltammetric analysis of the 'unknown' and standard additions gave an excellent correlation with the 'unknown' concentration of 7mM, as shown in Figure 8. It was

observed however that the best linearity, and most accurate estimation of glucose concentration from the calibration plot, was achieved using the second scan of each CV. As such, it was postulated that a pause in analysis was necessary, and that the corresponding amperometric analysis would involve a stabilisation period of known glucose additions prior to the addition of the 'unknown' and subsequent standard additions.

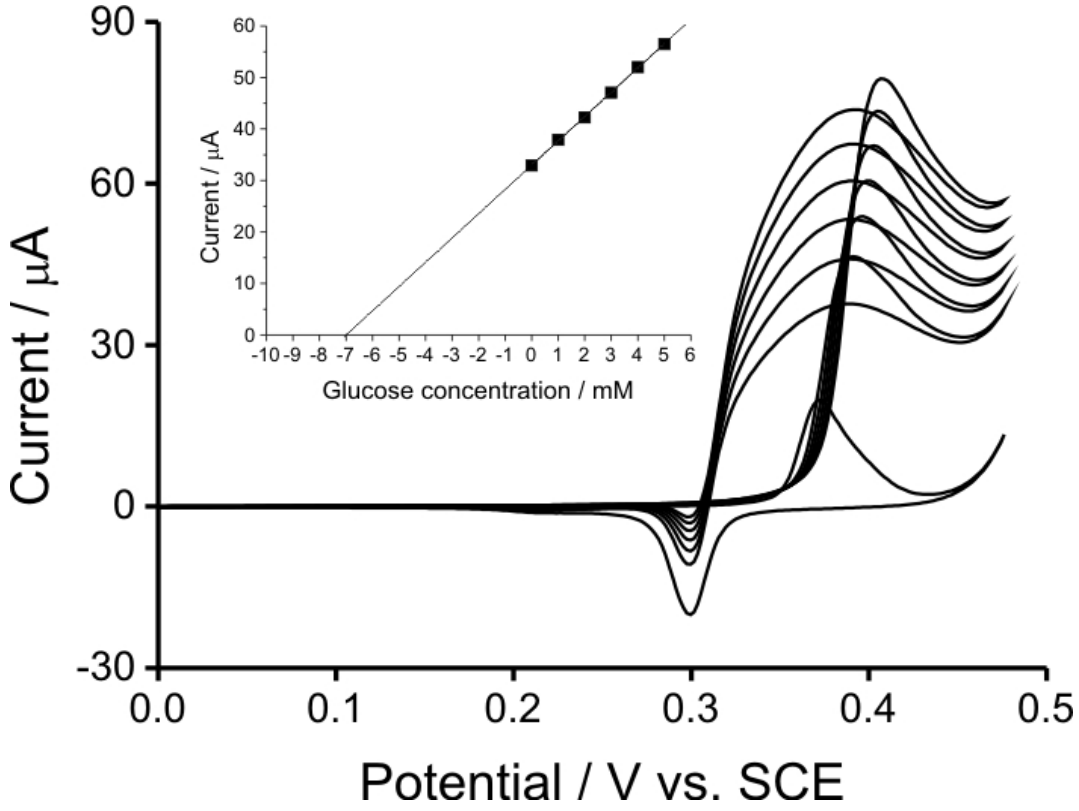


Figure 7.8: *An overlay of cyclic voltammograms for a Ni-BDD electrode in 1 M KOH, with a 7mM 'unknown' glucose addition followed by 1mM standard additions. In-set: the corresponding extrapolated standard addition calibration plot at a potential of 0.466 V vs. SCE, in which the unknown concentration is determined to be 7 mM*

In the experiment shown in Figure 7.9, the first three additions were 'known' 1mM glucose, to allow the Ni-BDD glucose response to stabilize. This was followed by the addition of the 'unknown' glucose concentration, and subsequently, the 1mM 'known' glucose standard additions. The calibration plots that resulted from this approach were much more successful than those obtained from conventional standard addition analysis, one of which is shown in-

set of Figure 7.9 with the corresponding amperometric plot. The difference in response to glucose before and after the 'unknown' glucose addition is evident in Figure 7.9, as the first three 1mM additions have noticeably greater currents than the later 1mM glucose additions.

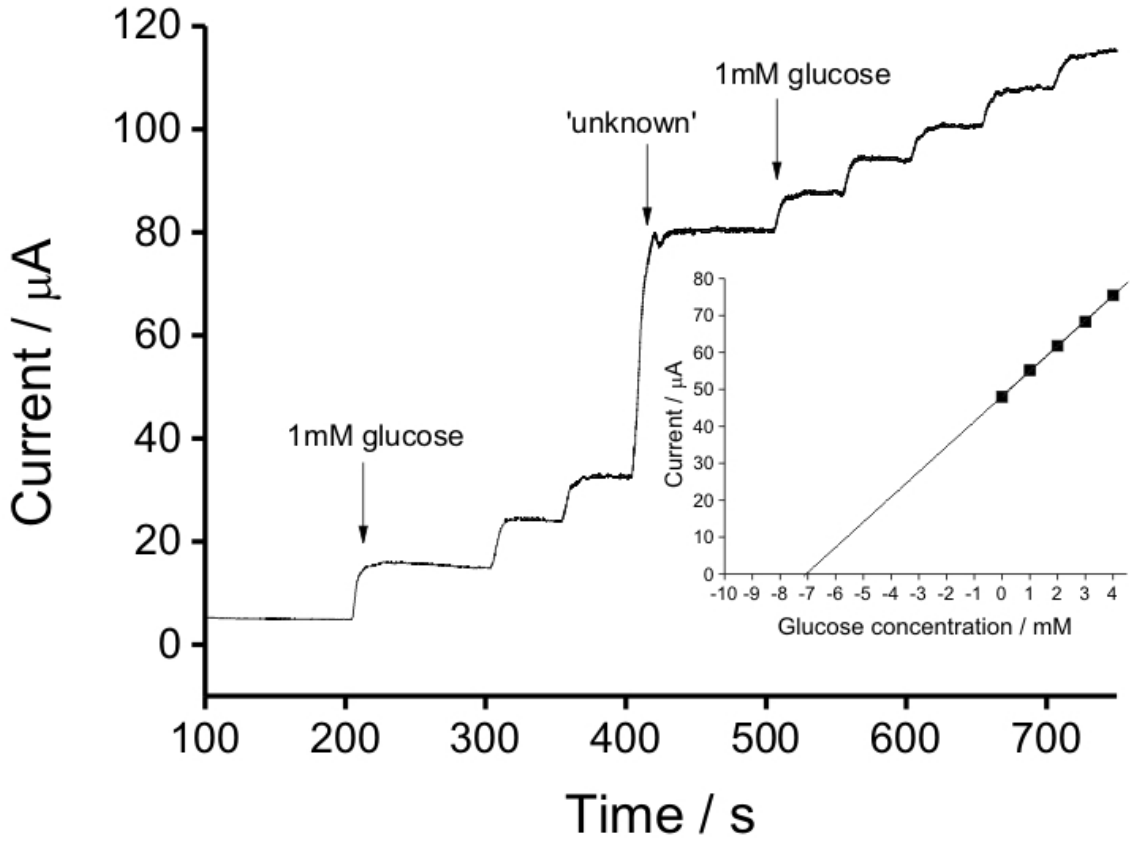


Figure 7.9: *Typical amperometric standard addition plot using a stabilizing pre-addition step at a Ni-BDD electrode. The amperometric potential was 0.46 V (vs. SCE) in a 1M KOH solution under constant stirring. 1mM 'known' glucose additions and a 7 mM 'unknown' addition (indicated in plot). In-set: the corresponding extrapolated standard addition calibration plot, in which the 'unknown' concentration is determined to be 7 mM.*

The Ni-BDD showed a highly reproducible and quantitatively accurate analytical response to determining unknown glucose concentrations. Over seven experiments, each using a different, freshly prepared Ni-BDD electrode following the previously discussed fabrication method (section 7.2), the response to a 7mM 'unknown' glucose addition gave a mean concentration of 7.15 mM with a relative standard deviation of 3.2%.

One major benefit of the latter analytical approach was the independence of the sensor to the electrode sensitivity. As the amount of nickel deposited on the electrode varied slightly, the sensitivity of the electrode also differed from one to the next. However, the stabilized standard addition approach discussed above allows the individual electrode to be calibrated and utilized effectively. The nickel oxidation peak height varied between ca. 20 and 70 μA, with an average of 43 μA, following a 600s stirred deposition at -1.3 V in 1mM $Ni(NO_3)_2$ in 0.1 M sodium acetate solution.

7.3.4 The effect of interferences on glucose oxidation

One main problem of non-enzymatic and enzymatic glucose sensors is the simultaneous oxidation of other organic substances in the blood that oxidise at a comparable potential to glucose. Other materials in the blood such as ascorbic acid (AA) and uric acid (UA), although at low concentrations relative to glucose, might, in principle, interfere with the determination of the desired analyte. These interfering species are known to sometimes have high electron transfer rates. As glucose oxidation is a catalytic process however, it is likely to be favoured by the high effective surface area offered by the presence of nickel nano and microparticles, a surface feature that would not aide the diffusion-controlled electro-oxidation of the interfering species [64-66].

The response of the Ni-BDD electrode to AA and UA was explored over concentration ranges comparable to blood glucose levels. At the bare BDD electrode, both AA and UA oxidised at 0 V and 0.17 V (vs. SCE) respectively, giving broad oxidation peaks. At the Ni-BDD this was not observed, but at relatively high concentrations (>0.5mM) of AA the Ni (II/III) peak shifted and increased in a manner akin to glucose additions. For UA however, the opposite effect was seen; increasing the concentration of UA (> 0.5 mM) slightly decreased the Ni(II/III) peak. These effects were observed using AA concentrations much greater than would be observed in a normal blood sample (ca.

0.02-0.08 mM) , and a high UA concentration relative to normal blood levels (ca. 0.1 – 0.4 mM) however.

The effect of AA and UA, separately and together, on the oxidation of glucose was also investigated, as shown in Figure 10. Here the amperometric response of the Ni-BDD to 1mM glucose additions in the presence of both 0.1 mM AA and 0.02 mM UA is shown. At these concentrations it is evident that they have little or no effect on the catalytic response to glucose.

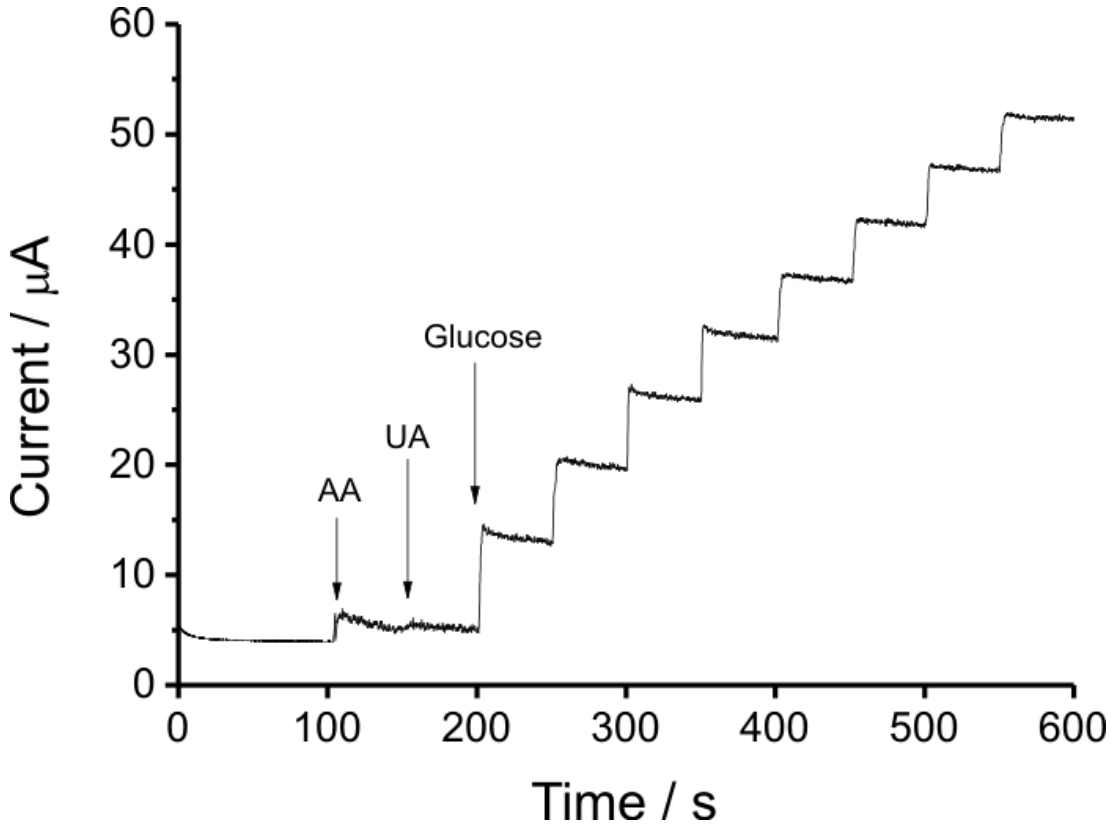


Figure 7.10: *Amperometric plot of 1mM glucose additions to a Ni-BDD electrode (modified as stated in section 2.4) in 1 M KOH, in the presence of 0.1 mM ascorbic acid (AA) and 0.02 mM uric acid (UA) (indicated in the plot), under constant stirring.*

7.3.5 Stability and lifetime of the Ni-BDD electrode

Figure 7.11 shows the current response of a Ni-BDD electrode, modified for 600s at -1.3 V in a stirred and degassed 1mM Ni (II) solution, towards 5mM of glucose over a period of 30

days. The initial glucose analysis occurred immediately after modification of the electrode, and the subsequent responses were recorded at the electrode following its storage in air in a dust free container, and washing with distilled water before and after use. Prior to the analysis the Ni-BDD was also cycled in 1M KOH twenty times between 0 and 0.5 V vs. SCE to recondition the $Ni(OH)_2$ layers.

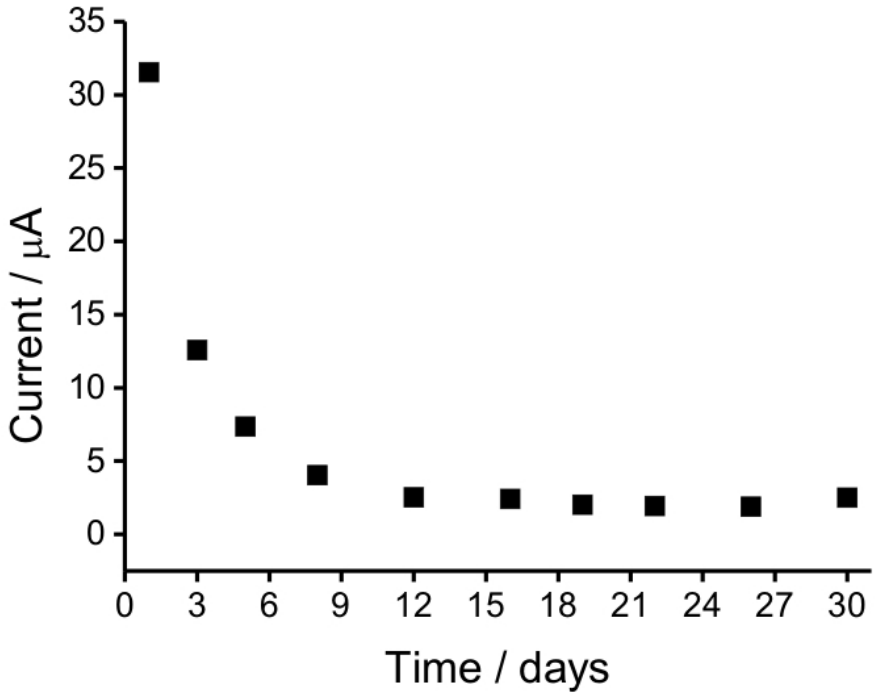


Figure 7.11: *Plot of the average amperometric current for a 5mM addition to 1M KOH using a Ni-BDD electrode (modified as stated in section 7.2.4), over a period of 30 days.*

It is evident that the sensitivity of the electrode immediately and significantly decreases within the first week, yet after 12 days the electrode reaches a current response of ca. 2 μA to 5mM glucose, which is consistently observed for the remainder of the month. This shows the long-standing adherence of the nickel microparticles to the diamond electrode surface, and implies a maximum loss of sensitivity in the electrode to be obtained in two weeks of storage in air, and the subsequent signal is then maintained.

7.3.6 Comparison of results to the literature review of non-enzymatic electrochemical glucose sensors in Chapter 6.

In the previous chapter (Chapter 6) an extensive, up-to-date review of non-enzymatic glucose sensors was provided, considering the numerous publications regarding non-enzymatic electrochemical glucose detection that have emerged over the past decade. Systems predominantly revolving around the use of gold, platinum, copper and nickel metals have been developed and adapted in a number of ways to improve sensitivity, selectivity and reproducibility of enzyme-free biosensors, and with much success. In this section, the results obtained in using the Ni-BDD and nickel foil electrodes are compared to other non-enzymatic systems.

Table 1 in Chapter 6 summarises non-enzymatic glucose electrochemical sensors in which the experimental parameters directly compare to the procedure discussed in this Chapter. That is to say, amperometry was used to determine glucose concentration without the aid of flow injection analysis (FIA), anion exchange columns, or high pressure liquid chromatography (HPLC). Listed in the table are the limits of detection (LOD), method used to determine the limit, the linear range observed and the sensitivity of the electrode (when the information was provided).

From Table 1 in Chapter 6, it is evident that most of the electrodes have comparable detection limits, roughly in the micromolar region. This includes the Ni-BDD and nickel foil electrodes reported in this research. Although each of the systems report a relatively low LOD, the majority of lowest detection limits are reported at copper based electrodes, particularly when combined with carbon nanotubes [72, 74, 75]. Nano structures, of copper based electrodes also seem to observe low detection limits, such as the CuO nanowires [76] reported to give an LOD of 4.9 nM based on S/N=3, or CuO nanorods [10] with a 1.2 μM detection limit based on 3 sigma [63]. Most of the sensitivities of the copper electrodes are difficult to compare to other electrodes however, due to the absence of surface area in the reported value.

Other than gold nanoparticles on a 3D silicate network [67], the gold based electrodes offered comparable or higher LODs than the nickel electrodes, with a considerably lower sensitivity, often 100 times lower than the nickel, platinum and carbon counterparts. Of the carbon based electrodes, the BDD nanoforest [68] and graphite pencil electrode [22] have reported the lowest LODs, though the sensitivity of the BDD nanoforest is again much lower than observed at nickel or platinum. As mentioned previously, copper modified carbon nanotubes electrode also offered relatively low detection limits, a behaviour also observed recently at platinum modified nanocrystal and carbon nanotube hybrid structures [79], but not at platinum modified MWCNTs or indeed PtRu modified MWCNTs [97, 98].

The best sensitivity observed seems to be from electrodes of nickel nanomaterials, with values as high as 7.32 mA mM^{-1} cm^{-2} [31] and 5.1 mA mM^{-1} cm^{-2} [83]. This is most probably due to a significantly large surface area within the nanoporous structure, highlighting the clear improvement in sensitivity that arises from having a nanostructured electrode. Platinum electrodes with a nanoporous structure show considerable variation in sensitivity, ranging from high values of 0.642 mA mM^{-1} cm^{-2} [7] to low values of ca. 1 μA mM^{-1} cm^{-2} [90, 91], as well as relatively higher LODs, whether being used as platinum alone [6, 8, 90], alloyed with other metals such as ruthenium [97, 98] and lead [94, 95], or combined with carbon nanotubes. Furthermore, platinum electrodes are known to suffer inhibitory effects from the presence of chloride ions, and general electrode fouling from other adsorbates [5].

On review, it is evident that nickel electrodes offer consistently low LODs and amongst the highest, and again most consistent sensitivities out of the tabulated electrode materials for non-enzymatic glucose detection. Regardless of fabrication method, the values are mostly comparable with each other, implying that elaborately modified systems are unnecessary and possibly overcomplicating an already sensitive electrode material. Nano sized materials do seem to improve sensitivity as a whole, with the Ni-BDD, nickel

nanowire array [87], nanoporous nickel film [83] and nickel titanium alloy nano [31] electrodes each reporting low micromolar detection limits and mA mM^{-1} cm^{-2} sensitivity.

7.4. Conclusions

A nickel microparticle modified boron doped diamond electrode (Ni-BDD) and nickel foil bulk electrode have been directly compared in their application towards the electrocatalytic oxidation of glucose in alkali solution. Both electrodes gave comparable performances, providing a linear range over three orders of magnitude from 10 μM to 10 mM, encompassing the human blood sugar levels of approximately 3 to 8 mM. The sensitivity was high with values of 1.04 and 0.67 mA mM^{-1} cm^{-2} observed, and amperometric analysis determined glucose limits of detection (3σ) [63] of 1.8 and 2.7 μM, for the foil and BDD electrodes respectively.

The use of a novel amperometric approach to determine an unknown sample concentration was successfully applied using different, freshly prepared Ni-BDD electrodes, achieving an accurate corroboration with the 'unknown' sample concentration with a relative standard deviation of 3.2 % (n=7). The electrode showed a very small electrochemical response to human blood levels of common interfering species, ascorbic acid and uric acid, which would therefore have little or no effect on glucose analysis given the much greater concentration of blood glucose. The long term stability of the Ni-BDD electrode, stored in normal atmosphere but in a dust free environment, showed a significant decrease in sensitivity in the first 2 weeks, but then showed a sustained sensitivity of ca. 2 μA towards 5mM of glucose for the remainder of the 1 month analysis period.

These results regarding the Ni-BDD and nickel foil electrodes have shown a very good response to glucose determination in alkali solutions. Comparison to other non-enzymatic electrodes shows that the nickel electrodes reported here offer comparable detection limits, and higher than average sensitivity to glucose, especially the Ni-BDD electrode. Platinum electrodes offer the only comparable, and sometimes improved,

sensitivity, yet they are known to be strongly and detrimentally affected by chloride ions fouling by adsorbates [5], disadvantages that are not associated with nickel electrodes.

7.5. References

[1] WHO factsheet No. 312; http://www.who.int/mediacentre/factsheets/fs312/en/ November 20th, 2009

[2] L.C. Clark, Jr., C. Lyons, *Ann N Y Acad. Sci.* (**1962)** 102, 29.

[3] S.J. Updike, G.P. Hicks, *Nature* **(1967)** 214, 986.

[4] R. Wilson, A.P.F. Turner, *Biosens. Bioelectron*. **(1992)** 7, 165

[5] S. Park, H. Boo, T.D. Chung, *Anal. Chim. Acta* **(2006)** 556, 46

[6] Y.-J. Lee, D.-J. Park, J.-Y. Park, Y. Kim, *Sensors* **(2008)** 8, 6154

[7] J.-F. Huang, *Electroanalysis* **(2008)** 20, 2229

[8] Z. Cao, Y. Zou, C. Xiang, L.-X. Sun, F. Xu, *Anal. Lett*. **(2007)** 40, 2116

[9] T.-K. Huang, K.-W. Lin, S.-P. Tung, T.-M. Cheng, I.C. Chang, Y.-Z. Hsieh, C.-Y. Lee, H.-T. Chiu, *J. Electroanal. Chem*. **(2009)** 636 123

[10] C. Batchelor-McAuley, Y. Du, G.G. Wildgoose, R.G. Compton, *Sens. Actuators, B* **(2008)** B135 230

[11] A. Stitz, and W. Buchberger, *Electroanalysis* **(1994)** 6 251

[12] T.A. Ivandini, R. Sato, Y. Makide, A. Fujishima, Y. Einaga, *Diamond Relat. Mater.* **(2004)** 13 2003

[13] Y. Li, Y.-Y. Song, C. Yang, X.-H. Xia, *Electrochem. Commun*. **(2007)** 9 981

[14] Y.-G. Zhou, S. Yang, Q.-Y. Qian, X.-H. Xia, *Electrochem. Commun*. **(2009)** 11 216

[15] S. Cho, C. Kang, *Electroanalysis* **(2007)** 19 2315

[16] L.E. Welch, D.A. Mead, Jr., D.C. Johnson*, Anal. Chim. Acta* **(1988)** 204 323

[17] M. Fleischmann, K. Korinek, D. Pletcher, *J. Electroanal. Chem*. **(1971)** 31 39

[18] M. Jafarian, F. Forouzandeh, I. Danaee, F. Gobal, and M.G. Mahjani, *J. Solid State Electrochem*. **(2009)** 13 1171

[19] A. Salimi, M. Roushani, *Electrochem. Commun*. **(2005)** 7 879

[20] C. Zhao, C. Shao, M. Li, and K. Jiao, *Talanta* **(2007)** 71 1769

[21] J. Lee, and S.-M. Park, *Anal. Chim. Acta* **(2005)** 545 27

[22] S.Y. Ly, Curr. *Anal. Chem*. **(2009)** 5 59

[23] J.-S. Ye, Y. Wen, W.D. Zhang, L.M. Gan, G.Q. Xu, and F.-S. Sheu, *Electrochem. Commun*. **(2004)** 6 66

[24] J. Wang, X. Sun, X. Cai, Y. Lei, L. Song, S. Xie, *Electrochem. Solid-State Lett*. **(2007)** 10 J58

[25] M. Fleischmann, K. Korinek, D. Pletcher, *J. Chem. Soc., Perkin Trans.* **(1972)** 2 1396

[26] I.G. Casella, E. Desimoni, T.R.I. Cataldi, *Anal. Chim. Acta* **(1991)** 248 117

[27] R.E. Reim, R.M. Van Effen, *Anal. Chem*. **(1986)** 58 3203

[28] T.R.I. Cataldi, E. Desimoni, G. Ricciardi, F. Lelj, *Electroanalysis* **(1995)** 7 435

[29] I.G. Casella, E. Desimoni, A.M. Salvi, *Anal. Chim. Acta* **(1991)** 243 61

[30] R. Uchikado, T. N. Rao, D. A.. Tryk A. Fujishima, *Chem. Lett.* **(2001),** 144

[31] Q. Yi, W. Huang, W. Yu, L. Li, X. Liu, *Electroanalysis* **(2008)** 20 2016

[32] P.F. Luo, T. Kuwana, *Anal. Chem***. (1994)** 66 2775

[33] M. Morita, O. Niwa, S. Tou, N. Watanabe, *J. Chromatogr*., *A* **(1999)** 837 17

[34] J.M. Marioli, P.F. Luo, T. Kuwana, *Anal. Chim. Acta* **(1993)** 282 571

[35] J.M. Marioli, T. Kuwana. Electroanalysis **(1993)** 5 11

[36] M. Li, S. Xu, F. Ni, Y. Wang, S. Chen, L. Wang, *Microchim*. *Acta* **(2009)** 166 203

[37] H. Chung, H. Yang, W. Kim, and J. Park, *Anal. Chim. Acta* **(2002)** 471 195

[38] X.-Y. Peng, W. Li, X.-X. Liu, and P.-J. Hua,. *J. Appl. Polym. Sci*. **(2007)** 105 2260

[39] E. Scavetta, S. Stipa, D. Tonelli, *Electrochem. Commun*. **(2007)** 9 2838

[40] I.G. Casella, M. Gatta, *Electroanalysis* **(2001)** 13 549

[41] N.R. Stradiotto, K.E. Toghill, L. Xiao, A. Moshar, R.G. Compton, *Electroanalysis***, (2009)** 21 2627

[42] K. E.Toghill L Xiao, N. R. Stradiotto, R. G. Compton, *Electroanalysis***, (2010),** 22, 491

[43] Q. Chen, M.C. Granger, T.E. Lister, and G.M. Swain, *J. Electrochem. Soc.* **(1997)** 144 3806.

[44] R.G. Compton, F. Marken, C.H. Goeting, R.A.J. McKeown, J.S. Foord, G. Scarsbrook, R.S. Sussmann, A.J. Whitehead, *Chemical Communications* **(1998)** 1961.

[45] C.H. Goeting, J.S. Foord, F. Marken, and R.G. Compton, *Diamond Relat. Mater*. **(1999)** 8 824

[46] J.W. Strojek, M.C. Granger, G.M. Swain, T. Dallas, M.W. Holtz, *Anal. Chem*. **(1996)** 68 2031

[47] R.G. Compton, J.S. Foord, F. Marken, *Electroanalysis* **(2003)** 15 1349

[48] C.H. Goeting, F. Jones, J.S. Foord, J.C. Eklund, F. Marken, R.G. Compton, P.R. Chalker, C. Johnston, *J. Electroanal. Chem*. **(1998)** 442 207

[49] C.H. Goeting, F. Marken, A. Gutierrez-Sosa, R.G. Compton, J.S. Foord, *New Diamond Front. Carbon Technol*. **(1999)** 9 207.

[50] C.H. Goeting, F. Marken, A. Gutierrez-Sosa, R.G. Compton, J.S. Foord*, J Diamond Relat. Mater*. **(2000)** 9 390

[51] C. Batchelor-McAuley, C.E. Banks, A.O. Simm, T.G.J. Jones, R.G. Compton, *Analyst* **(2006)** 131 106

[52] T.J. Davies, C.E. Banks, R.G. Compton, *J. Solid State Electrochem*. **(2005)** 9797

[53] B.A. Brookes, T.J. Davies, A.C. Fisher, R.G. Evans, S.J. Wilkins, K. Yunus, J.D. Wadhawan, R.G. Compton, *J. Phys. Chem. B* **(2003)** 107 1616

[54] T.J. Davies, S. Ward-Jones, C.E. Banks, J. Del Campo, R. Mas, F.X. Munoz, R.G. Compton*, J. Electroanal. Chem*. **(2005)** 585 51

[55] G.M. Swain, R. Ramesham, *Anal. Chem*. **(1993)** 65 345

[56] R. Barnard, C.F. Randell, F.L. Tye, *J. Appl. Electrochem*. **(1980)** 10 109

[57] H. Bode, K. Dehmelt, J. Witte, *Electrochim. Acta* **(1966)** 11 1079

[58] J. Desilvestro, D.A. Corrigan, M.J. Weaver, *J. Electrochem. Soc.* **(1988)** 135 885

[59] D.M. MacArthur*, J. Electrochem. Soc*. **(1970)** 117 422

[60] P. Oliva, J. Leonardi, J.F. Laurent, C. Delmas, J.J. Braconnier, M. Figlarz, F. Fievet, A. De Guibert, *J. Power Sources* **(1982)** 8 229

[61] R.S. Schrebler Guzman, J.R. Vilche, A.J. Arvia, *J. Appl. Electrochem*. **(1978)** 8 67.

[62] A.J. Bard, L.R. Faulkner, *Electrochemical Methods: Fundamentals and Applications,* 2nd edition, John Wiley & Sons, **2001**

[63] C.M. Brett, A.M. Oliveira-Brett, *Electroanalysis*, Oxford University Press, Oxford, **1998**

[64] L. Meng, J. Jin, G. Yang, T. Lu, H. Zhang, C. Cai, *Anal. Chem* **(2009)** 81 7271

[65] Y.-Y. Song, D. Zhang, W. Gao, X.-H. Xia, *Chem.--Eur. J.* **(2005)** 11 2177

[66] J. Yuan, K. Wang, X. Xia, *Adv. Funct. Mater*. **(2005)** 15 803

[67] Y. Bai, W. Yang, Y. Sun, C. Sun, *Sens. Actuators, B* **(2008)** B134 471

[68] B.K. Jena, C.R. Raj, *Chem.--Eur. J.* **(2006)** 12 2702

[69] J. Zhao, L. Wu, J. Zhi, *Analyst* **(2009)** 134 794

[70] J.C. Ndamanisha, L. Guo, *Bioelectrochem.* **(2009)** 77 60

[71] T. Watanabe, T.A. Ivandini, Y. Makide, A. Fujishima, Y. Einaga, *Anal. Chem*. **(2006)** 78 7857

[72] K.B. Male, S. Hrapovic, Y. Liu, D. Wang, J.H.T. Luong, *Anal. Chim. Acta* **(2004)** 516 35

[73] J. Zhao, F. Wang, J. Yu, S. Hu, *Talanta* **(2006)** 70 449

[74] X. Zhang, G. Wang, W. Zhang, Y. Wei, B. Fang, *Biosens*. *Bioelectron*. **(2009)** 24 3395

[75] X. Kang, Z. Mai, X. Zou, P. Cai, J. Mo, *Anal*. *Biochem*. **(2007)** 363 143

[76] Z. Zhuang, X. Su, H. Yuan, Q. Sun, D. Xiao, M.M.F. Choi, *Analyst* **(2008)** 133 126

[77] E. Reitz, W. Jia, M. Gentile, Y. Wang, Y. Lei, *Electroanalysis* **(2008)** 20 2482

[78] W. Wang, L. Zhang, S. Tong, X. Li, W. Song, *Biosens. Bioelectron.* **(2009)** 25 708

[79] X. Zhang, G. Wang, A. Gu, Y. Wei, B. Fang, *Chem*. *Commun*. **(2008)** 5945

[80] Y. Myung, D.M. Jang, Y.J. Cho, H.S. Kim, J. Park, J.-U. Kim, Y. Choi, C.J. Lee, *J. Phys. Chem. C* **(2009)** 113 1251

[81] S. Tong, H. Jin, D. Zheng, W. Wang, X. Li, Y. Xu, W. Song *Biosens*. *Bioelectron*. **(2009)** 24 2404

[82] L. Zheng, J.-Q. Zhang, J.-F. Song, *Electrochim*. *Acta* **(2009)** 54 4559

[83] J.-F. Huang, *Chem*. *Commun***. (2009)** 1270

[84] A. Safavi, N. Maleki, and E. Farjami, *Biosens*. *Bioelectron***. (2009)** 24 1655

[85] M. Yousef Elahi, H. Heli, S.Z. Bathaie, and M.F. Mousavi, *J. Solid State Electrochem*. **(2006)** 11 273

[86] Y. Liu, H. Teng, H. Hou, and T. You, *Biosens*. *Bioelectron*. **(2009)** 24 3329

[87] L.-M. Lu, L. Zhang, F.-L. Qu, H.-X. Lu, X.-B. Zhang, Z.-S. Wu, S.-Y. Huan, Q.-A. Wang, G.-L. Shen, and R.-Q. Yu, *Biosens*. *Bioelectron*. **(2009)** 25 218

[88] Q. Shen, L. Jiang, H. Zhang, Q. Min, W. Hou, and J.-J. Zhu, *J. Phys. Chem. C* **(2008)** 112 16385

[89] C.-H. Chou, J.-C. Chen, C.-C. Tai, I.W. Sun, and J.-M. Zen, *Electroanalysis* **(2008)** 20 771

[90] Y.J. Lee, D.J. Park, and J.Y. Park, *IEEE Sens*. *J*. **(2008)** 8 1922

[91] S. Joo, S. Park, T.D. Chung, and H.C. Kim, *Anal*. *Sci*. **(2007)** 23 277

[92] L.-H. Li, and W.-D. Zhang, *Microchim*. *Acta* **(2008)** 163 305

[93] P. Holt-Hindle, S. Nigro, M. Asmussen, and A. Chen, *Electrochem*. *Commun*. **(2008)** 10 1438

[94] L.-Q. Rong, C. Yang, Q.-Y. Qian, and X.-H. Xia, *Talanta* **(2007)** 72 819

[95] J. Wang, D.F. Thomas, and A. Chen, *Anal. Chem.* **(2008)** 80 997

[96] Y. Bai, Y. Sun, and C. Sun, *Biosens. Bioelectron*. **(2008)** 24 579

[97] H.-F. Cui, J.-S. Ye, W.-D. Zhang, C.-M. Li, J.H.T. Luong, and F.-S. Sheu, *Anal. Chim. Acta* **(2007)** 594 175

[98] F. Xiao, F. Zhao, D. Mei, Z. Mo, and B. Zeng, *Biosens. Bioelectron.* **(2009)** 24 3481

[99] L.-H. Li, W.-D. Zhang, and J.-S. Ye, *Electroanalysis* **(2008)** 20 2212

[100] J. Lu, I. Do, L.T. Drzal, R.M. Worden, and I. Lee, *ACS Nano* **(2008)** 2 1825

[101] J. Chen, W.-D. Zhang, and J.-S. Ye, *Electrochem. Commun*. **(2008)** 10 1268

[102] W. Gorski, and R.T. Kennedy, *J. Electroanal. Chem.* **(1997)** 424 43

[103] S. Buratti, B. Brunetti, S. Mannino, *Talanta* **(2008)** 76 454

Chapter 8

The determination of primary alcohols using an electrolytically fabricated nickel modified boron doped diamond electrode

The work presented in this chapter has been published in

Electroanalysis, **2009,** *21*, 2627

Electroanalysis, **2010**, *22*, 491

In this chapter a nickel modified boron doped diamond (Ni-BDD) electrode and nickel foil electrode were used in the determination of methanol, ethanol and glycerol in alkaline solutions. Based on the same principles as glucose determination in the previous chapter, the modified electrode was also applied to small primary alcohols. The nickel was electrodeposited from a 1mM $Ni(NO_3)_2$ solution in 0.1 M acetate buffer (pH 5). Subsequent analysis utilised the $Ni(OH)_2$/NiOOH redox couple to electrocatalyse the oxidation of each alcohol.

SEM analysis of the electrodes found the Ni-BDD to be modified by a quasi-random nano or microparticle array depending on nickel deposition time. Methanol was determined using chronoamperometric methods to limits of 0.3 mM with a sensitivity of 110nA/mM at the Ni-BDD electrode. The foil electrode was less sensitive achieving a limit of 1.6 mM and sensitivity of 27 nA/mM. Using cyclic voltammetry, linear calibration plots were obtained for the ethanol and glycerol additions over concentration ranges of 2.8 – 28.0 mM and 23 – 230 μM respectively. This gave detection limits of 1.7 mM and 10.3 μM and sensitivities 0.31 mA/M and 35 mA/M for ethanol and glycerol respectively.

8.1. Introduction

The electrocatalytic oxidation of small organic compounds at nickel electrodes has been extensively studied since the early work of Fleischmann et al in the 1970's [1] and is well documented in the literature[1-12]. A large number of molecules have been investigated, including simple alcohols [2, 5, 11], amines [12, 13], glucose [14-18] and methane [19]. Alcohols have been of specific interest in recent years, due to their application in direct alcohol fuel cells (DAFCs).

Direct alcohol fuel cells (DAFC) are one viable alternative to petroleum driven vehicles, offering a more compact, easily contained fuel and relatively safe by-products, as well as a low-cost, sustainable renewable fuel source [20]. DAFCs are electrochemical conversion devices in which the primary alcohol fuel is electrocatalytically oxidised to generate electricity. At present platinum and platinum based materials are the catalysts of choice [20, 21], though extensive research into alternative catalysts have recognised numerous other suitable metals, such as Pd, Ru, Ir, Co, and Ni, [22-26]. These base metal alternatives are available at a much lower cost and in greater abundance than the platinum catalysts, and therefore have greater potential for wide spread use in the automotive industry. Development over recent years in alkaline fuel cells has lead to vital improvements that should allow more widespread use of the alkaline electrolyte for use in conjunction with alcohol fuel cells [27].

The catalytic use of nickel hydroxide towards alcohols has been well researched and there is an established mechanism for reaction [1, 12, 28, 29]. In aerated alkaline solution, nickel reacts with dissolved oxygen to form a $Ni(OH)_2$ layer, which in turn is reversibly oxidised to NiOOH at low potentials of approximately 400 mV[30]. This potential varies depending on the pH of the electrolyte, with decreasing pH associated with an anodic shift of the redox couple. The NiOOH is catalytically active towards some small organic compounds, and mediates their subsequent irreversible oxidation [1, 28]. Coupled with amperometry, this reaction becomes a quantifiable system, as has been demonstrated in a

number of publications [4, 5, 31-33]. With regard to alcohols however, the system has been overshadowed by the search for DAFCs. Therefore the analytical determination of alcohol at nickel modified electrodes is relatively unexplored. The few papers that do utilise the $Ni(OH)_2$ couple in alcohol analysis however, have observed encouraging results [4, 5, 7, 11, 34-36].

In this chapter the use of boron doped diamond (BDD) electrodes electrochemically modified with nickel for the determination of low methanol, ethanol and glycerol concentrations is presented. BDD has been frequently used in electrocatalysis as a substrate material for catalytic particles [37-39], but is also used directly in the oxidation and reduction of organic materials as a bare electrode [40-43], as well as in electroanalysis of numerous analytes. The chemical durability of the electrode means it tolerates ordinarily electrode fouling analytes [41-43], and therefore is an ideal substrate for the electroanalysis of alcohol and potentially other aggressive analytes.

8.2. Experimental

Apparatus

All voltammetric measurements were recorded using an Autolab PGSTAT20 computer controlled potentiostat (EcoChemie, Utrecht, The Netherlands). A standard three-electrode configuration was used throughout, consisting of a boron doped diamond (BDD, diameter 3mm, Windsor Scientific, Slough, UK) working electrode, with a saturated calomel reference electrode (SCE) and graphite rod or platinum wire counter electrode. The BDD disk working electrode was incorporated into a custom built PEEK housing, equipped with a stainless steel piston to make electrical contact.

The nickel bulk electrode (nickel foil) was prepared from a nickel foil, 0.025mm thick (Goodfellow Advanced Materials, Surrey, UK) which was attached to a stainless steel piston and also incorporated into a custom built PEEK housing. The nickel foil electrode

was prepared with the same surface area as the BDD electrode, to allow direct comparison to be made.

Atomic force microscopy (AFM) was conducted on a MFP-3D stand alone microscope (Asylum Research, Santa Barbara, CA) using AC 240 cantilever from Olympus, spring constant 2 N/m in AC mode. The software used for data acquisition and analysis was IGOR Pro 6.0 (Wavemetrics) with 3D imaging provided by Argyle- 3D imaging software.

Scanning electron microscopy (SEM) was performed using a JEOL 6300 F instrument (FEG-SEM, tungsten filament as electron source, acceleration voltage 20keV) images with energy dispersive X-ray (EDX) spectra analysis performed simultaneously to the SEM. Particle analysis was conducted using Image J software, a Java based program provided through the National Institute of Health (NIH).

Reagents and solutions

All chemicals were purchased from Sigma-Aldrich (Gillingham, UK) were of analytical grade and were used as received without any further purification. These were nickel (II) nitrate hexahydrate, methanol anhydrous 99.7%, ethanol anhydrous 99.5%, and glycerol GC 99%. A standard solution of nickel (II) nitrate 1 mM was prepared in 0.1 M sodium acetate buffer solution (pH 5), the latter received as a 3 M biological standard solution from Aldrich, and diluted to 0.1 M using deionised water of resistivity not less than 18.2 MΩ cm^{-1} at 298 K (Millipore UHQ, Vivendi, UK). For the alcohol oxidation experiments a standard 1.0 M solution of potassium hydroxide (ca. pH 14) was used, prepared using potassium hydroxide pellets purchased from BDH Laboratories (Poole, UK) in deionised water.

Experimental procedure

Prior to each set of standard alcohol additions the surface of the BDD electrode was cleaned using a diamond slurry of 0.1 μm particle size, followed by sonication for 1 minute in ethanol/water and thorough rinsing using deionised water. This was also the procedure

prior to modification by the nickel nanoparticles. The surface of the bulk nickel electrode was renewed via the same procedure prior to use. In addition to this, the electrodes were electrolytically cleaned by running 5 consecutive cycles from -1.4 V to +1.4 V at a scan rate of 50 mVs^{-1}.

Alcohol oxidation experiments were performed using cyclic voltammetry with a start and cathodic potential limit of 0 V and an anodic potential limit of ca. +0.5 V. Chronoamperometric analysis of methanol additions was also performed using a fixed potential of ca. 0.42 V vs. SCE, under constant stirring.

Ni-BDD formation

Nickel was deposited on to the BDD by cathodic reduction of a degassed 1mM $Ni(NO_3)_2$ solution in 0.1 M acetate buffer solution (pH 5) in which the BDD was held at -1.3 V for varying deposition times under stirring. This was followed by removal of the modified electrode from the deposition solution to a non-degassed potassium hydroxide solution.

8.3. Results and discussion

8.3.1 Characterisation of the nickel- nanoparticle modified BDD electrodes

8.3.1.1 Scanning electron microscopy (SEM) and energy dispersive x-ray spectroscopy (EDX)

Nickel was deposited onto the BDD electrode from a degassed 1 mM $Ni(NO_3)_3$ in 0.1 M acetate buffer solution for a period of 300 s or 600 s. Representative SEM images are illustrated in Figure 8.1 of the BDD electrode nickel modified for 300 s, with images of the 600 s modification shown in the previous chapter. Also shown is the unmodified BDD surface (a, b) for comparison.

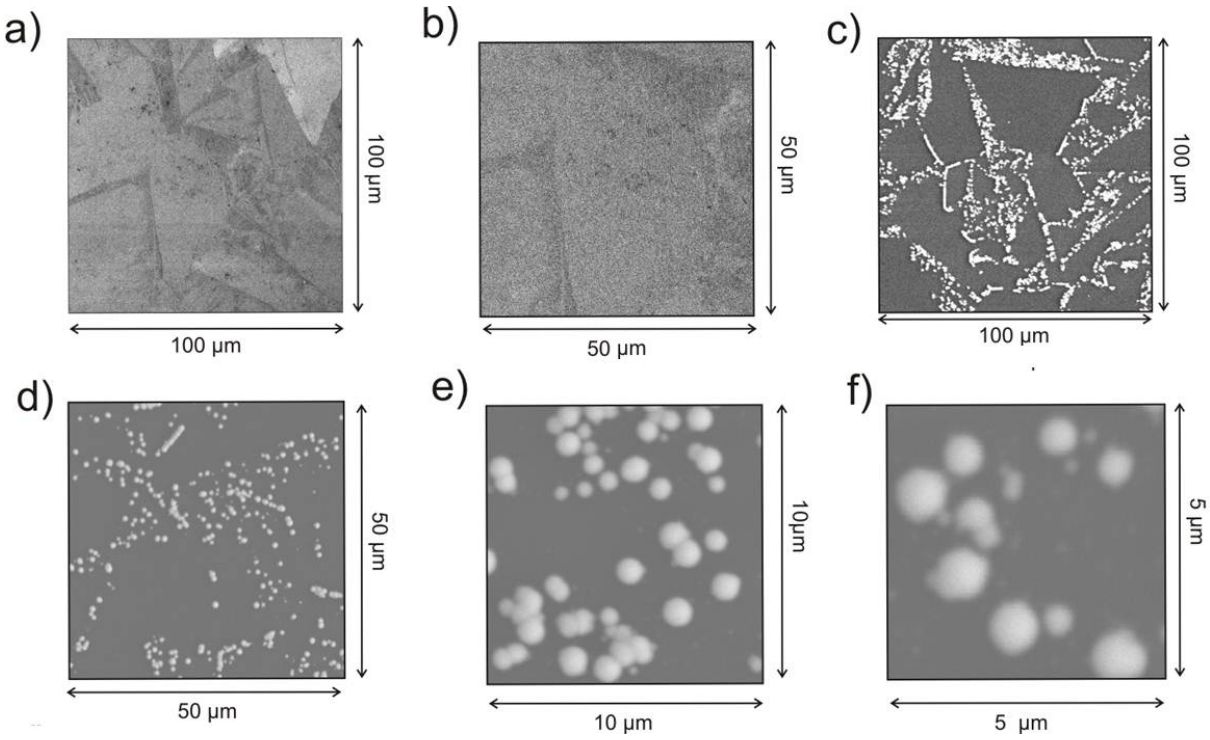


Figure 8.1: *SEM images of the unmodified (a,b) and Ni modified (c-f) BDD electrode. The Ni-BDD was imaged following a* ***300 s*** *stirred deposition of Ni at -1.2 V (vs SCE) in 0.1 M acetate buffer degassed solution (pH 5)*

The Ni-BDD electrode modified for 300 s was rinsed immediately after modification with deionised water and dried in air before imaging with a scanning electron microscope. Following the 600 s deposition of nickel onto the BDD electrode, the electrode was cycled in 1M KOH for 300 cycles at 50 mVs^{-1} to fully develop the $Ni(OH)_2$ layers. The electrode was dried in air and imaged using a SEM.

From Figure 8.1c the nickel deposits have evidently nucleated on particularly active areas of the BDD electrode, likely growing at the polycrystalline grain boundaries present across the diamond surface. This behaviour has been shown in earlier chapters and has also been reported by Swain and Ramesham [44]. The wide range in particle size suggests a progressive growth processes stemming from continued nucleation of metallic nickel to the active BDD electrode areas.

On increased magnification of the surface, the hemispherical nanoparticles of nickel are clearly observed. Calculations based on these images, and others (not shown), give an estimated nickel nanoparticle radius of 295 nm over a range of 60nm to 890 nm. The surface coverage was calculated to be ca. 15% of the electrode, which based on the average nanoparticle area, corresponds to an average total surface coverage of approximately 5.20 $x10^7$ nanoparticles cm^{-2}, and a nickel mass of 34 μg cm^{-2}.

The 600s deposition of nickel gave much larger nano and microparticles particles with an average nickel microparticle radius of 595 nm over a range of 0.05 to 1.9 μm. The average number of particles on the electrode was calculated to be approximately $1.20x10^7$ particles cm^{-2}, and nickel coverage by mass to be ca. 50 μg cm^{-2}.

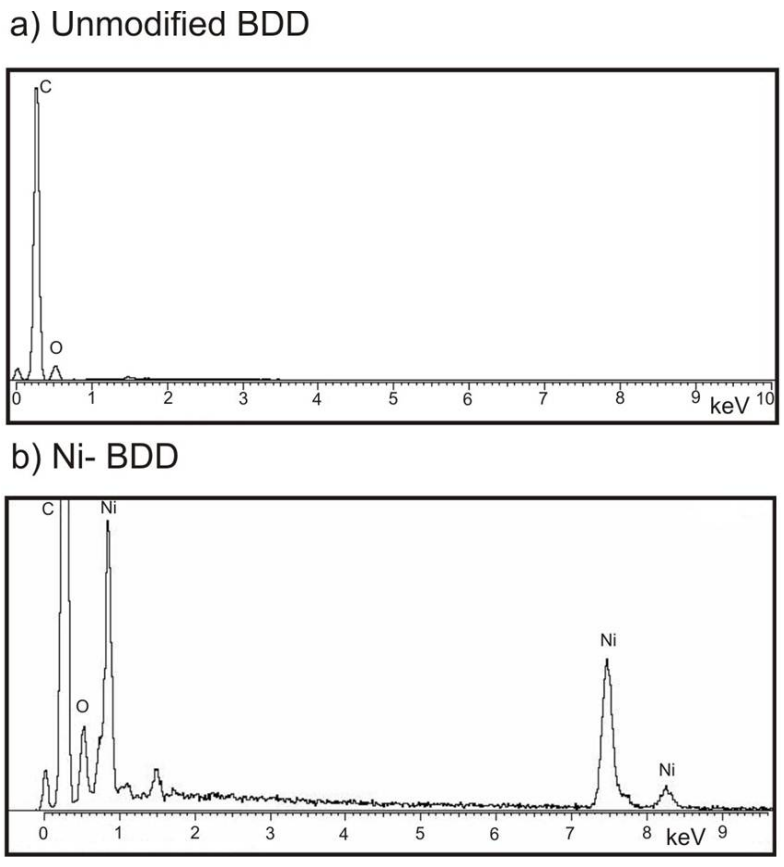


Figure 8.2: *EDX data for the unmodified (a) and Ni-modified (b) BDD electrode. The Ni-BDD was imaged following a 300 s stirred deposition of Ni at -1.2 V (vs SCE) in 0.1 M acetate buffer degassed solution (pH 5)*

For both the 300s and 600s Ni-BDD electrodes EDX spectroscopic data was acquired simultaneously to the SEM data, and is shown in Figure 8.2 for the 300s Ni-BDD. The bare BDD electrode data is also shown for comparison. Three peaks corresponding to the nickel are clearly observed at approx. 0.8, 7.5 and 8.2 keV in the modified BDD electrode and nickel foil spectrum.

8.3.1.2 Ex-situ atomic force microscopy (AFM)

Ex-situ AFM was conducted on the air dried Ni-BDD following modification in the same method as described above. Characterisation of the nanoparticles using AFM allowed for the particle heights to be determined, and therefore completed the picture of the modified surface. The image of the bare BDD surface in Figure 8.3a, again illustrates a patchy surface very similar to that shown by the SEM images, demonstrating that the BDD surface is not perfectly flat when observed on a 5 nm scale.

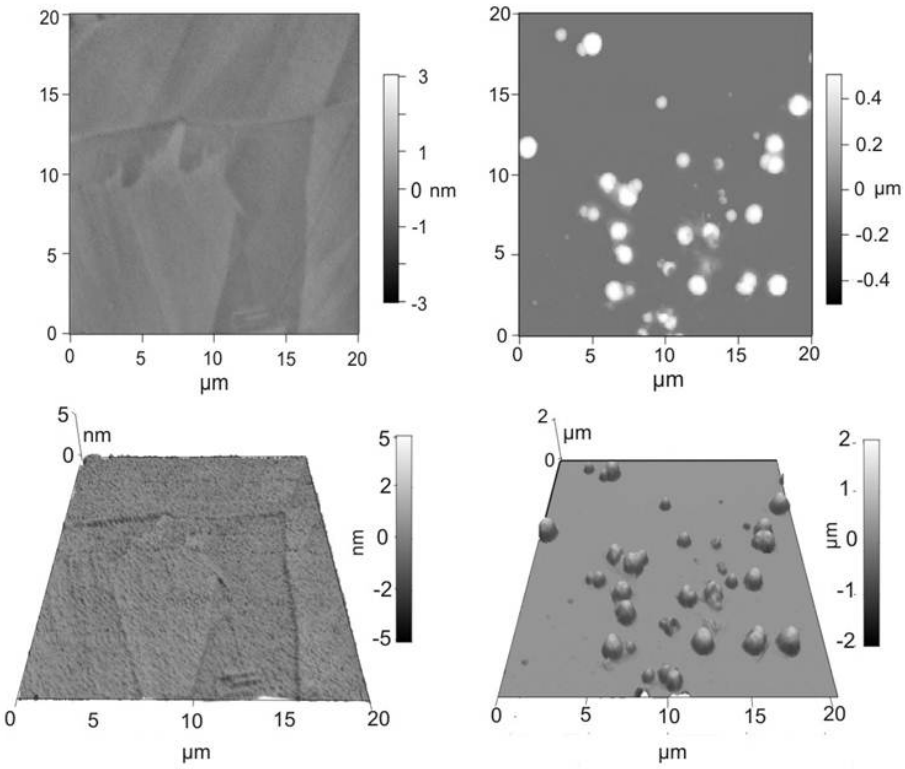


Figure 8.3: *Ex-situ AFM images of the BDD electrode before (a) and after (b,c) Ni modification, following stirred electrodeposition of Ni from a 1 mM Ni(II) in 0.1 M acetate buffer degassed solution (pH5). The figure shows the scan and 3D image.*

It is evident from the AFM images that the nickel deposits have a hemispherical form, with the average height determined to be ca. 350 nm over a range of 5 nm to 690 nm, again emphasising the progressive nucleation of nickel onto the BDD surface. Surface analysis using the Igor Pro software determined the average total volume of the nickel deposit to be 2.1 $x10^{-6}$ cm^3 per cm^2 area. This equates to an average total mass of nickel on the electrode to be 19 μg cm^{-2}, which is less than the value established from multiple SEM images, yet is in accordance with the SEM estimate of 34 μg cm^{-2}.

8.3.1.3. Enrichment of the $Ni(OH)_2$ layer

For the methanol experiments the Ni-BDD electrode was modified by electrodeposition of nickel for 600s from an aqueous $Ni(NO_3)_2$ solution as detailed in numerous publications [30, 45-47]. This deposition and enrichment proces was briefly described in the previous chapter with respect to the Ni-BDD used in glucose analysis. Studies by Desilvestro et al [46] and McArthur [47] explored deposition from this medium, and found that $Ni(OH)_2$ was precipitated along with nickel metal. This process may be described by the following equation [46] also expressed in Chapter 7;

$$NO_3^- + 7H_2O + 8e^- \longrightarrow NH_4^+ + 10OH^- \quad (1a)$$

$$Ni^{2+} + 2OH^- \longrightarrow Ni(OH)_2 \quad (1b)$$

$$Ni^{2+} \longrightarrow Ni^0 \quad (1c)$$

The release of OH^- ions by the electro-reduction of NO_3^- anions therefore precipitate the Ni^{2+} as $Ni(OH)_2$ as well as nickel metal. This is suggested by the initial cyclic voltammetry of the Ni-BDD in 1.0 M KOH, in which the oxidation of $Ni(OH)_2$ to NiOOH is observed from the first scan as shown in Figure 8.4.

The presence of $Ni(OH)_2$ on the electrode surface and not exclusively nickel metal is also well established in literature [1, 46, 48-53], whereby nickel is observed to spontaneously form $Ni(OH)_2$ in strongly alkaline, aerated solutions. There is evidence in

the first anodic sweep of the scan however that some nickel metal may be present on the electrode surface, as a notable oxidative wave is observed preceding the Ni(II)/Ni(III) peak, which in itself occurs at a more anodic potential due to a higher overpotential required to instigate the initial oxidation .

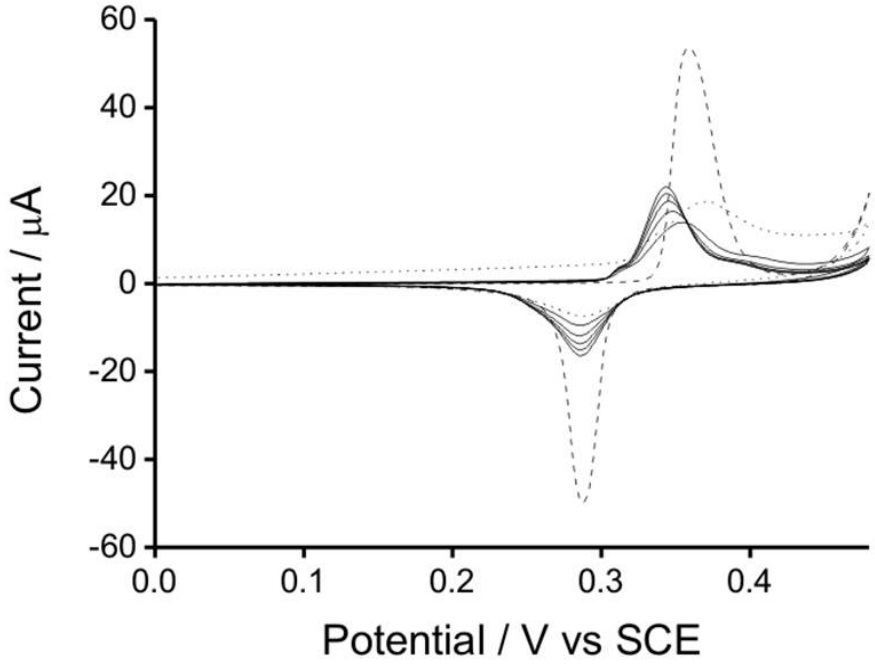


Figure 8.4: *Overlay of the first CVs (scans 1,2,4,6,8, and 10) and 300th CV for a 600 s Ni-BDD in 1M KOH, scan rate 50 mV* s^{-1}*. The first CV is shown as a dotted line and the final (300*th*) CV is a dashed line.*

Electrodeposition of $Ni(OH)_2$ from nitrate solution and subsequent immersion into an alkaline electrolyte leads to the formation of two crystallographic species, the hydrated α-$Ni(OH)_2$ and anhydrous β-$Ni(OH)_2$ [45, 49, 52, 54]. The β species is the more stable of the two with a structure of nickel octahedrally coordinated to eight oxygen atoms. The hydrated α structure however is much less crystalline, and has water molecules intercalated between the layers of NiO_2 that form the $Ni(OH)_2$ crystal structure [54, 55]. On electrooxidation of the nickel hydroxides, two corresponding oxyhydroxide species are formed, γ-NiOOH and β- NiOOH. The former γ structure is relatively unstable, and when oxidised to the

oxyhydroxide in an alkaline medium, ionic species intercalate the layers along with water. It can be considered to have the general formula of $A_xH_y(H_2O)_zNiO_2$ (x,y < 1), in which A represents an alkali ion [54, 55].

On deposition of the $Ni(OH)_2$ the α and β species are present in non-stoichiometric amounts. Potential cycling of the nickel in strong alkali leads to ageing of the material however, characterised by a potential shift to more anodic values [56]. This is evident in Figure 8.4 in which the final oxidation peak (dashed line) has shifted ca. 30 mV anodic of the first 10 oxidation peaks (except the very first scan). This indicates that the presence of the stable β species has increased in the course of conditioning and $Ni(OH)_2$ layer enrichment [56, 57].

The $Ni(OH)_2$ is still present in a non-stoichiometric mix of the α and β nickel crystal structures following extensive cycling however, a point corroborated by the study of pOH on the peak potential of the Ni(II)/Ni(III) redox couple. Figure 8.5 is an overlay of the CVs for the redox couple at varying concentrations of KOH, and therefore varying pOH. As the pOH increases, a shift to more anodic potentials is observed. Inset of Fig. 8.5 the pOH is plotted against peak potential for the anodic and cathodic reactions.

The slopes of these plots show a shift by ca. 88 mV and not by 60mV as would be expected from the one electron redox process depicted by the equation;

$$Ni(OH)_2 \rightarrow NiOOH + H^+ e^- \quad [2]$$

The latter equation is associated with the oxidation of β-$Ni(OH)_2$ to β-NiOOH [30, 54] which is a simple one electron process. The oxidation of α-$Ni(OH)_2$ to γ-NiOOH is consider much more complicated however, involving the intercalation of K^+ and OH^- as mentioned above, thus presumably resulting in the unusual OH^- dependence. Using the Nernst equation, the OH^- dependence is formally 1.5 OH^- per mole of electrons, and might be explained by the following equation

$$NiO + 1.5OH^- + 0.5K^+ \rightarrow K^+_{0.5}OH^-_{0.5}NiOOH + e^- \quad (3)$$

Species akin to the product shown in equation 3 have been discussed extensively in numerous papers regarding the oxidation of nickel hydroxide [30, 54, 55], and have long been determined as present in chemically and electrochemically deposited films.

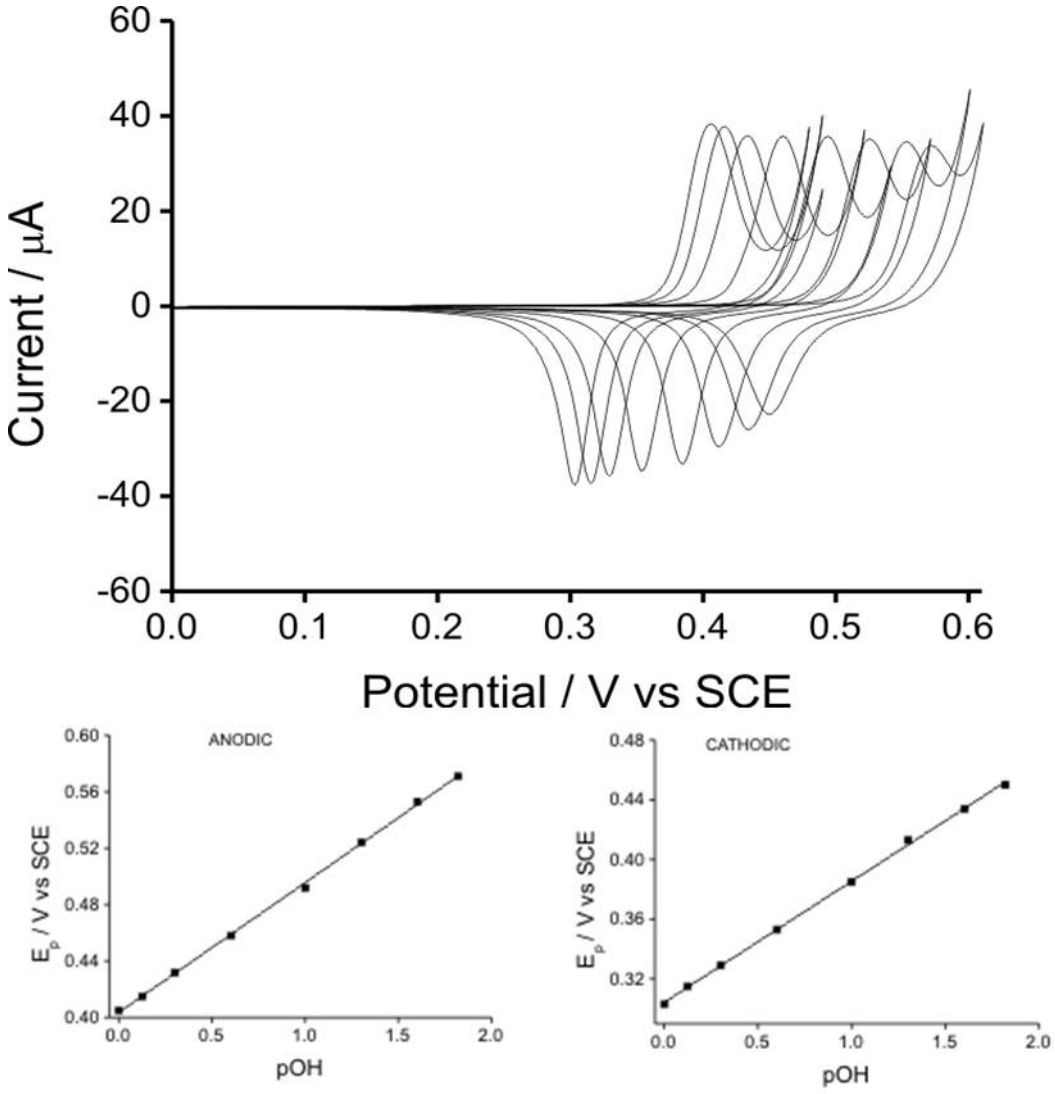


Figure 8.5: *Overlay of CVs for the 600s Ni-BDD following $Ni(OH)_2$ enrichment in varying concentration of KOH. Concentration of KOH from 0.02 M to 1.0 M, ionic strength maintained at 1.0 M using relative amounts of KNO_3. Below: Plots of the peak potential vs. pOH for the anodic (left) and cathodic (right) peaks each with a linearity of $R^2 = 0.999$.*

The presence of two nickel structures is also indicated by two oxidation peaks observed in the initial scans of the Ni-BDD. Continuous cycling of the nickel boron doped diamond electrode in 1.0 M KOH leads to the merging of these peaks, and a significant increase in

the redox peak currents. As can be seen in Figure 8.4, the first 10 scans have a potential more cathodic to the final scan after 300 CVs shown as a dashed line. This is indicative of an initially more hydrated nickel species, with the α- $Ni(OH)_2$ dominating the voltammetry [56]. By the 300th scan, only one oxidative peak is present, that is considered to be a non-stoichiometric thin layer of α and β $Ni(OH)_2$ which is predominantly the latter species due to the high KOH concentration, anodically shifted peak position, and the tendency for the α species to age to β [45].

The number of monolayers of $Ni(OH)_2$ present on the Ni-BDD and Ni-foil surfaces was calculated to comparable values of 15.3 and 17.6 respectively. This was based on the area under the reduction wave of NiOOH to $Ni(OH)_2$ providing the charge required to fully reduce to oxy hydroxide layer. Using the equation $Q = nFA\Gamma_o^*$ [58], in which Q is charge, n the number of electrons, F is the Faraday constant, and A the surface area of Ni, the number of moles per square centimetre of NiOOH, Γ_o^*, was calculated. The crystallographic value for a $Ni(OH)_2$ monolayer of 1.06×10^{-9} mol cm^{-2} was obtained from Bode et al [55]. Thus the nickel foil electrode, with a surface area of 0.07 cm^2, and a cathodic charge of 1.26×10^{-4} C, the number of monolayers is calculated to be 17.6. With the Ni-BDD, the surface area of the nickel was estimated based on the SEM data to be 0.02 cm^2, 3.5 times less than the nickel foil. The average cathodic charge was determined as 3.16×10^{-5} C, which is four times lower than the nickel foil, and calculates to 15.4 monolayers of $Ni(OH)_2$. The SEM estimate and voltammetric data therefore correspond well, and imply that the same degree of nickel enrichment is achieved during the same cycling procedure.

The mass of nickel on the foil electrode was determined by calculating the foil volume and multiplying it by the density of nickel. A mass of 22.3 mg cm^{-2} of nickel was calculated, a considerably greater mass relative to the 49.8 μg cm^{-2} approximated and discussed in the previous section. Therefore it can be seen that a considerably lower amount of nickel in a random microparticle array has a much greater relative surface area to a film like electrode.

8.3.2. The electrocatalysis of methanol electrooxidation

Methanol additions were made to a 1.0 M KOH aerated solution using a bare BDD, nickel BDD and nickel foil electrode. Methanol was not observed as an electrochemical signal at the bare BDD in either cyclic voltammetry or amperometry. Figure 8.6 shows an overlay of 10 successive 5 mM additions of methanol to the 1.0 M KOH solution using the Ni-BDD electrode.

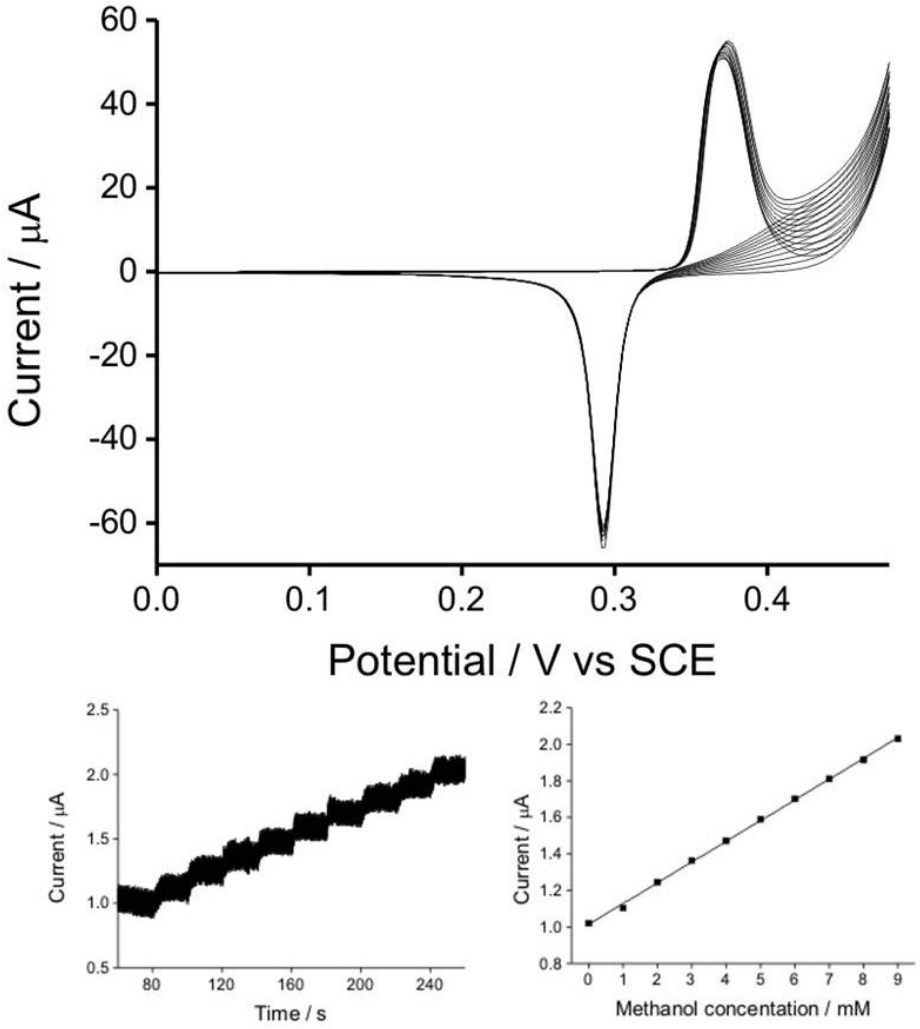


Figure 8.6: *Overlay of 10 successive CVs following 10, 1 mM additions of methanol to a 1 M KOH solution, using the 600 s Ni-BDD, aerated. Below – (left) Amperometric analysis of 0.5 mM methanol additions to the Ni-BDD in 1M KOH and (right) Plot of current vs. methanol concentration from the amperometric data*

The catalytic oxidation of methanol at the Ni-BDD is evident in an increase in the Ni(II)/(III) oxidation peak, shifting of the peak anodically, and most significantly, the increase in current after the nickel oxidation peak. Methanol additions were subsequently analysed using amperometry, with the potential fixed at the post nickel oxidation potential of 0.42 V vs. SCE. Inset of Figure 8.6 is a current vs. time plot for the Ni-BDD, in which 1mM methanol additions were made to the KOH solution at 20s intervals. The experiment was performed under stirring and in a non-degassed solution. Note that the noise in the current derives from the magnetic stirrer used to mix the solution. This would unlikely be observed in practical sensor application where other approaches would probably be used. Figure 8.6b is an averaged current vs. methanol concentration calibration plot for the latter experiment. The additions showed high linearity of $R^2 = 0.999$ with a limit of detection calculated from 3σ [59] of 0.28 mM and a sensitivity of 110 nA/mM of methanol. Over six separate experiments using a newly prepared Ni-BDD, the average LOD was found to be 0.33 mM, and the electrochemical response was highly consistent.

The same experiment was performed using a nickel foil electrode for comparison of the bulk nickel behaviour to that of nickel nanoparticles. The nickel foil was thoroughly polished using various sizes of diamond spray, then subsequently cycled in 1.0M KOH for 300 cycles. The potential range for the nickel foil CVs was compared to the Ni-BDD owing to the onset of Ni^{2+} reduction at 0.06 V vs. SCE. Expansion of the cathodic potential window to -0.5 V observed a broad reductive peak in the nickel foil voltammetry, which was complimented by a broad oxidative pre-wave on the following anodic sweep of the voltammogram. This broad peak at ca. 0.28 V is believed to correspond to the oxidation of nickel metal to Ni^{2+}, and is followed by the oxidation of Ni^{2+} to Ni^{3+}. This pre wave is only observed on the initial anodic scan of the nickel foil, and when the cathodic potential is taken to beyond the reduction of Ni^{2+}. A comparative experiment was performed on the Ni-BDD, shown in Figure 8.7, but no reduction was observed, even when the cathodic potential was taken to -1.0 V.

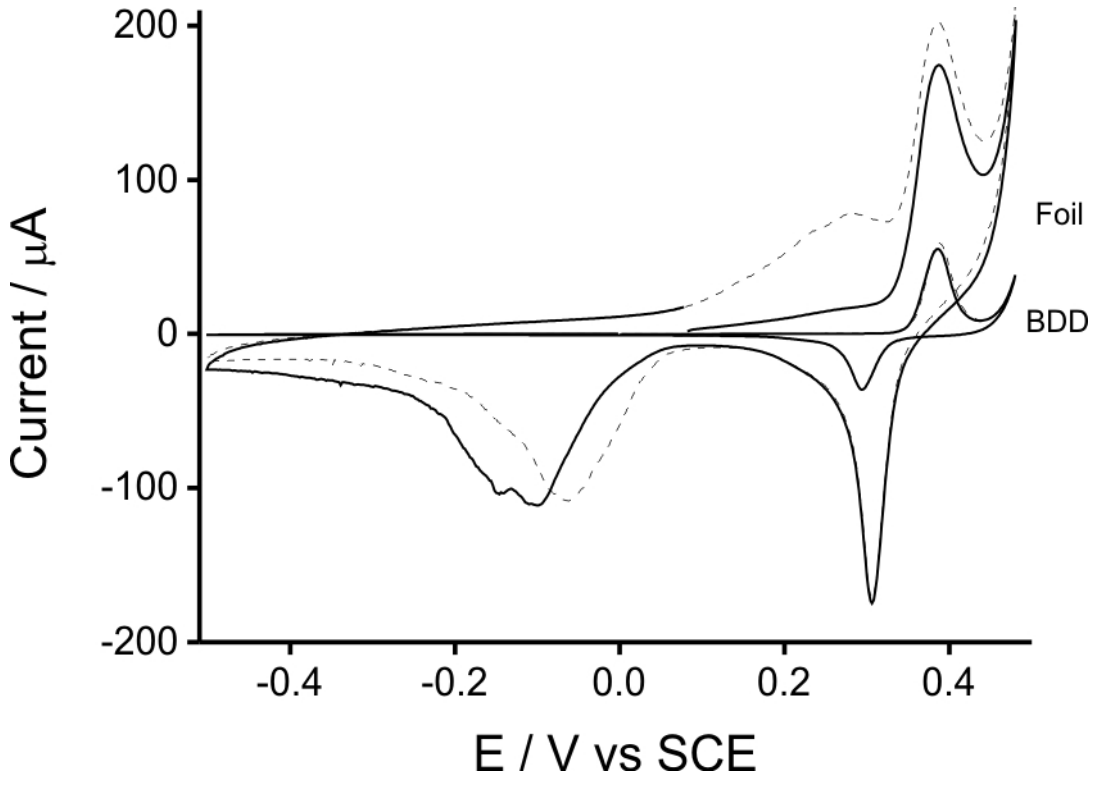


Figure 8.7: *Overlay of Ni-BDD and Ni-foil electrodes in 1.0 M KOH with an extended cathodic potential window. Two consecutive scans shown, with the second scan of each represented by a dashed line.*

Figure 8.8 shows an overlay of CVs for the Ni-foil electrode in 1M KOH following 10 mM additions of methanol. The capacitative current was much greater for nickel foil electrode, yet clear oxidation and reduction peaks are observed. A marked shift in the peak potentials is observed on addition of the methanol, followed by a linear increase in peak current and gradual anodic shift on subsequent additions. This was again coupled with the significant increase in the current post oxidation peak, with the potential of 0.42 V again chosen for amperometric analysis. Below-left in Figure 8.8 is the current vs. time plot for 10 mM methanol additions to the nickel foil electrode in 1.0 M KOH (a) and the corresponding calibration plot of average current vs. methanol concentration. Again the noise in the current derives from the stirrer.

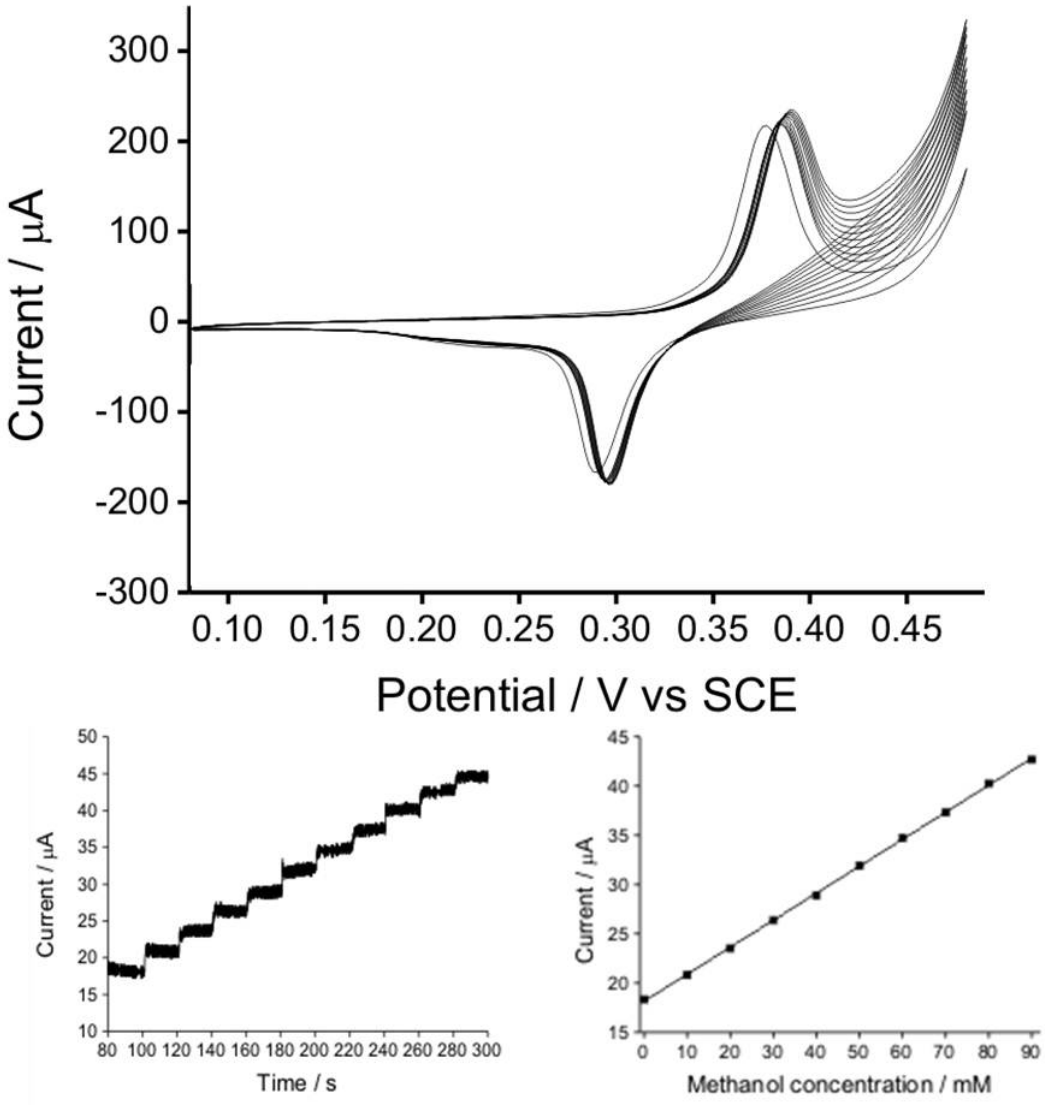


Figure 8.8: *Overlay of 10 successive CVs following 10, 1 mM additions of methanol to a 1 M KOH solution, using the 600 s Ni foil, aerated. Below – (left) Amperometric analysis of 0.5 mM methanol additions to the Ni-BDD in 1M KOH and (right) Plot of current vs. methanol concentration from the amperometric data*

With the nickel foil, a well-defined amperometric analysis was only attainable at additions of 10 mM methanol. Consequently, the linear calibration plot of $R^2 = 0.999$ gave a LOD of 1.61mM methanol and a sensitivity of 29 nA/mM methanol. This shows a 10 fold increase in limit of detection and decrease in sensitivity compared to the Ni-BDD. The improved sensitivity and LOD of the Ni-BDD compared to the nickel foil electrode may be attributed to better diffusion to what is effectively a nickel micro array on the Ni-BDD.

8.3.3. The *electrocatalysis of ethanol and glycerol electrooxidation*

When placed in the alkaline KOH solution, without the enrichment procedure, the 300s Ni-BDD electrode gave a typical cyclic voltammogram (CV) corresponding to the formation of $Ni(OH)_2$ as discussed above. The CVs in Figure 8.9 compare the bare and the Ni-BDD, in which it is evident that the Ni-BDD is modified.

Two oxidation peaks are observed, believed to correspond to the hydrated α-$Ni(OH)_2$ and anhydrous β-$Ni(OH)_2$ crystallographic forms [51, 54]. At concentrations of 1 M KOH, β-$Ni(OH)_2$ is favoured, and therefore dominates the voltammetry. The relative formation of α- to β varies with each newly modified electrode, but invariably favours the catalytically active β form, which is the second oxidation peak [54]. It is therefore this peak, due to the oxidation of β- $Ni(OH)_2$ to β-NiO(OH), that is the peak of interest during alcohol additions in the following experiments.

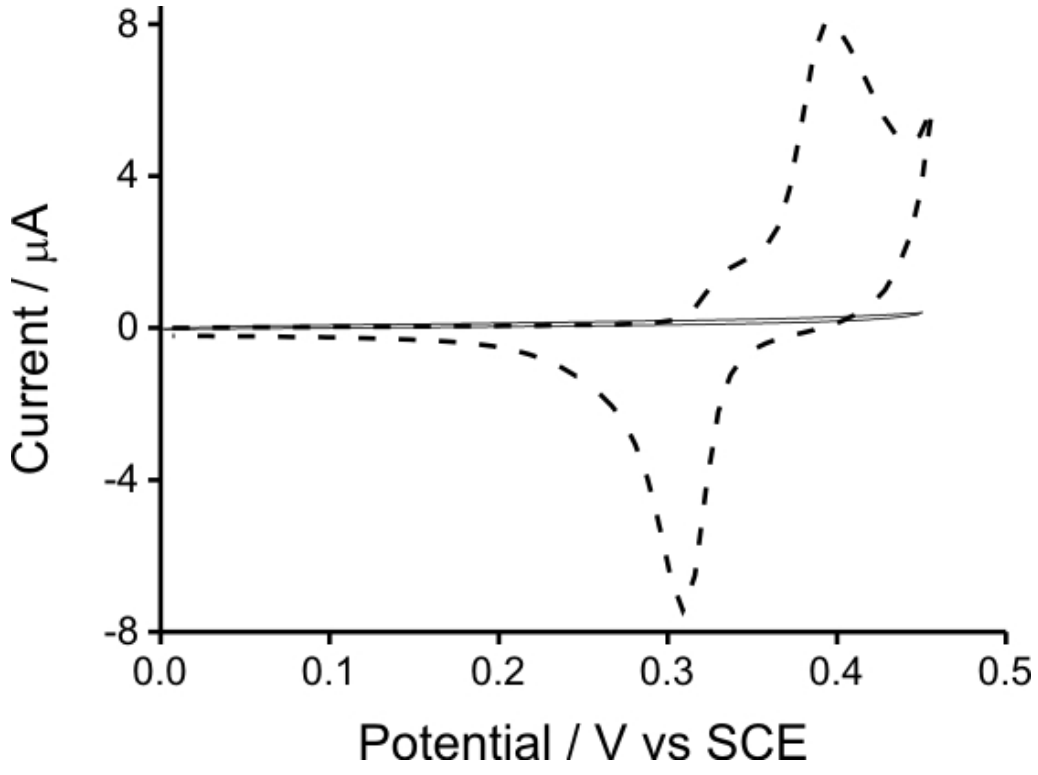


Figure 8.9: *Overlay of CVs for the bare BDD (solid line) and Ni-BDD (dashed line) in a 1.0 M KOH solution, deaerated.*

8.3.3.1 Ethanol

Ethanol additions were made to a 1.0 M KOH degassed solution using a bare BDD, Ni-BDD and nickel foil electrode. The bare BDD observed no change in CV following the ethanol additions, even at concentrations of 28 mM of ethanol. Figure 8.10 illustrates the difference between the bare BDD and Ni-BDD at this ethanol concentration.

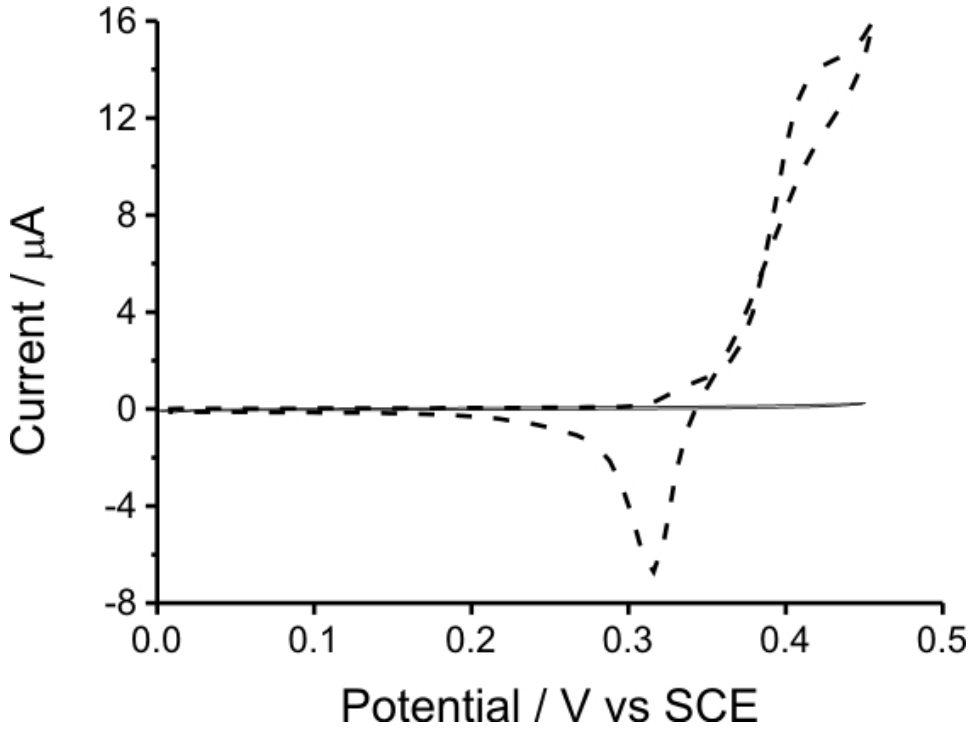


Figure 8.10: *Overlay of CVs for the bare BDD (solid line) and Ni-BDD (dashed line) in a 1 M KOH solution and 28 mM of ethanol, deaerated.*

Figure 8.11 shows an overlay of ten successive 2.8 mM additions of ethanol to the 1.0 M KOH solution using the Ni-BDD electrode. The enhancement of the NiOOH oxidation peak with each addition is evident, providing a highly linear calibration plot of R^2 = 0.996 and a limit of detection (3σ) of 1.7×10^{-3} M of ethanol, and a sensitivity of 0.31 mA/M in the best instance. Over three separate experiments using a 'freshly' prepared Ni-BDD, the average LOD was found to be 1.8 mM, and highly consistent.

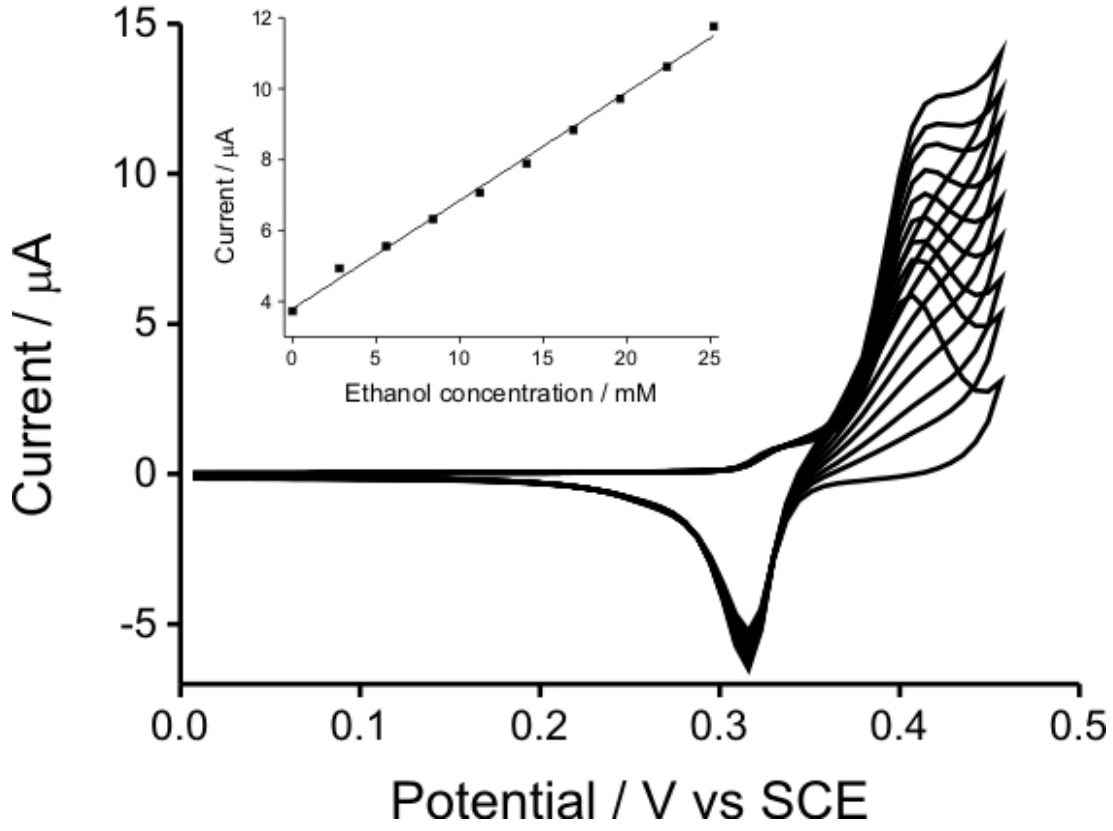


Figure 8.11: *Overlay of eleven successive CVs following ten, 2.8 mM additions of ethanol to a 1.0 M KOH solution, using the Ni-BDD, deaerated. Inset – Calibration plot for NiOOH peak height vs. ethanol concentration*

The same experiment was performed using a nickel foil electrode for comparison of the bulk nickel behaviour to that of nickel nanoparticles. The capacitative current was much greater for nickel foil electrode, as would be expected, yet clear oxidation and reduction peaks are observed. Although the ethanol additions enhanced the NiOOH peak as expected, the effect was not as linearly defined as for the nanoparticles, providing a calibration plot of R^2 = 0.927 and a limit of detection of 6.2 x10^{-3} M. The sensitivity of the nickel foil electrode is deceptively greater than that of the Ni-BDD which was calculated to be 2.42 mA/M. This is due to the much greater surface area of the former electrode relative to the Ni-BDD. The latter experiment is shown in Figure 8.12.

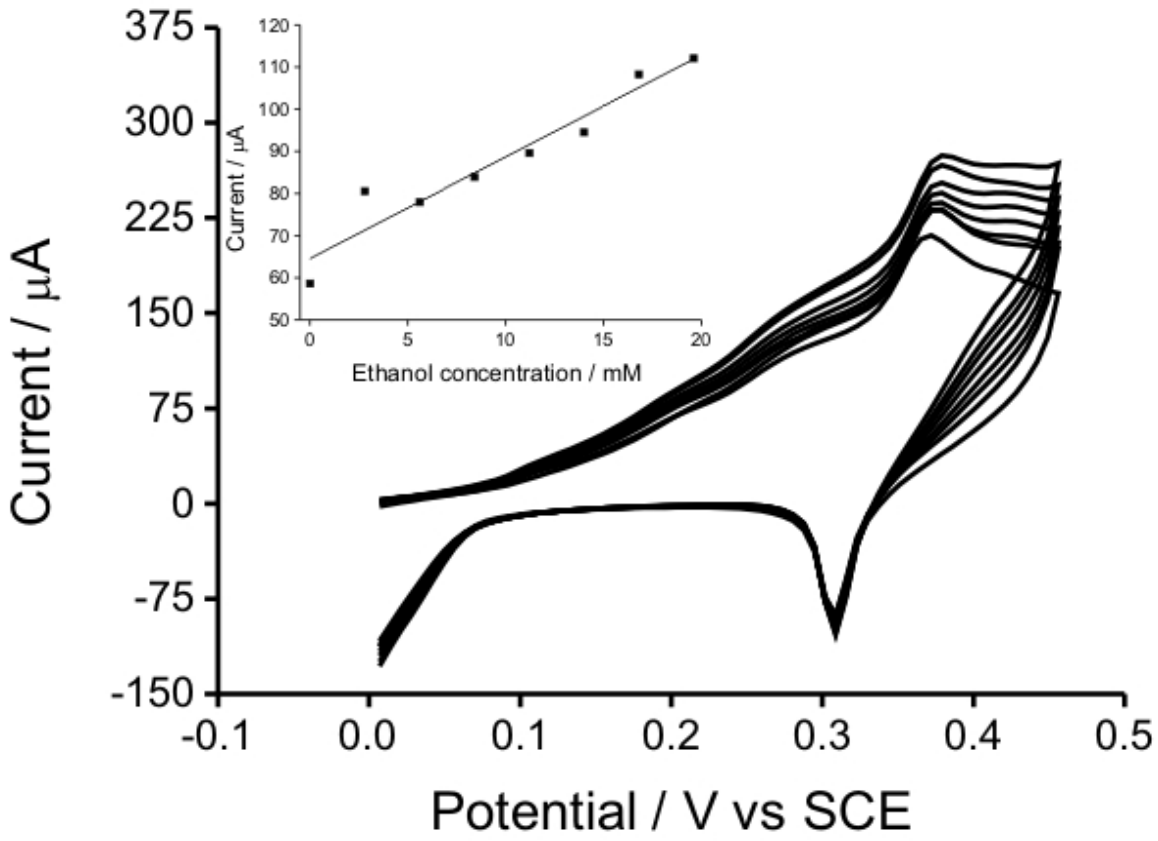


Figure 8.12: *Overlay of eleven successive CVs following 10, 2.8 mM additions of ethanol to a 1.0 M KOH solution, using the nickel bulk electrode, deaerated. Inset – Calibration plot for NiOOH peak height vs. ethanol concentration*

8.3.3.2. Glycerol

The same experiments as discussed above were performed with 23 μM additions of glycerol to a 1.0 M KOH solution. Again, the bare BDD electrode did not give any response to the glycerol additions, even at relatively high concentrations (23 mM), whereas the Ni-BDD gave a very clear response. In Figure 8.13 the additions of glycerol to the Ni-BDD electrode are shown, with the corresponding calibration plot of peak height to glycerol concentration inset.

The calibration plot was linear with an R^2 value of 0.998 and a limit of detection of 1.03 $x10^{-5}$ M of glycerol. The sensitivity was much greater for the glycerol detection also, giving a value of 35 mA/M of glycerol. The average LOD for glycerol additions was observed to be 1.71 $x10^{-5}$ M over three experiments using a 'freshly' prepared Ni-BDD in

each instance therefore demonstrating good reproducibility of the method and modified electrode performance.

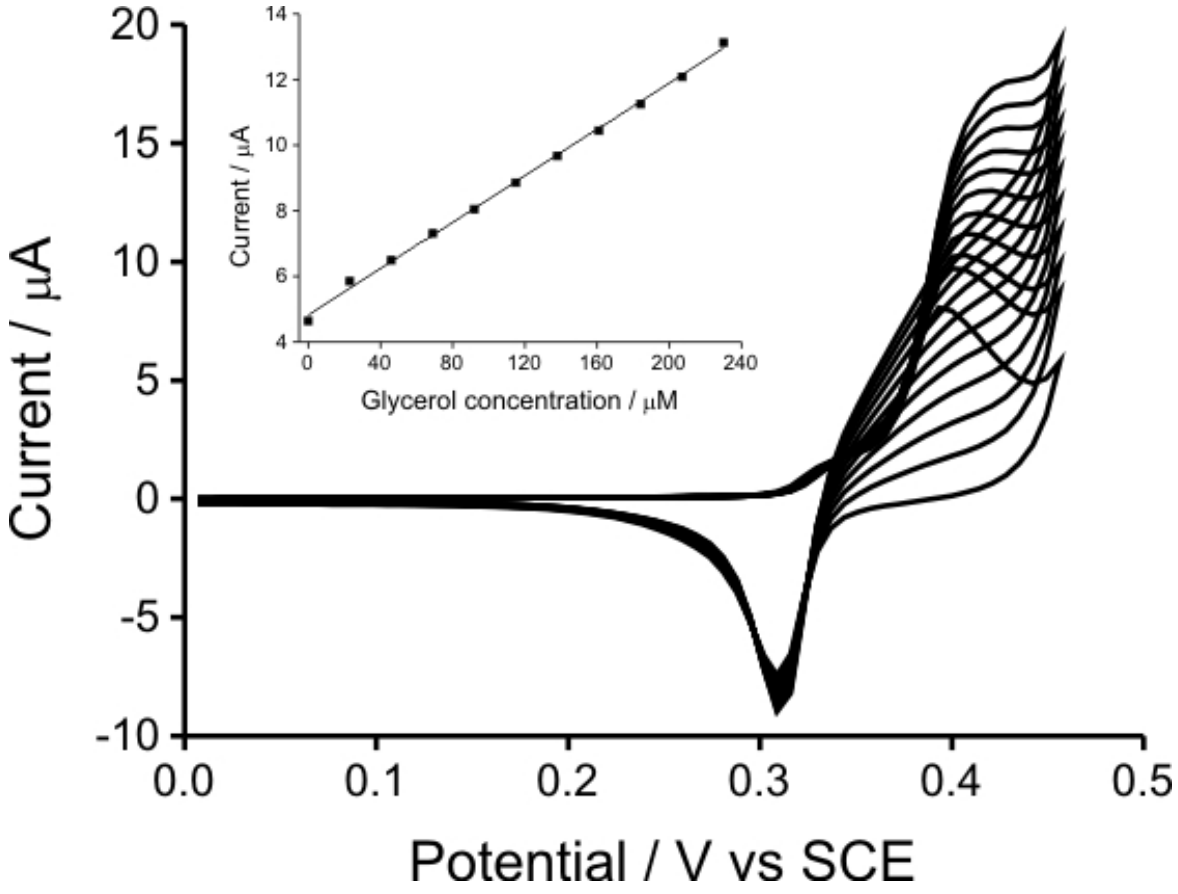


Figure 8.13: *Overlay of eleven successive CVs following ten, 23 μM additions of glycerol to a 1.0 M KOH solution, using the Ni-BDD, deaerated. Inset – Calibration plot for NiOOH peak height vs. glycerol concentration*

The equivalent bulk nickel experiment was more successful for the glycerol additions than the ethanol, as can be seen in Figure 14. The NiOOH peak enhancement was better observed, providing a linear calibration plot (inset) of R^2 = 0.992 and a limit of detection of 2.2 x10^{-5} M. The Ni-BE sensitivity was 279 mA/M, again significantly greater than for the Ni-BDD, but for the same reason of relative nickel surface area.

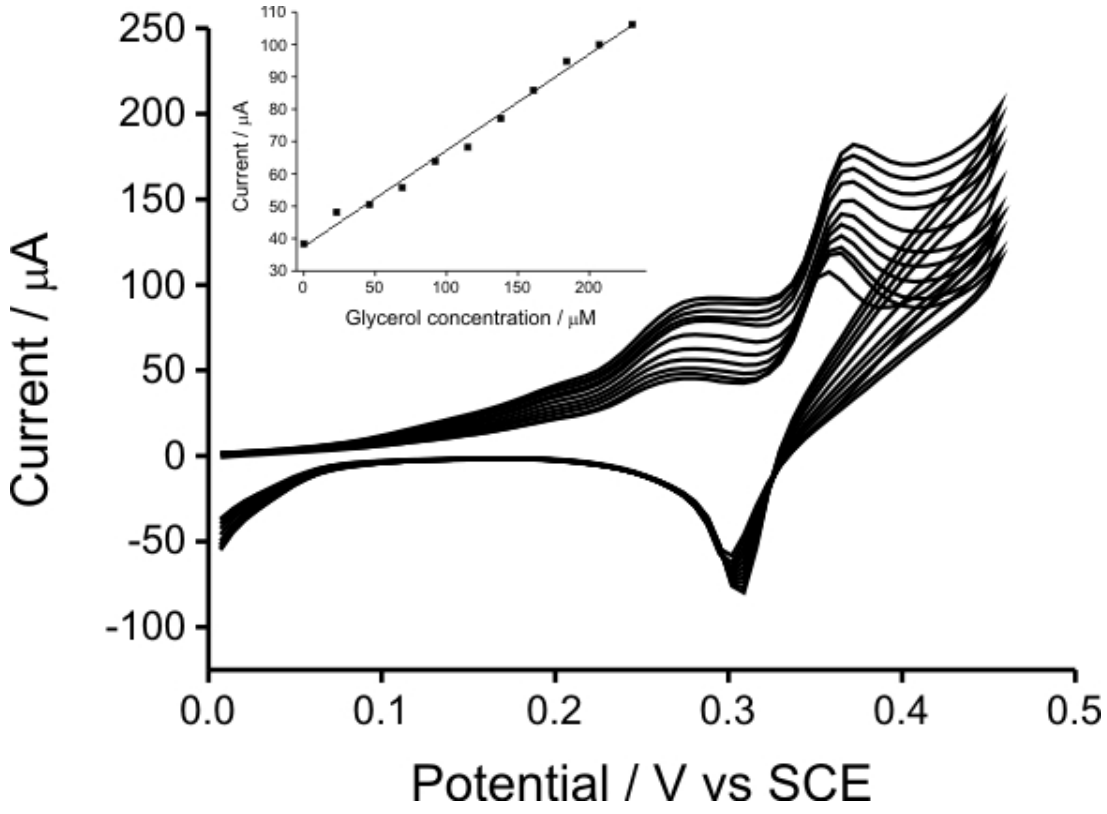


Figure 8.14: *Overlay of eleven successive CVs following ten, 23 μM additions of glycerol to a 1.0 M KOH solution, using the nickel bulk electrode, deaerated. Inset – Calibration plot for NiOOH peak height vs. glycerol concentration*

8.3.4 Comparison of electrochemical methanol sensors

Despite a large volume of research dedicated to methanol oxidation, relatively very little has utilized the electrocatalytic oxidation of the alcohol in its detection. Table 1 details *all* the literature regarding electrochemical methanol detection, including the electrode used, method of analysis, limits of detection, linear range and sensitivity when reported. The table is divided into nickel based electrodes, other electrodes and gaseous methanol detection.

Alcohol levels may be determined by three primary methods; 1) solid state electrodes 2) gas chromatography and 3) enzymatic analysis on automated analysers or spectrophotometers. Many of these analytical approaches utilize electrochemical reactions to establish alcohol concentration, predominantly amperometric methods in which small changes in current over time relating to the electrooxidation or reduction of the analyte can

be observed and quantified, yet there are numerous advantages and disadvantages to each method. Gas chromatography is a sensitive method but it requires expensive laboratory equipment that is quite exclusive, and the analyte must be in a gaseous state for detection. Enzymatic systems are fragile, requiring extensive electrode preparation and optimum pH and temperature conditions at all times. The direct oxidation and reduction of alcohols by non-biological electrodes however can be robust, renewable, and experimentally diverse in its approach, and can also be a low cost and simple system.

In Table 1 reported limits of detection vary from 15 nM [23] to 1.9 mM [60], though there is great discrepancy between the linear ranges, sensitivity and, in particular method, for determining the LOD between the data. Amperometric methods feature significantly as a detection method, though the coupling of the technique with flow injection analysis (FIA) and/or liquid chromatography (LC) is shown to greatly improve detection limits.

Platinum [4, 5, 7, 34, 35] and ruthenium [5] modified electrodes are listed a number of times in the table due to their well known application as catalysts in direct methanol fuel cells. The references report micromolar limits of detection for platinum in amperometric systems coupled with FIA and/or LC, and the mixed valent ruthenium electrode reportedly giving the 15 nM LOD, though the corresponding linear range and sensitivity are evidently not comparable with the LOD reported. Though the stated LODs are up to 100 fold lower than the Ni-BDD, platinum is a precious metal and relatively much higher cost than nickel. It is therefore not realistic as a commercial sensor, especially if disposable devices are sought. The ruthenium with carbon paste electrode is reportedly less sensitive than the Ni-BDD however, despite coupling with FIA.

Of the nickel based electrode modifications [7], all report a lower detection limit for methanol than the Ni-BDD electrode, with only one reporting a comparable detection limit of 0.125 mM [32, 60, 64-66]. The latter publication was the only other publication to report an alternative method of calculating LOD to S/N=3 however. Three of the reported modifications are highly elaborate [11] and involve extensive electrode preparation.

Table 1: A comparison of methanol analysis conducted by electrochemical methods reported in the literature. The table reports the electrode used, method of detection, medium of analysis, limit of detection (LOD), method of determining the LOD, linear range and sensitivity of the system.

Electrode	Method	Medium	LOD	LOD meth.	Linear range	Sensitivity	Ref
NICKEL ELECTRODES							
CEF[a] -Ni(II)/chitosan GC[b]	amperometry	NaOH	5.24 µM	S/N = 3	20 µM to 12 mM	none given	[11]
Ni/Al-Cl anionic clay	amperometry/ CV	NaOH	0.125mM	intercept x 3 s.d	2-4000 ppm	none given	[5, 34]
GC Ni modified	amperometry/ FIA	NaOH	0.31 µM	S/N = 3	1.6 µM to 3.12 mM	1.3µA mM^{-1}	[4]
Pt with Ni oxide surface	amperometry	NaOH	0.05 mM	S/N = 3	none given	0.36µA mM^{-1}	[7]
NiII-DHS (N,N bis ligands)[c]	amperometry/CV	NaOH	26 nM	S/N = 3	0.050 to 0.30 µM	74 mA cm^2 mol^{-1} M^{-1}	[35]
OTHER ELECTRODES							
Pt bulk electrode	FIA/ LC/amperometry	acid	37 µM	S/N =3	37 – 624 µM	none given	[61]
Pt - GC	FIA/ LC/amperometry	acid	56 µM	S/N =3	56 µM – 3.1 mM	none given	[61]
Pt	PAD, CV, chromatography	MSA	14.81µM	S/N = 3	25.18–30,000 µM	none given	[62]
Pt	Pulsed amp/ LC	HClO4	0.16 µM	S/N =3	none given	383 pA/ppm	[31]
RuO_2 and RuCN[d] / GC	FIA/ LC/amperometry	H_2SO_4	15 nM	S/N =3	1.5-200 mM	15 nA/mM	[23]
RuO_2-C paste electrode	amperometry, FIA	NaOH	1.2 mM	none given	5-50 mM	1.86 nA/mM	[63]
Alc. Ox[g] enzyme	amperometric det. of H_2O_2	phosphate buffer	none given	none given	0.31µM to 0.4 mM	none given	[64]
Alc. Ox gelatin matrix/ Clark O_2 electrode	amperometric/FIA	phosphate	none given	none given	10 mM to 300 mM	none given	[65]
OCS[e] modified with MDH[f]	amperometry	phosphate buffer	none given	none given	none given	none given	[60]
GC CME[i] with MDH	amperometric	tris/HCl buffer	0.5 µM	S/N = 3	0.5-200 µM	none given	[66]
C paste/ Alc. Ox and HRP[h]	amperometry/FIA/ column LC	phosphate buffer	ca. 0.8µM	none given	0.8µM-2mM	none given	[32]
C paste Pd	amperometry	NaOH/$NaClO_4$	1.9 mM	none given	100-5000 mgL-1	1µA mM-1	[67]
bare BDD	amperometry	K_2 SO_4	none given	none given	none given	none given	[68]
GASEOUS SYSTEMS							
SnO_2 semiconductor	vapour/ avometer	air	0.05 g L^{-1}	none given	none given	none given	[69]
QCM[j] coated with PANI[k]	vapours	air	none given	none given	none given	1.75-4.05 Hz/ppm	[70]
Ppy/PVA[l] composite and pure polypyrrole	VOC sampling system	air	none given	none given	49-1059 ppm	none given	[71]
RuCN/GC/ Nafion	amperometric	air	none given	none given	2-5 µM	0.80 - 0.05 nA µL-l	[23]

This contrasts the simple and reproducible fabrication process of the Ni-BDD electrode. The nickel oxide electrode [5, 34] was fabricated on a platinum surface, thus negating the cost effectiveness of a nickel system. The chemically fabricated nickel modified glassy carbon electrode [4] is a more simplistic system akin to the Ni-BDD electrode, yet it is the one electrode coupled with FIA, and accordingly nanomolar detection limits are reported.

The enzyme based electrodes [7] are quite limited on analytical information, stating moderate linear ranges despite coupling with FIA or LC, and in one instance detecting H_2O_2 in an indirect analysis of methanol concentration.

Overall, nickel and platinum electrodes are shown to be the best methanol sensors, demonstrating comparable sensory ability with respect to methanol. Although the other nickel modified electrodes were reported to give lower LOD than the Ni-BDD, the difference was not excessive, and given the complexity of some of the systems compared to the simplicity of the BDD modification, the Ni-BDD may have a more viable application as a methanol sensor. It is also believed that on optimization and coupling of the Ni-BDD with FIA and/or LC much lower LODs, higher sensitivities and wider linear ranges would be obtained. Furthermore it is difficult to compare with the limit of detection method of "S/N=3" stated in most of the tabled references, as details as to how to make the measurement of either 'S' or especially 'N' are typically not provided.

8.4. Conclusions

A nickel microparticle modified boron doped diamond (Ni-BDD) has been fabricated by simple electrochemical deposition from a $Ni(NO_3)_2$ solution. Characterisation by SEM has estimated a relative mass of 50 μg cm^{-2} and 34 μg cm^{-2} of nickel to be present on the surface following 600s and 300 s deposition times respectively. The Ni-BDD modified for 600 s was also conditioned to enrich the $Ni(OH)_2$ layers, and an estimated 1.63 mol cm^2 of $Ni(OH)_2$ available for catalysis was determined from cyclic voltammetry.

Methanol, ethanol and glycerol were electrocatalytically oxidised by the $Ni(OH)_2$ species formed in the 1M KOH medium to give a quantifiable signal that was analysed by cyclic voltammetry and/or amperometric methods. Ethanol and glycerol concentrations were determined using cyclic voltammetry at Ni-BDD electrodes modified for 300s with nickel. The ex-situ application of the Ni-BDD to the electrocatalysis of ethanol and glycerol oxidation provided micromolar detection limits from highly linear calibration plots. The electrocatalytical ability of the nickel nanoparticles is evident, and provides a lower LOD than the nickel bulk electrode. In this simple approach, ethanol was determined to concentrations of 1.8 mM and glycerol to concentrations of 10.3 μM.

The 600s Ni-BDD was sensitive to methanol concentrations over a linear range for 0.5 to 500 mM, with a limit of detection calculated as 0.28 mM and a sensitivity of 110 nA/mM of methanol. For comparison of the bulk material to the random microparticle array, a nicekl foil electrode was also conditioned in 1 M KOH and subsequently used in the oxidation of methanol. The limit of detection for the foil electrode was calculated as 1.61 mM of methanol with a sensitivity of 27 nA/mM. This was a higher LOD by almost an order of magnitude and a sensitivity of one quarter the Ni-BDD, concluding that the random microparticle array was analytically superior.

In the review of electrochemical methanol sensors lower detection limits of methanol were reported compared to the Ni-BDD, yet none of the literature was directly comparable due to discrepancy in limit of detection determination. Further to this, the nickel electrodes reported mostly involved highly complicated modification of the surface. The Ni-BDD therefore offers ease of fabrication, a renewable surface and a relatively low cost approach to sensitive alcohol detection.

8.5. References

[1] M. Fleischmann, K. Korinek, D. Pletcher, *J. Electroanal. Chem.* **(1971)** 31, 39.

[2] C. Pang, M. Chen, T. Lin, T. Chou, *Electroanalysis* **(2001)** 13, 499.

[3] M.A. Abdel Rahim, R.M. Abdel Hameed, M.W. Khalil, *J. Power Sources* **(2004)** 134, 160.

[4] I.G. Casella, T.R.I. Cataldi, A.M. Salvi, E. Desimoni, *Anal. Chem.* **(1993)** 65, 3143.

[5] B. Ballarin, R. Seeber, D. Tonelli, C. Zanardi, *Electroanalysis* **(2000)** 12, 434.

[6] A. Ciszewski, *Electroanalysis* **(1995)** 7, 1132.

[7] B.S. Hui, C.O. Huber, *Anal. Chim. Acta* **(1991)** 243, 279.

[8] A. Kowal, S.N. Port, R.J. Nichols, *Catal. Today* **(1997)** 38, 483.

[9] A.A. El-Shafei, *J. Electroanal. Chem.* **(1999)** 471, 89.

[10] A.N. Golikand, S.M. Golabi, M.G. Maragheh, L. Irannejad, M. Asgari, *J. Iran. Chem. Soc.* **(2007)** 4, 304.

[11] Y. Liu, S. Luo, W. Wei, X. Liu, X. Zeng, *Microchim. Acta* **(2009)** 164, 351.

[12] P.M. Robertson, *J. Electroanal. Chem.* **(1980)** 111, 97.

[13] I. Carpani, D. Tonelli, *Electroanalysis* **(2006)** 18, 2421.

[14] A. Safavi, N. Maleki, E. Farjami, *Biosens. Bioelectron.* **(2009)** 24, 1655.

[15] M. Li, S. Xu, F. Ni, Y. Wang, S. Chen, L. Wang, *Microchim. Acta* **(2009)** 166, 203.

[16] K. Ohnishi, Y. Einaga, H. Notsu, C. Terashima, T.N. Rao, S. Park, A. Fujishima, *Electrochem. Solid-State Lett.* **(2002)** 5, D1.

[17] R. Ojani, J. Raoof, S. Fathi, *Electroanalysis* **(2008)** 20, 1825.

[18] G. Yang, E. Liu, N.W. Khun, S.P. Jiang, *J. Electroanal. Chem.* **(2009)** 627, 51.

[19] J. Qiao, H. Li, S. Shuang, C. Dong, *Res. Rev. Electrochem.* **(2008)** 1, 1.

[20] C. Lamy, A. Lima, V. LeRhun, F. Delime, C. Coutanceau, J. Leger, *J. Power Sources* **(2002)** 105, 283.

[21] E. Antolini, *J. Power Sources* **(2007)** 170, 1.

[22] L. Cao, G. Sun, H. Li, Q. Xin, *Electrochem. Commun.* **(2007)** 9, 2541.

[23] T.R.I. Cataldi, D. Centonze, A. Guerrieri, *Anal. Chem.* **(1995)** 67, 101.

[24] O. Savadogo, F.J.R. Varela, *J. New Mater. Electrochem. Syst.* **(2008)** 11, 69.

[25] Z. Wang, P. Zuo, G. Wang, C. Du, G. Yin, *J. Phys. Chem. C* **(2008)** 112, 6582.

[26] C. Xu, P.k. Shen, Y. Liu, *J. Power Sources* **(2007)** 164, 527.

[27] R. von Helmolt, U. Eberle, *J. Power Sources* **(2007)** 165, 833.

[28] M. Fleischmann, K. Korinek, D. Pletcher, *J. Chem. Soc. , Perkin Trans. 2* **(1972)**1396.

[29] G. Vertes, G. Horanyi, *J. Electroanal. Chem.* **(1974)** 52, 47.

[30] R. Barnard, C.F. Randell, F.L. Tye, *J. Appl. Electrochem.* **(1980)** 10, 109.

[31] W.R. LaCourse, D.C. Johnson, M.A. Rey, R.W. Slingsby, *Anal. Chem.* **(1991)** 63, 134.

[32] K. Johansson, G. Joensson-Pettersson, L. Gorton, G. Marko-Varga, E. Csoregi, *J. Biotechnol.* **(1993)** 31, 301.

[33] I.L. De Mattos, D. Melo, E.A.G. Zagatto, *Anal. Sci.* **(1999)** 15, 537.

[34] B. Ballarin, R. Seeber, D. Tonelli, A. Vaccari, *J. Electroanal. Chem.* **(1999)** 463, 123.

[35] M. Revenga-Parra, T. Garcia, E. Lorenzo, F. Pariente, *Sens. Actuators, B* **(2008)** B130, 730.

[36] I. Danaee, M. Jafarian, F. Forouzandeh, F. Gobal, M.G. Mahjani, *Int. J. Hydrogen Energy* **(2008)** 33, 4367.

[37] J. Gao, T. Arunagiri, J. Chen, P. Goodwill, O. Chyan, J. Perez, D. Golden, *Chem. Mater.* **(2000)** 12, 3495.

[38] K.J. McKenzie, D. Asogan, F. Marken, *Electrochem. Commun.* **(2002)** 4, 820.

[39] G. Zhao, X. Tong, Z. Hu, X. Xiao, D. Li, *Electrochim. Acta* **(2008)** 53, 4283.

[40] O. Chailapakul, E. Popa, H. Tai, B.V. Sarada, D.A. Tryk, A. Fujishima, *Electrochem. Commun.* **(2000)** 2, 422.

[41] C. Chang, L. Chen, S. Liu, H. Chang, *J. Phys. Chem. B* **(2006)** 110, 19426.

[42] C. Chang, L. Chen, S. Liu, H. Chang, *Anal. Lett.* **(2006)** 39, 2581.

[43] M. Chang, C. Gao, J. Jiang, *J. Electrochem. Soc.* **(2009)** 156, E50.

[44] G.M. Swain, R. Ramesham, *Anal. Chem.* **(1993)** 65, 345.

[45] H. Bode, K. Dehmelt, J. Witte, *Electrochim. Acta* **(1966)** 11, 1079.

[46] J. Desilvestro, D.A. Corrigan, M.J. Weaver, *J. Electrochem. Soc.* **(1988)** 135, 885.

[47] D.M. MacArthur, *J. Electrochem. Soc.* **(1970)** 117, 422.

[48] M.A. Hopper, J.L. Ord, *J. Electrochem. Soc.* **(1973)** 120, 183.

[49] R.S. Schrebler Guzman, J.R. Vilche, A.J. Arvia, *J. Appl. Electrochem.* **(1978)** 8, 67.

[50] R.S. Schrebler Guzman, J.R. Vilche, A.J. Arvia, *J. Appl. Electrochem.* **(1979)** 9, 183.

[51] W. Visscher, E. Barendrecht, *J. Electroanal. Chem.* **(1983)** 154, 69.

[52] J.F. Wolf, L.S.R. Yeh, A. Damjanovic, *Electrochim. Acta* **(1981)** 26, 409.

[53] J.F. Wolf, L.S.R. Yeh, A. Damjanovic, *Electrochim. Acta* **(1981)** 26, 811.

[54] P. Oliva, J. Leonardi, J.F. Laurent, C. Delmas, J.J. Braconnier, M. Figlarz, F. Fievet, A. De Guibert, *J. Power Sources* **(1982)** 8, 229.

[55] H. Bode, K. Dehmelt, J. Witte, *Z. Anorg. Allg. Chem.* **(1969)** 366, 1.

[56] R.S.S. Guzman, J.R. Vilche, A.J. Arvia, *J. Electrochem. Soc.* **(1978)** 125, 1578.

[57] G.W.D. Briggs, P.R. Snodin, *Electrochim. Acta* **(1982)** 27, 565.

[58] A.J. Bard, L.R. Faulkner, *Electrochemical methods : fundamentals and applications*, 2nd edition, John Wiley & Sons, New York ; Chichester, **2001**, p. 833.

[59] C.M.A. Brett, A.M.O. Brett, *Electroanalysis*, Oxford University Press, Oxford, **1998**.

[60] S. Zhao, R.B. Lennox, *Anal. Chem.* **(1991)** 63, 1174.

[61] I.G. Casella, *Anal. Chim. Acta* **(1995)** 311, 37.

[62] J. Cheng, P. Jandik, X. Liu, C. Pohl, *J. Electroanal. Chem.* **(2007)** 608, 117.

[63] D. Leech, J. Wang, M.R. Smythe, *Electroanalysis* **(1991)** 3, 37.

[64] G. Bardeletti, C. Carillon, *Appl. Biochem. Biotechnol.* **(1993)** 43, 177.

[65] H. Belghith, J.L. Romette, D. Thomas, *Biotechnol. Bioeng.* **(1987)** 30, 1001.

[66] Q. Liu, J.R. Kirchhoff, *J. Electroanal. Chem.* **(2007)** 601, 125.

[67] X. Cai, K. Kalcher, *Electroanalysis* **(1994)** 6, 397.

[68] C. Chang, L. Chen, S. Liu, H. Tien, H. Chang, *J. Chin. Chem. Soc.* **(2006)** 53, 839.

[69] R. Ramon, J.X. Feliu, O. Cos, J.L. Montesinos, F.X. Berthet, F. Valero, *Biotechnol. Lett.* **(2004)** 26, 1447.

[70] M.M. Ayad, G. El-Hefnawey, N.L. Torad, *J. Hazard. Mater.* **(2009)** 168, 85.

[71] L. Jiang, H. Jun, Y. Hoh, J. Lim, D. Lee, J. Huh, *Sens. Actuators, B* **(2005)** B105, 132.

Chapter 9

Overall Conclusions

Boron doped diamond (BDD) electrodes have been demonstrated to be excellent substrate materials for modification by metal nanoparticles and subsequent application to electroanalysis. The characteristic low capacitance of BDD makes it an ideal substrate for sensitive, dynamic electroanalytical experiments, a consistent advantage to the systems described, resulting in reduced signal-to-noise and consequently lower detection limits. Improved selectivity and sensory ability is also frequently noted, as the otherwise insensitive unmodified BDD electrode is electrochemically activated towards certain analytes by the presence of the metal modification. The BDD electrode is readily and renewably modified with a variety of metals, allowing one substrate for many nanoparticle modifications. Specifically, the electrodeposited metal nanoparticle modification of BDD offers a simple yet effective approach to enhancing the electroanalytical ability of the relatively unexplored electrode material.

The use of bismuth or antimony to modify boron doped diamond electrodes for improved simultaneous detection of cadmium and lead has been presented. Most notably was that the presence of antimony or bismuth allowed for simultaneous determination of lead and cadmium at the BDD electrode, that otherwise did not occur due to interference between the analytes in deposition. Bi-modified BDD electrodes have been shown to be a promising and reliable analytical candidate for the detection of low concentration heavy metals. The comparison of a bare BDD electrode and bismuth modified electrode has shown that the presence of bismuth allows the detection of lead to a 10 fold lower detection limit of 1.9 μgL^{-1}, and a 3 fold increase in peak current. In this preliminary investigation, the detection of lead and cadmium as individual analytes was not improved by the presence

of antimony, particularly evident in the case of cadmium, in which the metal remained undetectable to concentrations of 150 μgL^{-1} present.

A nickel modified BDD electrode and nickel foil bulk electrode have been directly compared in their application towards the electrocatalytic oxidation of glucose in alkali solution. Both electrodes gave comparable performances, providing a linear range over three orders of magnitude from 10 μM to 10 mM, encompassing the human blood sugar levels of approximately 3 to 8 mM. The sensitivity was high with values of 1.04 and 0.67 $mA\ mM^{-1}\ cm^{-2}$ observed, and amperometric analysis determined glucose limits of detection (3σ) of 1.8 and 2.7 μM, for the foil and BDD electrodes respectively.

Non-enzymatic glucose electrodes were discussed in an extensive literature review of the area. They were found to offer high sensitivity, the possibility of long term stability, a resistance to thermal implications, and a low cost, simple and reproducible fabrication method, yet renewed approach to their design and development is required to surpass enzymatic glucose sensors. The nickel microparticle modified BDD electrode and nickel foil electrodes have shown a very good response to glucose determination in alkali solutions. Comparison to other non-enzymatic electrodes shows that the nickel electrodes reported here offer comparable detection limits, and higher than average sensitivity to glucose, especially the Ni-BDD electrode. The Ni-BDD was also extended to the catalytic oxidation of primary alcohols, giving low detection limits, comparable to other non-enzymatic systems.

Throughout this thesis an electrochemical atomic force microscope (EC-AFM) cell has been used to investigate the nucleation and growth of nanoparticles onto the BDD surface. The EC-AFM cell was developed during this DPhil in an industrial collaboration with Asylum Research Ltd. The project was successful and the development and application of EC-AFM techniques is shown to be further improving the extent of particle growth control, allowing for surface characterization almost simultaneously to deposition.

APPENDIX 1

Asylum Research EC-AFM commercial cell brochure

Owing to the nature of this document it cannot be included in the digital version of this thesis. To find the brochure please refer to the hard bound copy of this thesis, or try the following internet link;

http://www.asylumresearch.com/Products/ECCell/ECCell.shtml

Much of the information detailed in the brochure is also presented in Chapter 3 of this thesis.